INFLUENCE OF TEST CONDITIONS ON POST-PEAK DEFORMATION BEHAVIOR OF ROCK

by

Yuhang Xu

A dissertation submitted in partial fulfillment
of the requirements for the degree of
Doctor of Philosophy (PhD) in Natural Resources Engineering

The Faculty of Graduate Studies
Laurentian University
Sudbury, Ontario, Canada

THESIS DEFENCE COMMITTEE/COMITÉ DE SOUTENANCE DE THÈSE
Laurentian Université/Université Laurentienne
Faculty of Graduate Studies/Faculté des études supérieures

Title of Thesis Titre de la thèse	INFLUENCE OF TEST CONDITIONS ON THE POST-PEAK DEFORMATION BEHAVIOR OF ROCKS
Name of Candidate Nom du candidat	Xu, Yuhang
Degree Diplôme	Doctor of Philosophy
Department/Program Département/Programme	Natural Resources Engineering
Date of Defence Date de la soutenance	April 10, 2017

APPROVED/APPROUVÉ

Thesis Examiners/Examinateurs de thèse:

Dr. Ming Cai
(Supervisor/Directeur(trice) de thèse)

Dr. Dean Millar
(Committee member/Membre du comité)

Dr. Eugene Ben-Awuah
(Committee member/Membre du comité)

Dr. Mike Yao
(Committee member/Membre du comité)

Dr. Hani Mitri
(External Examiner/Examinateur externe)

Dr. Nelson Belzile
(Internal Examiner/Examinateur interne)

Approved for the Faculty of Graduate Studies
Approuvé pour la Faculté des études supérieures
Dr. David Lesbarrères
Monsieur David Lesbarrères
Dean, Faculty of Graduate Studies
Doyen, Faculté des études supérieures

ACCESSIBILITY CLAUSE AND PERMISSION TO USE

Abstract

Understanding the post-peak deformation behavior of rock is important for underground rock engineering. Laboratory property testing is commonly employed to investigate the post-peak deformation behavior. However, the test conditions of laboratory testing, especially the Loading System Stiffness (*LSS*) of stiff test machines, are usually varied and the influence of this variation on the test results has not been fully elucidated. In addition, studying the influence of test conditions on the post-peak deformation behavior of rock is crucial for interpreting test results and subsequently applying the results to rock engineering design.

The goal of this dissertation is to identify how the post-peak deformation behavior of a rock specimen is affected by three major aspects of test conditions—the specimen geometry, the contact conditions, and the *LSS*. To achieve this goal, an FEM/Explicit tool was employed to carry out numerical experiments, in which the same material property was assumed for the rock specimens and each wanted test condition was isolated for analysis.

The well-observed slenderness effect and the recently-observed cross-sectional shape effect on the Uniaxial Compressive Strength (UCS) of rocks were studied. The modeling results suggest that the numerical tool and models are suitable for investigating the problem and the hoop tension theory could be flawed. Next, the cross-sectional shape effect on the post-peak deformation behavior was investigated. The modeling results reveal that although the influence of the cross-sectional shape on the UCS of rocks is small, the cross-sectional shape affects the post-peak deformation behavior considerably.

The actual contact condition and the end effect in true triaxial compression tests were simulated while the legitimate intermediate principal stress (σ_2) effect was excluded from the rock material

model. The modeling results reveal that the end effect can result in an apparent σ_2 effect if the contacts are frictional and the specimen in the σ_2 loading direction is squat. Thus, existing 3D empirical failure criteria based on previous true triaxial compression test results may overestimate the rock strength.

The influence of *LSS* on the post-peak stress–strain relations of stable rock failure was examined. Key loading components of stiff test machines were considered in the numerical model. The modeling results clarify that *LSS* affects the post-peak stress–strain curves of rocks even when the failure process is stable. Unless *LSS* is either perfectly rigid or equivalent to the critical *LSS* (λ), the post-peak stress–strain curves obtained under various *LSS* (with $LSS > \lambda$) are varied and all steeper than the one under an ideal loading condition.

This dissertation demonstrates the cross-sectional shape effect in the post-peak deformation stage, the long overlooked σ_2 effect caused by the end effect, and the variation of post-peak stress–strain curves due to the *LSS*. This dissertation also makes a contribution to examining the hoop tension theory and recognizing the correct choice of cross-sectional shape for test specimens, offers insights into improving 3D empirical failure criteria and true triaxial test settings, and suggests new requirements for developing stiff test machines in the future.

Keywords

Post-peak deformation behavior, stable rock failure, test conditions, laboratory property testing, numerical experiment, cross-sectional shape effect, end effect, loading system stiffness

Original Contributions

This dissertation aims at making contributions to understanding how the post-peak deformation behavior of rock is affected by test conditions in laboratory property testing. Some challenging issues are addressed and new methods are developed and the results are presented in respective chapters. Major contributions of the dissertation are listed below:

- Examined the hoop tension theory by considering rectangular-shaped specimens in numerical experiments in addition to numerically calibrating the recently-observed laboratory test results on different cross-sectional shaped specimens (Chapter 3).

- Demonstrated and clarified the cross-sectional shape effect and its impact on the post-peak deformation behavior of rock (Chapter 3).

- Recognized the correct choice of cross-sectional shape of specimens for presenting laboratory test and numerical modeling results consistently (Chapter 3).

- Confirmed the long overlooked σ_2 effect caused by the end effect in true triaxial compression tests, and stressed its potential influence on interpreting true σ_2 effect and the development 3D empirical failure criteria (Chapter 4).

- Proposed a method to quantify the end effect in true triaxial compression test results for improving 3D empirical failure criteria in the future (Chapter 4).

- Explored the influence of *LSS* on the stable post-peak failure of rocks by realistically simulating stiff test machines, and demonstrated that the post-peak stress–strain curves of rocks obtained in laboratory testing can be affected by *LSS* (Chapter 5).

- Suggested new requirements for developing stiff test machines in the future to obtain more meaningful test results for the rock engineering design (Chapter 5).

- Demonstrated the theory that depending on the *LSS* of a test machine, the stored energy of the test machine alone without additional energy supply for deforming rock specimens can drastically change rock failure types (Appendix A).

Acknowledgements

This research was supported by the Natural Sciences and Engineering Research Council of Canada (NSERC).

I would like to first thank my dissertation supervisor, Dr. Ming Cai, for offering me the opportunity of being here in Canada and opening myself up to an exciting new endeavour. His incessant prodding, invaluable counsel, and intellectual guidance made the successful completion of my dissertation possible. His patience and understanding allowed me to achieve a proper balance between academic pursuit and my other interests in life such as Marathon running and others. I have been inspired by Dr. Cai's academic integrity and dedication to work.

I also gratefully acknowledge the other members of my committee, Drs. Mike Yao, Dean Millar, and Eugene Ben-Awuah, for reviewing my research report and dissertation, attending my defences, and providing technical advice. In addition, I would like to thank my program coordinators, Drs. Ramesh Subramanian and Krishna Challagulla, for their persistent help.

Lastly, my thanks to all my colleagues at MIRARCO and the university, my friends at the university gymnasium, Sudbury Canoe club, and the Running Room in Sudbury, and other individuals including Frank Silc, Raymond Pong, and Hélène Lawler. Their much needed support, encouragement, and advice helped me considerably in the past three and a half years.

My parents, Yafei Xu and Niande Xu, as well as my other relatives, deserve special mention and my profound gratitude. Since my childhood, they have fostered my educational pursuit motivationally, financially, and in many other ways.

This dissertation is dedicated to my deceased but still beloved grandparents. They harbored great hopes that I would one day become a well-educated person. I hope I have lived up to their expectations.

Table of Contents

List of Tables

List of Figures

List of Symbols

A	Cross-sectional area (mm^2)
c	Cohesion (MPa)
c_r	Residual cohesion (MPa)
D	Diameter (mm)
δ	Displacement (mm)
$\Delta\sigma_1$	Increase of peak strength due to $\Delta\sigma_3$ (MPa)
$\Delta\sigma_2$	Difference between applied σ_2 and applied σ_3 (MPa)
$\Delta\sigma_3$	Difference between actual σ_3 and applied σ_3 (MPa)
ΔE_{in}	Energy input from an external energy source during post-peak deformation stage (J)
ΔE_r	Energy consumed in a rock during post-peak deformation stage (J)
ΔE_r^B	Energy item ΔE_r under the ideal loading condition (J)
ΔE_t	Energy released from a test machine (J)
$\Delta V/V$	Volumetric strain (%)
E	Young's modulus (GPa)
E_p	Post-peak stiffness of a rock specimen in stress–strain curve (GPa)
E_{in}	Accumulative energy input from an external energy source at peak load (J)
E_r	Accumulative energy consumed in a rock specimen at peak load (J)
E_t	Strain energy stored in a test machine at peak load (J)
E_{in}^*	Accumulative energy input from an external energy source at post-peak deformation stage (J)
E_r^*	Accumulative energy consumed in a rock specimen at post-peak deformation stage (J)
E_t^*	Strain energy stored in a test machine at post-peak deformation stage (J)
ε / ε_1	Strain / axial strain (%)
F_n	Normal force at a contact (N)
F_f	Friction force at a contact (N)
H	Height (mm)
φ	Friction angle (◦)
k	Stiffness of a column-shaped structure (GN/m)
λ	Post-peak stiffness of a rock specimen (GN/m)
μ	Coefficient of friction
μ_s	Coefficient of sliding friction of crack surfaces
ν	Poisson's ratio
ρ	Density (kg/m^3)
σ_1 / σ_2 / σ_3	The maximum / intermediate / minimum principal stress (MPa)
σ_c	Uniaxial compressive strength (MPa)
σ_t	Tension cut-off (MPa)
W	Width (mm)
ψ	Dilation angle (◦)

List of Acronyms

BEM	Boundary Element Method
DEM	Discrete Element Method
EDZ	Excavation Damaged Zone
FDM	Finite Difference Method
FEM	Finite Element Method
FLAC	Fast Lagrangian Analysis of Continua
GSI	Geological Strength Index
H-B	Hoek-Brown
H/*D*	Height to Diameter ratio
H/*W*	Height to Width ratio
ISRM	International Society of Rock Mechanics
LMS	Local Mine Stiffness
LSRI	Loading System Reaction Intensity
LSS	Loading System Stiffness
M-C	Mohr-Coulomb
PFC	Particle Flow Code
RT	Room Temperature
SMs	Suggested Methods
UCS	Uniaxial Compressive Strength

Preface

This research work has been accomplished at MIRARCO (Mining Innovation Rehabilitation and Applied Research Corporation) and the Bharti School of Engineering, Laurentian University, under the supervision of Prof. Ming Cai, and with the financial support of NSERC. Laboratory work was partially supported by the Beijing Research Institute of Uranium Geology and Northeastern University, both in China.

Three major studies of this dissertation are primarily presented from Chapter 3 to Chapter 5. The results presented in Chapter 3 are published in the proceedings of the 49th U.S. Rock Mechanics/Geomechanics Symposium, San Francisco, U.S. (Xu and Cai, 2015). More comprehensive results presented in Chapter 3 have been published in the journal of Computers and Geotechnics (Xu and Cai, 2017). The results presented in Chapter 4 have been published in the Canadian Geotechnical Journal (Xu and Cai, 2016a). The results presented in Chapter 5 have been submitted for publication in the journal of Rock Mechanics and Rock Engineering (Xu and Cai, 2016b).

The heuristic studies on the application of the three studies mentioned above in rock engineering and mining engineering are reflected in Section 4.4.5, Section 5.2.4, and Appendix A, respectively. Some follow-up work on these studies will be made and it is planned to submit the results to rock engineering related journals for publication in the future.

Chapter 1

1 Introduction

1.1 Statement of problem

1.1.1 Research background

Reliable estimation of rock strength is required for almost any form of analysis in rock engineering design (Hoek, 2007). However, estimating rock strength is a difficult and challenging task. As the rationale behind founding the International Society of Rock Mechanics (ISRM) in the 1960s, Leopold Muller explained that he did so "*because we do not know the rock mass strength*" (cited in Hudson, 2008). Fifty years later, the requirement for engineers to have a better knowledge of rock strength still holds true. A reliable estimation of rock strength is particularly critical for structures built on or in rocks, such as slopes, dam foundations, and underground excavations. In such cases, due to either loading of overburden or unloading of confining pressure, the rocks can go through a process of cracking, fracturing, and faulting, reaching its maximum load-carrying capacity and leading to a post-peak deformation response (Lo and Lee, 1973; Kawamoto et al., 1988; Ofoegbu and Curran, 1991; Martin and Chandler, 1994; Eberhardt et al., 1998; Cai et al., 2004a; Paterson and Wong, 2005). Therefore, in order to support the long-term operational safety of rock structures, it is crucial to estimate not only the peak strength but also understand the post-peak deformation behavior of rock.

Today, surface and shallow natural resources are being depleted rapidly and some mining operations are migrating to deep grounds where hard rocks are often encountered (e.g., mines in Sudbury, Canada). The rocks in such cases are subjected to high in situ stresses because of the great depths (Ingles et al., 1973; Zoback, 1992; Kaiser et al., 2001; Martin et al., 2003). Consequently, rocks near an underground opening are more likely driven into the post-peak

deformation stage, often resulting in strain-softening and brittle failures (Figure 1-1; details on the classification of post-peak deformation behaviors of rock are discussed in Section 2.4.1), leaving rocks exposed to a highly burst-prone ground condition (Bieniawski, 1968; Kaiser, 1996; Ortlepp, 1997; Hoek et al., 2000; Kaiser et al., 2000).

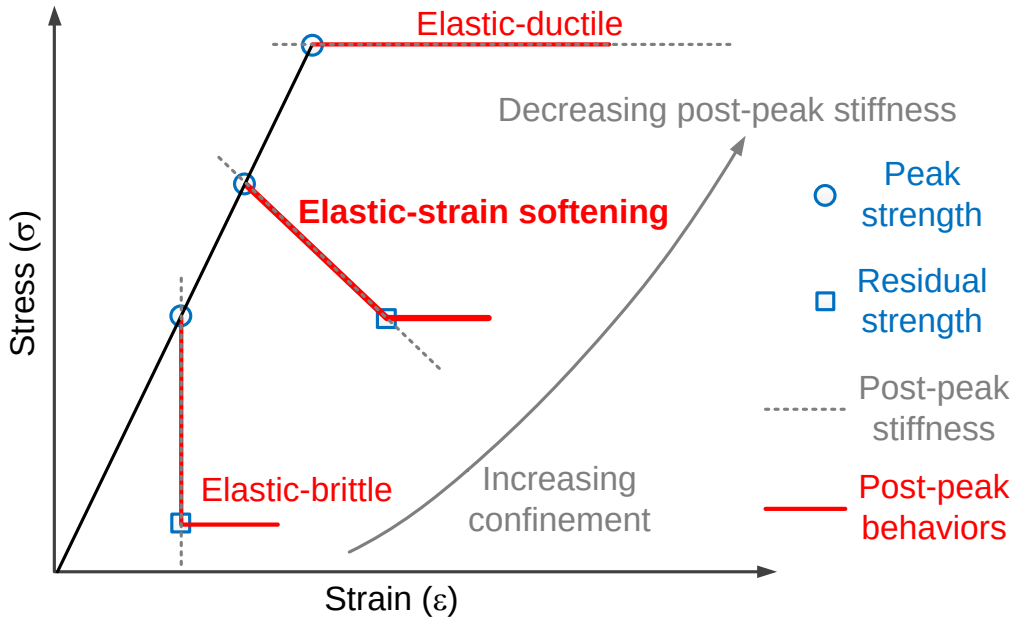

Figure 1-1 Simplified post-peak deformation behaviors of rock under different confining pressures, after Fang and Harrison (2001) and Hoek (2007).

The engineering significance of having a good knowledge of the post-peak deformation behavior of rock is closely related to two three aspects of ground control practices (Figure 1-1). First, the rock strength parameters, including the peak and residual in the post-peak deformation stage, provide key parameters for estimating the shape of an Excavation Damaged Zone (EDZ) (Egger, 2000; Varas et al., 2005; Park and Kim, 2006; Wang et al., 2011). Accurate estimation of an EDZ is important for obtaining a realistic ground response curve, and hence for ensuring a safe and economic support design (Alonso et al., 2003; Lee and Pietruszczak, 2008; Cai and Kaiser, 2014). Second, the relation between the post-peak deformation behavior of a pillar under

compression and Local Mine Stiffness (LMS) determines the likelihood of violent pillar failure (Salamon, 1970; Zipf, 1992b; Morsy and Peng, 2002). In addition, the post-peak deformation behavior can be used to predict the duration of rock failure as a result of rock creep (Goodman, 1989). Accordingly, provided that the post-peak deformation behavior of rock and pillars can be well understood, the confidence in predicting rock instability can be increased and the cost of rock support can be reduced.

1.1.2 Research motivation

Rock laboratory testing is one of the most straightforward approaches to investigate the post-peak deformation behavior of rock. Although theoretical efforts have been made to develop rock constitutive models in terms of stress–strain relation, existing models still cannot predict post-peak deformation behavior with a reasonable level of confidence (Read and Hegemier, 1984; Bazant et al., 1984; Claborn, 1988; Ofoegbu and Curran, 1992; Shao and Rudnicki, 2000). Similarly, the empirical approach has been used to characterize the failure process of rock but so far it has met with limited success in predicting post-peak deformation behavior of rock (Lockner, 1998a; Fang and Harrison, 2002; Joseph and Barron, 2003; Yuan and Harrison, 2004; Alejano and Alonso, 2005; Zhao and Cai, 2010; Han et al., 2012).

The major thrust of development in rock mechanics is rock laboratory testing (Ulusay, 2015a). Since this field's inception, rock laboratory testing has been proven to be useful, either as a research tool to assist in modeling rock behavior (Golder and Akroyd, 1954; Jaeger, 1960; Cook, 1965; Bieniawski, 1966; Mogi, 1967; Wiebols and Cook, 1968; Wawersik and Fairhurst, 1970; Young, 1993; Martin, 1997; Stephansson, 2001; Zhao et al., 2013), or as a practical tool to provide mechanical input parameters for rock engineering design (Carneiro, 1943; Terzaghi, 1946; Kaiser and McCreath, 1992; Amadei and Stephansson, 1997; Hoek and Brown, 1997;

Zhao, 2000; Cai et al., 2004a; Barla et al., 2007; Sakurai et al., 2009; Feng and Hudson, 2011). With the development of stiff and servo-controlled test machines, the post-peak deformation behaviors of most rock types can be observed in a well-controlled manner, and the strength parameters that characterize the post-peak stress–strain curve of rock under a specific loading condition can be obtained (Hudson et al., 1972b). Thus, rock laboratory testing is currently regarded as one of the most common approaches for studying the post-peak deformation behavior of rock.

Understanding the influence of test conditions on the post-peak deformation behavior of tested rock specimens is critical for rock engineering design. Laboratory studies have revealed that the way a test is performed has a pronounced influence on the post-peak deformation behavior (Hawkes and Mellor, 1970; Rummel and Fairhurst, 1970; Wawersik and Brace, 1971; Brown et al., 1972; Mogi, 1974; Kimura et al., 1987; Martin, 1997; Bobet, 2001; Mishra and Nie, 2013). In other words, the post-peak deformation behavior of a rock obtained by laboratory testing is not only a function of the real mechanical properties of the rock, but also affected by the experimental conditions and techniques used to obtain it. Furthermore, loading conditions of in situ rocks are complicated by local geology and geometry, mining sequences, etc., (Martin and Chandler, 1994; Kaiser et al., 2001; Cai, 2008a; Brady and Brown, 2013), and it is therefore erroneous to simply take the post-peak stress–strain curve of a rock specimen recorded in the laboratory and extrapolate it to the same rock in the field (Brady and Brown, 2013).

It is important to first understand the influence of test conditions on the post-peak deformation behavior of rock at the laboratory scale, because the loading conditions at the field scale are usually more complicated than those at the laboratory scale. The test conditions on a rock specimen in laboratory testing (Figure 1-2) include specimen geometry (e.g., slenderness ratio

and cross-sectional shape of the specimen), contact conditions (e.g., end effect in true triaxial compression test), Loading System Stiffness (*LSS*), and loading conditions (e.g., confining pressure, stress path, and strain rate) (Hudson and Harrison, 2000). Although routine rock laboratory testing follows the guidelines suggested by the ISRM—so that differences such as the slenderness ratios of tested specimens and loading conditions carried out in different laboratory tests can be minimized—the exact cross-sectional shape of a specimen is not specified in the guidelines (Fairhurst and Hudson, 1999; Ulusay, 2015b). In addition, the *LSS* values of various test machines apparently differ, as do the contact conditions. Hence, it is necessary to understand how the post-peak deformation behavior of a rock specimen is affected by those test conditions in laboratory property testing.

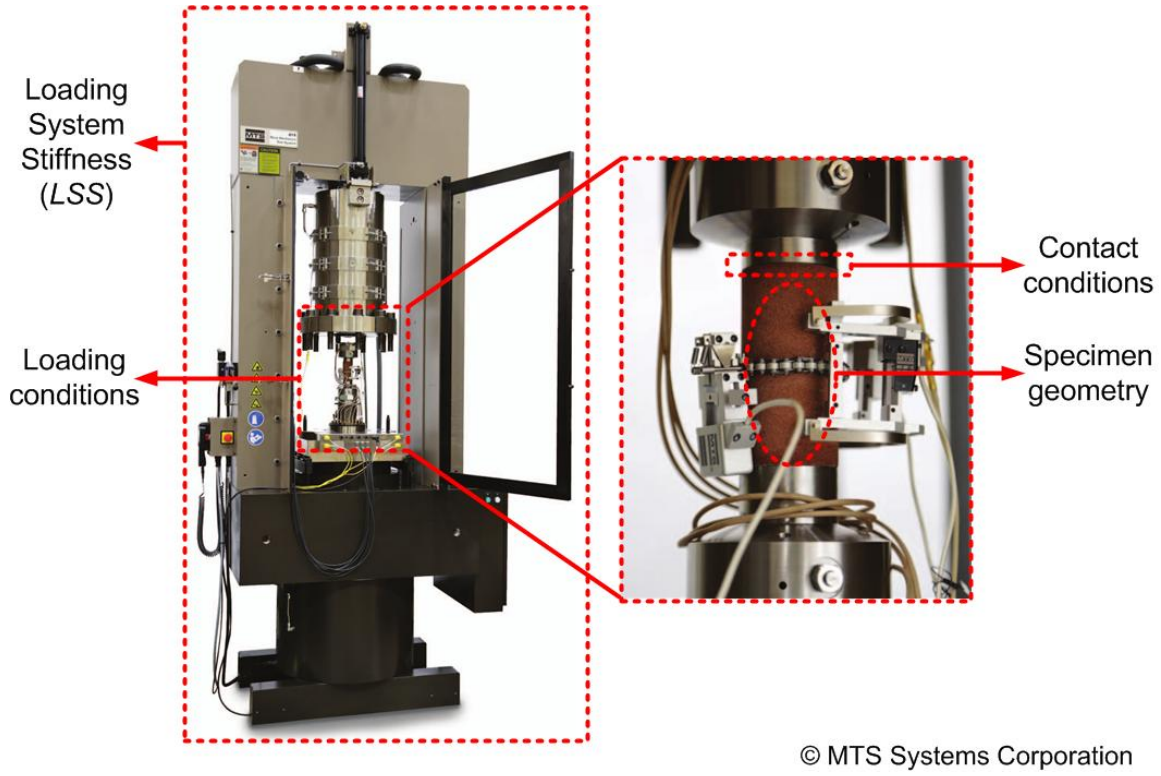

Figure 1-2 Illustration of the test conditions of a rock specimen during laboratory testing (MTS 815 as an illustration).

1.1.3 Research objectives

This dissertation focuses on the following four major research objectives:

(1) To study the geometry effect of rock, i.e., the cross-sectional shape effect and the strength and deformation behaviors of different cross-sectional-shaped specimens in laboratory uniaxial compression test.

(2) To study the end effect in laboratory true triaxial compression test, i.e., the influence of the end effect in true triaxial compression test on the observed intermediate principal stress (σ_2) effect and the post-peak deformation behavior of rock.

(3) To study the influence of *LSS* of stiff test machines on the stress–strain relations of rock in laboratory uniaxial compression test. This is the most important research topic because it has never been investigated thoroughly before. The potential influence of *LSS* on the stable post-peak failure of rocks will be clarified.

(4) To study the influence of strain energy released from test machines on the rock failure process.

Although estimating rock behavior at the field scale is the ultimate goal of rock engineering design, the scope of research in this dissertation is restricted to the laboratory scale for two major reasons. First, the test conditions in laboratory tests are simple and explicit whereas the loading conditions in situ are complicated. It is practical to prescribe and quantify the laboratory test conditions. Second, laboratory test results of intact rocks are important for estimating the rock mass strength (Bieniawski, 1976; Bieniawski, 1989; Hoek and Brown, 1997). For instance, the Hoek-Brown (H-B) failure criterion (Hoek et al., 2002) is widely used to estimate the strength of

jointed rock masses. With the knowledge of two parameters obtained from laboratory tests—the Uniaxial Compressive Strength (UCS) and the m_i value of the intact rock—together with the Geological Strength Index (GSI) that estimates the reduction in rock mass strength for different geological conditions, both the peak and the residual strengths of jointed rock masses can be reasonably estimated (Cai et al., 2004b; Cai et al., 2007).

The test conditions at the laboratory scale, including specimen geometry, contact conditions, *LSS*, and loading conditions, are considered in the investigation. As will be discussed in the literature review (Chapter 2), the slenderness ratio (height to diameter ratio, *H*/*D*, or height to width ratio, *H*/*W*) and the size of the tested specimen as well as the adopted loading conditions when performing a routine laboratory test are well-guided by the ISRM Suggested Methods (SMs) for rock characterization (Ulusay, 2015b). Hence, these test conditions are not focused in this dissertation.

This research also focuses on the post-peak deformation behavior of rock obtained by laboratory testing under various test conditions. Understanding the rock behavior in compression is important for rock engineering design. Therefore, rock laboratory property testing considered in this research is restricted to uniaxial compression test, conventional triaxial compression test, and true triaxial compression test. The stress–strain curves of rock specimens, especially in the post-peak deformation stage, are treated with priority in the discussion of the influence of test conditions on the rock behavior. To obtain the post-peak stress–strain curve of intact rock specimens, violent rock failures must be avoided and the loading condition is advised to be quasi-static loading (Cook, 1965).

It is necessary to stress that the laboratory property testing is important for the preliminary stage of engineering design where pre-existing methods and back analysis are sometimes restricted. Laboratory test results, however, are not the only data that determines the final design for rock engineering (Jing and Hudson, 2002; Bewick et al., 2015). The challenging issue of "scaling" laboratory test results to in situ rock mass behaviors should be addressed in rock engineering design (Pariseau, 2007). However, this issue is beyond the major research objectives of this dissertation. Some heuristic studies on applying the implications gained from this research to engineering design are briefly discussed (refer to research approaches in Section 1.2.3).

1.2 Research approaches

1.2.1 Numerical experiment

The numerical experiment approach is adopted in this research because rock property and test conditions can be specified and controlled explicitly in numerical modeling, whereas applying the laboratory test approach to study the influence of test conditions on the post-peak deformation behavior of rock is not a straightforward task due to the following reasons.

First, it is impractical to find specimens with the same rock property for testing and comparison (Zhao et al., 2015). The heterogeneous nature of rock becomes dominant in the post-peak deformation stage when local failures occur (Rudnicki and Rice, 1975; Bobet and Einstein, 1998; Hudson and Harrison, 2001), making it impossible to obtain identical stress–strain curves of rock specimens even if their test conditions are the same. Thus, when different test conditions are introduced in laboratory testing, it is hard to scrutinize if the differences in stress–strain curves are caused by the material heterogeneity of the specimens themselves or by the test conditions.

Second, using the laboratory test approach to study the role of test conditions in affecting laboratory test results is a paradox. Ideally, the influence of all the test conditions except an ideal loading condition[1] for obtaining the base case (obtained under the ideal loading condition) should be excluded at first. Then the influence of each individual test condition on the post-peak deformation behavior of rock can be investigated by introducing the wanted test condition into the test. However, all the test conditions are bounded by the testing process and the unwanted test conditions cannot be excluded completely from a laboratory test.

Additionally, laboratory test does not lend itself to such a situation where a solely wanted test condition is isolated for a parametric study, because different test conditions in a laboratory test mutually interact with each other. For instance, the end effect resulted by the friction at the rock specimen-metal platen contacts is also affected by the specimen geometry (Xu and Cai, 2015).

Lastly, some of the test conditions are difficult to measure and vary in laboratory tests. For instance, there is no agreed method to measure *LSS* in laboratory tests (Van Mier et al., 1997), and it is also impractical to vary *LSS* over a large range. Therefore, conducting laboratory tests to investigate how different test conditions affect the post-peak deformation behavior is untenable.

On the other hand, the numerical experiment approach provides a promising platform to overcome those difficulties lying in the laboratory test approach. The numerical experiment approach can be used to gradually decode the mechanism that governs a physical model, starting from simulating a simplified model with some necessary assumptions and ending up simulating more complicated and realistic models if the mechanism is well understood at an increased confidence level. In this study, the post-peak deformation behavior of rock is first calibrated

[1] A loading condition defined as free from the influence of LSS (refer to Section 5.1.2 for more details).

without considering the influence of test conditions, i.e., the rock is subjected to the ideal loading condition. Next, the sensitivity of the response of a rock subjected to a wanted test condition can be simulated independently, by excluding the influence of other test conditions. In this fashion, based on the comparison of the post-peak deformation behaviors resulted from the same test condition with different parameters, the post-peak deformation behavior of rock under each test condition can be revealed.

The numerical experiments begin with calibrating those well-understood phenomena observed in laboratory tests, such as the slenderness effect in uniaxial compression test. A full verification of the numerical model by comparing the modeling results with the test results in every aspect is impossible, but the confidence in the numerical model can be raised when the modeling results are successfully calibrated against the strengths and failure modes recorded in well-controlled laboratory tests. Next, with an improved knowledge gained from the numerical experiments on the studies of some test conditions, especially the contact behavior at the rock specimen-metal platen contacts, the numerical model can be applied to study test conditions that cannot be easily observed or measured in laboratory tests, e.g., the end effect in true triaxial compression test and the influence of *LSS* on stable rock failure. Thus, different test conditions in rock laboratory testing can be studied independently through a comprehensive numerical experiment approach.

1.2.2 Numerical modeling tool

Numerical experiment is suitable for this research, but the choice of the right modeling tool is important. The first step in numerical experiment is the conceptualization of the physical model regarding the dominant processes (Jing, 2003), i.e., the mathematical presentation of the dominate physical processes leads to the determination of modeling tool. As stated in Section 1.1.3, this research focuses on the test conditions in a rock specimen-test machine system and

their roles in affecting the peak strength and the post-peak deformation behavior of rock. The physical processes include the interactions between the rock specimen and the test machine, the collective structural response of the rock specimen-test machine system, and the overall post-peak stress–strain curves of rock, in response to different compression tests where the rock specimens are subjected to a quasi-static loading. In summary, an accurate presentation of the numerical model is required for obtaining structural response of the rock specimen-test machine system and the consequent macroscopic post-peak deformation behavior of rock.

The contact behavior that dominates the structural response of the rock specimen-test machine system is complicated (Wriggers, 2006; Laursen, 2013). The material behavior of rock in the post-peak deformation stage normally experiences a strain-softening behavior (Martin and Chandler, 1994; Lockner, 1995; Vardoulakis et al., 1998). Therefore, the main mathematical presentation of the physical processes is a macroscopic continuum constitutive model under a quasi-static loading condition, involving nonlinear contact behaviors and nonlinear material property. The adopted modeling tool should be robust and economical to implement these mathematical presentations.

The first step of selecting a numerical tool is to choose the numerical method. Finite Element Method (FEM), Boundary Element Method (BEM), and Discrete Element Method (DEM) are widely used to study rock deformation behaviors. FEM is a continuum based method used very early in rock mechanics, and long considered as an effective method for rock engineering design (Obert and Duvall, 1967; Zienkiewicz et al., 1969; Nayak and Zienkiewicz, 1972; Naylor et al., 1981; Hoek, 2007; Beck, 2015). FEM has well-recognized advantages in dealing with nonlinear material property and complex contact behaviors (Zienkiewicz and Taylor, 2005). Many FEM commercial software tools with proven maturity are used in rock engineering and many other

engineering fields (Potts et al., 2001). The shortcoming of FEM is that its modeling results are sometimes mesh-dependent, which is an unsettled problem in numerical modeling in continuum mechanics (Pietruszczak and Mroz, 1981; Needleman, 1988; Munjiza and John, 2002; Cook, 2007).

BEM has been successfully used for simulating fracture processes in solids including rocks (Katona, 1983). It is useful for stress analysis of excavation, where only the boundary of the excavation is divided into elements and the far field is represented as an infinite continuum (Zipf, 1992a; Cerrolaza and Garcia, 1997; Hoek, 2007). However, compared with domain discretization methods such as FEM, the benefit of using BEM is diminished when contact geometry is complex and material behavior is nonlinear and inelastic (Beskos, 1987; Jing and Hudson, 2002).

DEM employs small particles and their interactions to describe the microscopic physical evolution of rock. As a result, it not only gives a look into the micromechanics of the rock failure process that cannot be observed in laboratory tests (Cundall, 1971; Cundall, 1988) but also avoids the discretion of selecting an empirical failure criterion that only reflects the macromechanical behavior of rock (Yuan and Harrison, 2006; Ghazvinian et al., 2012; Lisjak and Grasselli, 2014). The disadvantage that hinders a wide application of DEM in rock engineering design is its prohibitive computational costs when dealing with large-scale models with many contacts. Moreover, the micromechanical parameters used in DEM are hypothetical and cannot be measured in laboratory tests. These parameters can only be obtained by trials-and-errors in the calibration process while they are changed systematically until a set of parameters yield a macroscopic behavior that best fits the actual one (Potyondy and Cundall, 2004; Cai, 2008a; Wang and Tonon, 2009; Sainsbury et al., 2011).

FEM is adopted in this numerical experiment because the method is adequate for the proposed research objectives (Section 1.1.3). First, precise modeling the fracture process of rock using DEM is not necessary, because the macroscopic responses of rocks such as the stress–strain curves in the post-peak deformation stage are the research interest. In addition, rock empirical failure criteria that characterize the macroscopic behaviors of rocks well can be easily incorporated in FEM tools and the parameters of empirical failure criteria (e.g., Mohr-Coulomb failure criterion) can be readily obtained by laboratory tests.

The second advantage of using an FEM tool for this research is that it can simulate the structural response of large-scale complex structures at a low computation cost. For instance, it is planned that those loading components (e.g., loading platen, loading frame, and fluid ram) consisting in a stiff test machine will be considered in the research objective (3) – *LSS*. If a DEM tool is used, the great computation cost can hinder a comprehensive parametric study on the influence of *LSS* on rock deformation behaviors.

Thirdly, the contact behaviors in both the normal and shear directions of the rock specimen-metal platen contacts need to be updated continuously in the numerical experiment, which can be handled well by FEM. As for the inherent mesh sensitivity of FEM, it is a fundamental problem of incorporating plastic analysis in a discretization tool (Needleman, 1988; Cook, 2007). If the mesh sizes for all the rock specimens under same test condition of various parameters are relatively fine and their shapes are the same (e.g., hexahedron), numerical errors associated with mesh size are minimized and a relative comparison of the modeling results can be made because all the models are within the same order of numerical errors.

The next step of selecting a numerical tool is to determine the algorithm for the numerical solutions. Explicit and implicit algorithms are available in FEM to integrate the discretized equations associated with time. The explicit algorithm updates the unknown field explicitly, while the implicit algorithm updates the unknown field implicitly by solving an algebraic equation. The computation cost of the explicit algorithm is low because neither iteration nor convergence checking is required for solving nonlinear problems, but the time incremental of which has to be small enough to achieve numerical stabilization. The implicit algorithm provides analysis capabilities for studying a wide variety of nonstructural problems, but its solution is hard to converge compared with explicit algorithm especially for problems associated with nonlinear materials and contact behaviors. In addition, the implicit algorithm can be much difficult to implement in a numerical tool (Hibbitt et al., 2011).

Again, it is the mathematical presentation leads to the selection between these two algorithms. First, the implicit algorithm is only suitable to find converge solutions of strain-hardening behavior, not the strain-softening behavior. The post-peak deformation behaviors of rocks are normally strain-softening, and in such a case the implicit algorithm will face a numerical singularity problem because the negative post-peak modulus can produce a non-positive definite structural stiffness matrix (Nayak and Zienkiewicz, 1972; Sture and Ko, 1978; Frantziskonis and Desai, 1987). Moreover, the contact behavior is highly nonlinear, in which little success can be made by using the implicit algorithm, and this is especially true for 3D problems involving contacts that need to be updated continually. Lastly, the loading rate applied to stable rock failures in laboratory tests is quasi-static (Lockner et al., 1991). For this class of loading condition, it is computationally impractical to model the process in its natural time period. Artificially increasing the speed of the loading rate to the quasi-static loading in the simulation is

necessary to obtain an economical solution. Because neither iteration nor convergence checking is required by the explicit algorithm, it is well-suited for quasi-static problems in which inertia forces are still insignificant. Therefore, a powerful explicit algorithm should be available in the chosen FEM tool.

Considering all the merits and demerits of available numerical tools, the software package ABAQUS, developed by 3DS, is employed to carry out the numerical experiment. ABAQUS is a powerful FEM tool in solving highly nonlinear system problems under transient loads by employing the explicit solver. It is also robust to solve problems involving complex boundary conditions with efficient contact convergence and oscillation control.

1.2.3 Summary of research approaches

The goal of this dissertation is to identify how the post-peak deformation behavior of a rock specimen is affected by three aspects of test conditions—the cross-sectional shape of the specimen, the end effect in true triaxial compression test, and the *LSS* of stiff test machines. To achieve this goal, the FEM ABAQUS/Explicit tool is employed to carry out a comprehensive numerical experiment, in which the same material property is assumed for the rock specimen and each wanted test condition is isolated for analysis.

Figure 1-3 presents a flow chart that summarizes the research topics and the adopted research approaches in this dissertation. Rectangular-boxed texts illustrate test conditions that can or might affect the post-peak deformation behavior of rock in laboratory testing. Rectangular-boxed texts with colored shade illustrate the research topics to be discussed in this dissertation. In particular, red texts with green shade illustrate the research objectives that will be focused using the numerical experiment approach, because others either have been well-studied using the

laboratory test approach (represented by rectangular-boxed texts with dash lines), or can be well-guided by the ISRM SMs to minimize their differences in laboratory tests (details on selecting the research objectives are discussed in Chapter 2).

First, the well-observed slenderness effect in uniaxial compression test ($\sigma_2 = \sigma_3 = 0$) will be examined in the numerical experiment (Chapter 3). Based on the modeling results of the slenderness effect, the recently-observed cross-sectional shape effect on the UCS of cylindrical and square cross-sectional-shaped specimens (Zhao et al., 2015) will be calibrated (Chapter 3). The modeling results obtained from these two numerical experiments can demonstrate the capability of the numerical models for studying the geometry effect of rock and the end effect in uniaxial compression test.

The second study is to examine the end effect in triaxial compression test (Chapter 4). The slenderness effect observed in conventional triaxial compression test ($\sigma_2 = \sigma_3 > 0$) will be modeled first, as a means to examine the capability of the chosen numerical tool for studying the end effect in true triaxial compression tests. Next, the actual contact behavior at the rock specimen-steel platen contacts and the end effect in true triaxial compression test ($\sigma_2 > \sigma_3 \geq 0$) will be simulated.

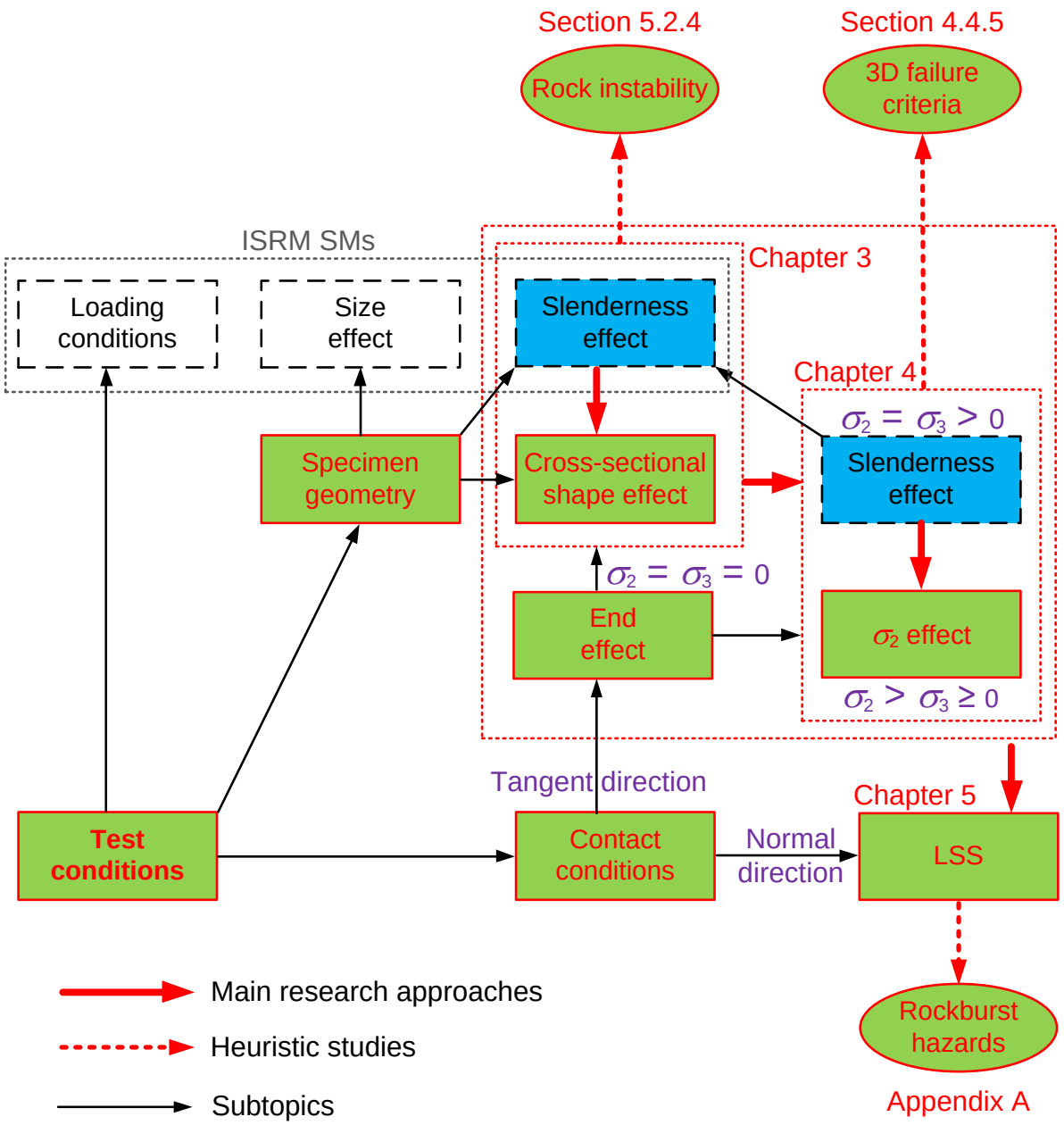

Figure 1-3 Flow of research topics and approaches in this dissertation.

Finally, with sufficient knowledge of the geometry effect and the end effect in rock laboratory testing gained from the above studies, a detailed numerical model that can realistically characterize the structural response of the rock specimen-stiff test machine system will be built

(Chapter 5). This numerical model will be employed to investigate the influence of *LSS* on the stable failure of rock.

Once these three major studies on the test conditions in laboratory testing have been completed, it is planned that the insights gained from these studies can be applied to assisting rock engineering design (illustrated as red dash arrows and texts in ellipses). For instance, the study of the cross-sectional shape effect can be useful for making the correct choice of the cross-sectional shape of pillars in pillar design. These heuristic studies are reflected in Section 4.4.5, Section 5.2.4, and Appendix A.

1.3 Scope of work

This dissertation comprises primarily three numerical studies, with results presented in Chapters 3 to 5. A brief summary of each chapter of this dissertation is provided below.

Chapter 1 provides an introduction into the research background, the motivation for carrying out the research, and its engineering significance. Three major research objectives are discussed, the research approaches are presented, and the reasoning for selecting the numerical tool to address the research objectives is justified.

Chapter 2 is a detailed literature review of the influence of different test conditions on the post-peak deformation behavior of rock. The test conditions that are less-studied and without clear guidelines (e.g., ISRM SMs) to unify them in laboratory tests are focused in this dissertation. These test conditions lead to the cross-sectional shape effect, the end effect in the true triaxial compression test, and the potential influence of *LSS* on the poste-peak deformation behavior of rock.

Chapter 3 presents the study of the cross-sectional shape effect in uniaxial compression test. First, the well-observed slenderness effect was captured by the numerical modeling. Next, the test results of the cross-sectional shape effect on the UCS of cylindrical and square shaped specimens were calibrated by the numerical modeling. A comprehensive numerical experiment was then carried out to study whether different cross-sectional-shaped rock specimens with the same slenderness ratio result in different post-peak deformation behaviors or not.

Chapter 4 focuses on the end effect in true triaxial compression test and its influence on the interpretation of the σ_2 effect. Previous laboratory test results were selected for numerical calibration. The legitimate σ_2 effect was excluded from the numerical modeling while the actual rock specimen-steel platen contact condition was realistically characterized. The contribution of the end effect to the observed σ_2 effect was further verified by bringing the theoretical σ_2 effect into account, and later confirmed by a follow-up laboratory work. With the confidence in the numerical model, the influence of the end effect on the post-peak deformation behavior of rock in true triaxial compression test was studied.

Chapter 5 aims at demonstrating that stable post-peak failure of rocks is affected by *LSS*. To overcome the shortcomings of previous numerical work, key loading components that contribute to the *LSS* of stiff test machines were considered in the test machine models. Moreover, the mechanism of different post-peak stress–strain curves caused by different test machine models was clarified with the insights gained from the numerical modeling.

Chapter 6 summaries the main achievements of this dissertation and closes it with suggestions for future work.

Chapter 2

2 Literature review on test conditions in laboratory compression tests of rock

A review of the literature on some of the test conditions in laboratory rock compression tests is presented in this chapter. These test conditions include the geometry of rock specimens, the contact conditions at the rock specimen-metal platen contacts, the *LSS* of test machines, and the loading conditions employed.

2.1 Specimen geometry

Rock is a special solid geomaterial that possesses two pronounced geometry effects which can complicate the test results. First, the strength of a rock is affected by the shape of the tested specimen, which is called the shape effect. The shape effect includes the influence of the slenderness ratio and the cross-sectional shape of a specimen on rock strength. Second, the strength of a rock specimen varies with specimen size, which is called the size effect.

2.1.1 Slenderness effect

The geometry effect of rock is best known by the slenderness effect on rock strength, which is a well-studied subject from the 1960s to the 1990s (Babcock, 1969; Brady, 1971; Kotsovos, 1983; Tang et al., 2000). Slenderness effect becomes significant in strengthening rock strength in squat specimens (Babcock, 1968; Hoskins and Horino, 1968; Thuro et al., 2001). Jaeger and Cook (1979) stated that compared with confining pressure, temperature, and loading rate, which affect the rock strength, the slenderness ratio played the most important role in underground pillar designs (Van Heerden, 1975; Bieniawski, 1984; Martin and Maybee, 2000).

It is generally assumed that the central zone at the mid-height of a slender specimen in uniaxial compressive loading is subjected to a uniform uniaxial stress state (Hudson and Harrison, 2000). For the hard contact condition (Figure 2-1a), a rock specimen in compression tends to expand radially relative to the metal platens (steel platens in general) due to the elastic mismatch between the rock specimen and the metal platen such that (Brady, 1971):

$$(\nu / E)_{\text{rock}} > (\nu / E)_{\text{metal}} \qquad 2\text{-}1$$

where ν is Poisson's ratio and E is Young's modulus. As a result, the ends of the specimen are restricted radially by the metal platens and the stress state near specimen ends is triaxial rather than uniaxial (Al-Chalabi and Huang, 1974).

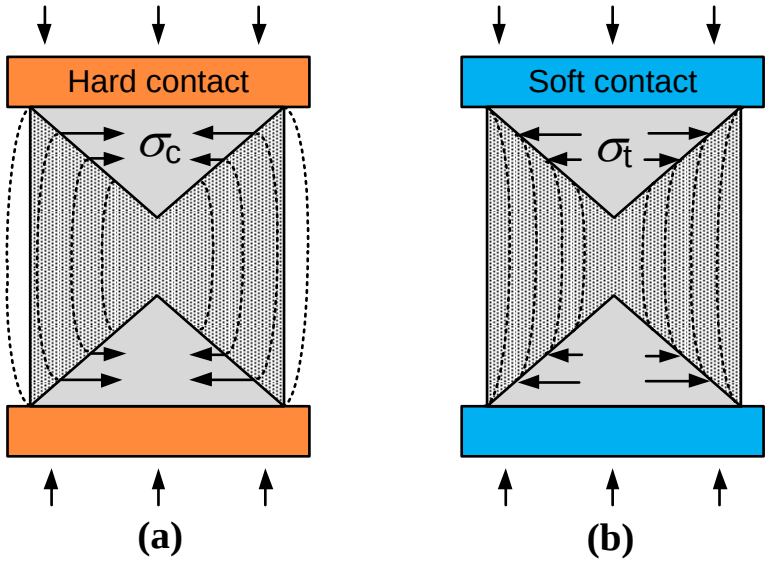

Figure 2-1 Idealized stress distributions in rock specimens under: (a) hard contact and (b) soft contact conditions, after Tang et al. (2000).

The rock strength strengthened in the hard contact condition is called the end effect and the zone of triaxial stress state activated by the end effect is called the end confined zone (Figure 2-1a). Figure 2-2 illustrates that the ratio of end confined zones to specimen volume is increased with

the decrease of slenderness ratio in uniaxial compression tests and the strength of rock or pillars can be increased. More details regarding the end effect in rock compression tests are discussed in Section 2.2.

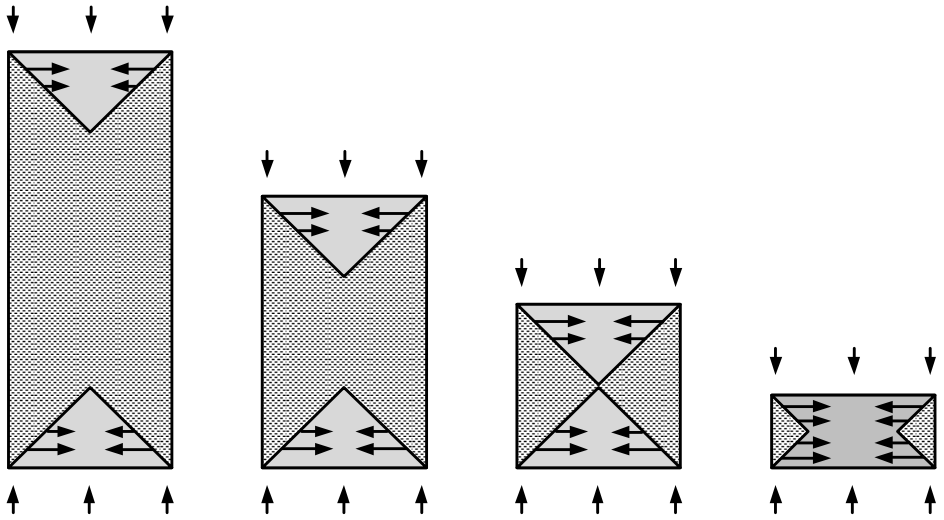

Figure 2-2 Illustration of confined zones due to the end effect in specimens with different slenderness ratios in uniaxial compression tests, after Van Vliet and Van Mier (1996).

On the other hand, if anti-friction measures are taken, the end effect on strengthening of rock strength by decreasing the slenderness ratio of specimens becomes milder (Labuz and Bridell, 1993). For instance, Teflon has been widely used as a lubricant in laboratory tests because it has a soft elastic property (its Young's modulus is smaller than that of metal and rock) and a very low coefficient of friction (μ) against many engineering materials (Rae and Dattelbaum, 2004). As a result, the elastic mismatch for the hard contact condition is reversed between the rock specimen and the soft lubricants like Teflon such that:

$$(\nu / E)_{\text{rock}} < (\nu / E)_{\text{Teflon}} \qquad 2\text{-}2$$

This is called the soft contact condition. Figure 2-1b explains that if the rock specimen-metal platen contact is inserted with soft lubricants such as Teflon as a means of anti-friction, end

tensile zones can be developed due to the extrusion of the inserts. In such a case, the influence of slenderness effect on strengthening of rock strength can be reversed. This was demonstrated by You and Su (2004) who used Teflon cushion of 0.5 mm in thickness to lubricate the end surfaces of marble specimens (Figure 2-3).

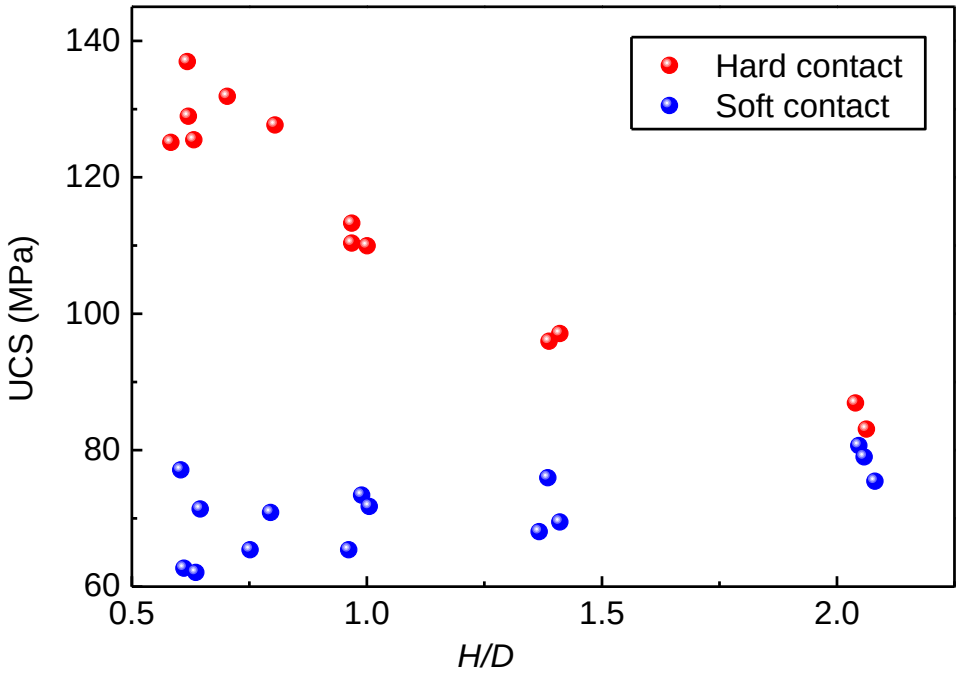

Figure 2-3 Laboratory test results showing the slenderness effect on UCS of marbles under the hard contact and soft contact conditions, digitized from You and Su (2004).

The slenderness effect also affects the post-peak deformation behavior of rock. Hudson et al. (1972a) studied the slenderness effect for Georgia Cherokee marble loaded in uniaxial compression by comparing the stress–strain curves of specimens with the same diameter but different slenderness ratios. It was found that the descending slope of the stress–strain curves decreased with the decrease of the slenderness ratio. When the slenderness ratio was decreased from 3 to 1/3, the post-peak ductility went through a transition from brittle to strain-softening, and finally a strain-hardening behavior was observed.

Different post-peak deformation behaviors of rock (Figure 1-1) with the variation of the specimen's slenderness ratio under compression observed by Hudson et al. (1972a) is consistent with that of other rock types (Labuz and Biolzi, 1991; You and Su, 2004) and concretes (Van Mier et al., 1997; Jansen and Shah, 1997). In particular, Das (1986) noticed that by further increasing the axial displacement when the Indian coal specimens reached flat residual stresses, those very squat specimens ($H/W < 1/3$) exhibited a strain-hardening behavior after stress drop. This observation was postulated by Das (1986) to be resulted from failure localization, and more importantly, the complicated end effect at the hard contacts.

The slenderness effect not only influences the stress–strain curves of rock, but also affects the failure modes. You and Su (2004) studied the slenderness effect on the failure characteristics of marble specimens in uniaxial compression tests. Three failure modes were identified (Figure 2-4): spalling failure ($H/D = 1$), hour-glassing failure ($H/D = 1.5$), and shear failure ($H/D = 2$).

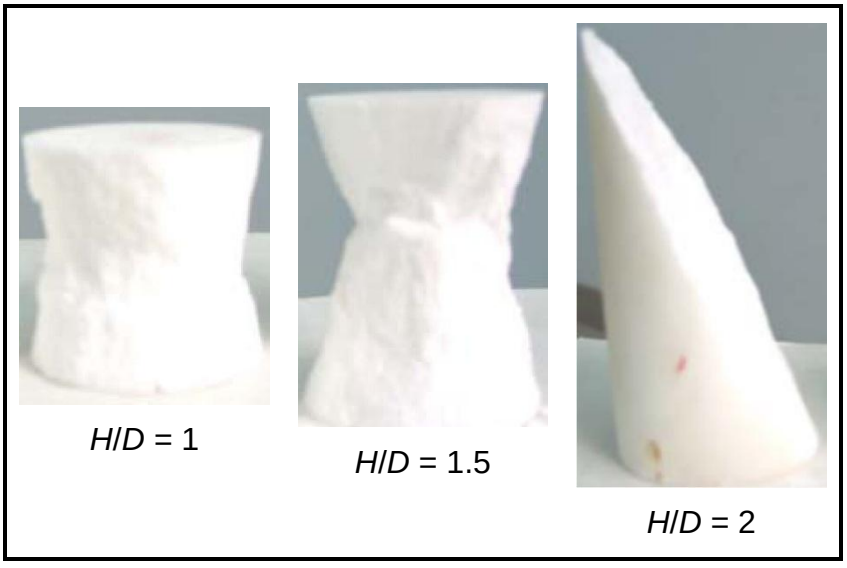

Figure 2-4 Different failure modes of marble specimens with different H/D ratios in uniaxial compression tests, after You and Su (2004).

Similar laboratory observations on the failure modes of rock specimens with varying slenderness ratios were reported by other researchers (Peng, 1971; Li et al., 2011; Liang et al., 2015). Choi et al. (1996) found that the post-peak lateral expansion behavior of concrete was noticeably affected by the *H*/*D* ratio of the specimen. Lateral strain localization was only observed in slender specimens. One interpretation was that compared with squatter specimens, the end confined zones acted less uniformly along the length of slender ones.

2.1.2 Cross-sectional shape effect

There are two types of cross-sectional-shaped specimens normally used in rock laboratory testing (Paterson and Wong, 2005): prismatic specimens usually with a square cross-section and cylindrical specimens with a cylindrical cross-section. Because borehole sampling technique is normally used to prepare rock specimens, cylindrical rather than square cross-sectional-shaped specimens are widely used in uniaxial and conventional triaxial compression tests as suggested by the ISRM (Fairhurst and Hudson, 1999). On the other hand, true triaxial compression test has become popular in the last two decades and prismatic (square or rectangular cross-section) specimens are routinely employed in true triaxial compression tests (Mogi, 1971; Takahashi and Koide, 1989; Haimson and Chang, 2000; He et al., 2010; Bobet, 2001).

There are few systematic researches that focused on the cross-sectional shape effect on rock strength. Hoop tension (Henkel and Gilbert, 1952; Meyerhof, 1953; Geertsma, 1985; Vernik and Zoback, 1992) which is induced by the specimen geometry in compression (Figure 2-5b & c), was cited to explain the strength difference between laboratory and in-situ rocks (Diederichs, 2007). It was hypothesized that hoop tension increases the radial constraint and provides a feedback confining pressure to a dilating crack. Consequently, an increase of the deviatoric stress is needed to promote further propagation of the crack and this eventually leads to a high UCS of

the rock specimen in laboratory tests. In comparison, due to the size of an underground tunnel and the large radius of curvature of the opening, cracks near an excavation boundary are less restricted and free to propagate (Figure 2-5a). Hence, the in-situ rock strength is lower than the rock strength obtained by laboratory tests that normally use cylindrical specimens (Diederichs, 2007).

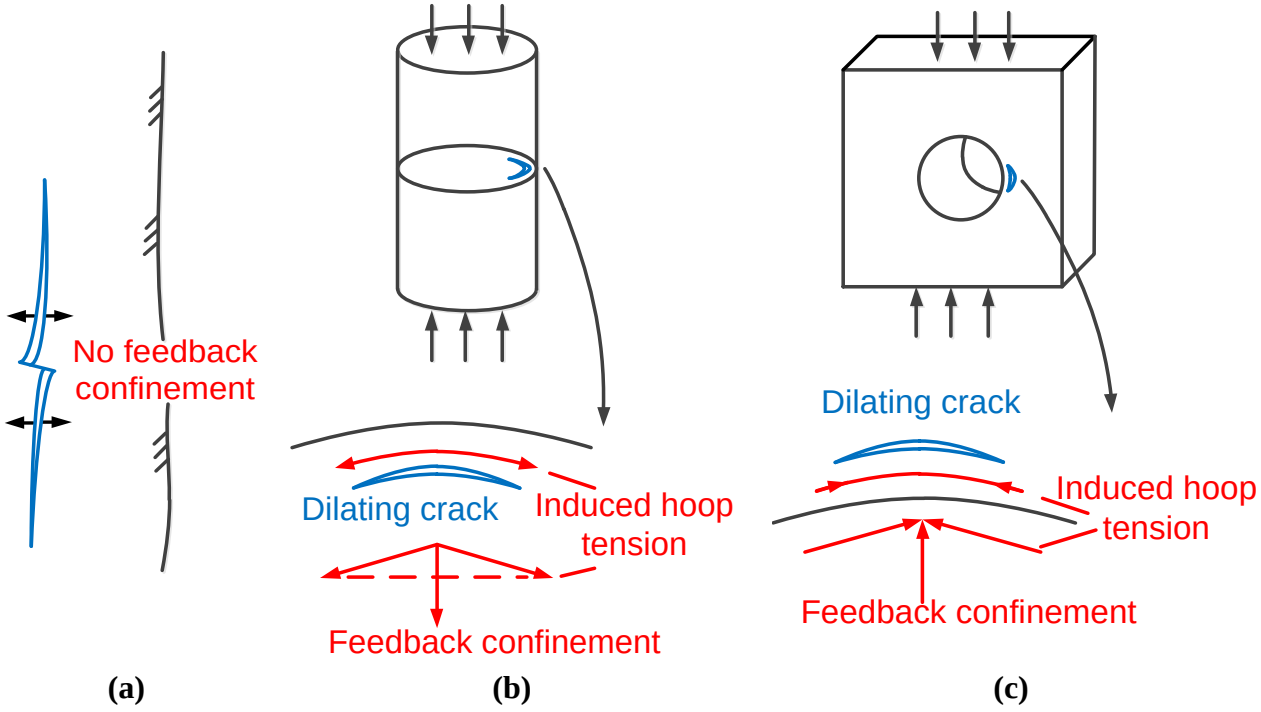

Figure 2-5 Illustrations of hoop tension: (a) unrestricted crack propagation near an excavation boundary; (b) crack in a cylindrical specimen in laboratory tests; (c) crack in a rock around a small borehole, redrawn based on Diederichs (2007).

Uniaxial compression tests using cylindrical and square prismatic specimens, sampled from a large block of Beishan granite, were conducted by Zhao et al. (2015) and the test results indicate that there is no significant cross-sectional shape effect on the UCS of the rock (Figure 2-6). Due to the difficulty in preparing and conducting uniaxial compression tests using rectangular prismatic specimens, the conclusion on the hoop tension theory was inclusive. Furthermore, the

post-peak deformation behaviors of rock specimens with cylindrical and square cross-sectional shapes were not investigated in the laboratory tests.

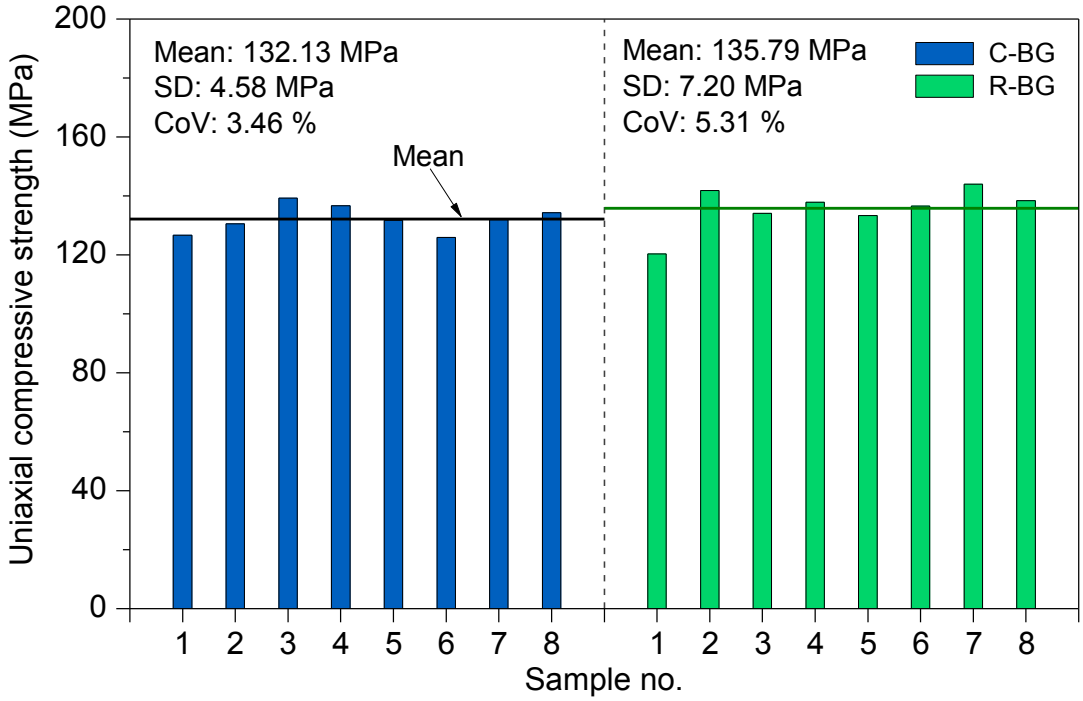

Figure 2-6 Comparison of UCS between cylindrical and square prismatic specimens of Beishan granite (Zhao et al., 2015).

2.1.3 Size effect

Laboratory and in-situ test results (Bazant, 1984; Khair, 1993; Bazant and Planas, 1997; Liu et al., 1998; Paterson and Wong, 2005) showed that there was a tendency that rock strength decreased with the increase of rock volume, which is called the size effect. The most common interpretation of the size effect is that larger samples usually contain more cracks and weaker elements because of material heterogeneity, and therefore are more likely to have a lower strength (Hudson and Harrison, 2000). Based on some test results, however, Hudson et al. (1972a), Hawkins (1998), and Thuro et al. (2001) argued that the size effect shown on the UCS of rocks was invalid, which could be a result of inappropriate testing procedure.

Although the existence of size effect on the peak strength of rocks is debatable, most references (Hudson et al., 1972a; Van Mier et al., 1997) showed that the post-peak failure characteristics of rock were affected by the specimen size. It is usually observed that for smaller specimens, their post-peak deformation behaviors appeared to be more ductile. It was interpreted (Van Mier et al., 1997) that smaller specimens are more likely to have shorter cracks, which in turn will result in more gentle rock failure, and vice versa for larger specimens.

2.2 Contact conditions

The contact conditions can be generally classified into two types: normal constraint along the normal direction of the contact and tangential constraint along the contact surfaces (Figure 2-7).

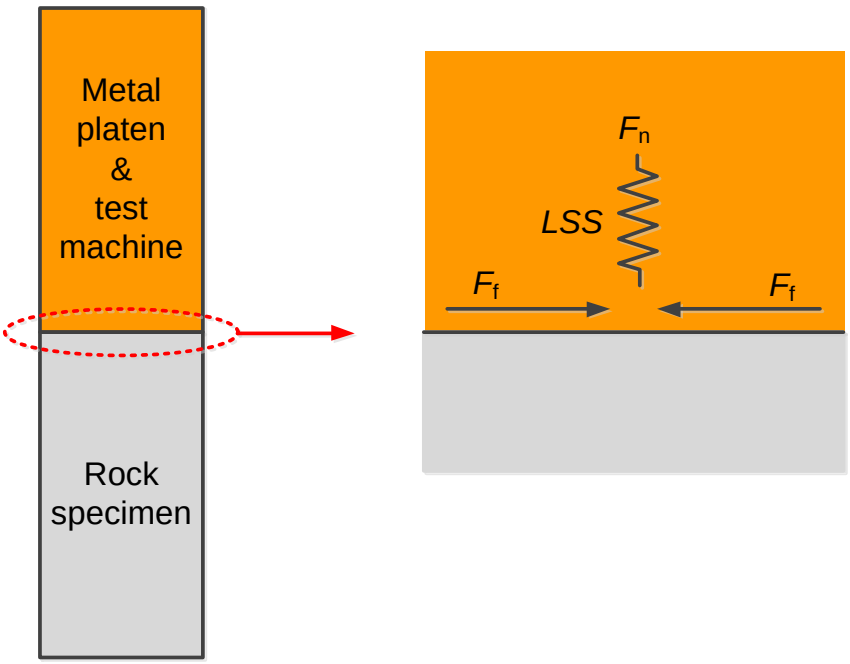

Figure 2-7 Illustrations of the contact conditions at rock specimen-metal platen contact (hard contact as an illustration, where F_f stands for friction force).

For the rock specimen-metal platen contact, the normal constraint is dominated by the structural property of the test machine including the metal platen, i.e., *LSS* (Baumgart, 2000). The

tangential constraint, which causes the end effect in the rock laboratory testing, is strongly related to the roughness of the contact surfaces (μ), the magnitude of the normal force (F_n), and the relatively displacements of the contact surfaces (Brady, 1971; Sheng et al., 1997; Grote and Antonsson, 2009). The potential influence of *LSS* on rock deformation behavior is poorly understood (Section 2.3.4); hence, *LSS* will be treated as an independent test condition and discussed separately in Section 2.3. Accordingly, the contact conditions in rock laboratory testing are referred as the end effect and it is reviewed in this section.

2.2.1 End effect in uniaxial compression test

End effect exists ubiquitously in rock uniaxial compression test, leading to the change of stress state near the ends of specimens (Figure 2-2). Therefore, it is always preferable to minimize the end effect near the rock specimen-metal platen contacts. Two measures are routinely employed to minimize the influence of the end effect on rock property testing results. One is by smearing the contact with a lubricant or by inserting a sheet of soft material between the specimen and the platens (Ojo, 1993; Labuz and Bridell, 1993). The other is the use of brush platens (Bobet, 2001).

However, the use of lubricants or soft materials can cause lateral tensile stresses to be applied to the specimen, either by fluid pressures set up inside flaws on the specimen ends (Brady and Brown, 2013) or by extrusion of the inserts (Figure 2-1b). The use of brush platens can cause indentation of the platens (Pellegrino et al., 1997), and it is difficult to prepare and maintain for their use in routine test (Brady and Brown, 2013). Therefore, anti-friction measures are not mandatory when performing rock property testing according to the ISRM SMs (Ulusay, 2015b). Instead, a slenderness ratio of 2.0 to 2.5 is recommended for uniaxial compression test.

It is practically impossible to exclude the end effect completely from rock property testing (Brady, 1971), even if anti-friction measures are employed. For instance, end effect dominates the slenderness effect in rock uniaxial compression test (Figure 2-2). Laboratory studies on the slenderness effect show that the use of lubricants to minimize the end effect is sometimes not effective. Meikle and Holland (1965) put a thin graphite layer and a thin layer of graphite laden grease on the smooth contacts between steel platens and coal specimens with different slenderness ratios. Based on their test results, they proposed Equation 2-3 to approximate the UCS (σ_c, unit: MPa) of coal specimens with different W/H ratios:

$$\sigma_c = 23.5\left(W / H\right)^{0.61} \qquad 2\text{-}3$$

Equation 2-3 indicates that the end effect exists even when lubricants are employed. Pellegrino et al. (1997) studied the effects of slenderness ratio and lubricants on the UCS of rocks and found that by decreasing the *H*/*D* ratio of lubricated specimens from 2.0 to 1.0, there was a 24.3% increase of rock strength. Recently, Liang et al. (2015) carried out a series of uniaxial compression tests to study the effect of specimen shape and strain rate on rock deformation behavior. It was observed that under different strain rates, the UCS increased 50% on average when the *H*/*D* ratio of lubricated specimens was decreased from 3.0 to 1.0.

2.2.2 End effect in conventional triaxial compression test

End effect plays a different role in affecting the rock strength in conventional triaxial compression test ($\sigma_1 > \sigma_2 = \sigma_3$) than that in uniaxial compression test. In uniaxial compression test, the end effect has a greater influence on the rock strength when the specimen is squatter (Section 2.1.1). In conventional triaxial compression test, the results from Mogi (2007) revealed that by increasing the confining pressure ($\sigma_2 = \sigma_3$), the confining pressure carries more weight on

enhancing the rock strength than the end effect does (Figure 2-8). Therefore, the slenderness effect which is caused by the end effect decreases with the increase of confining pressure. Conversely, if confining pressure is low in conventional triaxial compression tests, the slenderness effect has a noticeable influence on rock strength.

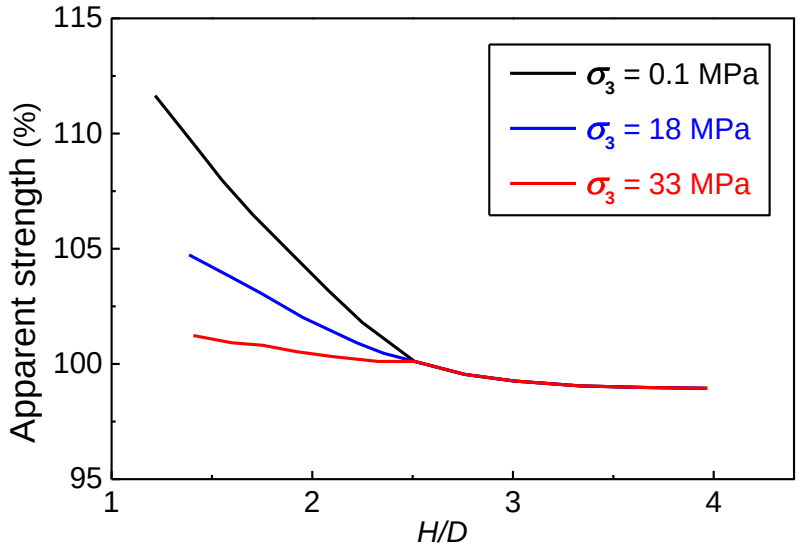

Figure 2-8 Relation between apparent strengths (normalized to the rock strength with *H*/*D* = 2.5) and *H*/*D* ratios of Dunham Dolomite under different confining pressures in conventional triaxial compression tests, digitized from Mogi (2007).

2.2.3 End effect in true triaxial compression test

True triaxial compression test machines were developed to investigate the σ_2 effect. A ground-breaking work was carried out by Mogi (1967), who designed a true triaxial compression test machine and tested the strengths of seven rock types using square prismatic specimens with an approximate length-width-height ratio of 2:1:1. His test results showed that σ_2 had a large effect on rock strength. Similar results were later reported by other researchers (Wiebols and Cook, 1968; Michelis, 1987; He et al., 2010; Li et al., 2015).

In particular, Haimson and Chang (2000) developed a new true triaxial compression test machine and studied the strengths of KTB amphibolite and Westerly granite. They observed that rock strength increased significantly with the increase of σ_2. The observed σ_2 effect is normally characterized by an increase of rock strength with the increase of σ_2, followed by reaching a strength plateau and a strength drop soon after with the further increase of σ_2. These laboratory observations provoked the attention of considering σ_2 in 3D empirical failure criteria for rock engineering design (Mogi, 1967, 1971; Haimson and Chang, 2000; Al-Ajmi and Zimmerman, 2005; You, 2009).

There are arguments against the adequacy of some of the test results that show significant influence of σ_2 on rock strength. For instance, Takahashi and Koide (1989) designed a new Mogi-type test machine slightly different from Mogi's design to accommodate larger specimens. Their test results indicated that σ_2 only resulted in a small but measurable increase in the strengths of Shirahama sandstone and Yuubari shale. Moreover, there are some rocks that do not show the strengthening effect of σ_2 on rock strength. Using the same test machine and testing method for studying KTB amphibolite and Westerly granite, Chang and Haimson (2005) found that the Long Valley Caldera rocks did not exhibit any meaningful σ_2 effect.

The 2D Mohr-Coulomb (M-C) and H-B failure criteria, which are based on conventional triaxial compression test results and do not take σ_2 into account, have been widely used to estimate rock strength. Although a rock mass is generally under a true triaxial stress state ($\sigma_1 > \sigma_2 > \sigma_3$) in situ, it is commonly accepted that "*a simplification to ignore the influence of intermediate principal stress on rock material strength is justifiable*" (Brown, 2008). Moreover, there is no significant deviation of predicted rock strengths between the results using these 2D failure criteria and field

measurements, suggesting that these simple 2D failure criteria are reliable (Hoek et al., 2002; Eberhardt, 2012; Labuz and Zang, 2012). In addition, the well-known Griffith theory, developed from a theoretical approach, also ignores the σ_2 effect in its original form.

Interpretations of such strength deviation predicted by the 2D and 3D failure criteria still remain a controversial topic, one of the popular explanations (Van Mier et al., 1997) is that boundary conditions might play a substantial role on the result difference. The lateral rock specimen-metal platen contacts in a true triaxial compression test create a boundary condition that is very different from the lateral contacts of cylindrical specimens in a conventional triaxial compression test. Gerstle et al. (1978) and Gerstle et al. (1980) carried out true triaxial compression tests on concrete specimens made from the same material composition and concluded that the σ_2 effect varied considerably due to different testing methods and anti-friction measures used.

Numerical modeling has become a powerful tool to interpret both laboratory and field observations (Pan et al., 2012; Dai et al., 2015). Cai (2008b) clarified numerically that spalling and onion-skin formation in underground opening is mainly attributed to the existence of σ_2. More importantly, he found that σ_2 had a limited influence on rock strength when σ_3 was low, showing that the rock strength increased by σ_2 from 0 to $\sigma_2/\sigma_c = 0.1$ was about 3.3% for $\sigma_3 = 0$. This statement tends to agree with the notion indicated by field observation at the URL Mine-by tunnel (Cai and Kaiser, 2014; Cai et al., 2014) and theoretical prediction from Wiebols and Cook (1968). Accordingly, Cai (2008b) pointed out that a large percentage increase of rock strength due to σ_2, as observed from some laboratory tests, was mainly attributed to the end effect. In addition, Shi et al. (2012) used FLAC3D to simulate the loading boundary effect in true triaxial compression test and revealed that the end effect can result in an apparent σ_2 effect.

2.3 Loading system stiffness and its influence on rock failure types

The subject of rock mechanics as an engineering discipline started in the 1960s, when the development of test machines permitted the study of rock behaviors (Ulusay, 2015a). Since then, great effort had been devoted to increasing the *LSS* of test machines to ensure that the post-peak failure of rock can be controlled and post-peak deformation behavior can be thus obtained for rock engineering design. In this section, the development of stiff test machines and the stable rock failure criterion along with the influence of *LSS* on rock failure types are reviewed.

2.3.1 Development of traditional stiff test machines

According to the review on rock laboratory testing by Ulusay (2015a), mechanical property testing of materials using simple test machines was first reported in the 16th century. Galileo (1638) discussed the calculation of the elastic properties of a material in direct tension and beam bending. According to Ulusay (2015a), Hooke published his experimental results in 1678 on the elasticity of wire and the extension of springs and found that the relation between the applied load and the elastic deformation of an elastic material is linear. In 1807, Young described the measurement of a parameter of elasticity that came to be known as Young's modulus (E) (Young and Kelland, 1845). According to Hudson et al. (1972b), in about 1770, Gauthey built a lever system and carried out the first rock property testing and measured the compressive strength of cubic rock specimens. Having developed a large horizontal hydraulic test machine, Kirkaldy opened the first commercial testing laboratory in London in 1865 (Smith, 1980).

From the 1930s to the 1950s, studies on the rock failure process began. Pioneer works were conducted by Griggs (1936), Kiendl and Maldari (1938), and Handin (1953), and this greatly promoted the development of rock laboratory test machines using stiff components. Since the 1960s, rock mechanics became a new discipline on its own (Ulusay, 2015a). Before 1966,

observations of the load–deformation curves of rock were limited in the pre-peak deformation stage because the rock failure process was violent immediately after the ultimate load-carrying capacity of rock had been reached, largely due to low *LSS* of the test machine relative to the post-peak stiffness of rock as we know it today (Section 2.3.3).

Cook (1965) explained the possibility of obtaining information on the post-peak deformation behavior of rock by increasing *LSS*. The first sets of complete load–deformation relations of rocks were obtained by Cook and Hojem (1966) and Bieniawski (1966) with the aid of stiff test machines. Since then, these precursors, along with other researchers (Wawersik and Fairhurst, 1970; Cook and Hojem, 1971; Stavrogin and Tarasov, 2001), had devoted great efforts to increasing the *LSS* of test machines. A test machine normally consists of a steel frame that accommodates the rock specimen inside, end platens contacting the specimen to distribute load, and a hydraulic ram to deform the specimen (Figure 2-9).

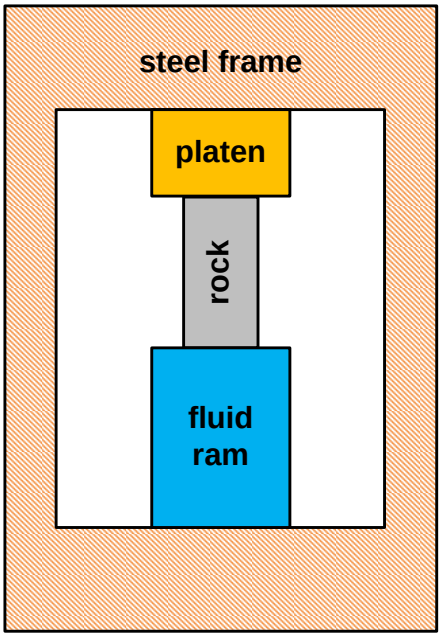

Figure 2-9 Schematic of a traditional stiff test machine for determining the complete stress–strain curve of rock, after Cook (1965).

According to Hudson et al. (1972b) and Stavrogin and Tarasov (2001), one technique to stiffen a test machine is to add stiff components (e.g., steel bars) in parallel with the rock specimen; another technique is to add a fluid ram with a large cross-sectional area and a small height. These types of test machines mentioned above belong to the traditional stiff test machine.

2.3.2 Other types of stiff test machines

On the basis of traditional stiff test machines, other types of stiff test machines were developed, with a focus on increasing *LSS* by alleviating the reduction of *LSS* due to the fluid ram. For instance, Cook and Hojem (1966) and Wawersik (1968) employed a thermal circuit in their loading frames as the means of contracting the frames to deform rock specimens. An advantage of employing the thermal contraction method is that the reduction of *LSS* due to the fluid ram is avoided but a disadvantage is that the loading rate is hard to be controlled in the post-peak deformation stage.

Bieniawski et al. (1969) designed a novel test machine where the fluid ram was separated from the rock specimen-steel frame system so that the compressibility of the fluid (e.g., oil) did not affect *LSS*. Figure 2-10 illustrates the design principle for the test machine described in Bieniawski et al. (1969) and in the subsequent discussions it is called Bieniawski-type test machine. The rock specimen tested by the Bieniawski-type test machine was arranged in parallel with steel bars of a large cross-sectional area so that the applied load to deform the rock specimens was shared with steel bars only.

According to Bieniawski (1967a) and Bieniawski et al. (1969), *LSS* of the Bieniawski-type test machine could be varied from 103 MN/m (0.105×10^6 kp/cm) to 1803 MN/m (1.84×10^6 kp/cm). Although the original descriptions regarding the design principle for varying *LSS* were given

elsewhere, based on Bieniawski (1967a) and Bieniawski et al. (1969), it is reasonable to reckon that by adjusting the number of steel bars in parallel with the rock specimen, it is possible to vary the *LSS* of Bieniawski-type test machine. However, one disadvantage of the Bieniawski-type test machine was that the effective loading capacity of the machine was reduced due to the low compressibility of the steel bars and the deformation range of specimens was also small (Hudson et al., 1972b).

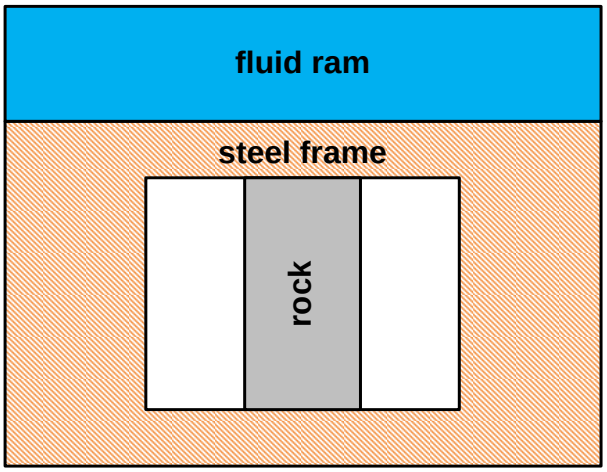

Figure 2-10 Schematic of the Bieniawski-type test machine, after Bieniawski et al. (1969).

The failure process must be controlled to obtain the complete load–deformation curves of rock. It was realized that in some cases the failure process of brittle rock could not be controlled even when a very stiff test machine was used (Wawersik and Fairhurst, 1970). Consequently, closed-loop, servo-controlled test machines were developed in the 1970s. The ground-breaking work of Fairhurst and his colleagues on rock laboratory testing (Rummel and Fairhurst, 1970; Hudson et al., 1971; Hudson et al., 1972b) paved the way for recognizing two advantages of using a servo-controlled test machine to obtain the complete load–deformation curve (Figure 2-11). First, the response time of the traducer in a servo-controlled test machine is shorter than the initiation of rock failure process; as a result, instability of the rock failure process can be detected in advance.

Second, a servo-controlled pump can be activated by the onset of instability to reduce the fluid pressure rapidly and thereby increase the effective unloading stiffness of the test machine.

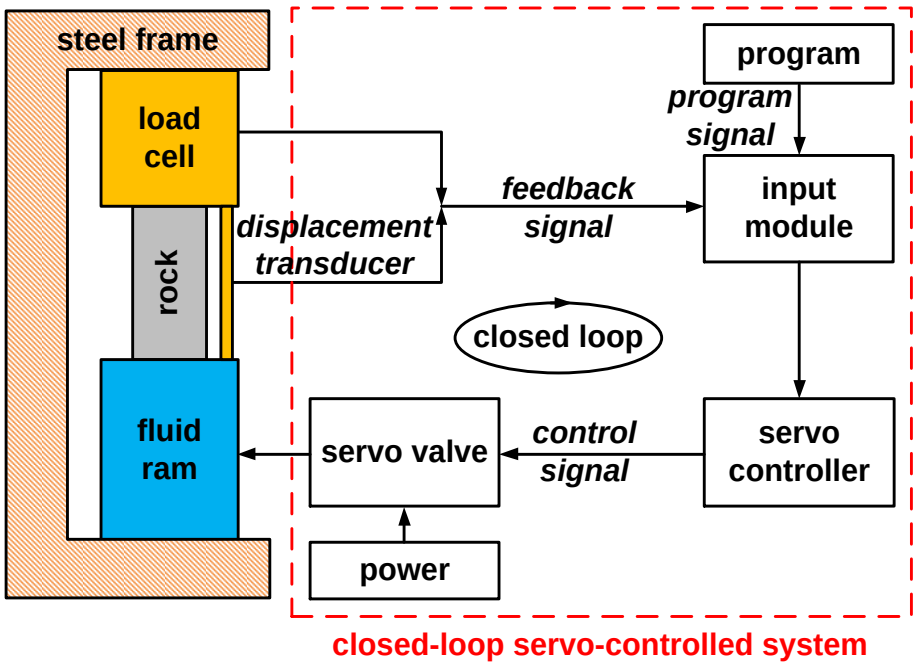

Figure 2-11 Schematic of a closed-loop, servo-controlled test machine, after Hudson et al. (1972b).

Figure 2-12 illustrates the relation between reducing the fluid pressure and increasing the effective unloading stiffness for a servo-controlled test machine. If no fluid is pumped out from the pressurized volume when the ultimate load-carrying capacity of rock is reached, a platen contraction (δx) will result in a fluid load drop (F_1), leading to unloading stiffness of the test machine of k_1. However, if a certain amount of fluid is quickly pumped out from the pressurized volume during the platen contraction δx is taking place, a greater load drop ($F_2 > F_1$) will occur and the effective unloading stiffness is increased ($k_2 = F_2/\delta x > k_1 = F_1/\delta x$). The servo-controlled test machine is designed to ensure that the contraction rate of the rock is relatively slow and the pumping rate is fast enough. Thus, the effective unloading stiffness can be greater than the steepest descending slope of the rock's load–deformation curve. As a result, no extra-large

energy is released from the test machine to deform the rock violently, and the failure process can be controlled (Rummel and Fairhurst, 1970).

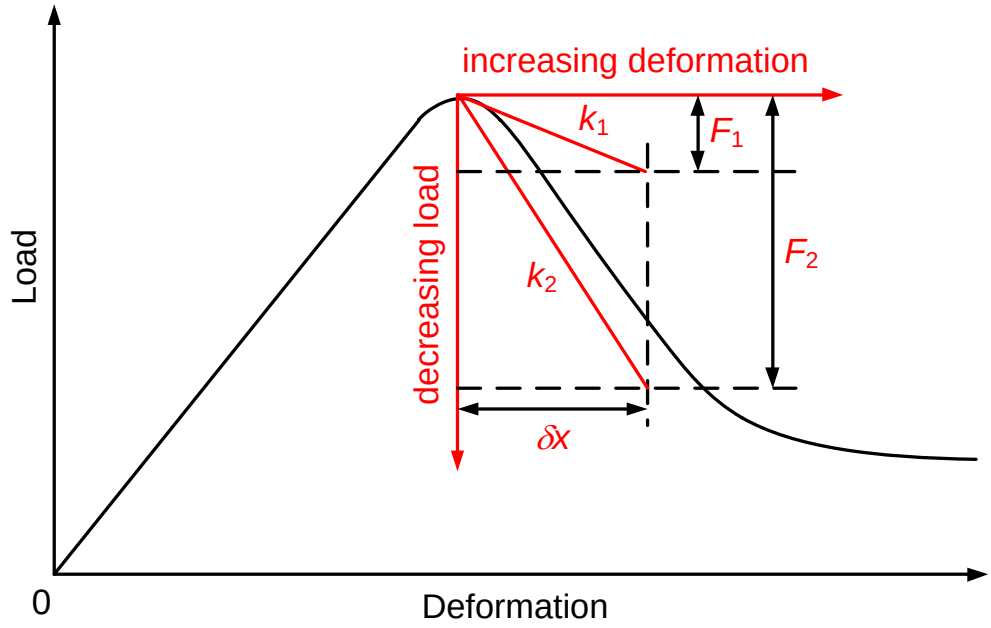

Figure 2-12 Schematic of the effective stiffness of a servo-controlled test machine, after Rummel and Fairhurst (1970).

If the failure process is potentially unstable due to the release of energy stored in the specimen (Wawersik and Fairhurst, 1970; He et al., 1990), using the lateral or radial displacement instead of the axial displacement as the control variable, a servo-controlled test machine allows any extra released energy to be extracted from the test machine (Okubo and Nishimatsu, 1985, Labuz and Biolzi, 2007). This often leads to a Class II type load–deformation (or stress–strain) relation. With the advancement of closed-loop, servo-controlled test machines, more sophisticated rock behaviors can be observed and studied under various loading conditions (Gettu et al., 1996; Paterson and Wong, 2005; Mogi, 2007; He et al., 2010; Zhao et al., 2013).

Stavrogin and Tarasov (2001) developed an "intrinsically" stiff test machine which had a stiffness of up to 2×10^4 MN/m. Similar to the test machine developed by Bieniawski et al. (1969),

the fluid ram in Stavrogin and Tarasov's test machine was intentionally separated from the rock specimen and the steel frame. Moreover, two different design arrangements were adopted to achieve high *LSS*. First and foremost, the alignment of the fluid pumping system and the fluid ram was perpendicular to the compression direction of the rock specimen (Figure 2-13). The horizontal movement of the ram was translated into a vertical movement via the wedge system underneath the specimen. As soon as the applied vertical load reached the ultimate load-carrying capacity of the rock specimen, the screw would prevent the wedge from moving, thereby prevent energy released from the pressurised fluid and fluid ram, and unstable rock failures could be prevented. In addition, the number of the loading components and the longitudinal height of these components subjected to compression were minimized (refer to discussion in Section 2.3.3).

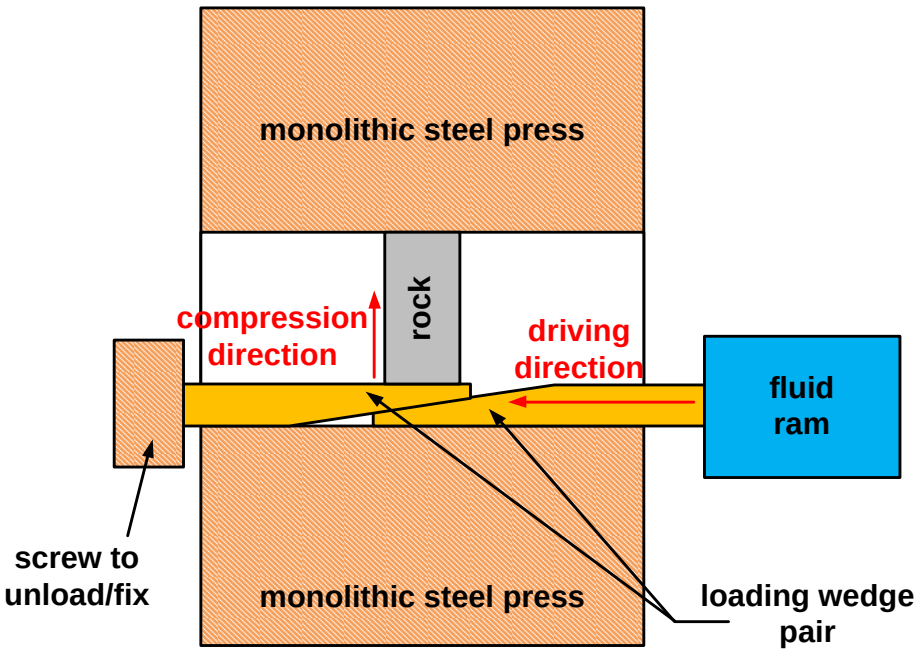

Figure 2-13 Simplified schematic of an "intrinsically" stiff test machine, after Stavrogin and Tarasov (2001).

Stavrogin and Tarasov (2001) believed that their test machine was stiff enough to minimize the release of extra-large strain energy stored in the test machine during the unloading process.

Hence, very brittle rocks could deform in a stable fashion in the post-peak deformation stage, even without the utilization of a servo-controlled test machine. It should be pointed out that although this test machine is stiff, this does not make it drastically different from other traditional stiff test machines (Figure 2-9) because its *LSS* is still finite.

2.3.3 Stable rock failure criterion for laboratory testing

LSS of a test machine is largely governed by the deformation characteristics of the loading frame, loading platens, hydraulic fluid and rams, and sometimes metal spacers if inserted between the metal platens and the rock specimen to reduce the end effect. The stiffness of an elastic structure is defined as the force per unit deformation required to deform the structure in a particular direction. Therefore, the unit of stiffness is N/m for load–deformation relation; for stress–strain relation, the unit of stiffness is N/m^2 or Pa. For a column-shaped elastic structure under axial loading (Baumgart, 2000, Chen and Han, 2007), its longitudinal stiffness (k) is determined by the cross-sectional area (A), Young's modulus (E), and height (H) as:

$$k = \frac{AE}{H} \tag{2-4}$$

Hudson et al. (1972b) provided Equation 2-5 to calculate the composite stiffness of a test machine:

$$LSS = \left[\sum_{i=1}^{N} \frac{1}{k_i} \right]^{-1} \tag{2-5}$$

where k_i is the stiffness of each loading component. The existence of any elastic loading component in a test machine reduces the composite *LSS* of the test machine, which makes the composite *LSS* always lower than the stiffness of any single loading component. Thus, to

increase the composite *LSS*, it is important to decrease the number of loading components and to increase their stiffness.

The loading frame has a large contribution to the composite stiffness of a test machine, the stiffness of loading frame is thus often quoted in manufacturer's specifications (MTS, 2013). The loading frame generally consists of a set of parallel steel columns, and its stiffness can be calculated using Equation 2-4. However, the deformation of the platen and the spacer is complicated by the combination of bending and indentation effects (Bobet, 2001). Furthermore, affected by the compressibility of fluid, the dilation of containing vessels and pipes, the incompatible deformation of seal, and the deflection of ram (Bieniawski et al., 1969; Snowdon et al., 1983; Zipf, 1992b), the stiffness of the hydraulic fluid in compression is even more complex. Because of the complex boundary condition and the interaction between different loading components of a test machine, Hudson et al. (1972b) suggested the use of numerical modeling to evaluate the influence of *LSS* on rock deformation behaviors.

LSS can be used to determine whether a rock failure process in laboratory testing is stable or not. Salamon (1970) summarized some laboratory test results of rocks in compression and reasoned that unstable rock failure would not occur if the test machine was unable to introduce further deformation without the supplement of additional external energy once the ultimate load-carrying capacity of rock had been reached. The stable rock failure criterion is formulated as (Salamon, 1970):

$$LSS > \lambda \tag{2-6}$$

where λ is the steepest post-peak stiffness of the rock specimen and it is equal to the steepest descending slope of the load–deformation curve of the rock specimen. Post-peak load–

deformation curves are assumed negative in this study. For simplicity, only the absolute values of the post-peak stiffness are compared.

2.3.4 Influence of LSS on stable rock failures

The stable rock failure criterion in Equation 2-6 states that unstable rock failure occurs when *LSS* < λ. However, laboratory evidences regarding the influence of *LSS* on the post-peak deformation behavior of rock are rare because the *LSS* value has to be sufficiently high to ensure that the rock failure process is stable. According to Hudson et al. (1972b), Späth (1935) provided a conceptual model (Figure 2-14) to explain the difference between the actual and the apparent material behaviors due to a difference in *LSS*. Only a very stiff machine can produce a material behavior that is close to the actual one.

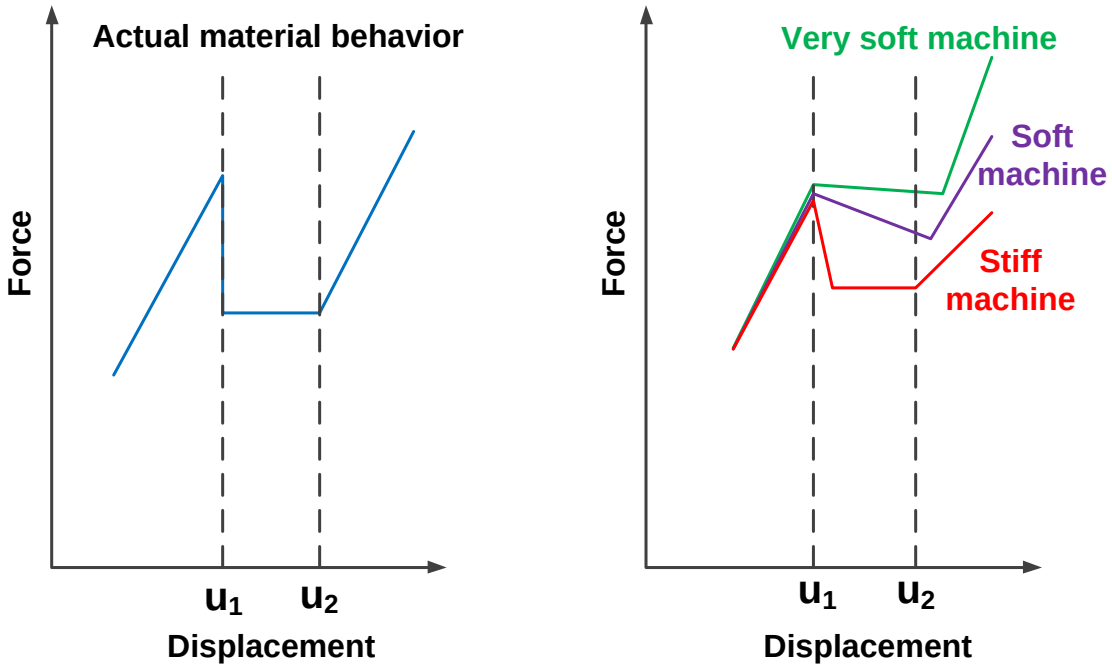

Figure 2-14 Conceptual illustration of the deviation between (a) actual material behavior and (b) obtained material behaviors under different *LSS* values, modified from Hudson et al. (1972b) who reproduced after Späth (1935).

Hudson et al. (1972b) reviewed that the first laboratory study concerning the effect of *LSS* on the observed material property was conducted by Whitney (1943). Whitney measured *LSS* of four test machines, and a difference between the descending slope in the stress–strain curve of concrete specimens and the unloading slope of scaled *LSS* in different test machines was noted. However, the descending slope of the stress–strain curve was just virtually extrapolated from the point of peak strength, and the method used to measure *LSS* was somewhat ambiguous and questionable. An extensive Round Robin test project aiming at studying the factors influencing the strain-softening behavior of concrete was carried out by the RILEM Technical Committee 148-SSC (Van Mier et al., 1997). *LSS* was first considered as one of the inspecting parameters. However, only a limited number of results were collected, and it was impossible to make a reasonable comparison based on these results.

To verify the assumption that different descending slopes of stress–strain curves may be obtained by different *LSS* of test machine, quartzite specimens were tested by Bieniawski et al. (1969) using the Bieniawski-type test machine (Section 2.3.2) in uniaxial compression. The Bieniawski-type test machine had three measured *LSS* values – 103 MN/m, 1029 MN/m, and 1803 MN/m. The test results confirmed that "*depending upon the stiffness of the loading system different negative slopes of the stress–strain curve are obtained resulting in different levels of stress and strain at rupture*" (cited in Bieniawski, 1967a). It is worth noting that the post-peak failure behaviors of the rocks (including some brittle rocks like norite) obtained by the Bieniawski-type test machine all showed strain-softening behaviors (Bieniawski, 1966; Bieniawski, 1967b; Bieniawski et al., 1969), which is different from the post-peak positive descending slopes of brittle rocks obtained by other types of stiff test machines (Wawersik and Fairhurst, 1970;

Tarasov and Potvin, 2013). This is an indirect evidence that shows that the obtained post-peak deformation characteristics of rock can be affected by different test machines.

It is preferable to carry out laboratory tests on specimens with the same rock property to study the influence of *LSS* on the rock deformation behavior. However, it is impossible to have rock specimens with exactly the same mechanical property, even if sampling is carefully conducted (Zhao et al., 2015). The behaviors of rock show variability due to rock heterogeneity, and this is especially the case in the post-peak deformation stage (refer to discussions in Section 1.2.1). Therefore, laboratory study on how *LSS* affects the post-peak deformation behavior of rock is extremely difficult.

On the other hand, laboratory evidence showing the influence of *LSS* on the response of elastic-plastic materials with relatively homogeneous properties can provide insights into this study (Schulson, 1999). Sinha and Frederking (1979) carried out a series of strength tests on ice and found that test machines of varying *LSS* values (i.e., Instron Model TTDM-L, Instron Model 112, and MTS Model 90) had a large influence on the stress–strain curves of ice. The ice specimens were made with care and could be considered as identical. Rist et al. (1991) further argued that different strain rates associated with different *LSS* values could be responsible for the difference in the strain-softening behaviors of ice observed in the triaxial compression tests.

Not only rock specimens with the same property are difficult to be prepared in rock laboratory testing, but also *LSS* of a test machine is difficult to be varied in a large range to study the influence of *LSS* on the post-peak deformation behaviors. Hence, numerical experiment seems to be the best approach for studying this problem (Cai, 2008b). Kias and Ozbay (2013) used a hybrid numerical method to study the influence of *LSS* on unstable pillar failures. Two codes,

Fast Lagrangian Analysis of Continua (FLAC2D), used for modeling elastic platens, and Particle Flow Code (PFC2D), used for modeling coal, were coupled. It was found that the parameters of the test machine could change the pillar failure mode drastically. Similarly, Hemami and Fakhimi (2014) used a hybrid FEM-DEM numerical model to study the rock specimen-test machine interaction. Their research focus was placed on the difference between a stiff test machine and a soft test machine. They noticed that the soft test machine underestimated the slope of the post-peak stress–strain curve.

2.4 Loading conditions

The loading conditions of in situ rock vary and the increasing demands on modeling in situ rock behaviors under different loading conditions resulted in the development of various rock laboratory loading methods (Tang et al., 2004). These loading methods are normally distinguished from the means to apply the confining pressure, the stress path, and the loading rate to the rock specimen in laboratory testing.

2.4.1 Confining pressure

Triaxial compression tests have been commonly used to study the rock behavior under a 3D stress state (von Kármán, 1911; Hoek and Franklin, 1968; Mogi, 2007; Zhao et al., 2014). It is through the results of triaxial compression tests that empirical failure criteria have been developed (Mogi, 1971; Hoek et al., 2002; Tarasov and Potvin, 2013) and strength parameters of rock are determined (Hudson, 1993; Zhao et al., 2013). In addition, it is through the complete stress–strain curves of rock obtained in conventional triaxial compression tests that the pronounced influence of confining pressure on maintaining rock's load-carrying capacity in the post-peak deformation stage has been identified (Golder and Akroyd, 1954; Jaeger et al., 2007; Brady and Brown, 2013).

Followed by the design principles outlined by Cook and Hojem (1966), Wawersik and Fairhurst (1970) developed a triaxial compression test machine and used it to carry out a study on the influence of confining pressure on Tennessee marble by increasing the confining pressures from 0 to 50 MPa (7000 psi). It was noted that brittle failure was not the only mechanism controlling the rock failure. For the marble under an uniaxial stress state or low confining pressures, fractures were observed mostly in a direction parallel with the σ_1 loading direction. Thus, the application of even a small confining pressure had a significant effect on inhibiting the development of cracks and thereby increasing the load-carrying capacity of rock in the post-peak deformation stage (Hudson and Harrison, 2000).

The general trend of the influence of increasing confining pressure on the post-peak stress–strain curves of rocks is shown in Figure 1-1. The brittle failure mode of rock under low confining pressures normally exhibits a sudden stress drop shortly after the ultimate load-carrying capacity of the rock has been reached, and hence the post-peak deformation behavior of perfectly brittle failure in this case can be idealized as a vertical line (Fang and Harrison, 2001).

The post-peak stress–strain curve at which the post-peak reduction in strength disappears indicates a ductile behavior, in which there is a special case that the curve is horizontal (Figure 1-1) and it is termed as brittle-ductile transition (Mogi, 1974). The confining pressure associated with the brittle-ductile transition is of engineering significance due to deep underground engineering activities, because it varies with rock type and is low in some cases (Goodman, 1989). Above the brittle-ductile transition, strain hardening occurs and it is characterized by the capacity for substantial change in volume without gross fracturing (Paterson and Wong, 2005).

The failure mode between the brittle-ductile transition and the perfectly brittle failure can be loosely grouped into strain-softening failure mode, strength decreases during progressive straining after the peak strength has been reached (Bazant et al., 1984; Frantziskonis and Desai, 1987), the most common failure mode observed in rock laboratory testing (Read and Hegemier, 1984) and the most common rock deformation behavior in the field (Bieniawski, 1976; Egger, 2000; Hoek, 2007).

Confining pressure also exerts a pronounced influence on the dilational behavior of rock. It is recognized that the volumetric strain change of rock becomes dilational with increasing deformation and continues in the post-peak deformation stage (Wawersik and Brace, 1971; Hallbauer et al., 1973; Brace, 1978; Vermeer and De Borst, 1984). At low confining pressures, failure mode of rock accompanied by volumetric dilation predominates, and the amount of dilation decreases with the increase of confining pressure (Alejano and Alonso, 2005; Zhao and Cai, 2010). At very high confining pressures, often outside the range of engineering interest, dilation may be totally suppressed throughout the test (Brady and Brown, 2013).

2.4.2 Stress path

The strength of rock is not a single-valued function of strain and it depends on the stress path in the rock (Jaeger et al., 2007). The control variables employed in rock laboratory testing can well illustrate the influence of stress path on the post-peak deformation behavior of rock. When the lateral (or circumferential for cylindrical specimens) strain is used as the control variable, Class II failure type is observed in brittle rock (Section 2.3.2), whereas Class I failure type can be observed if the axial strain is used as the control variable (Wawersik and Fairhurst, 1970; Labuz and Biolzi, 1991; Tarasov and Potvin, 2013; Meng et al., 2015). The stress path conducted by

different laboratory test settings also affects the mechanical behavior of rock from other aspects (Ingles et al., 1973; Lee et al., 1999; Dehler and Labuz, 2007).

The stress path applied in rock laboratory testing is not necessarily the same as that an element of rock influenced by an excavation will follow when the excavation is made (Brady and Brown, 2013). Martin and Chandler (1994) pointed out that compared with the stress path in rock laboratory tests, which are routinely subjected to a monotonic increase or decrease of load, the stress path around a tunnel was more complex. Spalling observed in the test tunnel roof was corresponding to an apparent stress state of σ_1 = 0.5 to 0.6 of UCS, while the crack damage strength in laboratory condition is approximately σ_1 = 0.7 to 0.8 of UCS. This was interpreted that the cohesive strength component of the in situ rock mass was lost because of the loading path experienced by the in situ rock mass.

Stress path is of practical concern in underground mine design. Because the local stress state is altered at each mining step, and different stress paths lead to different rock failures. Based on the simulation of a case study, Kaiser et al. (2001) identified two types of rock failure due to mining-induced stress changes, which were termed as hanging wall delamination and collapse, and wedge-like failures in the backs of sill drifts. Thus, different rock support schemes have to be taken into account to deal with the failure modes.

Cai (2008a) suggested that the proper selection of solution scheme in numerical simulation was important to capture the correct tunnel excavation response, otherwise different structural responses would be produced due to the different stress paths. The essence of this modeling result difference was that the mechanical response of rock, which is an elasto-plastic material, was stress path dependent.

2.4.3 Loading rate

The influence of loading rate on rock strength is of particular interest because it is associated with the long-term stability of rock structures. The post-peak deformation behavior of rock is also sensitive to the span of loading time, because the process of rock failure is in a continual state of progressive collapse (Hudson, 1971). Bieniawski (1970) found that both peak and post-peak strengths of rocks were affected by loading rate. The higher the strain rate was applied, the higher the peak strength and the steeper the descending slope of sandstone was observed. On the other hand, lower strain rates resulted in flatter post-peak strength, which means that less violent rock failure would be expected. Bieniawski (1970) interpreted that violent and uncontrollable rockburst occurred when the rock was subjected to a high loading rate, because the post-peak stability of the rock was diminished due to its steep post-peak deformation behavior. Therefore, a slower loading rate condition would be more desirable to conduct rock laboratory testing and to achieve a stable pillar loading condition.

The laboratory test result regarding the effect of applied deformation rate on the peak strength of coal rocks from Peng (1973) was the same as above mentioned, which showed that a high loading rate resulted in a high peak strength. However, a lower loading rate was found to have a negative effect on the post-peak stability of rocks, whereas more ductile curve and higher residual resistance for the post-peak region was observed at a faster loading rate.

2.5 Summary

A detailed literature review reveals that both the test conditions at the laboratory scale and the loading conditions at the field scale exert an influence on the ultimate load-carrying capacity of rock. The influence of test conditions on the rock behavior becomes evident in the post-peak deformation stage, indicating that the post-peak deformation behavior of rock depends not only

on the intrinsic material characteristics of the rock, but also on how the laboratory testing is performed. While the influence of several test conditions on the post-peak deformation behavior is well understood (e.g., the slenderness effect and the confining pressure), the influence of others is not. Four aspects of test conditions discussed in this literature review are briefly summarized in this section. Those test conditions, found to be poorly understood, are the research objectives in this dissertation.

2.5.1 Specimen geometry

It is well documented that, due to the end effect, both the peak and post-peak load-carrying capacities increases with the decrease slenderness ratio of rock specimens. In addition, the influence of the size effect on rock strength can be minimized, on condition that the preparation of specimens follows the ISRM SMs. On the other hand, cylindrical and prismatic shaped specimens are routinely employed in rock compression tests. Unfortunately, the cross-sectional shape effect on rock strength is not well studied.

The hoop tension theory (Diederichs, 2007) explained that the geometry of a cylindrical specimen in compression can affect crack propagation and hence in favor of the strengthening of rock strength, both in laboratory and in situ. Hoop tension also exists in square prismatic specimens; however, due to the shape difference, it would be less than that in cylindrical specimens. In a rectangular prismatic specimen, hoop tension would be even less.

If hoop tension does influence the rock strength, it can be hypothesized that the strength of a cylindrical specimen should be higher than that of a square or rectangular prismatic specimen. Recent laboratory testing results suggested that there is no significant cross-sectional shape effect on rock strength (Zhao et al., 2015). However, the laboratory test evidences on the hoop tension

theory were inconclusive, due to the difficulty in preparing rectangular prismatic specimens, and there is a lack of investigation on the post-peak deformation behavior with different cross-sectional-shaped specimens. The dissertation tries to fill the gap using the numerical experiment approach and the laboratory results are presented in Chapter 3.

2.5.2 End effect

End effect exists ubiquitously in rock compression tests. Due to the limited efficiency of anti-friction measures, the slenderness effect caused by the end effect affects rock strength in uniaxial compression test. There is a lack of systematic investigation into how the end effect affects the rock strength in true triaxial compression test, which normally employ anti-friction measures to minimize the end effect.

Based on the results of conventional triaxial compression test, Mogi (2007) concluded that the end effect in triaxial compression test can be reduced with the increase of confining pressure. However, compared with the conventional triaxial compression test—which employs hydraulic pressure to apply lateral confining pressure and hence has very little or no friction-induced constraint at the lateral contacts of the specimen—friction exists at the lateral rock specimen-metal platen contacts in true triaxial compression test because steel platens are normally used to apply either σ_2 or both σ_2 and σ_3. Thus, the influence of the end effect on the rock strength between these two types of triaxial compression tests is different.

More importantly, as previously mentioned in Section 2.1.1, the end effect usually becomes more significant when the specimen is squatter (e.g., H/W or $H/D < 2.0$; Bieniawski and Bernede, 1979). Figure 2-15 illustrates that the ratio of the length on the contact where σ_2 is applied (l_1) to the length on the contact where σ_3 is applied (l_2) is 1.0 in most true triaxial compression tests.

Hence, the relatively squat geometry of the tested specimens is another reason for why the end effect in true triaxial compression test cannot be omitted completely. The dissertation investigates the influence of end effect on the true triaxial compression test results and the content is presented in Chapter 4.

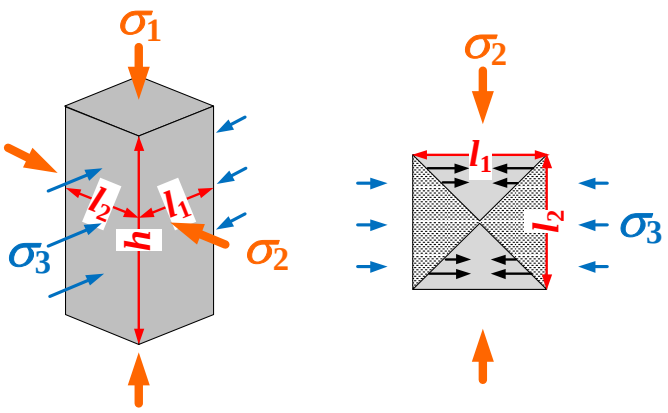

Figure 2-15 Illustration of the shape and the corresponding end effect in true triaxial compression test.

2.5.3 Loading system stiffness (*LSS*)

The literature review on the development of stiff test machines reveals that stiff test machines are important to obtain and to investigate the post-peak deformation behavior of rock. However, because of the differences in the manufacturing arrangements of different stiff test machines, the *LSS* values of stiff test machines are always finite and vary widely. So far the research on the influence of *LSS* on stable failure of rock is limited. This is partially due to the fact that there is no agreed upon the method to measure the *LSS* in laboratory tests (Van Mier et al., 1997). Furthermore, it is impractical to vary *LSS* over a large range to test rock specimens with "identical" rock properties.

The numerical experiment approach can be useful to investigate *LSS* with a promising capacity to prescribe the key variables. However, previous numerical experiments were focused on the

influence of *LSS* on the unstable failure of rock or pillar. In addition, most simulations were conducted using models with a loading platen atop the rock specimen that represented the test machine. The test machines in these models were perhaps over-simplified without considering the compounded influences of other loading components, such as loading frame and ram, which are important in defining *LSS* (Section 2.3.1). The dissertation investigates the influence *LSS* on the stress–strain curves of rock using a new modeling strategy and the results are presented in Chapter 5.

2.5.4 Loading conditions

With the aid of modern servo-controlled test machines, rock specimens in compression tests can be subjected to a loading condition prescribed by desired a confining pressure, a stress path, and a loading rate. It is well recognized that loading conditions have a pronounced influence on the post-peak deformation behavior of rock. As a result, since 1974, the Commissions on Testing Methods established by the ISRM has made considerable effort to develop a succession of the ISRM SMs for guiding the testing methods (Ulusay, 2015b). The differences in loading conditions employed by different laboratory tests can be minimized as long as the testing methods are adhering to the ISRM SMs. Thus, the variation of post-peak deformation behaviors of rock due to varied loading conditions is small for routine rock property testing.

2.5.5 Final remarks

In a short summary of previous discussions, three test conditions stand out because they have been treated with less attention. The cross-sectional shape effect has not been thoroughly investigated, especially with respect to its influence on the post-peak deformation behavior. The end effect in the true triaxial compression test is less studied, which might mislead the interpretation of the true σ_2 effect and subsequently the development of 3D empirical failure

criteria. Most importantly, it is found that stiff test machines are widely used to study the post-peak deformation behavior of rock, because the *LSS* of a stiff test machine is an important test condition in controlling rock failure type. However, *LSS* varies with different laboratory tests considerably, and it is still unknown whether the influence of this variation can affect the obtained post-peak stress–strain curves or not. This literature review helps to identify the research objectives and in the subsequent chapters the research results are presented.

Chapter 3

3 Cross-sectional shape effect in uniaxial compression test

The cross-sectional shape effect on the strength and deformation behavior of rock is studied in this chapter. Inspired by the laboratory tests conducted by Zhao et al. (2015), a comprehensive numerical experiment was carried out to simulate the deformation responses of cylindrical, square, and rectangular cross-sectional-shaped specimens under compression. In this fashion, the potential strengthening effect on rock strength due to different cross-sectional shapes of the specimens can be examined. In addition, a discussion on the hoop tension theory can also be made. Uniaxial compression test was adopted by Zhao et al. (2015) and the numerical experiment was restricted to this type of compression test.

To study the cross-sectional shape effect numerically, one of the geometry effect of rock which is poorly understood (Section 2.1), it is planned to first examine the validity of the numerical models by modeling some well-observed geometry effect in laboratory tests (Section 1.2.3). Once the confidence in the modeling tool and numerical models is gained from successful calibration of laboratory test results, numerical experiments can be conducted to further investigate the hoop tension theory, as well as the influence of cross-sectional shape effect on the post-peak deformation behavior of rock.

Note that the post-peak deformation characteristics of pillars in some cases can be modeled by conducting uniaxial compression test using the axial-strain-controlled loading method (Meikle and Holland, 1965; Babcock, 1968; Babcock, 1968; Cook et al., 1971; Van Heerden, 1975). Insights gained from this numerical experiment can be applied to the stability design analysis of pillars with different cross-sectional shapes in future study (as illustrated in Section 5.2.4).

3.1 Verification of numerical models

The verification of numerical model begins with simulating the opposite slenderness effects on the rock strength between the hard contact and soft contact conditions in rock laboratory tests (You and Su, 2004). Next, the numerical model is used to calibrate the cross-sectional shape effect on UCS of Beishan granite obtained by Zhao et al. (2015). The strength parameters of the Beishan granite are obtained for the numerical modeling through a detailed model calibration (Zhao et al., 2013; Zhao et al., 2015).

3.1.1 Slenderness effect under different contact conditions

This numerical experiment is aimed at calibrating the slenderness effect under different contact conditions observed by You and Su (2004). There were not enough testing data available from You and Su (2004) to determine the strength parameters for the rock and the coefficient of friction (μ) for the contact conditions, both of which are important for using the numerical modeling to calibrate laboratory test results. Therefore, the modeling results in this section will be compared with the test results in a qualitative way, as an illustration to demonstrate the capability of the numerical model for studying the shape effect of rock.

A 3D simulation model of a cylindrical specimen subjected to uniaxial compression under the hard contact by two steel platens and two rigid rams is shown in Figure 3-1. The diameter of the cylindrical specimen is 50 mm. A constant loading velocity at a rate of 0.015 m/s (note that the rate applied by using an explicit algorithm for solving quasi-static problems is not comparable to that in reality in rock testing, refer to discussion in Section 1.2.2) is applied at the top and bottom rams and a symmetrical loading condition is achieved in the specimen.

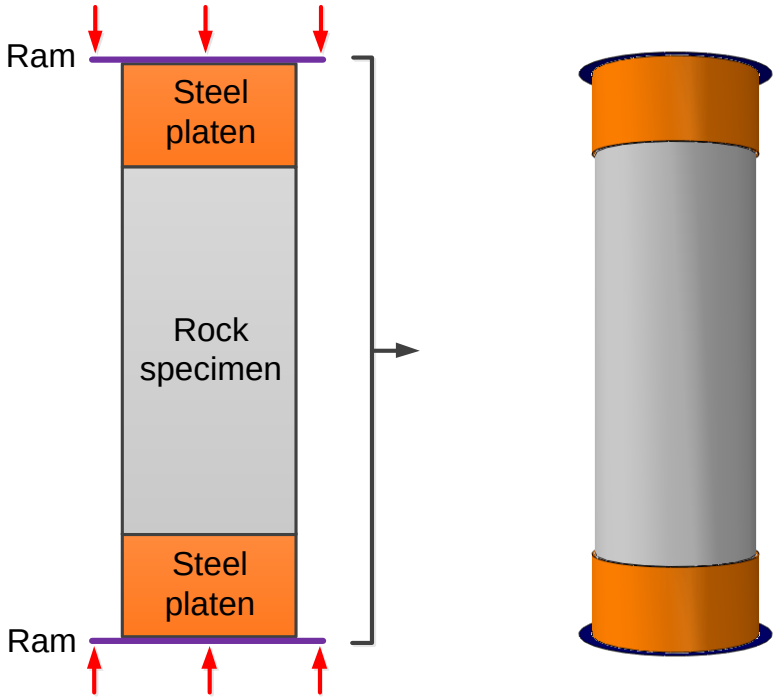

Figure 3-1 3D simulation model of a cylindrical specimen under the hard contact condition in uniaxial compression (*H*/*D* = 2.0 as an illustration).

The μ value is important for this study because it determines the contact condition at the specimen ends (Gaffney, 1976). Hence, a set of laboratory tilt tests is performed to determine a reasonable range of the μ values for the rock specimen-steel platen contacts. For a well-polished, parallel and dry rock specimen-steel platen contact without any lubricants, the average tilting angle is 15.1 °, which gives a static μ value of 0.27.

Depending on the surface roughness resulted by sample preparation and whether an anti-friction measure is used or not, the μ values for the rock specimen-steel platen contacts can be in a range of 0.1 to 0.3 (Vutukuri et al., 1974; Labuz and Bridell, 1993). Hence in this numerical experiment, a base μ value of 0.2 is used for the rock specimen-steel platen contact without anti-friction measures. In addition, a μ value of 0.1 is used to define the contact condition between

the platen and the ram. Because the friction at the platen-ram contacts is small and the *H*/*D* ratio of the platens is 0.5, the friction at the platen-ram contacts has a negligible influence on the rock strength. The geometrical and mechanical parameters of the steel platens used in the simulation are listed in Table 3-1.

Table 3-1 Geometrical and mechanical parameters of the steel platens

Parameters	Value
Diameter, *D* (mm)	51
H/*D* ratio	0.5
Poisson's ratio, ν	0.3
Young's modulus, *E* (GPa)	200

The FEM model of a cylindrical specimen and loading platens in uniaxial compression test is presented in Figure 3-2. The size of the elements is 3 mm in its longest dimension; the maximum deviation factor for the curvature control of element size is 0.1. The shape of the elements is hexahedron; the elements are generated by the sweep technique using medial axis algorithm. The element type is 8-node linear brick; the integration algorithm for the chosen element type is reduced integration using hourglass control. Based on the mesh sensitivity analysis, relatively fine element size was chosen. Most importantly, the shape (hexahedron) and the integration algorithm for all the rock specimens under same test condition of various parameters are same to ensure that the numerical errors associated with mesh size are minimized and a relative comparison of the modeling results can be made because all the models are within the same order of numerical errors (refer to discussions in Section 1.2.2).

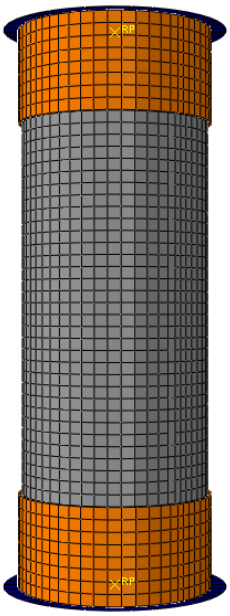

Figure 3-2 FEM model of a cylindrical specimen and loading platens in uniaxial compression test.

To simplify the constitutive model, a homogeneous material with the M-C failure criterion and a tension cut-off is considered in the simulation. The 2D M-C failure criterion is one of the most commonly used failure criteria in rock engineering. As a failure criterion with mathematical simplicity, the physical meaning of the strength parameters is clear. The rock strength of the M-C failure criterion is defined by the cohesive strength component and the frictional strength component (Martin, 1997; Mogi, 2007). The strength parameters of the M-C failure criterion can be readily obtained or calibrated by performing simple rock property testing. More importantly, unlike other materials, rock exhibits a confining pressure-dependent mechanical behavior, and rock failure under a moderate confining pressure is typically characterized by an inclined shear failure plane relative to the σ_1 loading direction (Hudson and Harrison, 2000). The M-C failure criterion depicts the characteristic of rock strength and failure type under confined condition satisfactorily.

The mechanical parameters of the rock used in the simulation are listed in Table 3-2. Note that non-associated flow rule is not available in ABAQUS; thus, friction angle and dilation angle are assumed the same.

Table 3-2 Strength and deformation parameters of the rock

Parameters	Value
Poisson's ratio, ν	0.22
Young's modulus, E (GPa)	60
Cohesion, c (MPa)	35
Residual cohesion, c_r (MPa)	0.1
Tension cut-off, σ_t (MPa)	9.5
Friction angle, φ (◦)	40
Dilation angle, ψ (◦)	40

Similar to that used in the laboratory tests conducted by You and Su (2004), Figure 3-3 shows the simulation model of an elastic material with a very small thickness that represents Teflon sheets is inserted between the rock specimen and the ram in the numerical experiment. Thus, the contact behavior at the rock specimen-Teflon sheet contact is the soft contact condition discussed in Section 2.1.1 (Figure 2-1b).

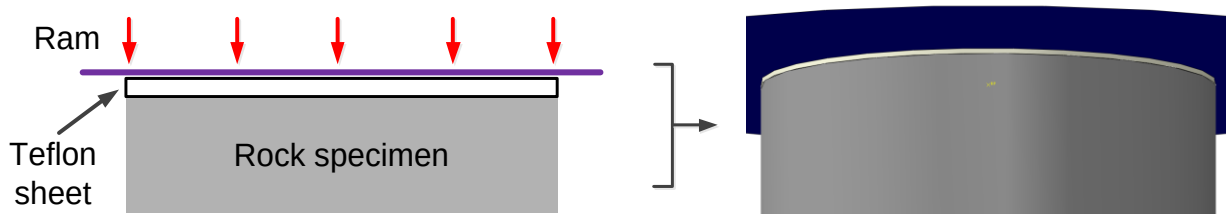

Figure 3-3 3D simulation model of the soft contact in uniaxial compression test.

Teflon is a low friction polymeric solid which is highly deformable and used as an anti-friction material (Rae and Dattelbaum, 2004). Table 3-3 lists the geometrical and mechanical parameters

of the Teflon sheet used in the simulation. The μ value of the rock specimen-Teflon sheet contacts is also important to define the soft contact condition. Laboratory test results found that the μ value for a rock specimen-Teflon sheet contact can be in a range from 0.02 to 0.20, and 0.05 – 0.10 is a more common range (Hawkes and Mellor, 1970; Gaffney, 1976; Labuz and Bridell, 1993; Grote and Antonsson, 2009; He et al., 2014). In this study, μ = 0.05 is used for the rock specimen-Teflon sheet contacts.

Table 3-3 Geometrical and mechanical parameters of the Teflon sheet (Rae and Dattelbaum, 2004; You and Su, 2004)

Parameters	Value
Thickness (mm)	0.5
Diameter, *D* (mm)	51
Poisson's ratio, ν	0.45
Young's modulus, *E* (GPa)	2
Yielding strength, σ (MPa)	80

The relation between the UCS of the cylindrical specimens and the *H*/*D* ratio under the hard contact and soft contact conditions obtained from numerical modeling is presented in Figure 3-4. For the hard contact condition, UCS increases as the *H*/*D* ratio decreases because the end effect on strengthening the rock strength becomes greater when the specimen is squatter (Figure 2-2). In contrast, UCS decreases as the *H*/*D* ratio decreases if the specimens are under the soft contact condition; the slenderness effect on rock strength is reversed in this case. This is because that the lateral expansion capacity of the Teflon sheet is larger than that of the rock specimen (Equation 2-2). Consequently, the relative expansion of the Teflon sheet is restricted by the rock specimen and this in turn caused tensile stress near the ends of the specimens (Figure 2-1). The treads of the slenderness effect in rock specimens under the hard and soft contact conditions revealed from

the numerical modeling is in a good agreement with those observed in the laboratory test results (Figure 2-3).

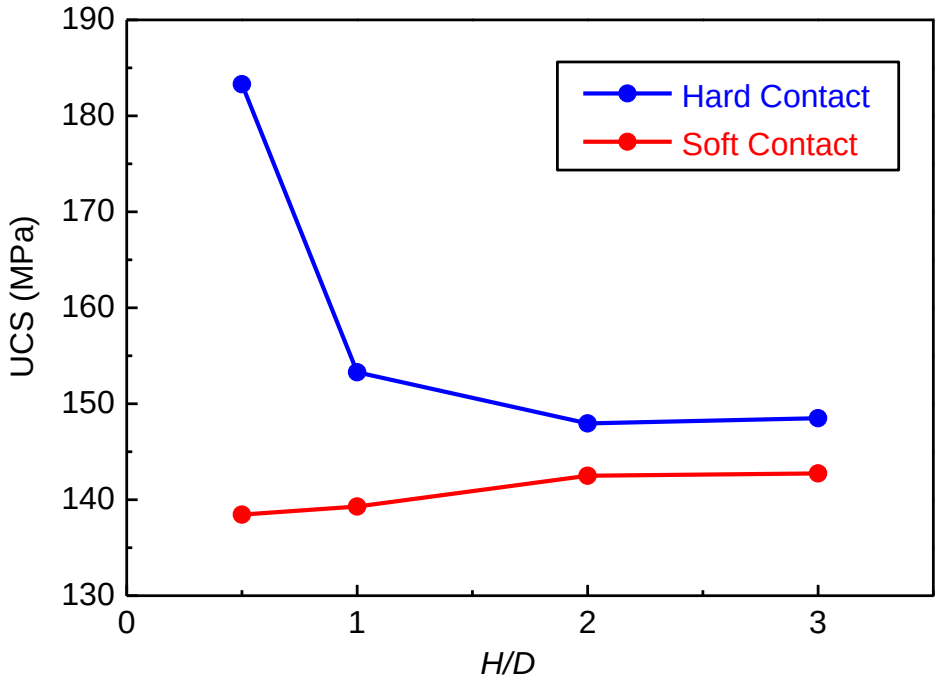

Figure 3-4 UCS of cylindrical specimens with different *H*/*D* ratios under the hard contact and soft contact conditions obtained from numerical modeling.

Figure 3-5 presents the 3D failure modes in the cylindrical specimens with different *H*/*D* ratios. The red zones represent the zones in which large plastic strains occur, which can be used to indicate strain localization (failed elements). Three failure modes are identified: spalling failure ($H/D \leq 1.0$), hour-glassing failure ($H/D = 1.5$), and shear failure ($H/D \geq 2.0$). Due to the strong confining pressures in the end confined zones, element yielding can hardly develop near the ends of the squat specimens, but shear failure can occur in the mid-height of the slender specimens (Figure 2-2). The modeling results agree with the laboratory test results (Figure 2-4) and in-situ observations (Martin and Maybee, 2000).

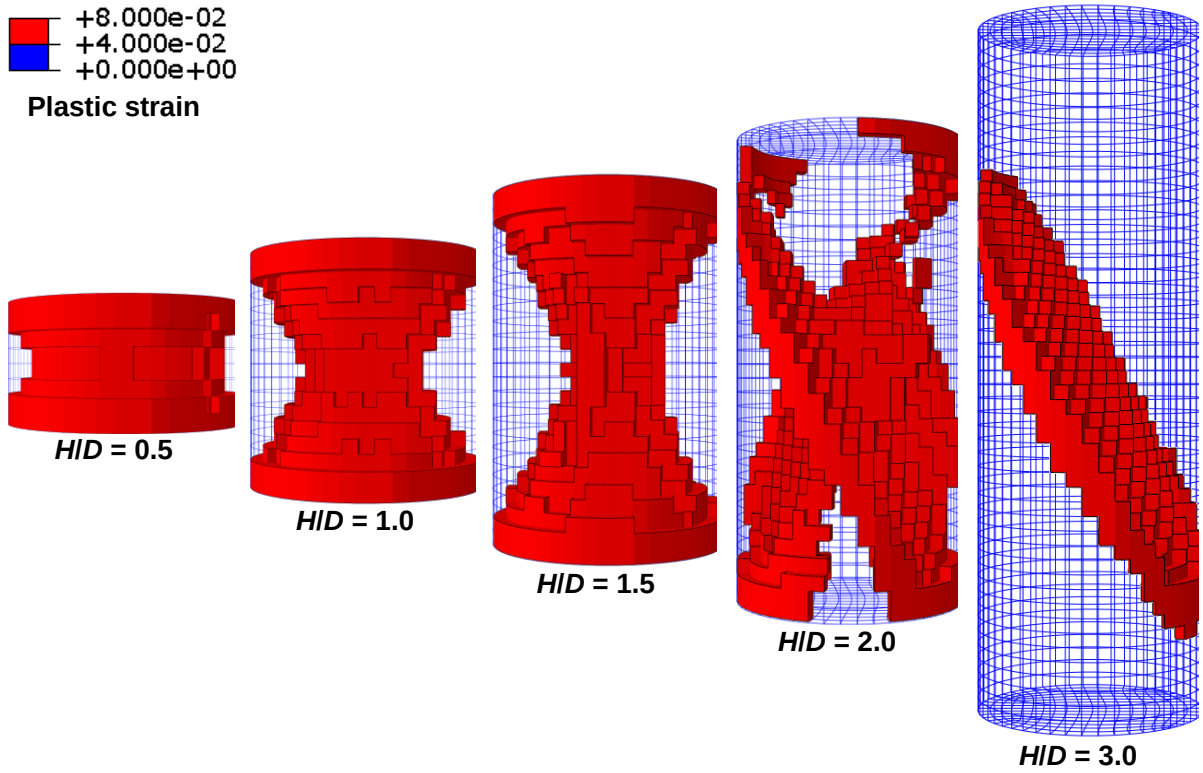

Figure 3-5 3D failure modes of the cylindrical specimens with different *H*/*D* ratios under the hard contact condition.

3.1.2 Cross-sectional shape effect on UCS of rock specimens

3D simulation models of cylindrical, square prismatic, and rectangular prismatic specimens with the standard slenderness ratio of 2.0 in uniaxial compression are shown in Figure 3-6. The geometry of the cylindrical specimen is 50 mm in diameter and 100 mm in height (Figure 3-6a), and that of the square prismatic specimen is 50 mm in width and 100 mm in height (Figure 3-6b), which are same as the dimensions of the laboratory tested specimens (Zhao et al., 2015). In addition to the simulation of the cylindrical and square prismatic specimens used in the laboratory tests, a rectangular prismatic specimen is considered in the numerical modeling to study the cross-sectional shape effect (Figure 3-6c). The cross-section of the rectangular prismatic specimen is 70 mm in length and 35 mm in width, with a cross-sectional area of 2450 mm^2, which is very close to the cross-sectional area of the square prismatic specimen (2500 mm^2). The height of the rectangular prismatic specimen is 100 mm, which is the same as that of the cylindrical and the square prismatic specimens.

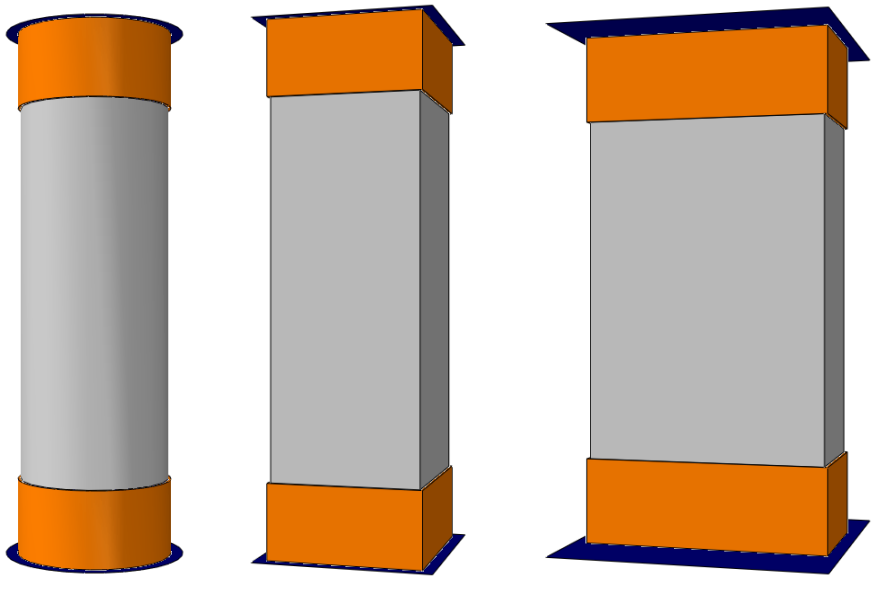

Figure 3-6 3D simulation models of (a) cylindrical, (b) square prismatic, and (c) rectangular prismatic specimens (slenderness ratio of 2.0 as an illustration).

Similar to the models used in the study of the slenderness effect (Figure 3-1), steel platens used to apply a constant loading velocity (0.015 m/s) onto the specimen ends are modeled to honor laboratory test conditions (mechanical parameters of the steel platens are the same as those listed in Table 3-1). In the laboratory tests, the specimen ends were lubricated with a thin layer of Vaseline to reduce the end effect. A μ value of 0.1, recommended from some researchers (Grote and Antonsson, 2009; Rashed and Peng, 2015), is used for the lubricated rock specimen-steel platen contacts.

The material properties of Beishan granite are calibrated first to simulate the uniaxial compression tests. The stress–strain curves of Beishan granite are relatively linear in the pre-peak deformation stage. Hence, the pre-peak behavior of the rock specimens in the numerical modeling is simplified as linear elastic, and the elastic properties obtained from the test results are summarized in Table 3-4.

Table 3-4 Laboratory test data for model parameter calibration

<table>
<tr><td colspan="2">Elastic properties</td><td colspan="4">M-C strength parameters</td></tr>
<tr><td>Poisson’s ratio, ν</td><td>0.22</td><td rowspan="2">($\sigma_2 = \sigma_3$, σ_1) (MPa)</td><td>(0, 145.99)</td><td>(1, 154.63)</td><td>(2, 163.83)</td></tr>
<tr><td>Young’s modulus, E (GPa)</td><td>38</td><td>(3.5, 182.44)</td><td>(5, 206.91)</td><td></td></tr>
<tr><td>UCS (MPa)</td><td>132</td><td>Fitting equation</td><td colspan="3">$\sigma_1 = 12.1\sigma_3 + 142.9$</td></tr>
<tr><td colspan="2">Data source: Zhao et al. (2015)</td><td colspan="4">Data source: Zhao et al. (2013)</td></tr>
</table>

The M-C failure criterion is again employed to define the rock strength. The origin work did not include triaxial compression tests of Beishan granite (Zhao et al., 2015); hence, the calibration of the M-C strength parameters is referred to different laboratory work conducted by Zhao et al. (2013). Based on the fitting equation for the triaxial compression test results of Beishan granite in a low confining pressure range (0 – 5 MPa) (Table 3-4), the frictional strength parameter of

the rock is obtained (Table 3-5). Then, based on the UCS of Beishan granite (Table 3-4), cohesive strength parameter of the rock is calibrated (Table 3-5). Tensile strength was not provided in these test results of Beishan granite; thus the calibration for tension cut-off is based on the data compiled in Cai (2010), and the strength ratio of UCS to tensile strength is taken as 20.

Table 3-5 Strength and deformation parameters of Beishan granite used in simulation

Parameters	Value
Poisson's ratio, ν	0.22
Young's modulus, E (GPa)	38
Cohesion, c (MPa)	19
Residual cohesion, c_r (MPa)	1
Tension cut-off, σ_t (MPa)	7
Friction angle, φ (◦)	58
Dilation angle, ψ (◦)	58

Figure 3-7 presents the modeling results of the UCS of the cylindrical, square prismatic, and rectangular prismatic specimens with different slenderness ratios varying from 2.5 to 1.0, along with the UCS obtained from the laboratory tests for a slenderness ratio of 2.0 (Zhao et al., 2015). Because there is no agreed definition of the slenderness ratio of a rectangular prismatic specimen, the slenderness ratio of the rectangular prismatic specimens presented in the figure is defined by the specimen height divided by the specimen's equivalent width that results in the same cross-sectional area as the square prismatic specimen. Due to the slenderness effect, the UCS of the specimens is increased as the slenderness ratio decreases. It is seen that there is no significant difference of UCS among different cross-sectional-shaped specimens with the same slenderness ratio. The UCS of the square prismatic specimens is, in fact, slightly higher than that of the cylindrical specimens of the same slenderness ratio. The difference of the UCS between the

cylindrical and the square prismatic specimens increases with the decrease of the slenderness ratio due to the increased end effect.

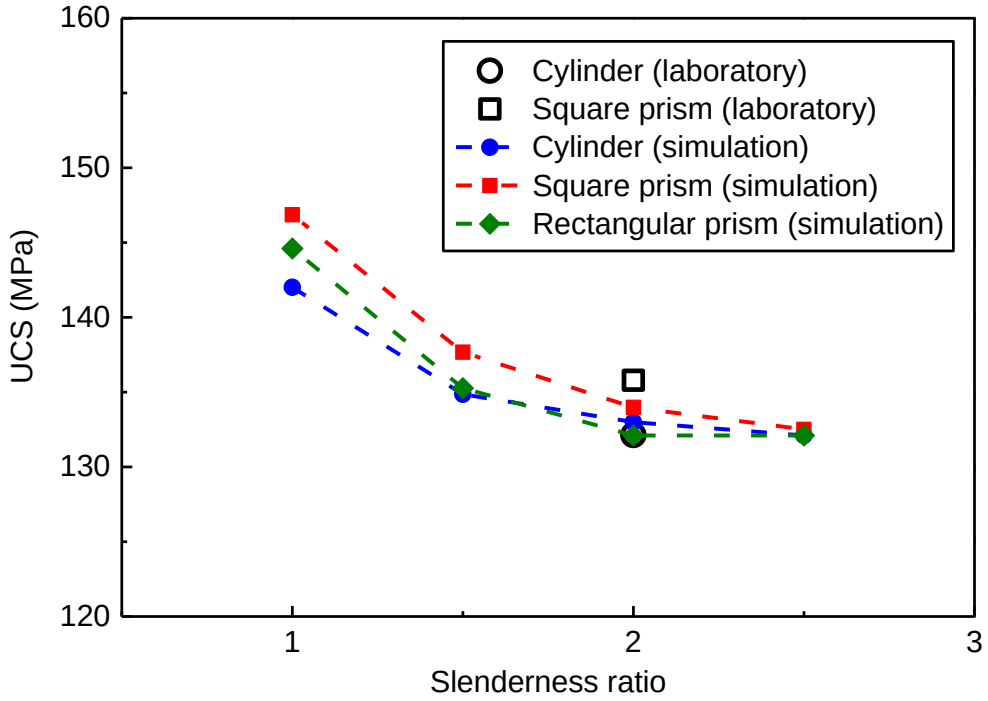

Figure 3-7 UCS of cylindrical, square, and rectangular cross-sectional-shaped specimens with different slenderness ratios obtained from numerical modeling, along with laboratory test results for a slenderness ratio of 2.0 (Zhao et al., 2015).

The modeling results are in good agreement with the laboratory test results (Figure 2-6). In the laboratory tests, eight cylindrical specimens and eight square prismatic specimens with a slenderness ratio of 2.0 were tested and the mean UCS and the standard deviations of the cylindrical and the square prismatic specimens were 132.1 MPa, 4.58 MPa, and 135.8 MPa, 7.20 MPa, respectively. The laboratory test results showed that using carefully prepared specimens for testing, the average UCS of the cylindrical and the square prismatic specimens were close to each other. In fact, the average UCS of the square prismatic specimens is 2.7% higher than that

of the cylindrical specimens. Therefore, it is proven both experimentally and numerically that the cross-sectional shape has a limited influence on the UCS of rock specimens.

3.2 Influence of cross-sectional shape on post-peak deformation behavior of rock specimens

In this section, the influence the cross-sectional shape of a rock specimen on its post-peak deformation behavior is investigated. Obviously, it is difficult to calibrate the post-peak deformation behavior of the Beishan granite specimens in the numerical experiment by referring to the laboratory test results, because the post-peak stress–strain curves obtained by the laboratory tests with rock specimens of the same geometry are variable (Zhao et al., 2015). The mechanical behavior of rock is essentially heterogeneous, and this is especially the case in the post-peak deformation stage, where localized failure normally takes place (Rudnicki and Rice, 1975; Bobet and Einstein, 1998; Hudson and Harrison, 2001). In addition, direct measurement of the stress state and the development of plastic strain in the specimens in laboratory tests are difficult. Moreover, as justified later that instead of using the lateral-strain-controlled loading as in the laboratory tests, the axial-strain-controlled loading is used in the simulation. Hence, the post-peak deformation behavior of the rock is assumed in this numerical experiment and the same justification is applied to the following numerical experiments (Chapters 4 and 5).

The post-peak deformation behaviors of rock in uniaxial compression are usually classified into Class I and Class II failure types (Wawersik and Fairhurst, 1970). Class I failure type shows a strain-softening behavior (Martin and Chandler, 1994; Lockner, 1995; Vardoulakis et al., 1998). Class II failure type, on the other hand, shows that the strength decreases with the decrease of axial strain in the post-peak deformation stage. Both Class I and Class II failure types can be observed in uniaxial compression test results of the same rock type, depending on the servo-

control loading methods used (Section 2.4.2). The risk of violent rock failure often forces tests to be conducted using the lateral or circumferential strain-controlled loading. Therefore, stress–strain curves that show Class II failure type are commonly seen in most laboratory test results (Wawersik and Fairhurst, 1970; Tarasov and Potvin, 2013).

Class I failure type is considered for the Beishan granite specimens in this and the following numerical experiments. Because the influence of different test conditions such as the cross-sectional shape on post-peak deformation behavior of rock is the research focus, and it is better to keep the loading condition simple. Class II failure type can only be obtained using the lateral or circumferential-strain-controlled loading, but it is simple to use the axial-strain-controlled loading in a numerical experiment. More importantly, using the axial-strain-controlled loading might be more appropriate to reflect the actual loading condition in situ. For instance, the loading condition in a pillar is axial-deformation control, and the in situ complete load–deformation curves of pillars obtained by field testing so far show mostly Class I failure type (Cook et al., 1971; Van Heerden, 1975).

Strain-softening behavior is assumed in the numerical experiment to capture the post-peak deformation behaviors of different cross-sectional-shaped specimens in uniaxial compression tests. On one hand, this study focuses on the post-peak stress–strain curves of rock, and the simulation of fracture process at a microscopic scale is beyond the scope this research. On the other hand, the fracture process in the post-peak deformation stage marks the breakage of rock structure, leading to the cohesion loss (Martin, 1997). Accordingly, the strain-softening behavior of the rock can be defined by degrading the rock's cohesion strength as a function of plastic strain (Table 3-6).

Table 3-6 Strain-softening parameters of the rock

Cohesion yield stress (MPa)	Plastic strain
19.0	0
16.0	0.008
9.5	0.035
1.0	0.090

Figure 3-8 presents the complete stress–strain curves of different cross-sectional-shaped specimens in uniaxial compression obtained from numerical modeling. It is seen that the post-peak stress–strain curves of the specimens are influenced by their cross-sectional shapes. The square prismatic specimen shows the flattest post-peak descending slope of the stress–strain curve, that of the rectangular prismatic specimen is the steepest, and the cylindrical specimen is between these two.

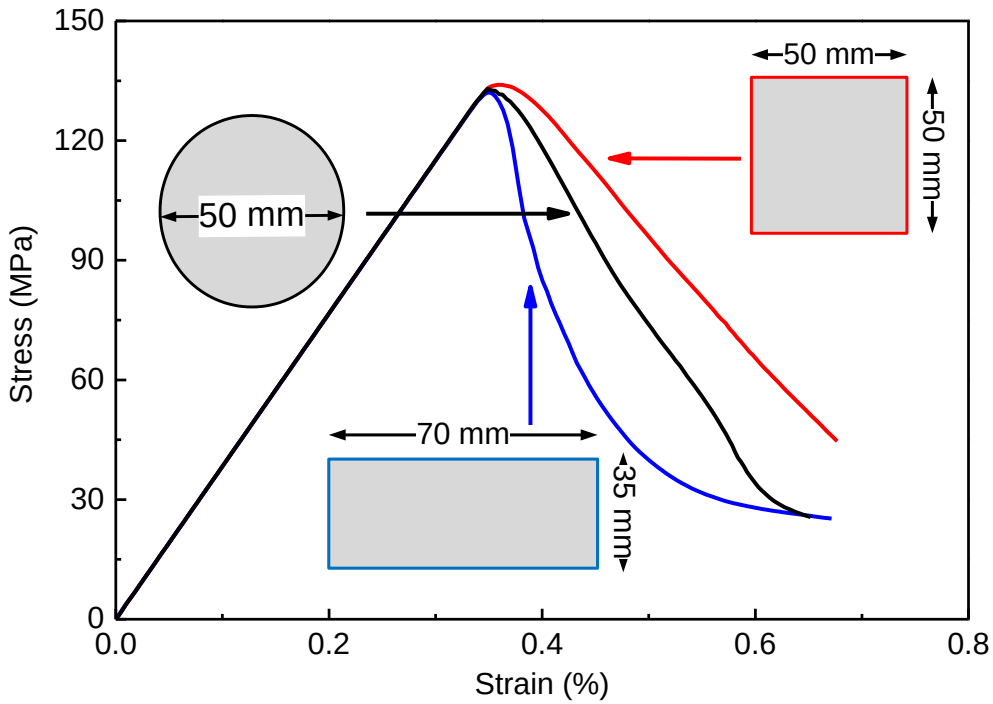

Figure 3-8 Stress–strain curves of different cross-sectional-shaped specimens in uniaxial compression obtained from numerical modeling.

3.3 Discussions

3.3.1 End effect on peak strength of rock specimens

The modeling results demonstrate that there is no significant influence of cross-sectional shape on the peak strength of rock, which is supported by the laboratory test results (Zhao et al., 2015). An advantage of numerical modeling is that it allows a detailed investigation of the mechanism that governs the observed phenomena. Figure 3-9 presents the distributions of confined elements ($\sigma_3 < 0$, compression is negative in ABAQUS) in the specimens (the 1st row), the contours of σ_3 on the side, top, and two vertical surfaces revealed from a quarter cut of the specimens (the 2nd row), and the distribution of confined elements with relatively high confining pressures ($\sigma_3 < -1.5$ MPa) in the specimens (the 3rd row) at peak load.

The distributions of the confined elements and the σ_3 contours in different cross-sectional-shaped specimens are similar at their peak loads because their slenderness ratios and contact friction are the same. Consequently, specimens with different cross-sectional shapes have similar peak strengths. The confined elements whose confining pressures (absolute values) are greater than 1.5 MPa at the peak load are lumped near the specimen's ends, forming cone-shaped confined zones, and the tops of which are approximately 15 mm from the ends of the specimens. The elements in these "highly" confined zones have higher peak strengths due to increased confining pressures. Therefore, hour-glassing failure mode is normally observed in uniaxial compression tests; it can also be observed in pillar failure in the field because of strong end constraint to the pillars (Figure 3-5).

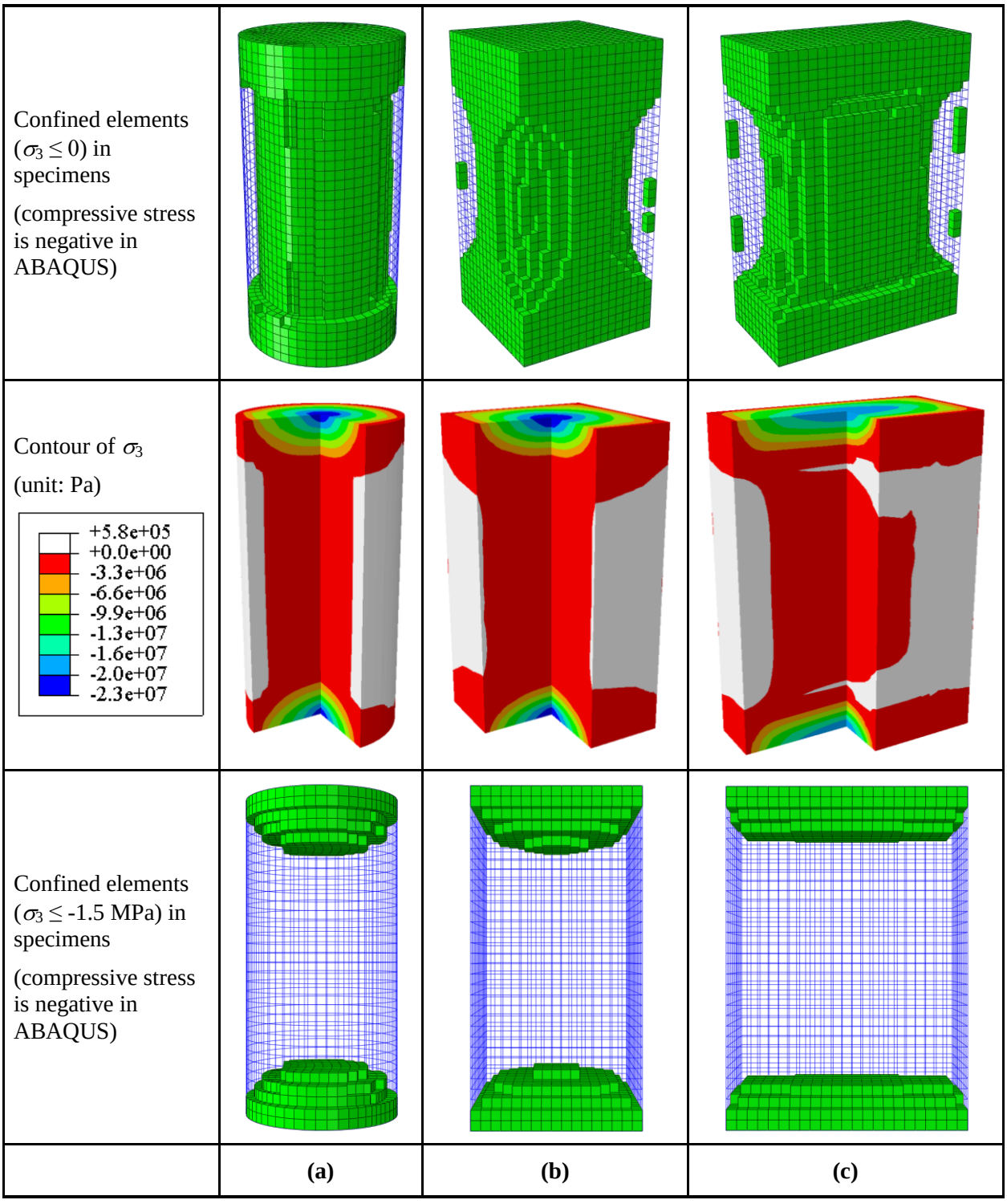

Figure 3-9 Distributions of confined elements at two σ_3 thresholds and σ_3 contours in different cross-sectional-shaped specimens at peak load: (a) cylindrical, (b) square prismatic, and (c) rectangular prismatic specimens.

Both the numerical modeling and the laboratory test results show that the peak strength of a square prismatic specimen with a slenderness ratio of 2.0 is higher than that of a cylindrical specimen of the same slenderness ratio. Table 3-7 presents the percentages of the confined elements ($\sigma_3 < 0$) to the total number of elements in each specimen, along with the average σ_3 in the whole specimen, in the portion of 15 mm to the specimen's end, and in the 70 mm middle portion of the specimen at peak load.

Table 3-7 Percentages of confined elements to the total number of elements and average σ_3 in various portions of the specimens at peak load

	Cylindrical specimen	Square prismatic specimen	Rectangular prismatic specimen
Total number of elements	8844	9537	9108
Number of confined elements	6836	8531	7178
Percentage of confined elements at peak load	**77%**	**89%**	**79%**
Average σ_3 (MPa) in the whole specimen	-1.22	-1.40	-1.15
Average σ_3 (MPa) in the portion of 15 mm to the specimen end	-3.95	-4.00	-3.70
Average σ_3 (MPa) in the 70 mm middle portion of the specimen at peak load	-0.04	-0.27	-0.04

The σ_3 value in each confined element due to end constraint controls the overall strength enhancement of the specimen. The square prismatic specimen has the highest percentage of confined elements in its volume and the highest confining pressure (absolute value) than the other two specimens. This is why it has a higher peak strength than the other two specimens. For

all specimens, the average σ_3 in their end zones is much higher than that in their middle portions, demonstrating that the end effect has a large influence on the σ_3 distribution near the specimen ends (Brady, 1971).

3.3.2 End effect on the post-peak deformation behavior of rock specimens

As seen in Figure 3-8, the post-peak deformation behavior of a specimen depends on its cross-sectional shape. Figure 3-10 presents the distributions of confined elements at two σ_3 thresholds and the σ_3 contours in the three cross-sectional-shaped specimens at an axial strain of $\varepsilon = 0.5\%$ in the post-peak deformation stage. It is seen that due to the end effect, the square prismatic specimen has the highest local confining pressure in the post-peak deformation stage and the rectangular prismatic specimen has the lowest one. Table 3-8 presents the percentages of confined elements and the average σ_3 in the three cross-sectional-shaped specimens at $\varepsilon = 0.5\%$. The results show that locally confined elements in a specimen are reduced (comparing with the numbers shown in Table 3-7) due to the progressive failure of the rocks, and the degrees of decrease of the confined elements in the post-peak deformation stage are different for the three specimens. The square prismatic specimen has the highest percentage of confined elements and the smallest tensile stress σ_3; hence, its strength reduction in the post-peak deformation stage is the smallest. In contrast, the rectangular prismatic specimen has the lowest percentage of confined elements and the largest tensile stress σ_3, and its post-peak curve is the most brittle.

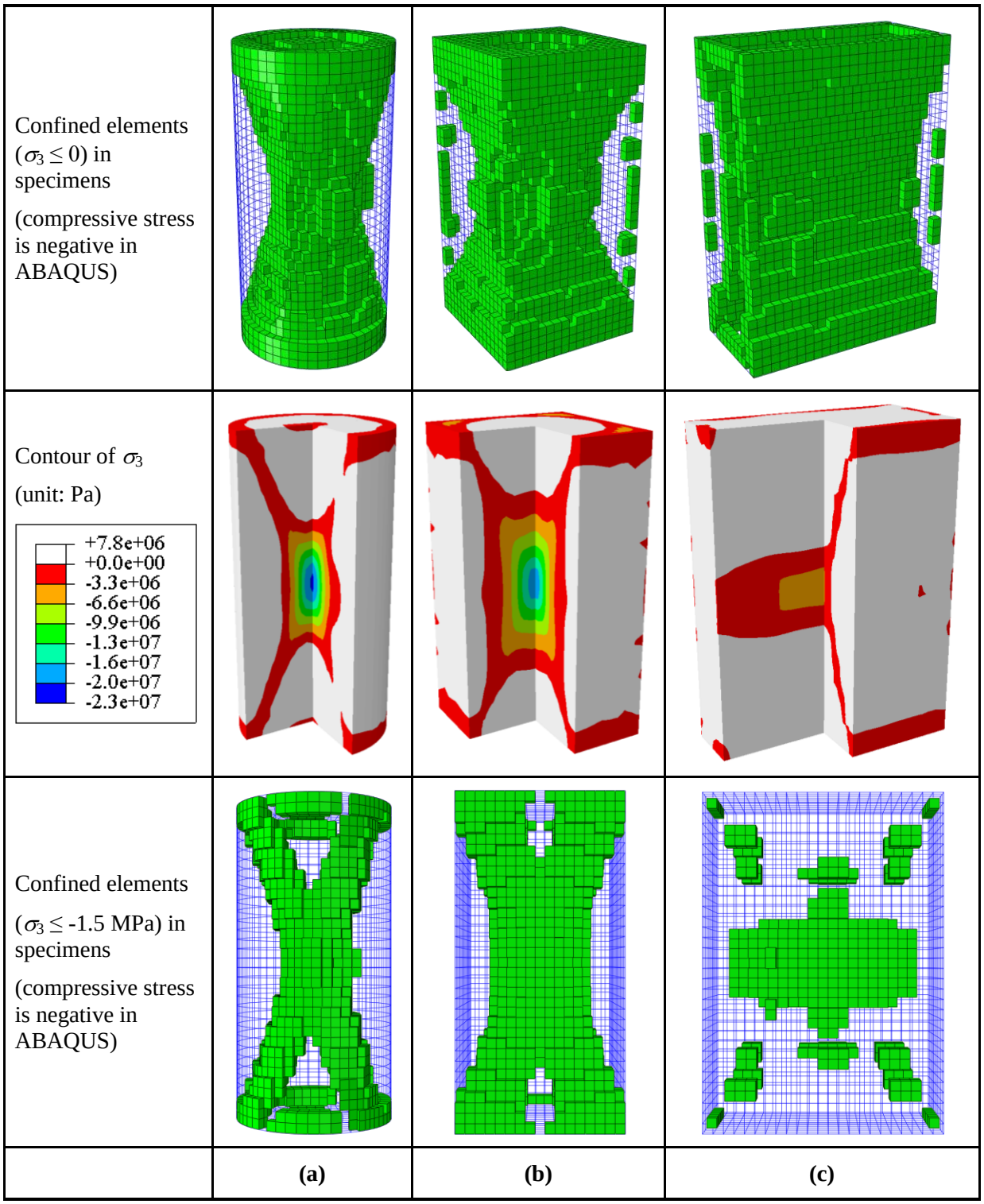

Figure 3-10 Distributions of confined elements at two σ_3 thresholds and σ_3 contours in different cross-sectional-shaped specimens at ε = 0.5% in the post-peak deformation stage: (a) cylindrical, (b) square prismatic, and (c) rectangular prismatic specimens.

As can be noticed from Table 3-7 and Table 3-8, the average σ_3 in each specimen changes from compression at the peak load to tension in the post-peak loading stage at $\varepsilon = 0.5\%$. Figure 3-11 presents the evolution of tensile stress ($\sigma_3 > 0$) at different loading stages in the three cross-sectional-shaped specimens. Tensile stress becomes more prominent with the increase of axial strain in the post-peak deformation stage. At peak load, tensile stress appears only near the edge in the central areas of the specimens. In the post-peak deformation stage, σ_3 in the cone-shaped confined zones seen before at peak load gradually become tensile as deformation increases.

Table 3-8 Percentages of confined elements to the total number of elements and average σ_3 in various portions of the specimens at $\varepsilon = 0.5\%$ in the post-peak deformation stage

	Cylindrical specimen	Square prismatic specimen	Rectangular prismatic specimen
Total number of elements	8844	9537	9108
Number of confined elements	3978	5582	3670
Percentage of confined elements at $\varepsilon = 0.5\%$	**45%**	**59%**	**40%**
Average σ_3 (MPa) in the whole specimen at $\varepsilon = 0.5\%$	1.54	0.12	2.68
Average σ_3 (MPa) in the portion of 15 mm to the specimen end at $\varepsilon = 0.5\%$	1.36	0.18	3.05
Average σ_3 (MPa) in the 70 mm middle portion of the specimen at $\varepsilon = 0.5\%$	1.62	0.09	2.62

Referring to Equation 2-1, the lateral expansion rate of the rock is higher than that of the steel platens as the load increases. The elements near the steel platens are restricted by the platens and therefore subjected to compressive stresses if there is no rock failure. In the post-peak deformation stage, on the other hand, tensile stresses are generated in these elements because

their lateral contraction rate is higher than that of the steel platens as the load decreases. However, the evolutions of σ_3 in the post-peak deformation stage are different for different cross-sectional-shaped specimens. The rectangular prismatic specimen shows the largest tensile stress zones in the specimen, while the cylindrical and the square prismatic specimens show relatively smaller tensile stress zones.

The slenderness effect becomes more significant in uniaxial compression tests when the slenderness ratio of a specimen decreases (Figure 2-2). In essence, it is the change of the specimen geometry that leads to an increase or a decrease of the influence of the end effect on the rock strength. In other words, the geometry effect of a rock specimen is essentially manifested by the distribution of confined zones caused by the end effect. The cross-sectional shape effect can be seen clearly in the post-peak deformation stage, when progressive failure of elements gradually decreases the effective bearing area of a specimen and consequently changes the effective specimen geometry.

Failures occur first locally in elements whose confining pressure is small, and the locations of these elements depend on the cross-sectional shape of the specimen. The degree of the effective specimen geometry change is also dependent on the cross-sectional shape of the specimen. Therefore, the confined zones in a specimen are more dependent on the cross-sectional shape of the specimen in the post-peak deformation stage and so is the post-peak stress–strain curve. For instance, the elements of the rectangular prismatic are non-uniformly confined (Figure 3-10c) and there are many of them subjected to tensile σ_3 (Figure 3-11c); hence, the overall post-peak strength of the rectangular prismatic specimen is lower than these of the other two specimens. The cylindrical and square prismatic specimens are uniformly restricted (Figure 3-10a & b) and

there are less elements whose σ_3 is tensile within the specimens (Figure 3-11a & b) in the post-peak deformation stage. Therefore, the post-peak strengths of these two specimens are relatively high. Furthermore, the post-peak strengths of the cylindrical and the square prismatic specimens are different because the σ_3 contours in the two specimens are not the same. Thus, it is concluded that the cross-sectional shape affects the post-peak deformation behavior of rock.

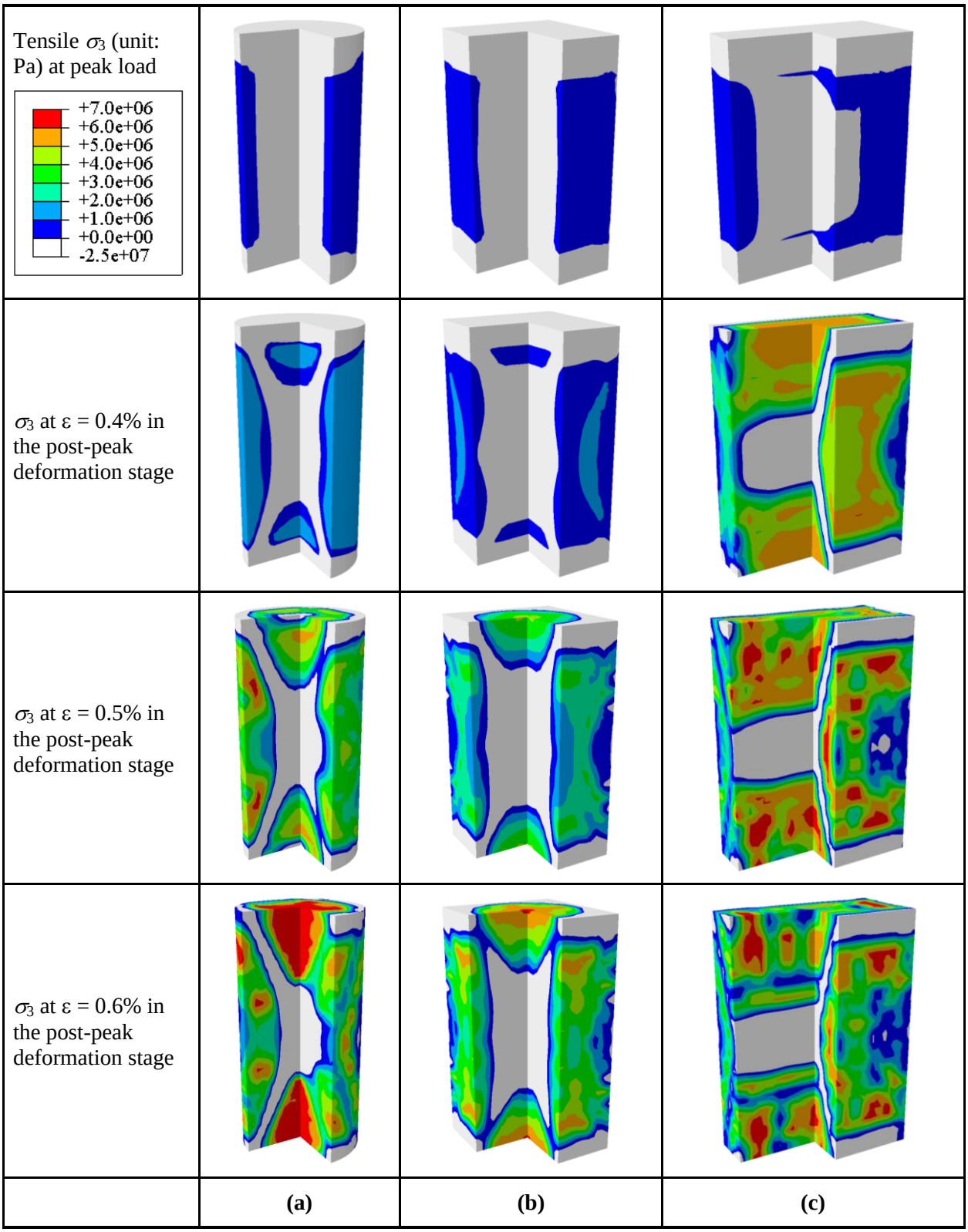

Figure 3-11 Evolutions of tensile σ_3 ($\sigma_3 > 0$ contours) in different cross-sectional-shaped specimens at different deformation stages: (a) cylindrical, (b) square prismatic, and (c) rectangular prismatic specimens.

3.3.3 Hoop tension theory

Because a continuum numerical tool is used in this study, it is not possible to capture explicitly the crack initiation and propagation processes that lead to discontinuous failure of rock (Senent et al., 2013). Although the influence of hoop tension on a dilating crack cannot be simulated explicitly, it is still reasonable to verify the hoop tension theory by comparing the confined elements and the σ_3 value on average in the cylindrical specimen with those in the prismatic specimens. Based on the hoop tension theory, it can be reckoned that the number of confined elements and the average compressive σ_3 value in a cylindrical specimen should be greater than that in a square or a rectangular prismatic specimen. Hence, the strength of the cylindrical specimen should be the highest because the cylindrical shape favors the development of hoop tension(Figure 2-5).

The modeling results show that for the same slenderness ratio of different shaped specimens, it is the square prismatic specimen rather than the cylindrical specimen that has the highest percentage of confined elements and the highest confining pressure (or the lowest tension), both at the peak and the post-peak loading stages (Table 3-7 and Table 3-8). In addition, both the laboratory and the modeling results show that the strength of the square prismatic specimen is higher than that of the cylindrical specimen (Figure 3-7). The strength of the rectangular prismatic specimen is also very close to that of the cylindrical and the square prismatic specimens. Thus, it is concluded that hoop tension contributes little to affecting rock strength.

A major difference between the strengths obtained from laboratory tests (using specimens) and field data interpretation is that the interpreted field rock strength depends on the interpretation model used. When a numerical model reflects the field condition better, the interpreted rock strength of massive rocks is closer to that obtained from laboratory tests and this was

demonstrated by Cai and Kaiser (2014) using the Mine-by tunnel case history. Although the height (100 mm) and the slenderness ratio (2.0) of the cylindrical and the square prismatic specimens are the same in the laboratory tests, the cross-sectional area of the square prismatic specimen (50 × 50 = 2500 mm^2) is larger than that of the cylindrical specimen ($\pi \times 25^2$ = 1963 mm^2). In such a case, the equivalent diameter of the square specimen is 56.4 mm, resulting in an equivalent slenderness ratio of H/D = 1.8 that is squatter than the cylindrical specimen with H/D = 2.0. Therefore, the end effect has a greater influence on the strength of the square prismatic specimen. Additional modeling results shown in Figure 3-12 reveal that if a square prismatic specimen with a width of 44 mm is used in uniaxial compression tests, it gives almost the same cross-sectional area (1936 mm^2) as that of a cylindrical specimen with a diameter of 50 mm. In such a case, the UCS of the square prismatic specimens is very close to that of the cylindrical specimens.

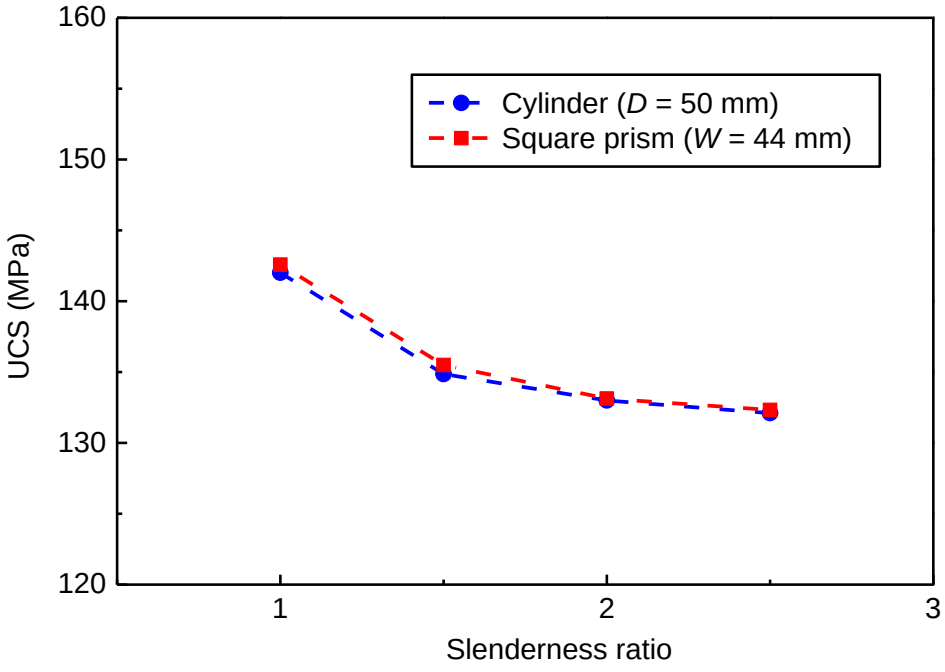

Figure 3-12 UCS of cylindrical (D = 50 mm) and square (W = 44 mm) cross-sectional-shaped specimens with different slenderness ratios obtained from numerical modeling.

3.4 Summary

The validity of the numerical model was firstly examined by modeling the slenderness effect under the hard contact and soft contact conditions. The opposite trends of the slenderness effect on UCS under the two contact conditions obtained from the numerical modeling agree well with the laboratory observations. The numerical model was then further verified by comparing the UCS of cylindrical and square prismatic specimens obtained from the numerical modeling with that obtained from laboratory tests. Both the numerical modeling and the laboratory test results show that the cross-sectional shape has a very small influence on the UCS of rock specimens.

Although the influence of the cross-sectional shape on the peak strength of rock specimens is small, the modeling results reveal that the cross-sectional shape affects the post-peak deformation behavior considerably. They also demonstrate that hoop tension contributes little to affecting rock strength. It is revealed through the numerical modeling that because the square prismatic specimen with a slenderness ratio the same as that of a cylindrical specimen has a larger equivalent diameter, the square prismatic specimen has a slightly higher UCS and this was observed in the laboratory test results. It is therefore suggested that the equivalent diameter of a non-cylindrical cross-section be used to define the slenderness ratio so as to present laboratory test and numerical modeling results consistently.

The studies presented in this chapter demonstrated that the end effect has a great impact on rock laboratory test results in several ways, e.g., it results in the slenderness effect and the cross-sectional shape effect, as observed in uniaxial compression test results. In next chapter, the potential influence of the end friction on the σ_2 effect observed in true triaxial compression test results is investigated.

Chapter 4

4 End effect in true triaxial compression test

To date, the importance of accurately estimating rock strength in a true triaxial stress state, especially near the low confining pressure range, is driven by increased deep tunneling activities (Brady and Brown, 2013). A comprehensive numerical experiment on the influence of the end effect on rock strength in true triaxial compression test was carried out and the results are presented in this chapter.

The validity of the modeling tool and numerical model on simulating the end effect in uniaxial compression test was examined in Chapter 3. In this study, it is hypothesized that the confined zones, which is caused by the end constraints near the rock specimen-steel platen contacts where σ_2 is applied, can increase the actual σ_3 in true triaxial compression test and hence the rock strength. First, the validity of the numerical model to simulate the end effect in conventional triaxial compression test was examined. Next, a comprehensive numerical experiment on the end effect in true triaxial compression test was presented. Insights from the modeling results suggest that there is a contribution of the end effect to the observed σ_2 effect. Subsequently, the theoretical and laboratory approaches were employed to confirm the modeling results.

4.1 Verification of numerical models

A numerical experiment is carried out to simulate the reduction of the slenderness effect with the increase of confining pressure, which was observed in the conventional triaxial compression test results (Section 2.2.2). Similar to the motivation of the numerical experiment presented in Section 3.1.1, this numerical experiment is conducted as a means of illustrating the validity of

the chosen numerical model for modeling the end effect in triaxial compression tests before modeling the end effect in true triaxial compression tests.

The cylindrical specimen the same as that shown in Figure 3-1 and the material parameters the same as those listed in Table 3-1 and Table 3-2 are employed in this numerical experiment. No special anti-friction measures were taken in the laboratory tests (Mogi, 2007); thus μ = 0.2 is assumed for the rock specimen-steel platen contacts (refer to discussion in Section 3.1.1). The confining pressure ($\sigma_2 = \sigma_3$) is applied to the outer surfaces of the cylindrical specimen, meanwhile a constant loading velocity (0.016 m/s) is applied to the top and bottom rams. In this fashion, a conventional triaxial stress state ($\sigma_1 > \sigma_2 = \sigma_3 > 0$) can be established in the specimen.

Figure 4-1 present the modeling results of peak strengths (σ_1) of the specimens with different *H*/*D* ratios under two levels of confining pressures (5 and 10 MPa).

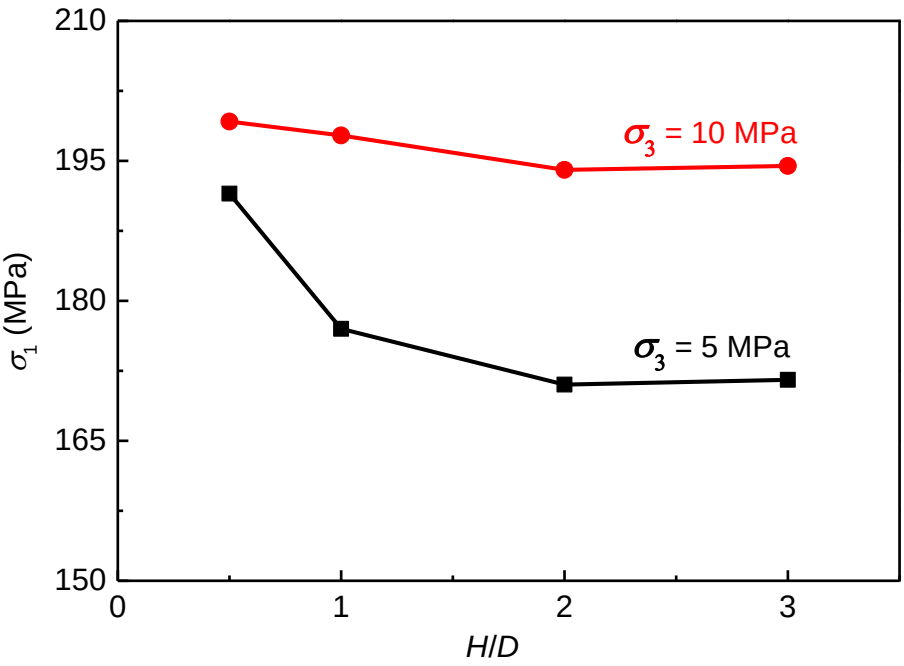

Figure 4-1 Peak strengths (σ_1) of specimens with different *H*/*D* ratios and confining pressures ($\sigma_2 = \sigma_3$) obtained from numerical modeling.

With the increase of confining pressure in the conventional triaxial compression tests, the slenderness effect results in a gradual decrease of the end effect. When a rock specimen is subjected to a high confining pressure, the rock strength is more dependent on the confining pressure and the influence of the end effect and specimen's slenderness ratio on rock strength becomes less dominant. This is because that compared with the end constraint at the top and bottom rock specimen-steel platen contacts (refer to Figure 3-9), the lateral constraint (confining pressure) has a greater influence on the increase of σ_3 in the specimen and thus dominates the enhancement of the rock strength. The modeling results agree well with the laboratory test results (Figure 2-8).

4.2 Numerical simulation of true triaxial compression test

4.2.1 A proposed method to quantify the observed σ_2 effect

The literature review in Section 2.2.3 shows that the observed strengthening effect of σ_2 on different rocks is varied. In addition, enlightened by some indirect evidences, it is reckoned that different deformation behaviors of rocks can result in different levels of end constraint near the contacts where σ_2 is applied, thus the observed σ_2 effect can be different. Furthermore, in true triaxial compression tests, the strengthening effect due to end constraint on rock strength may be more significant at low confining pressures and so is the observed σ_2 effect. Thus, the observed σ_2 effect needs to be compared in a quantitative manner.

A method to quantify the observed σ_2 effect is proposed in this study and is schematically shown in Figure 4-2. Blue point (0, σ_c) represents UCS (σ_c); blue points (σ_2, σ_1) represent conventional triaxial stress states at different σ_3; red points (σ_2^*, σ_1^*) represent the stress state at the strength plateaus in the σ_1–σ_2 curves at different σ_3. The slope between point (σ_2, σ_1) at the origin of the

σ_1–σ_2 curve and point (σ_2^*, σ_1^*) at the summit of the σ_1–σ_2 curve gives the maximum percentage increase of rock strength caused by σ_2. In this way, the strengthening effect of σ_2 on different rocks can be quantified.

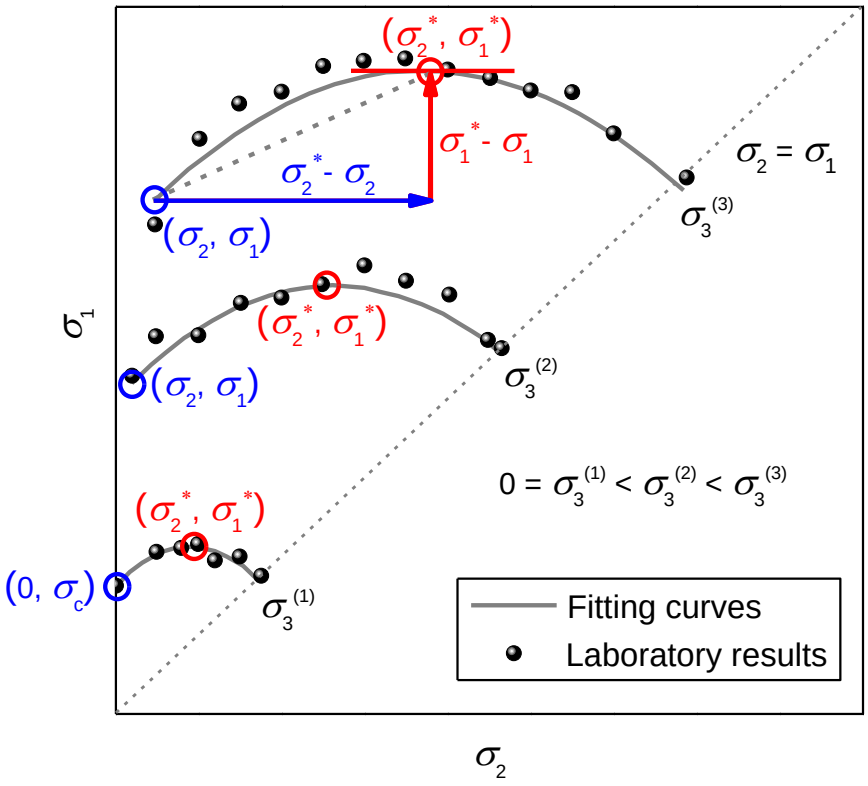

Figure 4-2 Schematic of proposed method to quantify σ_2 effect (laboratory results are only used for illustrative purpose).

Basing on the published data of true triaxial compression tests, some of the observed σ_2 effect are quantified and summarized in Table 4-1. Test results that do not show the strength plateau in the σ_1–σ_2 curves are not included. It is seen that the σ_2 effect on rock strength increase is not the same for different rocks. Moreover, it seems that the observed σ_2 effect on rock strength is more significant when the applied σ_3 is low, and it decreases with the increase of σ_3. For instance, an

unusually high percentage of strength increase of 114% for Westerly granite is observed for $\sigma_3/\sigma_c = 0$, and it drops to 49% for $\sigma_3/\sigma_c = 0.38$.

Table 4-1 Quantified σ_2 effect in different rocks (data from Chang and Haimson, 2000; Haimson and Chang, 2000; Mogi, 2007)

KTB amphibolite	σ_3/σ_c	0.00	0.19	0.38	0.63	0.95	
	$(\sigma_1^* - \sigma_1) / (\sigma_2^* - \sigma_2)$	69%	70%	39%	45%	29%	
Westerly granite	σ_3/σ_c	0.00	0.10	0.19	0.30	0.38	0.50
	$(\sigma_1^* - \sigma_1) / (\sigma_2^* - \sigma_2)$	114%	103%	88%	59%	49%	58%
Dunham dolomite	σ_3/σ_c	0.09	0.17	0.25	0.32	0.40	0.47
	$(\sigma_1^* - \sigma_1) / (\sigma_2^* - \sigma_2)$	78%	63%	43%	42%	38%	32%
Solnhofen limestone	σ_3/σ_c	0.06	0.13	0.26			
	$(\sigma_1^* - \sigma_1) / (\sigma_2^* - \sigma_2)$	34%	33%	36%			
Yamaguchi marble	σ_3/σ_c	0.15	0.30	0.49			
	$(\sigma_1^* - \sigma_1) / (\sigma_2^* - \sigma_2)$	104%	79%	53%			
Mizuho trachyte	σ_3/σ_c	0.45	0.60	0.75	1.00		
	$(\sigma_1^* - \sigma_1) / (\sigma_2^* - \sigma_2)$	34%	30%	26%	25%		
Manazuru andesite	σ_3/σ_c	0.14	0.29	0.50			
	$(\sigma_1^* - \sigma_1) / (\sigma_2^* - \sigma_2)$	82%	54%	52%			
Inada granite	σ_3/σ_c	0.09	0.18	0.44	0.66	0.88	
	$(\sigma_1^* - \sigma_1) / (\sigma_2^* - \sigma_2)$	104%	71%	57%	65%	69%	
Orikabe monzonite	σ_3/σ_c	0.17	0.34	0.59	0.85		
	$(\sigma_1^* - \sigma_1) / (\sigma_2^* - \sigma_2)$	115%	80%	66%	67%		

4.2.2 Selection of published true triaxial compression test results

There are a number of true triaxial compression test machines for soil, concrete and rock testing (Shi et al., 2012). It is necessary to select test results with precaution for this numerical experiment. First, the reliability of a true triaxial compression test machine should be well recognized and the tests should be conducted with a high level of repeatability under carefully

controlled test conditions. Second, test results with various types of rocks should be considered to ensure the validity of this numerical experiment.

Basing on above considerations, two types of true triaxial compression test machines and their corresponding test results are chosen. The first one is the Mogi-type machine, which had been used to test seven types of rocks. Test results of Solnhofen limestone are selected (Mogi, 2007), which show clearly the influence of σ_2 on rock strength. In addition, test results of Takahashi and Koide (1989), who designed a new Mogi-type machine, are selected (Section 2.2.3). The second type of test machine was developed by Chang and Haimson (2000), and it is called the Haimson-type machine. The major difference between these two types of test machines is that the pistons of the Mogi-type machine that apply two perpendicular principal stresses σ_1 and σ_2 are positioned in the vertical direction, while a biaxial test machine is positioned horizontally in the Haimson-type machine to apply σ_1 and σ_2. The test results of KTB amphibolite and Westerly granite by Chang and Haimson (2000), which are well known in the field of true triaxial compression testing, are selected. Thus, representative test data of igneous (granite), sedimentary (limestone and shale), and metamorphic (amphibolite) rocks are all included in this study.

4.2.3 M-C failure criterion and modeling strategy

The research focus is the influence of end effect on true triaxial compression test results. Because the end effect inevitably exists in rock compression tests (Section 2.2), 3D empirical failure criteria (Mogi, 1967; Al-Ajmi and Zimmerman, 2005) developed from true triaxial compression test results might also contain rock strength strengthening due to the end effect. Therefore, a rock material model that excludes the influence of σ_2 effect on rock strength is preferable to study the

contribution of end effect to the observed σ_2 effect. As a result, the M-C failure criterion[2], which does not consider σ_2, is used to define the rock strength while the actual contact condition of rock specimens in true triaxial compression test is modeled explicitly.

The 2D M-C failure criterion is one of the most commonly used failure criteria in rock engineering (Section 3.1.1). Despite one of its shortcomings, i.e., the linear nature of this failure criterion which may make it difficult to predict rock strength accurately when the applied confining pressures are within a large range (Hoek and Brown, 1997; Jaeger et al., 2007), the strength parameters of the M-C failure criterion can be readily obtained or calibrated by performing simple rock property testing. More importantly, the M-C failure criterion depicts the characteristic of rock strength and failure type under confining pressure condition satisfactorily. The shortcoming of the M-C failure criterion for representing nonlinear failure envelopes of rocks in the σ_1–σ_3 space can be overcome by restricting confining pressure to a limited range of interest (Pariseau, 2007; Mogi, 2007; Labuz and Zang, 2012; Brady and Brown, 2013).

The modeling strategy of using a simple failure criterion can isolate the end effect in the true triaxial compression test. As it is hypothesized in this study, the end effect in a true triaxial compression test can result in confined zones similar to that in an uniaxial compression test and enhance the actual σ_3 in the rock and hence its strength. By increasing σ_2 in true triaxial compression test, if it is verified that a material whose strength is only σ_3-dependent experiences a strength enhancement due to the end effect with the increase of σ_2, then a both σ_3 and σ_2 dependent material, which is more likely being the real material property of rock, should be able to experience at least the same or even higher strengthening with the same strengthening effect

[2] 3D failure criteria considering σ_2 effect are not available in ABAQUS.

due to the end effect. This is because that for rock which is inherently confining pressure-dependent, the confining pressures it is subjected to might not be exclusively caused by σ_3 loading. Instead, the confining pressure might be influenced by σ_2 loading, leading to a combined influence of both σ_3 and σ_2 on rock strength. As a result, the M-C failure criterion is considered suitable for the proposed investigation.

4.2.4 Numerical models

In true triaxial compression test, friction-reducing materials are routinely employed to reduce the end effect. Mogi (2007) employed Teflon sheets and thin copper shims as lubricants. Takahashi and Koide (1989) used thin copper sheets and Teflon sheets with silicon grease. Haimson and Chang (2000) inserted thin copper shims and stearic lubricant at the rock specimen-steel platen contacts.

According to the aggregate state of the material zones involved, friction states can be classified as: solid friction, boundary friction, mixed friction, and fluid friction (Grote and Antonsson, 2009). Solid friction acts at direct contacts where material zones exhibit solid properties; boundary friction refers to the boundary layers on the contacts, each consists of a molecular film coming from a lubricant; fluid friction occurs when lubricating film is created between the friction body surfaces to reduce wear; mixed friction is a mixed form of boundary and fluid frictions. Apparently, the friction state at a lubricated specimen-platen contact is neither a solid friction nor a fluid friction state. According to the Handbook of Mechanical Engineering (Grote and Antonsson, 2009), the μ value ranges for boundary and mixed frictions are 0.1 – 0.2 and 0.01 – 0.1, respectively.

For lubricated rock specimen-steel platen contacts, it is reported that the μ values can be as low as 0.024 (He et al., 2014) and as high as 0.1 (Rashed and Peng, 2015), or even 0.39 in some cases (Hawkes and Mellor, 1970). A μ value of 0.05 is reported in Labuz and Bridell (1993) and a μ range of 0.04 $\pm$ 0.003 is given in the Handbook on Mechanical Properties of Rocks by Vutukuri et al. (1974). Accordingly, friction at lubricated specimen-platen contacts can be in a mixed friction state. Hence, μ = 0.05–0.1 may seem to be an appropriate range to reflect the friction at lubricated rock specimen-steel platen contacts.

It must be pointed out that the loading conditions in sliding tests (or direct shear test) designed specifically to measure μ value and that in rock laboratory strength tests are different. It is stated in the Handbook of Mechanical Engineering that "friction does not represent a constant property of a material but rather depends on variables, e.g., on the load and the elements involved in the friction process with their properties and interactions." In this numerical experiment, acknowledging that all the considered true triaxial compression tests had employed anti-friction measures, base values of μ in the range of 0.05 to 0.1 at the specimen-platen contacts were used in the modeling. To exclude the actual end effect as well as the potential σ_2 effect due to the end effect from true triaxial compression test results, a minimum μ value of 0 was used. Finally, to appreciate the fact that the actual μ value under high normal stresses for some rocks might be different from that obtained by sliding tests, a maximum μ value of 0.2 was used.

3D simulation models of cylindrical specimens in uniaxial and conventional triaxial compression tests, and a square prismatic specimen in true triaxial compression test, as well as their corresponding loading conditions are shown in Figure 4-3a, b, and c, respectively. Arrows in these figures show the direction of the principal stresses. Thick orange arrows indicate that the

principal stress is applied by steel platens and thin blue arrows indicate that the principal stress is applied by hydraulic pressure. In the modeling, the applied σ_3 (to the specimen) and σ_2 (to the platens) are pressure controlled, which means that once the applied principal stresses reach an assigned magnitude, the pressure will be hold constant on the applied surface. The applied σ_1 is axial-strain-controlled loading, which means that σ_1 is applied at a constant loading velocity (0.015 m/s).

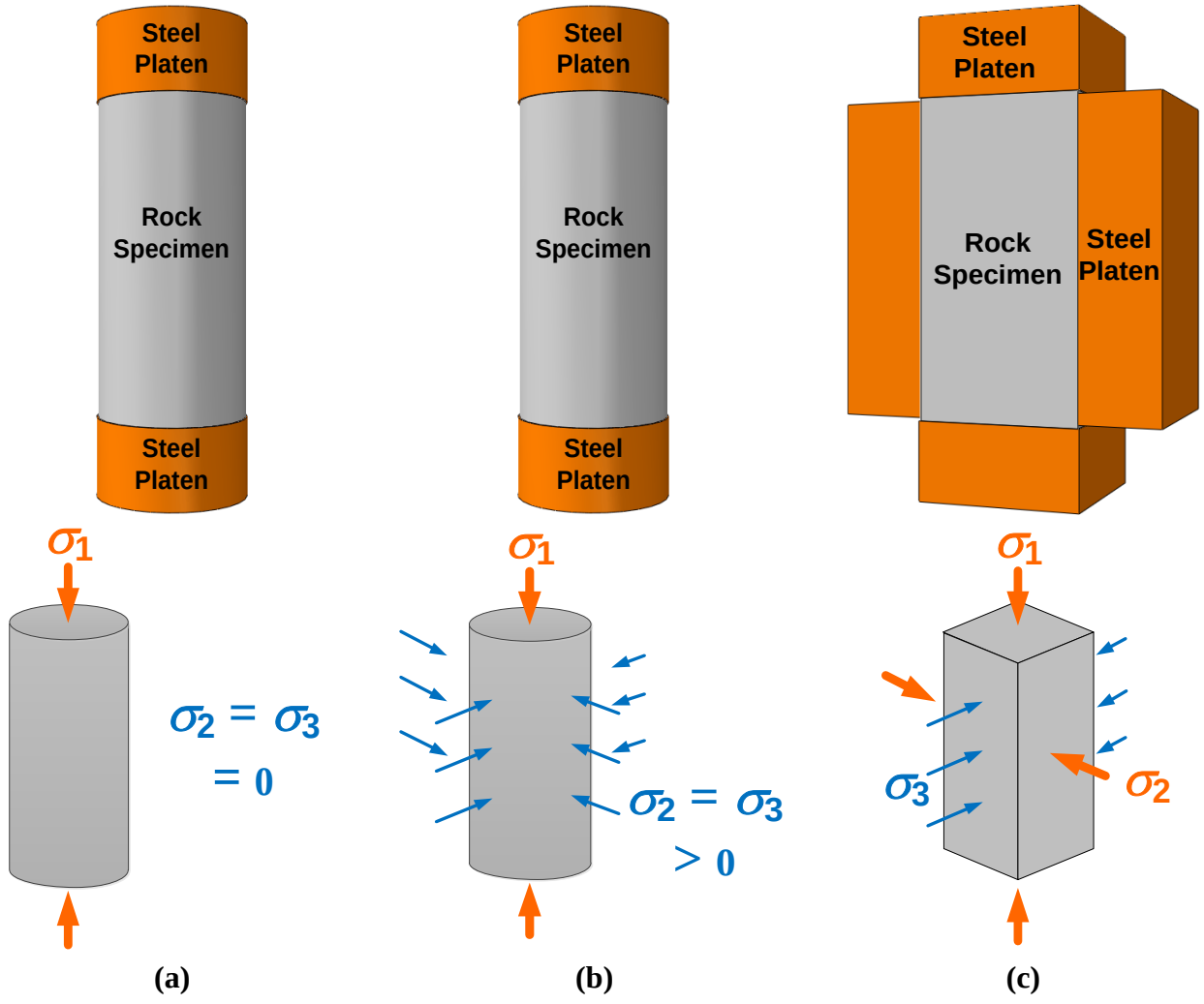

Figure 4-3 3D simulation models of three types of compression tests in numerical experiment: (a) uniaxial compression test, (b) conventional triaxial compression test, and (c) true triaxial compression test.

The diameter of the cylindrical and the width of the square prismatic specimens are 50 mm and the heights of the specimens are 100 mm. This gives an H/W (or H/D for cylindrical specimens) ratio of 2.0, which is the same as that used in the laboratory tests. The top and bottom steel platens are 51 mm in width (or diameter) and 25 mm in height (Figure 4-3a–c). To honor the laboratory test conditions, steel platen loading instead of hydraulic pressure loading is used to apply σ_2 in the true triaxial compression test simulations. Two lateral steel platens used for applying σ_2 are 50 mm in width, 98 mm in height, and 25 mm in thickness (Figure 4-3c). Mechanical properties of steel are assigned to the platens (Table 3-1).

The FEM models of a cylindrical specimen in both uniaxial and triaxial loading tests ($\sigma_2 = \sigma_3 \geq 0$) and a square prismatic specimen in true triaxial compression test are presented in Figure 4-4. The approximate size of the elements is 3 mm in its longest dimension; the maximum deviation factor for the curvature control of element size is 0.1. The shape of the elements is hexahedron; the elements are generated by the sweep technique using medial axis algorithm. The element type is 8-node linear brick; the integration algorithm for the chosen element type is reduced integration using hourglass control.

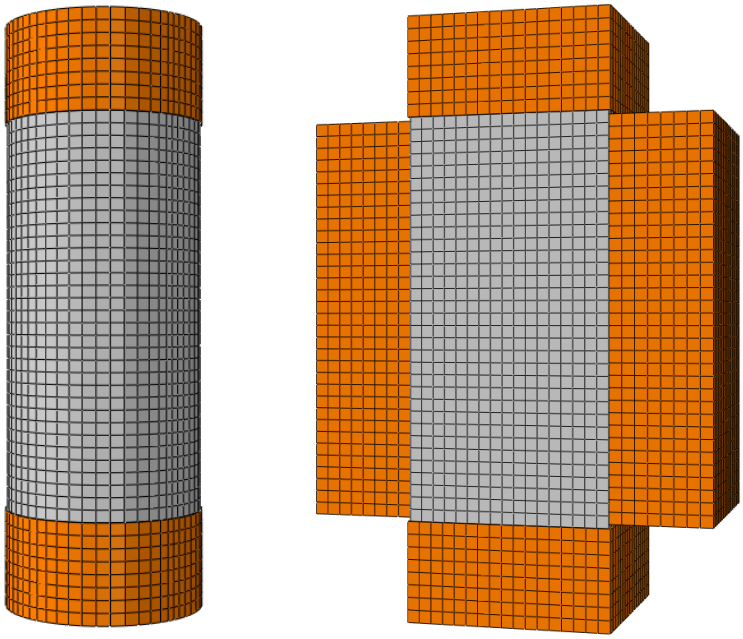

8844 elements in specimen 9537 elements in specimen

(a) **(b)**

Figure 4-4 FEM models of rock specimens and loading platens for different compression test simulations: (a) uniaxial and triaxial and (b) true triaxial compression tests.

The total numbers of hexagonal elements in the cylindrical and prismatic specimens are 8844 and 9537, respectively, which are relatively fine for the stress modeling. The slight difference in element numbers between the two specimens has little influence on their peak strengths, and this can later be verified by examining the modeling results of the peak strengths. Moreover, the FEM geometrical models for different rock types under different true triaxial stress states are all the same (Figure 4-4b).

4.2.5 Calibration of material parameters

Rock properties need to be calibrated first to carry out the numerical experiment. The rocks calibrated in this study are hard rocks with UCS over 100 MPa, and some are over 200 and 300 MPa (Section 4.2.2). The stress–strain curves of the hard rocks are relatively linear in the pre-peak deformation stage (Chang and Haimson, 2000; Haimson and Chang, 2000; Mogi, 2007),

especially before reaching the crack damage threshold at a stress level of approximately 0.7–0.8 times of the peak strength where hard rocks basically exhibit elastic behavior. Therefore, the pre-peak deformation behavior of the rocks in compression is simplified as linear elastic (refer to justifications in Section 3.1.2).

Young's modulus and Poisson's ratio are important elastic parameters to characterize the deformation behavior of rocks (Equation 2-1), and their values can be readily obtained from the laboratory test results provided in the origin works. Table 4-2 presents the physical and deformation parameters of the rocks considered in the study.

The M-C failure criterion is used to determine the rock strength (Section 4.2.3). The M-C strength parameters can be calibrated based on the relations between σ_1 and σ_3 obtained from conventional triaxial test results (refer to calculation process presented in Section 3.1.2). The M-C failure criterion is a linear failure criterion that depicts a linear relation between σ_1 and σ_3. However, the relation between σ_1 and σ_3 shown in conventional triaxial tests is nonlinear when the rocks are subjected to a large range of confining pressures (Section 4.2.3). Thus, if only one set of M-C strength parameters are used to characterize the rock behavior, a mismatch between the numerical and experimental results may occur, especially when the range of confining pressure being simulated is large (e.g., σ_3 of 0 to 150 MPa for KTB amphibolite). Therefore, to characterize the rock behaviors well under different applied σ_3 in the true triaxial compression tests, specimens under each applied σ_3 was assigned with different sets of M-C strength parameters, calibrated based on the conventional triaxial test results in a range of confining pressures which are close to the applied range of σ_3.

Table 4-2 Physical and deformation parameters of the rocks

Rock types	Density, ρ (kg/m^3)	Young's modulus, E (GPa)	Poisson's ratio, ν	References
KTB amphibolite	2920	65	0.29	Haimson and Chang (2002)
Westerly granite	2700	60	0.28	Bhat et al. (2011)
Solnhofen limestone	2500	80	0.20	Renner and Rummel (1996)
Yuubari shale	2200	40	0.20	Gercek (2007)

Table 4-3 to Table 4-6 present the M-C strength parameters of KTB amphibolite, Westerly granite, Solnhofen limestone, and Yuubari shale, respectively. The fitting equations based on the test data (σ_1, $\sigma_2 = \sigma_3$) at different applied σ_3 give the linear form of the M-C failure criterion in the σ_1–σ_3 space (refer to Table 3-4 in Section 3.1.2). Thus, the M-C strength parameters, the cohesion and the friction angle, at each applied σ_3 can be calibrated accordingly.

Table 4-3 Calculation of the M-C strength parameters of KTB amphibolite (data from Colmenares and Zoback, 2002, original data from Chang and Haimson, 2000)

Applied σ_3 (MPa)	Data (σ_1, $\sigma_2 = \sigma_3$) (MPa)	Fitting equation	Cohesion, c (MPa)	Friction angle, φ (°)
0	(158, 0) (176, 0) (410, 30)	$\sigma_1 = 8.4\sigma_3 + 176$	31	52
30	(158, 0) (410, 30) (702, 60)	$\sigma_1 = 9.1\sigma_3 + 151$	26	53
60	(410, 30) (702, 60) (868, 100)	$\sigma_1 = 6.4\sigma_3 + 318$	62	47
100	(410, 30) (702, 60) (868, 100) (1147, 150)	$\sigma_1 = 6.2\sigma_3 + 232$	48	46.5
150	(868, 100) (1147, 150)	$\sigma_1 = 5.6\sigma_3 + 310$	66	44

Table 4-4 Calculation of the M-C strength parameters of Westerly granite (data from Al-Ajmi and Zimmerman, 2005, digitized from Haimson and Chang, 2000)

Applied σ_3 (MPa)	Data (σ_1, $\sigma_2 = \sigma_3$) (MPa)	Fitting equation	Cohesion, c (MPa)	Friction angle, φ (°)
0	(201, 0) (231, 2)	$\sigma_1 = 15.0\sigma_3 + 201$	26	61
20	(201, 0) (430, 20) (605, 38)	$\sigma_1 = 10.7\sigma_3 + 206$	33	56
38	(430, 20) (605, 38) (747, 60)	$\sigma_1 = 7.9\sigma_3 + 306$	54	51
60	(605, 38) (747, 60) (889, 77)	$\sigma_1 = 7.3\sigma_3 + 325$	60	49
77	(747, 60) (889, 77) (1012, 100)	$\sigma_1 = 6.6\sigma_3 + 385$	76	47
100	(889, 77) (1012, 100)	$\sigma_1 = 5.4\sigma_3 + 477$	101	44

Table 4-5 Calculation of the M-C strength parameters of Solnhofen limestone (data from Mogi, 2007)

Applied σ_3 (MPa)	Data (σ_1, $\sigma_2 = \sigma_3$) (MPa)	Fitting equation	Cohesion, c (MPa)	Friction angle, φ (°)
20	(310, 0) (397, 20) (449, 40)	$\sigma_1 = 3.5\sigma_3 + 328$	88	34
40	(310, 0) (397, 20) (449, 40)	$\sigma_1 = 3.5\sigma_3 + 316$	84	34
60 *	(310, 0) (397, 20) (449, 40) (473, 60)	$\sigma_1 = 2.7\sigma_3 + 326$	98	28
80	(473, 60) (528, 80)	$\sigma_1 = 2.8\sigma_3 + 308$	93	28

* Conventional triaxial compression test data at $\sigma_3 = 60$ MPa diverges somewhat from the failure envelop; hence, calculation of the friction angle was adjusted accordingly.

Table 4-6 Calculation of the M-C strength parameters of Yuubari shale (data from Colmenares and Zoback, 2002, digitized from Takahashi and Koide, 1989)

Applied σ_3 (MPa)	Data (σ_1, $\sigma_2 = \sigma_3$) (MPa)	Fitting equation	Cohesion, c (MPa)	Friction angle, φ (°)
25	(161, 25) (228, 50)	$\sigma_1 = 2.7\sigma_3 + 94$	29	27
50	(161, 25) (228, 50)	$\sigma_1 = 2.7\sigma_3 + 94$	29	27

4.3 Simulation results

4.3.1 Deformation behavior

The deformation behavior of rocks obtained from numerical modeling fits the laboratory test data well, as long as the pre-peak deformation behavior of the rocks obtained in laboratory testing is relatively linear. For instance, Westerly granite is a fine-grained, uniform, nearly isotropic rock (Lockner, 1998b). As illustrated in Figure 4-5, the slope of the rock's pre-peak stress–strain curve is basically linear. Using the same Young's modulus and Poisson's ratio

obtained from the laboratory test (Table 4-2), the modeling results of both the deformation behavior and the peak strength agree well with the test results, indicating that the numerical model is suitable for rock behavior modeling in uniaxial or triaxial stress states.

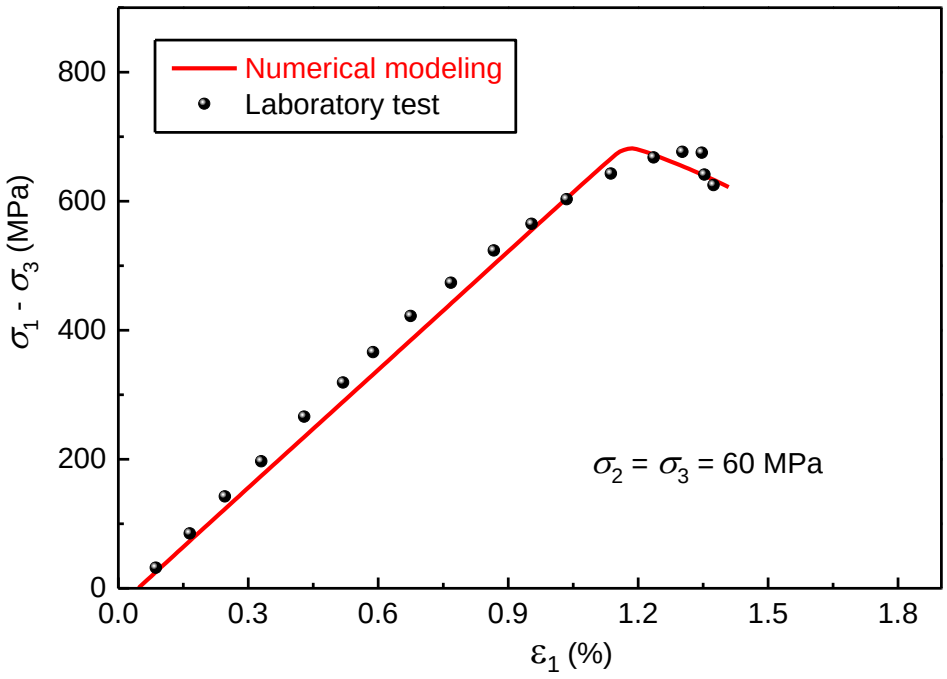

Figure 4-5 Deformation behavior of Westerly granite under confining pressure of σ_2 = σ_3 = 60 MPa obtained from numerical modeling together with laboratory test data.

4.3.2 Rock strength

Figure 4-6 to Figure 4-9 compare the modeling results with the laboratory test results for KTB amphibolite, Westerly granite, Solnhofen limestone, and Yuubari shale, respectively. As mentioned in Section 4.2.4, the exact μ values at the rock specimen-steel platen contacts that apply σ_2 are unknown in the laboratory tests and four values (μ = 0, 0.05, 0.1, 0.2) have been used in the numerical simulation. The μ values beside the rock name indicate the coefficient of friction at the specimen-platen contacts in the modeling, for both σ_1 and σ_2 loadings.

The dash curves in Figure 4-6 to Figure 4-9 are the modeling results of conventional triaxial compression tests. All modeling results agree with the laboratory test results well. Hence, the modeling strategy of using the linear M-C failure criterion to predict the rock strength under a given range of confining pressure is demonstrated. The applicability of the M-C failure criterion for predicting rock strength illustrated in this numerical experiment agrees with the conclusions drawn by other researchers (Pariseau, 2007; Labuz and Zang, 2012; Brady and Brown, 2013).

The solid curves in Figure 4-6 to Figure 4-9 are the modeling results of true triaxial compression tests. All modeling results show that under each applied σ_3, rock strength (σ_1) increases with the increase of σ_2 if the $\mu > 0$. There is a measurable increase of rock strength for $\mu = 0.05$, a noteworthy increase for $\mu = 0.1$, and a significant increase for $\mu = 0.2$. It seems that all the simulation results agree with the laboratory test results well for $\mu = 0.2$, suggesting that the simulation captured that the observed σ_2 effect decreases with the increase of applied σ_3.

If there is no end effect ($\mu = 0$), the modeling results show that the strength of specimens is independent of σ_2. This is because that the 2D M-C failure criterion was used and the increase of the strength of specimens is irrelevant of σ_2. Note that the small difference in the rock strengths given by the cylindrical ($\sigma_2 = \sigma_3$) and square prismatic ($\sigma_2 > \sigma_3$) models is caused by the geometrical model difference, which is negligible as long as their contact conditions are the same ($\mu = 0$). For $\mu > 0$, the strengthening of the specimen is exclusively attributed to the end effect caused by σ_2.

On the other hand, the mismatch between the modeling results and the test results indicates the strengthening of rock strength due to the real σ_2 effect. As will be discussed in Section 4.4, there

is a legitimate σ_2 effect on rock strength. However, due to the way that loads were applied in laboratory true triaxial compression tests, the test results inevitably contain the influence of the end effect and a method to isolate the end effect from the test results is proposed in Section 4.4.

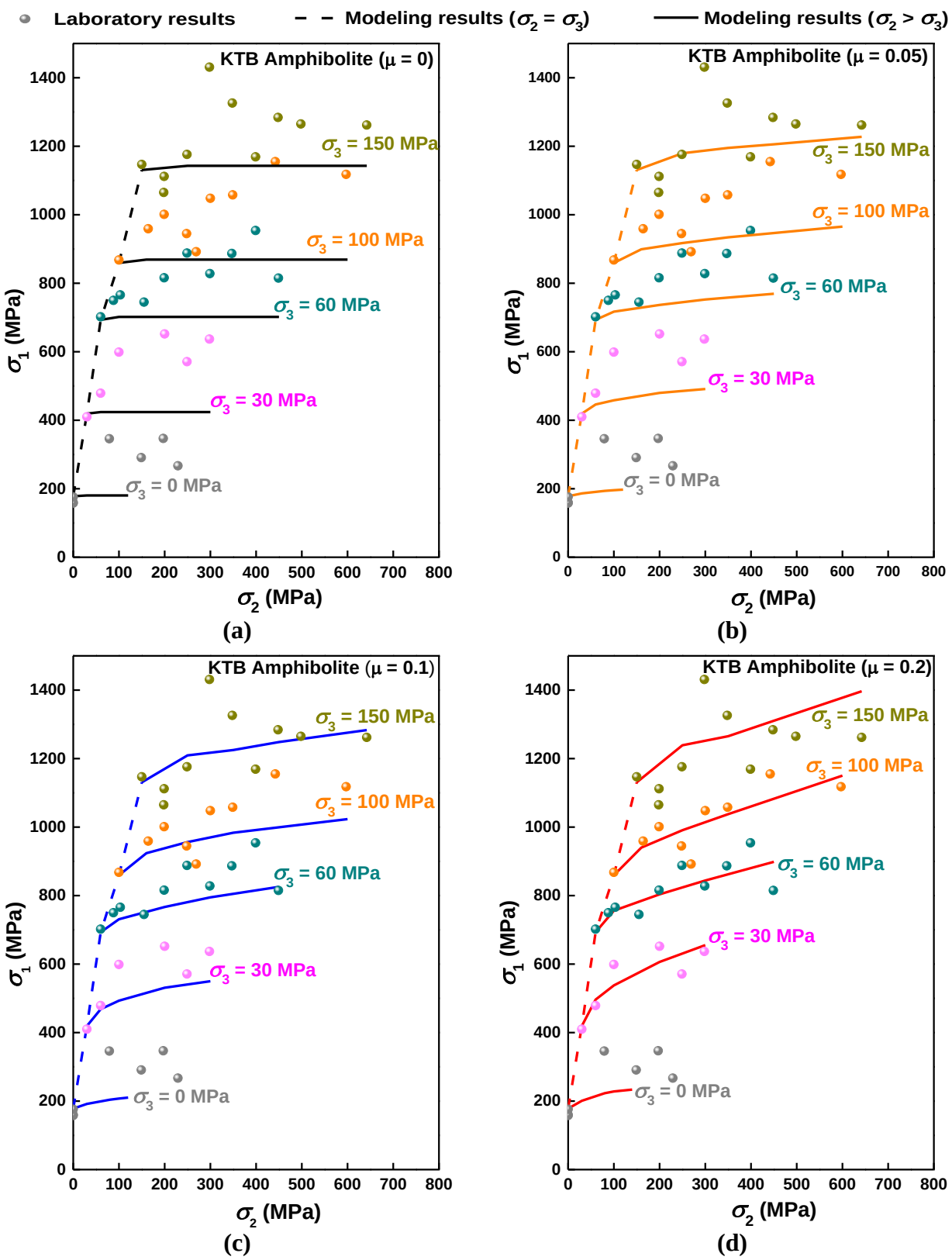

Figure 4-6 Simulation of true triaxial compression tests of KTB amphibolite: (a) $\mu = 0$, (b) $\mu = 0.05$, (c) $\mu = 0.1$, and (d) $\mu = 0.2$.

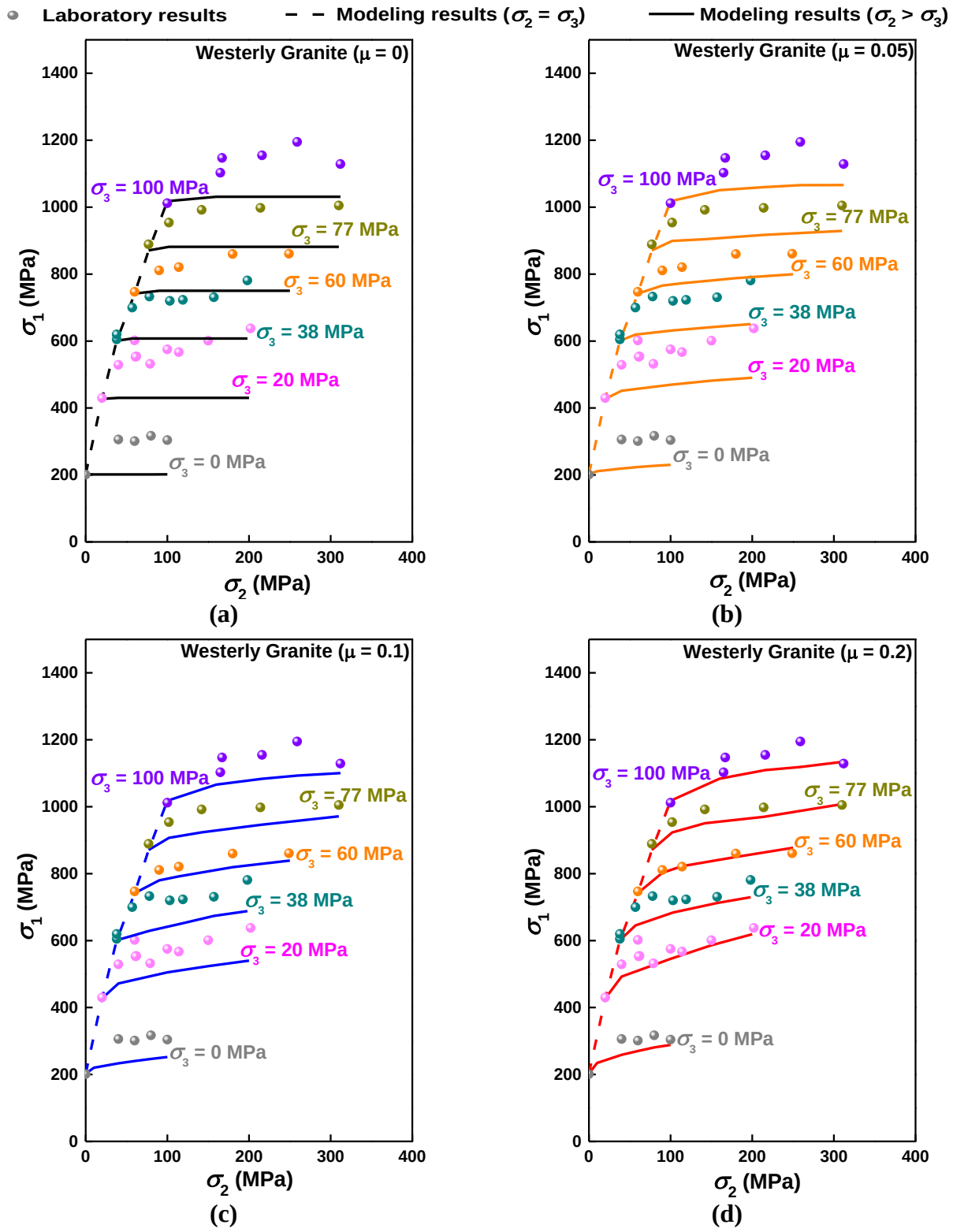

Figure 4-7 Simulation of true triaxial compression tests of Westerly granite: (a) $\mu = 0$, (b) $\mu = 0.05$, (c) $\mu = 0.1$, and (d) $\mu = 0.2$.

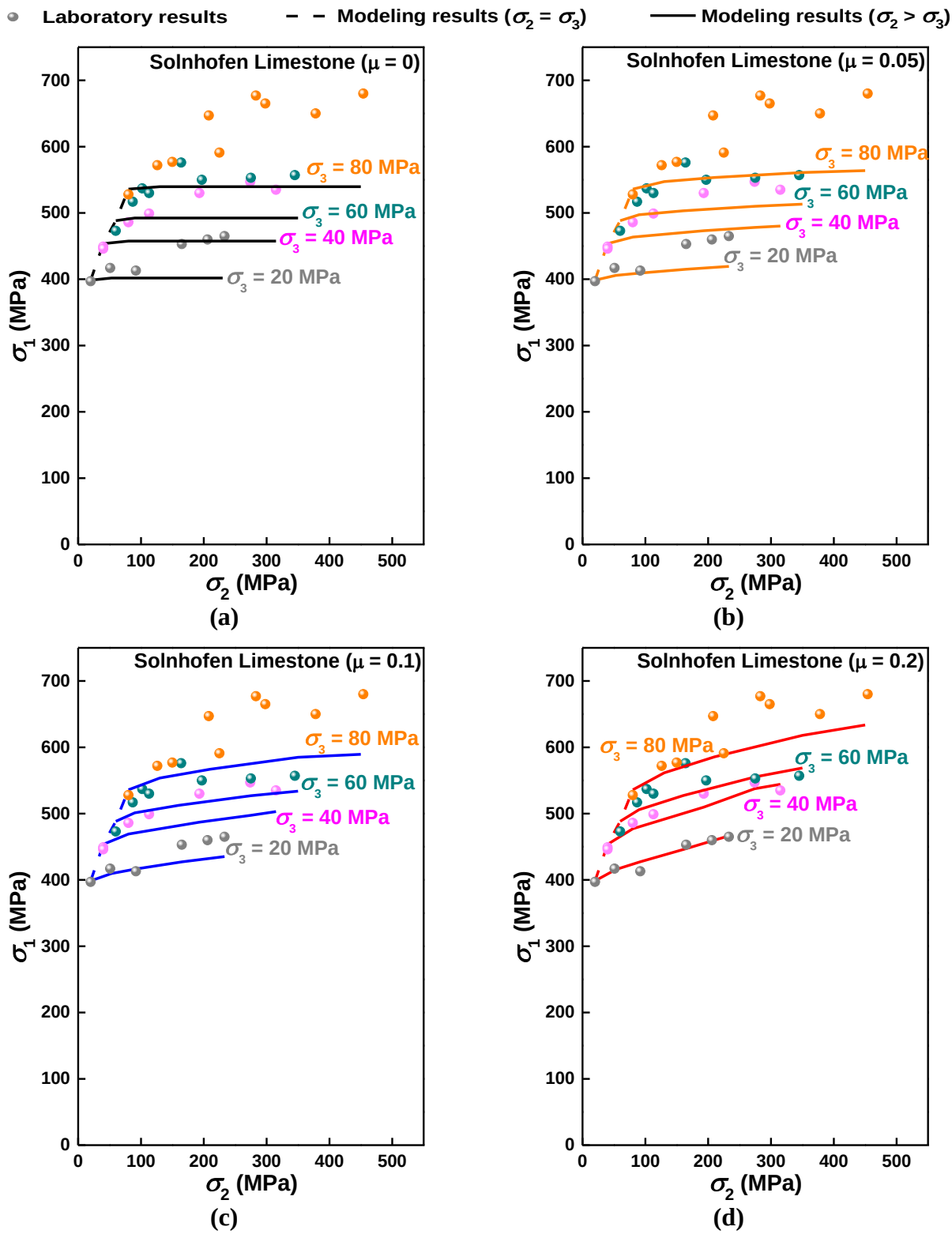

Figure 4-8 Simulation of true triaxial compression tests of Solnhofen limestone: (a) $\mu = 0$, (b) $\mu = 0.05$, (c) $\mu = 0.1$, and (d) $\mu = 0.2$.

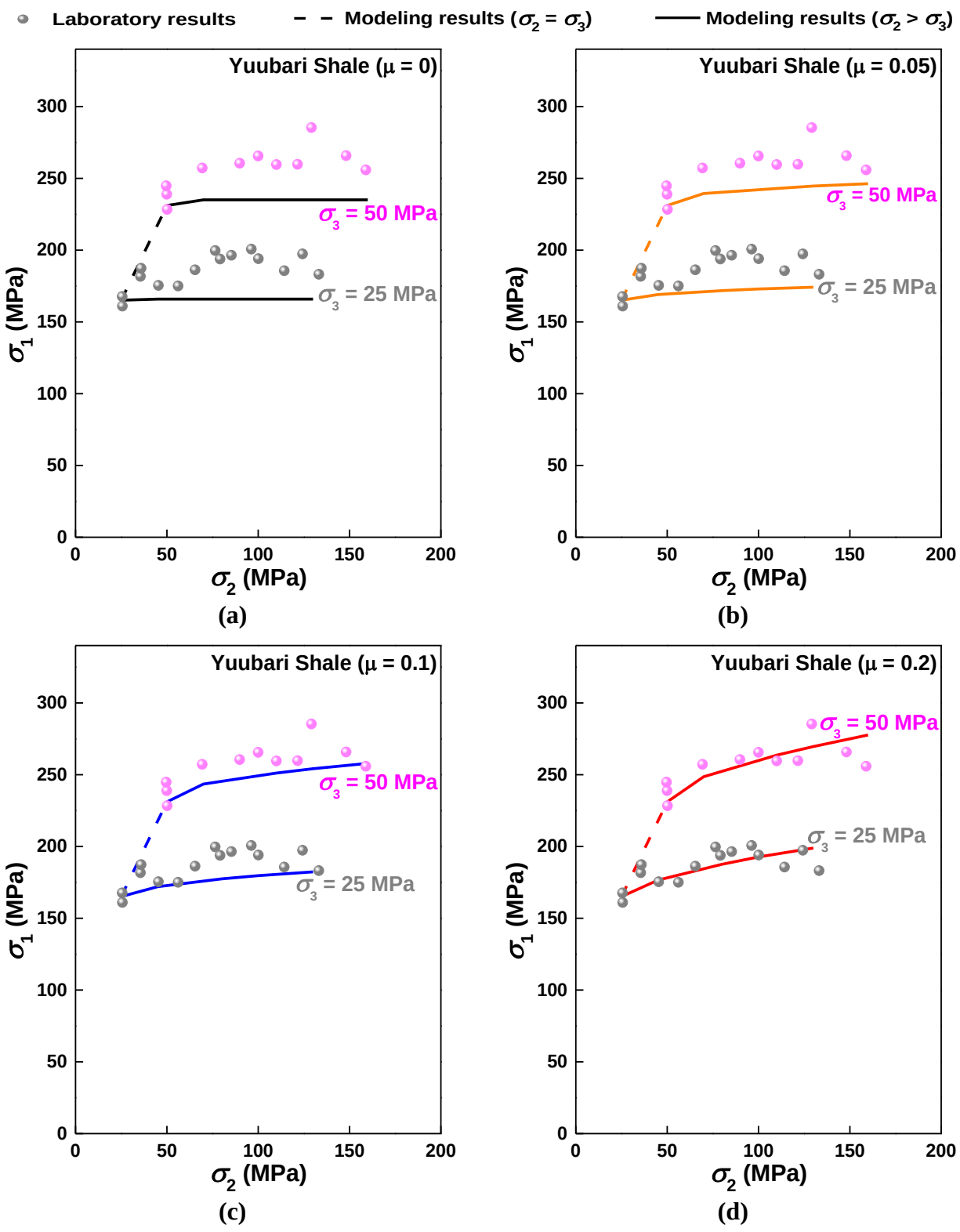

Figure 4-9 Simulation of true triaxial compression tests of Yuubari shale: (a) $\mu = 0$, (b) $\mu = 0.05$, (c) $\mu = 0.1$, and (d) $\mu = 0.2$.

4.3.3 Failure modes

Figure 4-10 to Figure 4-12 present typical failure modes by the numerical modeling and the laboratory tests of KTB amphibolite, Westerly granite, and Solnhofen limestone, respectively (failure modes of Yuubari shale were missing in the laboratory test results). The red zones in numerical 2D and 3D views represent the zones in which large plastic strains occur, which can be used to indicate strain localization. The viewing plane for all the three figures is the σ_1–σ_3 plane (15 °rotation of the σ_1 axis for the 3D view).

The simulation captures the characteristics of the failure modes in the true triaxial compression tests. With regard to the failure planes occurring on the σ_1–σ_3 plane and striking in the σ_2 loading direction, it is understood that σ_2 will constrain the failure planes in a way that the rock is easier to fail in a direction parallel to the σ_2 loading direction (Cai, 2008b). For the KTB amphibolite and the Westerly granite specimens, the numerical simulation results show conjugate fault planes but only one fault plane was observed in the laboratory test. This may be due to the reason that material heterogeneity was not considered in the numerical modeling. An approach had been adopted in the numerical work of Senent et al. (2013) by introducing a very small defect in the homogenous specimen to break the symmetry of the shear bands and a single fault plane was successfully captured.

Plastic strains	Numerical 3D view	Numerical 2D view	Laboratory test result
+4.0e-02 +2.0e-02 +0.0e+00 Plastic strain **(numerical parameters: σ_3 = 0 MPa, σ_2 = 30 MPa μ = 0.05)**	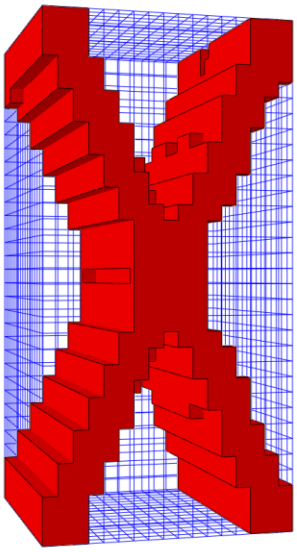	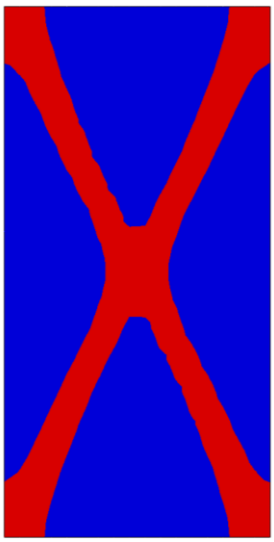	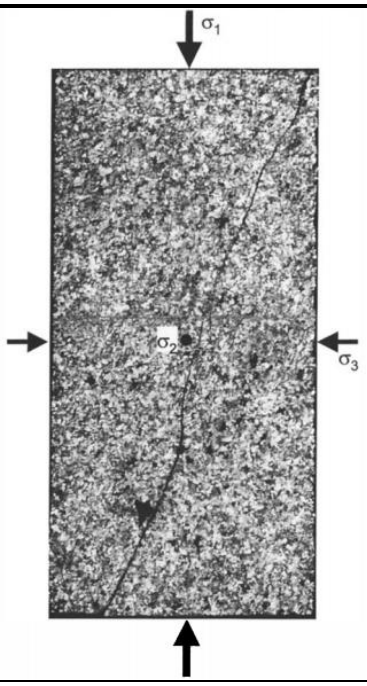

Figure 4-10 Numerical and laboratory (Chang and Haimson, 2000) results of typical failure modes of a KTB amphibolite specimen.

Plastic strains	Numerical 3D view	Numerical 2D view	Laboratory test result
+8.0e-02 +4.0e-02 +0.0e+00 Plastic strain **(numerical parameters: σ_3 = 100 MPa, σ_2 = 312 MPa μ = 0.2)**	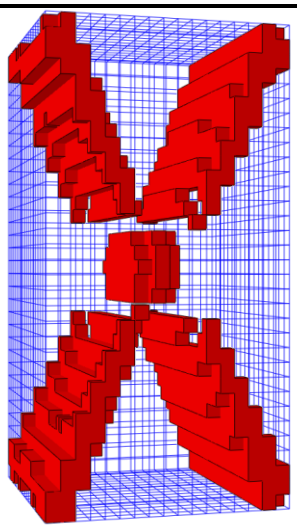	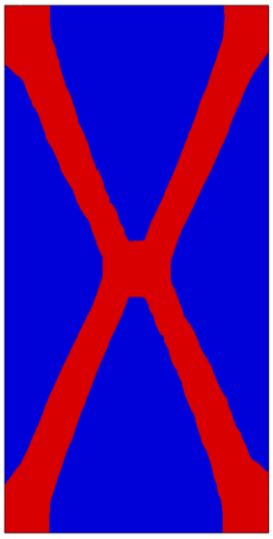	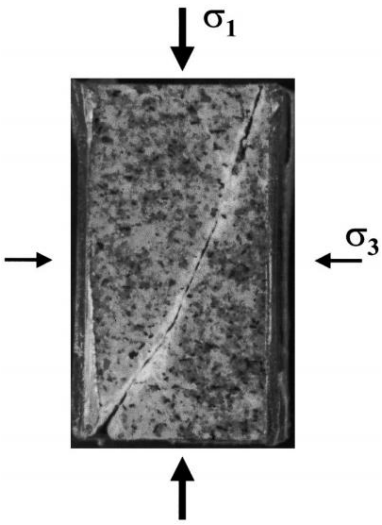

Figure 4-11 Numerical and laboratory (Haimson and Chang, 2000) results of typical failure modes of a Westerly granite specimen.

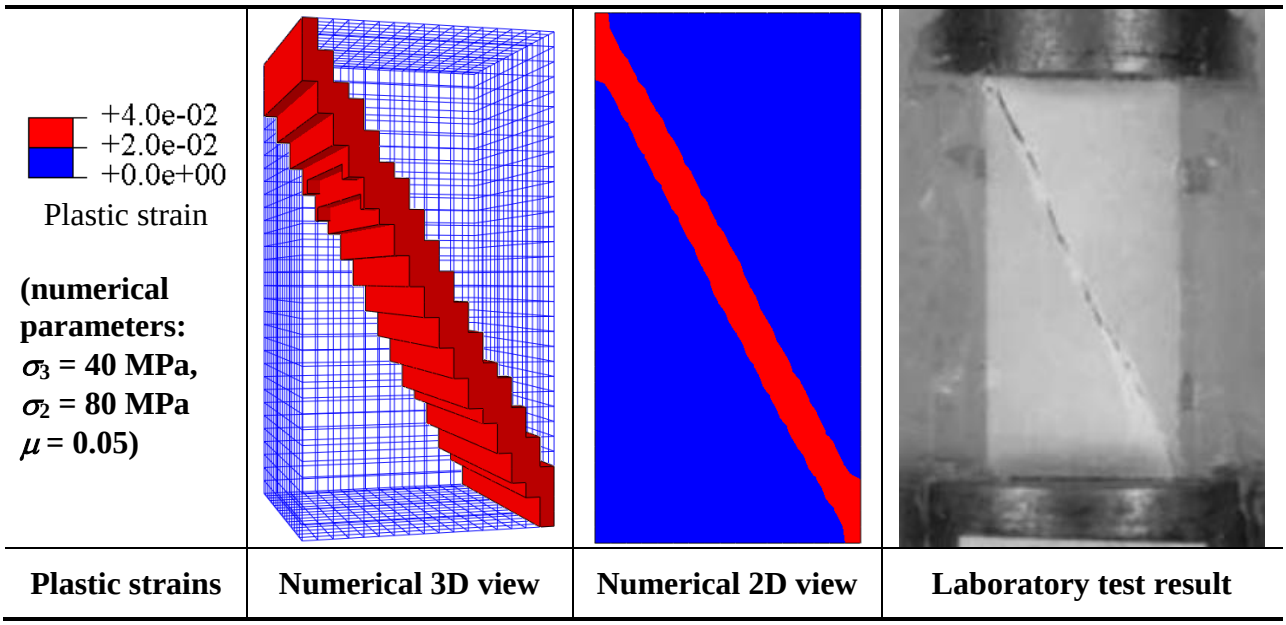

Figure 4-12 Numerical and laboratory (Mogi, 2007) results of typical failure modes of a Solnhofen limestone specimen.

4.4 Discussions

4.4.1 Relation between the σ_2 effect and the increase of actual σ_3

The increase of rock strength shown in the numerical modeling result is not directly related to the increase of σ_2, because the actual σ_2 effect is deliberately excluded from the assigned material model. It is seen that friction mobilized at the specimen-platen contacts increases σ_3 in the specimen and as a result the specimen's strength is increased.

Resultant displacements on planes cutting through the mid-height of the Westerly granite specimen in Figure 4-13 show different modes of lateral expansion under three loading conditions. In the conventional triaxial compression test (Figure 4-13a), the lateral expansions are relatively uniform and normal to the surface where the confining pressure is applied (σ_2 = σ_3 = 60 MPa). In the true triaxial compression test, the expansions in the direction where σ_2 is applied are smaller than that in the direction where σ_3 is applied. This is because that it is easier

for a specimen to expand in a direction in which it has less resistance. For the specimen under the same applied σ_3 (60 MPa), the lateral expansions in the direction where σ_3 is applied increase with the increase of σ_2, leading to a larger relative deformation and hence a greater end constraint at the contacts where σ_2 is applied (Figure 4-13b and c).

Figure 4-14 presents the contours of σ_3 on the side, top, and two vertical surfaces revealed from a quarter cut of the specimen at peak load. Specifically, red zones, which represent a range of σ_3 that is very close to the applied σ_3 (60 MPa), can be focused to evaluate the disturbance of the actual σ_3 distribution due to the end effect. For the specimen under conventional triaxial loading (Figure 4-14a), because hydraulic pressure loading and pressure control are employed to apply the confining pressure, σ_3 = 60 MPa is maintained around the lateral surface of the cylindrical specimen. Therefore, the red zone is uniformly distributed and consists of the largest percentage of the specimen volume.

In comparison, even though hydraulic pressure loading and pressure control are employed to apply σ_3 in true triaxial loadings, σ_3 = 60 MPa is maintained only on the contacts where σ_3 is applied. In fact, there are more non-uniform distributions of σ_3 observed on the contacts where σ_2 is applied and inside the specimen (Figure 4-14b and c). Moreover, the transition of the contour zones in the true triaxial loadings indicates that the actual σ_3 is increased with the increase of σ_2.

It is concluded that the end constraint is activated on the specimen-platen contacts where σ_2 is applied because of the relative deformations of the specimen and the platens. The end constraint acts on the contacts and inside specimen in a direction coinciding with the σ_3 direction, the

actual σ_3 is thus increased in the specimen, leading to an increase of the strength of specimens. End constraint acting on the specimen-platen contacts can be increased either the contact roughness (μ value) or the normal stress (σ_2) is increased (more details are discussed in Section 4.4.5). As a result, the strength of specimens is increased with the increase of σ_2, even though the specimen strength is prescribed as independent of σ_2.

In this numerical experiment of true triaxial compression test, the influence of end effect on the increase of rock strength is studied. It is found that as long as the end effect exists (i.e., the μ value is greater than 0), strengthening of rock strength due to the end effect exists as well. In the laboratory test results, this long ignored σ_2 effect due to the end effect was not excluded and it constituted part of the observed σ_2 effect.

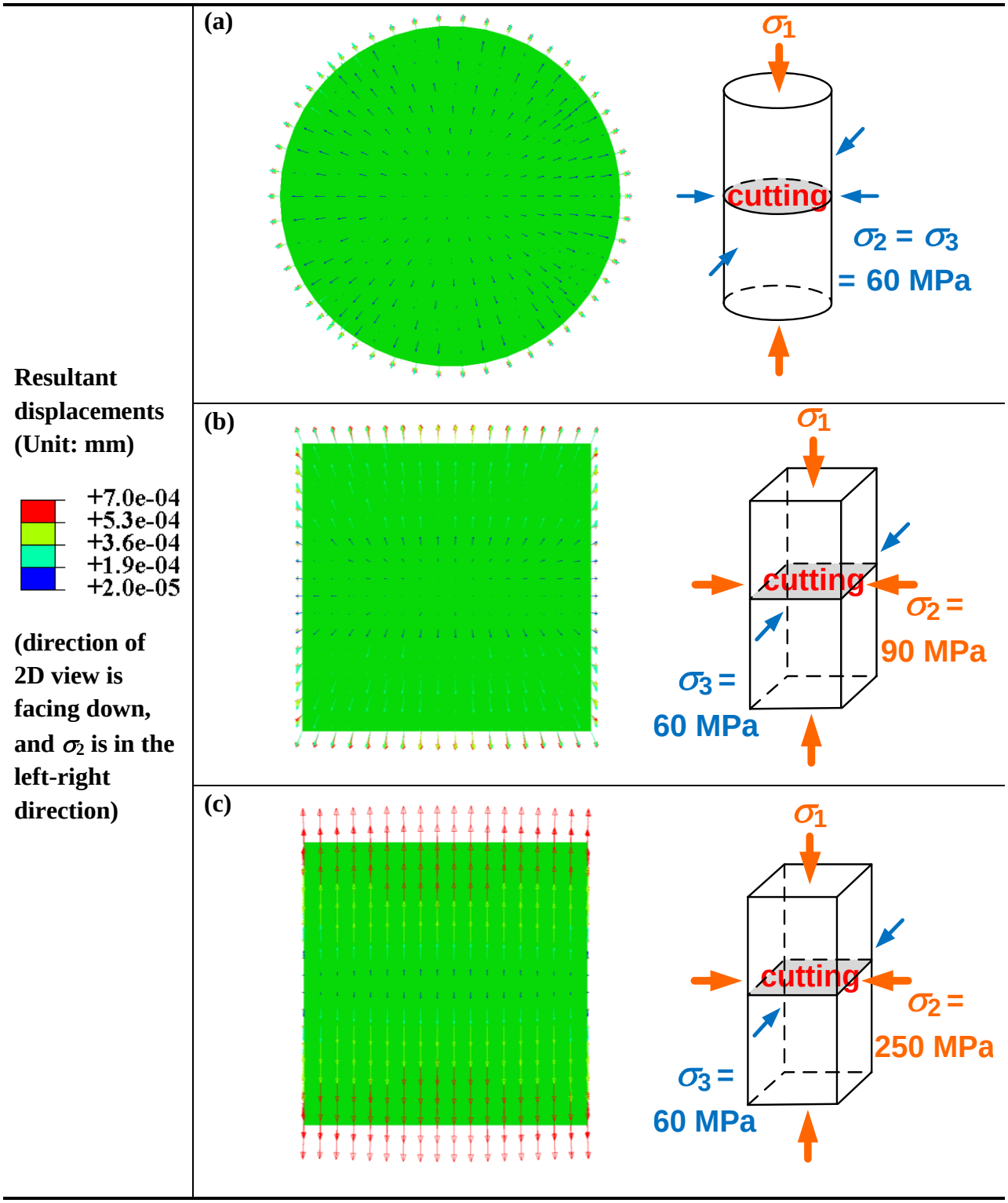

Figure 4-13 Resultant displacements at peak load on the plane cutting through the mid-height of the Westerly granite specimens under different loading conditions.

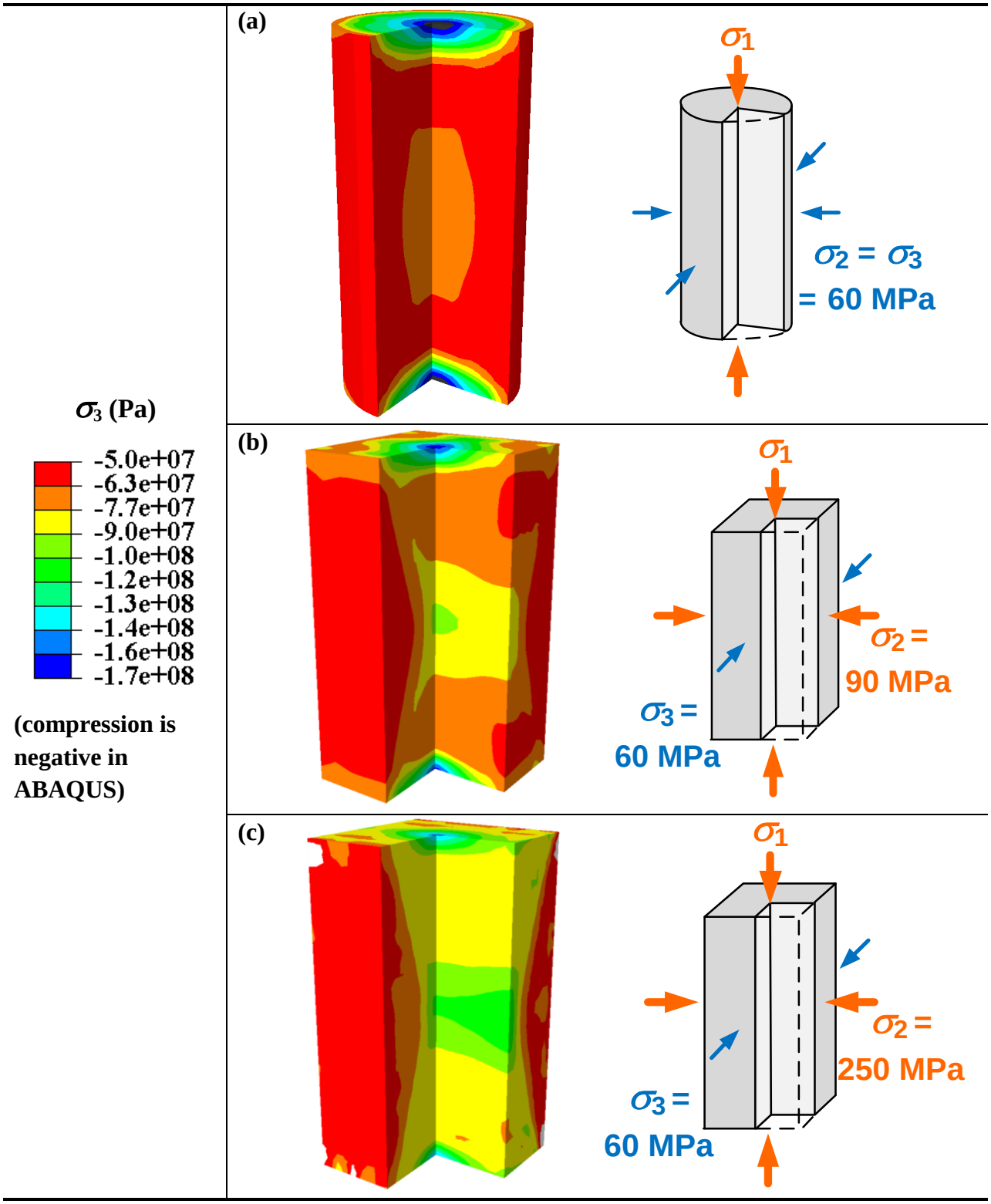

Figure 4-14 σ_3 contours in the Westerly granite specimens at peak load under different loading conditions.

4.4.2 Complementary evidences related to the end effect in true triaxial compression tests

Some rocks show a strength increase due to σ_2 while others do not; different end constraints initiated by different deformation behaviors of rocks could be the culprit. Using the same true triaxial compression test machine and testing method, Chang and Haimson (2005) found that the Long Valley Caldera rocks did not exhibit any meaningful σ_2 effect. After examining the deviatoric stress ($\sigma_1 - \sigma_3$)–volumetric strain ($\Delta V/V$) curves and the scanning electron microscope results, it is noticed that the strength independency on σ_2 of the Long Valley Caldera rocks is due to the non-dilatant deformation behavior of the rocks.

Figure 4-15 show the deviatoric stress–volumetric strain curves for KTB amphibolite and Long Valley Caldera metapelite in true triaxial compression tests (Chang and Haimson, 2000; Chang and Haimson, 2005). It is seen that even though these two metamorphic rocks were tested by the same true triaxial compression test machine, their deformation behaviors are different.

The deviatoric stress–volumetric strain curve of the amphibolite is nonlinear, indicating that dilation develops gradually when the deviatoric stress is above 700 MPa, while that of the metapelite is almost linear to the peak stress, indicating that there is an absence of dilation before peak load. The reversal point in the amphibolite's deviatoric stress–volumetric strain curve marks the onset of unstable crack growth (i.e., crack damage threshold; refer to discussion in Section 4.2.5). From this point, the plastic volumetric strain rate outnumbers the elastic volumetric strain rate, leading to a substantial growth of microcracks and dilation. Hence, for an amphibolite specimen that experiences dilatancy in compression, the plastic volumetric strain resulting from the dilation contributes to a large lateral expansion of the specimen before the

peak load is reached. This large lateral deformation of the rock led to high constraint from the loading platens and thus the strength increase due to σ_2 was large.

Enlightened by the modeling results—the lateral expansion in the mid-height of specimens shown in Figure 4-13 and the disturbance of actual σ_3 distribution in specimens in Figure 4-14—it becomes clear that if there is little lateral expansion (e.g., those two Long Valley Caldera rocks), there would be very small relative deformation at the rock specimen-steel platen contacts and the end effect is thus small.

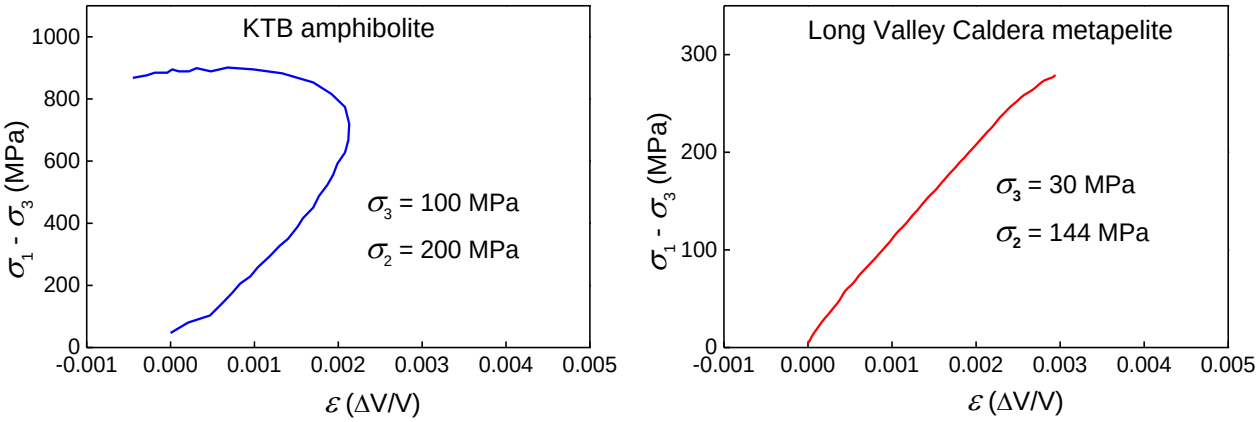

Figure 4-15 Deviatoric stress–volumetric strain curves for: (a) KTB amphibolite and (b) Long Valley Caldera metapelite in true triaxial compression tests (digitized and modified from Chang and Haimson, 2000 and Chang and Haimson, 2005, respectively).

Some true triaxial compression test results are calibrated numerically and the modeling results suggest that the end effect due to σ_2 can result in a strength increase even if the rock strength used in the numerical modeling is independent of σ_2. Shi et al. (2012) used FLAC3D to simulate the loading boundary effects in true triaxial compression test and revealed that the end effect can result in an apparent σ_2 effect. Gerstle et al. (1978) carried out true triaxial compression tests on concrete specimens made from the same material composition and concluded that the σ_2 effect

varied considerably due to the different loading methods and anti-friction measures. Therefore, the point highlighted in this study, i.e., the end effect can result in a different interpretation of the σ_2 effect on rock strength, is supported by the experimental results of Gerstle et al. (1978).

4.4.3 Contribution of end effect to observed σ_2 effect

It is numerically proven that when testing a rock-like material whose strength is independent of σ_2, there is an apparent σ_2 effect caused exclusively by the end effect. The next step is to confirm that the apparent σ_2 effect constitutes part of the observed σ_2 effect in laboratory test results. Although the actual μ values in previous true triaxial compression tests are unknown, the μ values can never be 0 and a range of 0.05 to 0.1 seems to be appropriate for lubricated rock specimen-steel platen contacts (Section 4.2.4). Accordingly, laboratory test results that show a significant σ_2 effect might contain an apparent σ_2 effect resulted from the end effect in a way similar to that revealed in the modeling results.

It is worth noting that, as justified in Section 4.2.3, although a σ_3-only-dependent material property might not be precise enough to characterize the actual rock strength property, it is sufficient to emphasize the contribution of the end effect to the observed σ_2 effect. The increase of rock strength due to the end effect in true triaxial compression test simulations based on a both-σ_3-and-σ_2-dependent material model should not be less than that based on a σ_3-only-dependent material model.

In order to further verify the influence of the end effect on true triaxial compression test results, the modeling results of the apparent σ_2 effect needs to be added to the actual σ_2 effect and compared with the observed σ_2 effect in laboratory test results. Approaches that can consider the actual σ_2 effect while excluding the end effect include theoretical approach (Wiebols and Cook,

1968) and numerical investigation using DEM (Fjær and Ruistuen, 2002; Cai, 2008a; Schöpfer et al., 2013). DEM modeling employs micromechanical properties to capture the failure process of rock and thereby avoids the discretion of selecting an empirical failure criterion that only reflects the macro-mechanical behavior of rock. However, the micromechanical parameters used in DEM modeling are hypothetical and cannot be measured in laboratory tests. These parameters can only be obtained by trials-and-errors in the calibration process while they are changed systematically until a set of parameters yield a macroscopic behavior that best fit the actual one (Potyondy and Cundall, 2004).

In this study, the theoretically-based effective strain energy criterion developed by Wiebols and Cook (1968) instead of the DEM modeling approach is chosen to characterize the actual σ_2 effect. The effective strain energy criterion (Wiebols and Cook, 1968) was derived based on a hypothesis that the effective shear strain energy stores around Griffith cracks due to the sliding of crack surfaces, and rock failure occurs when the total effective shear strain energy, which depends on the coefficient of sliding friction (μ_s) of the crack surfaces, reaches a critical value. It predicts a strengthening of rock from increasing σ_2 followed by a strength plateau and a weakening of rock once σ_2 exceeds a certain magnitude, which was verified experimentally by Wiebols and Cook (1968) and later confirmed by other researchers (Mogi, 1971; Chang and Haimson, 2000). Because the σ_2 effect predicted by the effective strain energy criterion excludes the end effect, it can be considered as a "true" or the "actual" σ_2 effect.

All failure criteria have their limitations in representing the true physics of rock deformation under complex loading conditions, and the effective strain energy criterion has with no exception. Laboratory test results show that the failure envelopes of rocks in conventional triaxial

compression tests are normally nonlinear, especially near the brittle-ductile transition zones (Mogi, 1974), but the failure envelopes of conventional triaxial compression tests predicted by the effective strain energy criterion are linear. A precise prediction of a rock's failure envelope in the conventional triaxial stress state is the benchmark to ensure the accuracy of the predicted σ_1–σ_2 curve in the true triaxial stress state, because the conventional triaxial stress state is the origin of the σ_1–σ_2 curve.

Acknowledging the shortcoming of the effective strain energy criterion, only the failure envelopes in the low confining pressure range will be considered. In addition, it is preferable to choose rocks whose σ_1–σ_3 relations in conventional triaxial compression tests are relatively linear. Another shortcoming of the effective strain energy criterion is that the μ_s value is difficult to be determined. Wiebols and Cook (1968) provided failure envelopes for five μ_s values (0.25, 0.5, 0.667, 0.85, and 1) and pointed out that there is a relation between μ_s and $\tan\varphi$ (where μ_s and $\tan\varphi$ are close to each other but $\mu_s < \tan\varphi$). Accordingly, the μ_s value is chosen based on the $\tan\varphi$ value of a rock.

The failure envelopes of KTB amphibolite with applied σ_3 ranging from 0 to 60 MPa are used for validation. The calibrated φ values of KTB amphibolite in this applied σ_3 range (Table 4-3) are relatively constant compared with other rocks (Table 4-4 and Table 4-5), denoting relatively linear σ_1–σ_3 relations. Furthermore, the calibrated $\tan\varphi$ in this σ_3 range is slightly higher than μ_s = 1. Therefore, the theoretical σ_2 effect predicted by the effective strain energy criterion for KTB amphibolite in the true triaxial compression tests can be obtained by assuming μ_s = 1. Then, the influence of end effect on the observed σ_2 effect can be analyzed by adding the modeling results,

which quantifies the end effect in the true triaxial compression tests, to the theoretical results which reflect the actual σ_2 effect only.

The combination of the numerical end effect and the theoretical σ_2 effect on rock strength is shown in Figure 4-16 and compared with the experimental test results, where σ_1, σ_2, and σ_3 are normalized to the UCS of KTB amphibolite (σ_c). The lower bound (dash curves) corresponds to the theoretical result of Wiebols and Cook (1968), which includes only the influence of σ_2 on rock strength for μ_s = 1. The upper bound (solid curves) corresponds to the results of strength increase due to both the actual σ_2 effect for μ_s = 1 (according to Wiebols and Cook, 1968) and the end effect for μ = 0.1 (obtained from the modeling results in Figure 4-6c). Thus, the yellow highlighted zones between the upper bound and lower bound of the σ_1–σ_2 curves represent the apparent σ_2 effect due to the end effect for a μ value ranging from 0 to 0.1.

Although there was strength variability in the test results of KTB amphibolite, most test data fell within the yellow highlighted zones, indicating that the end effect caused by σ_2 loading somehow constituted part of the observed σ_2 effect. Because a laboratory test result inevitably contains an apparent σ_2 effect if the friction at the rock specimen-steel platen contacts is not zero, 3D empirical failure criteria developed from such a true triaxial compression test result may overestimate the rock strength. Although the actual μ values in the previous laboratory tests were unknown, this study shows that the end effect exists in true triaxial compression test for $\mu > 0$ and the μ values in those tests could range from 0.05 to 0.1. Therefore, it is suggested that when using previous and future true triaxial compression test results, the influence of the end effect on the test results needs to be investigated.

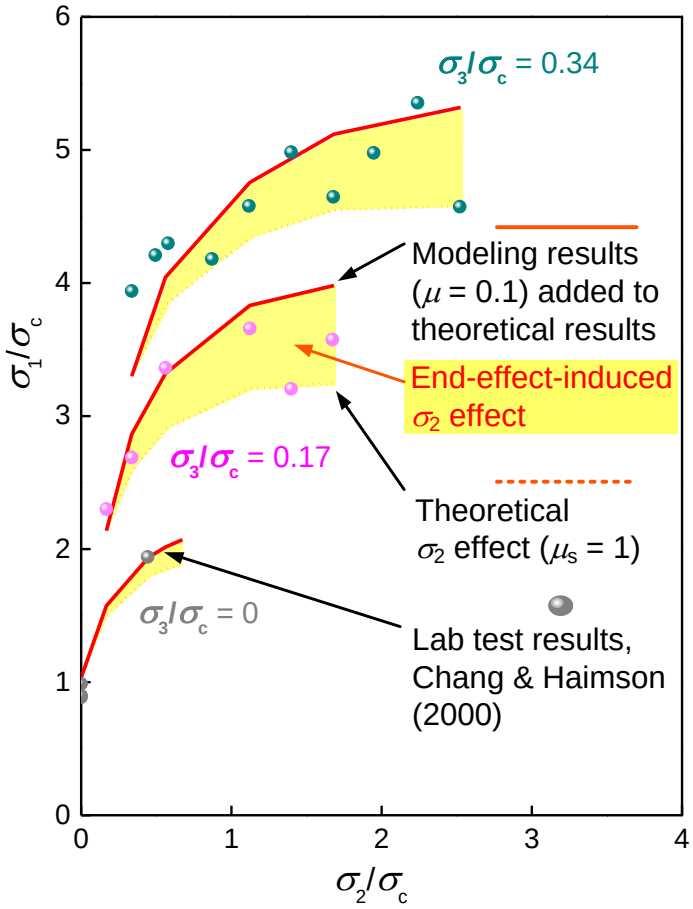

Figure 4-16 Combination of numerical end effect and theoretical σ_2 effect on rock strength, compared with the experimental data of KTB amphibolite.

As illustrated in this study, with the knowledge of the actual μ value at the rock specimen-steel platen contacts, the apparent σ_2 effect may be separated from the observed σ_2 effect. In this way, the true σ_2 effect could be characterized for the development of 3D empirical failure criteria in the future. This proposed approach is verified in Section 4.4.5.

4.4.4 Recent laboratory work to minimize the end effect and to characterize actual σ_2 effect

It was proposed in Section 4.4.3 that with knowledge of the apparent σ_2 effect resulted by end constraint, it is possible to correct previous true triaxial compression test data for the development of 3D empirical failure criteria for rocks. However, this approach should be applied individually to each laboratory test because the μ values at the rock specimen-steel platen contacts were not the same in the tests.

An alternative approach is to decrease the friction at the rock specimen-steel platen contacts to a level where the contribution of the end effect to the observed σ_2 effect is very small such that the obtained test data can be used directly to develop 3D empirical failure criteria. To achieve this goal, the end effect should be greatly reduced. Based on the modeling results, it is concluded that the strengthening of rock due to the end effect for a μ value ranging from 0.05 to 0.1 cannot be neglected. Hence, the μ value at the rock specimen-steel platen contacts must be reduced to a value much less than 0.05. In addition, the characteristics of the obtained test results should be somehow in accordance with that predicted by theoretical results (e.g., Wiebols and Cook, 1968).

A series of laboratory tests were carried out at Northeastern University (China) to study how friction at the rock specimen-steel platen contacts can be reduced (Xu and Cai, 2016b). Test specimens were prepared using Linghai granite specimens collected from a quarry site in Liaoning Province, China. Linghai granite is a homogeneous and isotropic hard rock with high strength. Using a polishing machine with a very high machining accuracy, the specimen ends were ground flat and polished down to $\pm$ 0.01 mm. To prevent the anti-friction material from flowing into rock specimen, a copper sheet of 0.02 mm thickness was set on the surface of the specimen. Then, friction tests with increasing normal forces were conducted to study the

effectiveness of two anti-friction measures, one by using Teflon and the other by using a mixture of stearic acid and Vaseline at a 1:1 ratio, recommended by Labuz and Bridell (1993).

The black line in Figure 4-17 shows the μ values of the specimens' polished surfaces without lubricant. Because the specimens' end and the platen's end surfaces had been polished smoothly, the obtained average μ value of 0.15 is low, which is even lower than that of some contacts smeared with lubricants (Section 4.2.4). The results shown in Figure 4-17 clearly indicate that the mixture of stearic acid and Vaseline at a 1:1 ratio in combination with a thin copper sheet can reduce the μ value of the lubricated rock specimen-steel platen contact to about 0.02. Referring to the numerical simulation results in Section 4.3, it can be deduced that the end effect caused by $\mu = 0.02$ is small and can be neglected.

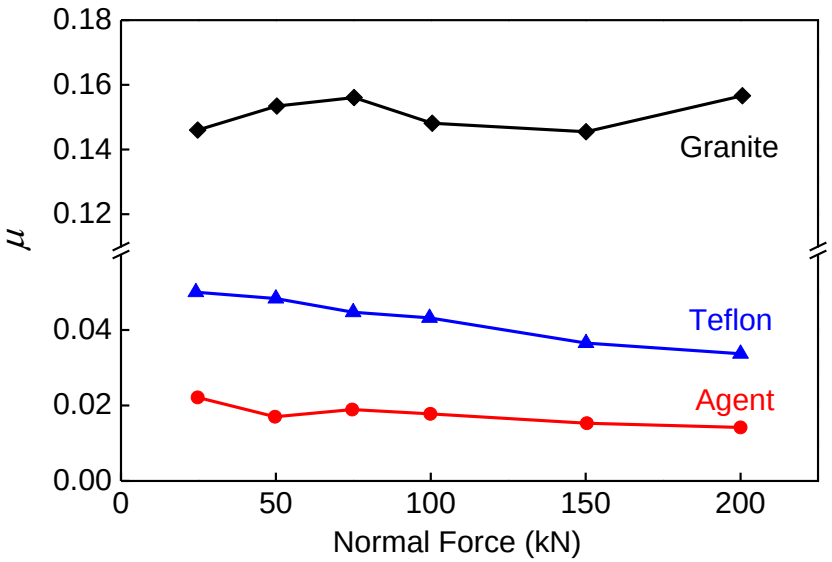

Figure 4-17 μ values of rock specimen-steel platen contacts measured by shear tests with different normal forces.

True triaxial compression tests were conducted using a newly developed true triaxial compression test machine (Feng et al., 2016). This novel test machine was designed and

fabricated on the basis of the Mogi-type test machine with many improvements implemented to address key issues such as off-center suppression, loading gap removal, and more importantly, end effect reduction (Feng et al., 2016). Linghai granite specimens, with a square prism of 50 × 50 × 100 mm^3, were used in the test. The effect of σ_2 on rock strength at low σ_3 (up to 50 MPa) was focused in this laboratory test. The mixture of stearic acid and Vaseline at a 1:1 ratio and thin copper sheets were used to reduce friction at the contacts. Additionally, compared with some previous triaxial compression tests that barely reached the strength plateau in the σ_1–σ_2 curves, the full range of σ_2 loading ($\sigma_1 \geq \sigma_2 \geq \sigma_3$) was attempted to obtain the complete σ_2 effect curves. The laboratory test results are shown in Figure 4-18.

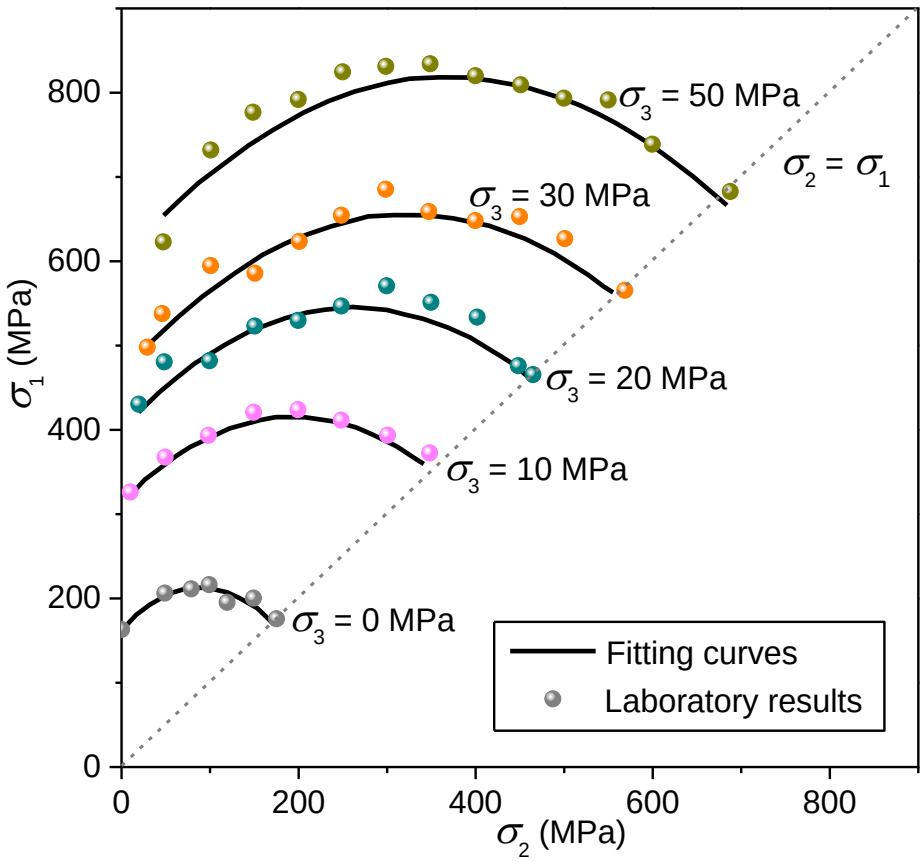

Figure 4-18 Laboratory true triaxial compression test results showing the σ_2 effect on the strength of Linghai granite.

The overall characteristics of the observed σ_2 effect on the strength of Linghai granite agree with that of previous laboratory test results, showing an increase of rock strength with the increase of σ_2 before reaching the strength plateau and then a decrease of rock strength as σ_2 further increases. The complete strength drop from the strength plateau to the maximum loading range of σ_2 ($\sigma_2 = \sigma_1$), a characteristic predicted by Wiebols and Cook (1968) but normally missed in some previous laboratory test results, was captured in this test results. Additionally, a characteristic of the observed σ_2 effect in Linghai granite that differs from previous laboratory test results is noticed. The σ_2 effect on rock strength as observed in previous test results is normally the greatest at low σ_3 and drastically decreased with the increase of σ_3 (Table 4-1); however, in the Linghai granite test results the rates of rock strength increase at the peak due to σ_2 are similar at different σ_3 (Table 4-7), which are about 51% to 56% in all cases.

Table 4-7 Quantified σ_2 effect on Linghai granite

σ_3/σ_c	0.00	0.06	0.12	0.18	0.31
$(\sigma_1^* - \sigma_1)/(\sigma_2^* - \sigma_2)$	56%	52%	52%	53%	51%

It is numerically proven in Sections 4.3.2 and 4.4.3 that the apparent σ_2 effect resulted by the end constraint can lead to an overestimation of the actual σ_2 effect. On the other hand, the theoretical results (Wiebols and Cook, 1968) that exclude the end effect show a very small decrease of the peak strength increase due to σ_2 with the increase of σ_3 (Table 4-8, with different μ_s). Therefore, these indirect evidences, supported by numerical and theoretical results, suggest that the anti-friction measure adopted in the laboratory test of Linghai granite is effective. In other words, the σ_2 effect shown in the test results is dominantly the actual σ_2 effect. The apparent σ_2 effect due to the end effect is small in the laboratory test results.

Next, the phenomenon of the drastic decrease of σ_2 effect with the increase of σ_3 in the test results found in literature is re-examined. It was experimentally confirmed by Mogi (2007) that rock strength increase due to the end effect increases with the decrease of confining pressure (Figure 2-8). As explained in Section 4.4.1, the apparent σ_2 effect (i.e., rock strength increase $\Delta\sigma_1$) due to the end effect is essentially resulted from an increase of actual σ_3 (i.e., $\Delta\sigma_3$ increase), and this apparent σ_2 effect decreases with the increase of applied σ_3 (Figure 4-6 to Figure 4-9). Hence, it can be interpreted that in the previous laboratory test results, the end-effect-induced rock strength increase was high when the applied σ_3 was low, which resulted in a greater apparent σ_2 effect. The end effect became smaller at high applied σ_3.

Table 4-8 Quantified σ_2 effect predicted by the theory of Wiebols and Cook (1968) for different μ_s

μ_s = 0.25	σ_3/σ_c	0.00	0.20	0.40	0.60	0.80
	$(\sigma_1^* - \sigma_1)/(\sigma_2^* - \sigma_2)$	44%	43%	43%	43%	43%
μ_s = 0.50	σ_3/σ_c	0.00	0.10	0.20	0.30	0.40
	$(\sigma_1^* - \sigma_1)/(\sigma_2^* - \sigma_2)$	67%	66%	65%	64%	64%
μ_s = 0.67	σ_3/σ_c	0.00	0.05	0.10	0.15	0.20
	$(\sigma_1^* - \sigma_1)/(\sigma_2^* - \sigma_2)$	79%	78%	77%	75%	74%
μ_s = 0.80	σ_3/σ_c	0.00	0.05	0.10	0.15	0.20
	$(\sigma_1^* - \sigma_1)/(\sigma_2^* - \sigma_2)$	87%	83%	80%	79%	78%
μ_s = 1.00	σ_3/σ_c	0.00	0.05	0.10	0.15	0.20
	$(\sigma_1^* - \sigma_1)/(\sigma_2^* - \sigma_2)$	101%	88%	83%	81%	79%

Figure 4-19 presents some conventional triaxial compression test results of rocks and their H-B fitting curves. Nonlinearity of the failure envelopes is observed ubiquitously in these rocks, illustrating that the same $\Delta\sigma_3$ at a low σ_3 will result in a greater increase of rock strength $\Delta\sigma_1$

than that at a high σ_3. Therefore, the end effect can result in a large apparent σ_2 effect when σ_3 is low and the observed σ_2 effect at low confining pressures in some previous test results might be exaggerated. It is suggested that if true triaxial compression test results contain an unknown influence of end effect on rock strength, the test results at high σ_3, which are less influenced by the end effect, might be more appropriate for developing 3D empirical failure criteria for rocks.

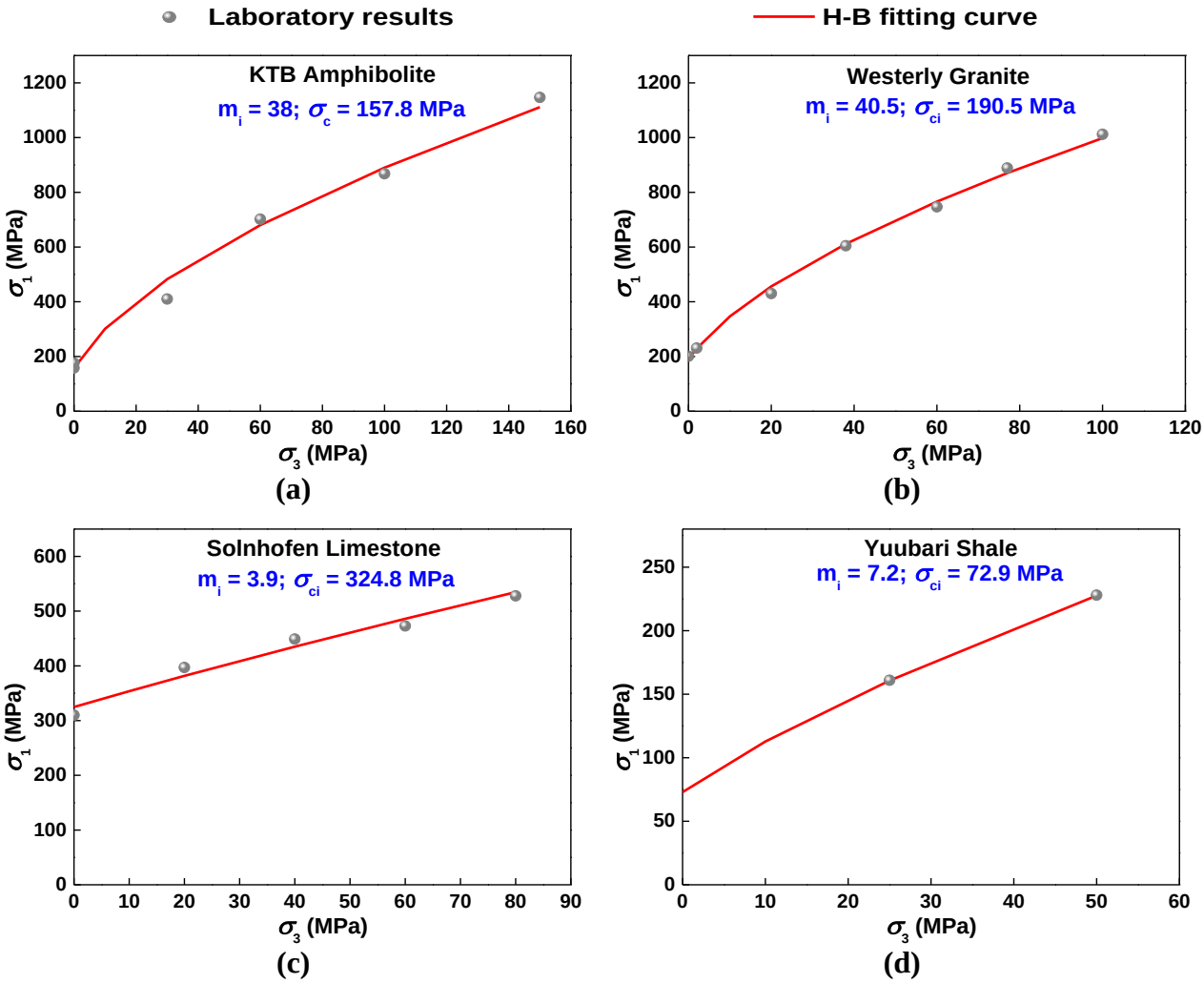

Figure 4-19 Conventional triaxial compression test results of some rocks and their H-B fitting curves: (a) KTB amphibolite, (b) Westerly granite, (c) Solnhofen limestone, and (d) Yuubari shale (Takahashi and Koide, 1989; Chang and Haimson, 2000; Haimson and Chang, 2000; Mogi, 2007).

4.4.5 Heuristic study on using a proposed method to quantify the end effect in true triaxial compression tests

In this section, a method to quantify the end effect in true triaxial compression test results is proposed. The method aims at excluding the influence of the end effect from triaxial compression test results so that the corrected test results can be more useful for developing 3D empirical failure criteria.

It is proposed that if the increase of σ_3 due to the end effect can be quantified, the enhancement of rock strength ($\Delta\sigma_1$) due to increased σ_3, which alters the true σ_2 effect, could be quantified and excluded from the true triaxial compression test results. The modeling results of KTB amphibolite are used to illustrate the proposed method.

Figure 4-20 presents the modeling results of the relation between actual σ_3 and σ_2 under different μ values. The vertical axis plots the actual average σ_3 of all the elements in the rock specimen at its peak load. The rock material model is σ_3-only-dependent (Section 4.2.3); thus, the increase of actual σ_3 in the rock, relative to the applied σ_3 (the origins of coordinates in Figure 4-20), is exclusively resulted from the end effect caused by the loading platens for applying σ_2. It is seen that the relation between actual σ_3 and σ_2 is approximately linear, and is a function of the μ values at the rock specimen-steel platen contacts such that:

$$\Delta\sigma_3 = f_1(\Delta\sigma_2, \mu) \qquad 3\text{-}1$$

where $\Delta\sigma_3$ is the difference between actual σ_3 and applied σ_3 (refer to discussion in Section 4.4.4), and $\Delta\sigma_2$ is the difference between applied σ_2 and applied σ_3.

The linear relation between $\Delta\sigma_3$ and $\Delta\sigma_2$ permits the quantification of $\Delta\sigma_3$ (Equation 3-1) due to the end effect. As a result, the relation between $\Delta\sigma_1$ and $\Delta\sigma_3$ due to the end effect can be quantified using the M-C failure criterion:

$$\Delta\sigma_1 = f_2(\Delta\sigma_3) = \frac{1+\sin\varphi}{1-\sin\varphi}\Delta\sigma_3 \qquad 3\text{-}2$$

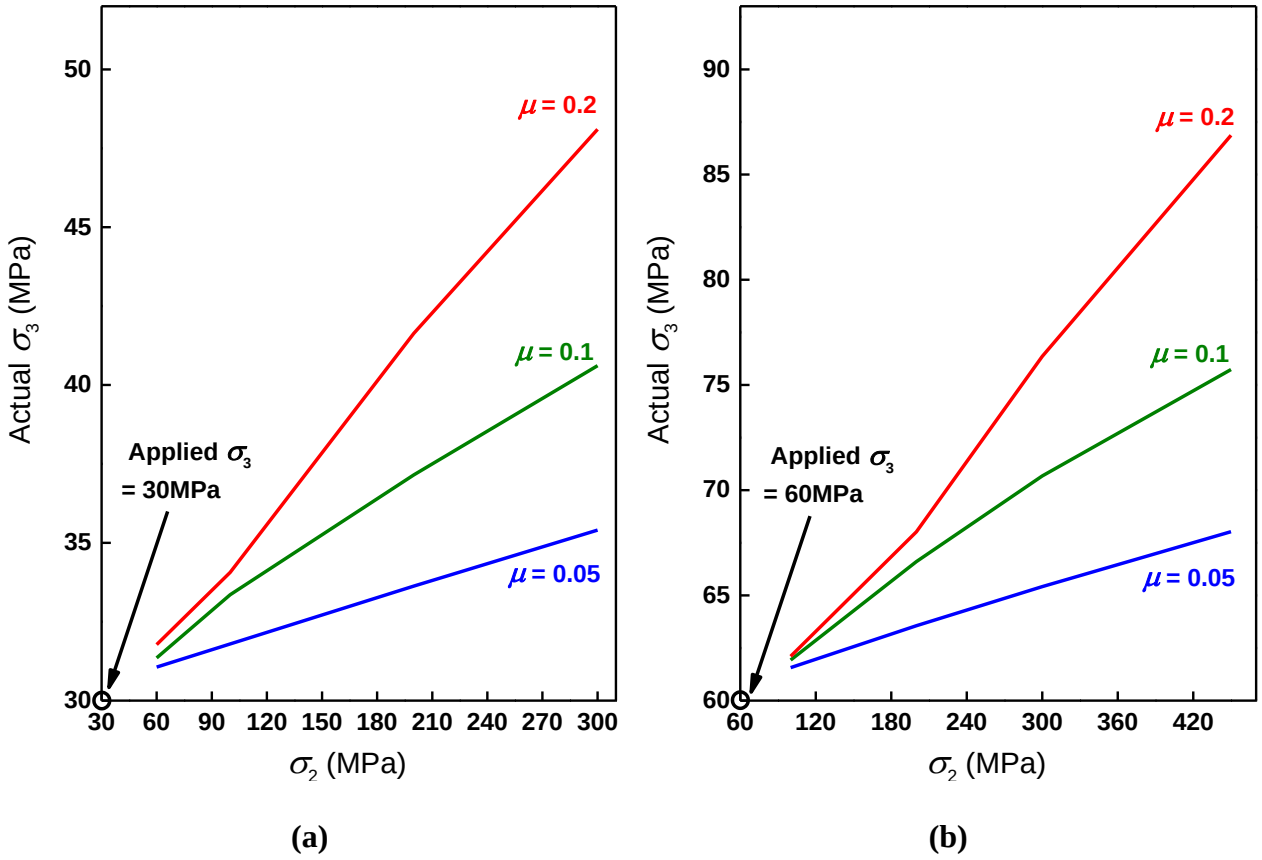

Figure 4-20 Relation between average σ_3 in the rock specimen and applied σ_2 for different μ values: (a) applied σ_3 = 30 MPa and (b) applied σ_3 = 60 MPa.

Figure 4-21 illustrates how the proposed method could be used to correct true triaxial compression test results for developing 3D empirical failure criteria. As long as the actual μ value at the rock specimen-steel platen contacts can be estimated within a reasonable range, the

relation between $\Delta\sigma_3$ and $\Delta\sigma_2$ as well as the relation between $\Delta\sigma_1$ and $\Delta\sigma_2$ can be calculated (using Equations 3-1 and 3-2).

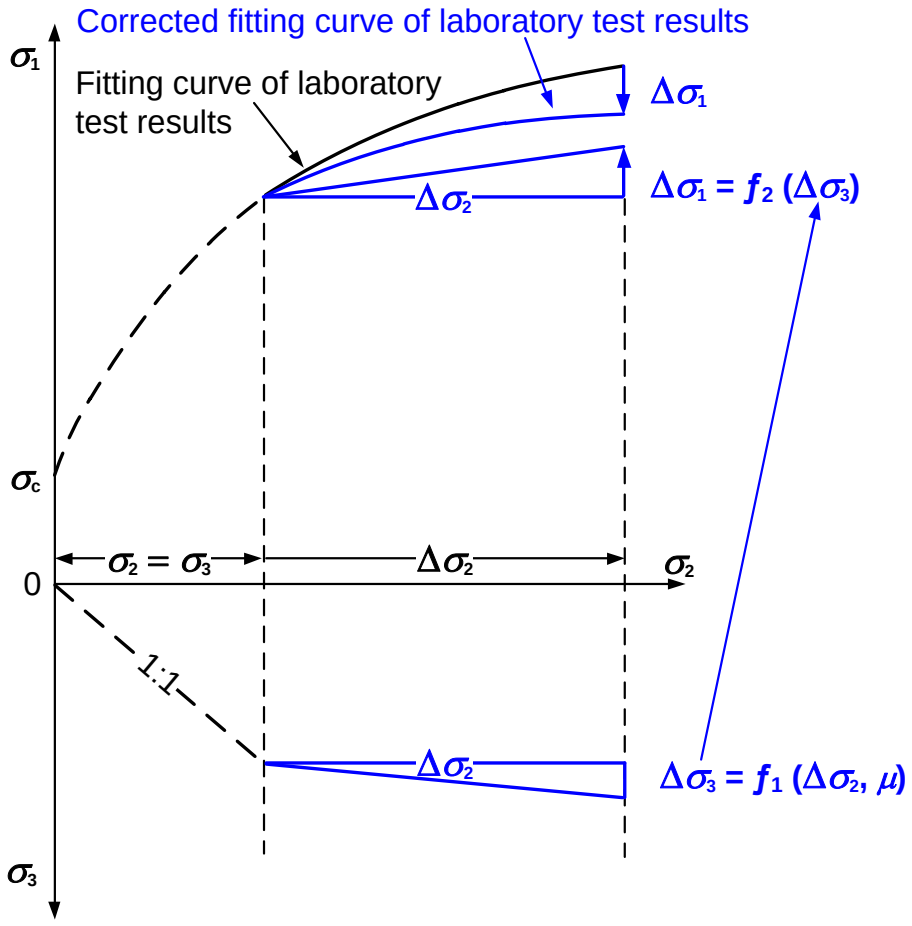

Figure 4-21 Illustration of the proposed method for quantifying the end effect in true triaxial compression test results.

The failure envelopes of KTB amphibolite with applied σ_3 ranging from 30 to 60 MPa are used to verify the proposed method (refer to justification in Section 4.4.3). Referring to the discussions in Section 4.2.4, the μ value is important for characterizing the end effect in true triaxial compression test results, and a range of 0.05–0.1 is assumed for the μ value at the lubricated rock specimen-steel platen contacts (Vutukuri et al., 1974; Labuz and Bridell, 1993;

Grote and Antonsson, 2009; Rashed and Peng, 2015). Using the modeling results of μ = 0.05 and 0.1, the relation between actual σ_3 and σ_2 at each applied σ_3 is obtained (Figure 4-20). Next, using the calibrated M-C strength parameters of KTB amphibolite listed in Table 4-3, the relation between $\Delta\sigma_1$ and $\Delta\sigma_3$ can be obtained (Equation 3-2).

The results of using the proposed method to exclude the strengthening effect of σ_2-induced end effect is presented in Figure 4-22, where all the stresses are normalized to the UCS of KTB amphibolite (σ_c). Black solid curves are the fitting curves based on the true triaxial compression test results (scatter data). Blue and green solid curves are the fitting curves of the corrected test results with the consideration of excluding the end-effect-induced σ_2 effect for μ = 0.05 and 0.1, respectively.

In addition, theoretical results (red dot curves) based on the strain energy criterion developed by Wiebols and Cook (1968) are added for comparison. Rock property and applied σ_3 are the same as those discussed in Section 4.4.3; μ_s = 1 is assumed for the theoretical results based on the strain energy criterion. The theoretical result curves are mostly between the blue and green solid curves. In other words, the selected parameters of μ = 0.05–0.1 for the corrected test results that exclude the end-effect-induced σ_2 effect match well with the selected parameter of μ_s = 1 for the theoretical results that describe the actual σ_2 effect. Therefore, this heuristic study demonstrates that the corrected test results could be used for developing 3D empirical failure criteria that can reflect better the true σ_2 effect. Note that the proposed method depends on the knowledge of the μ value. Unfortunately, it is unlikely to know the exact μ values in previous tests. Hence, this approach is likely useful to correct future test results when the μ values in the tests are determined within a small reasonable range.

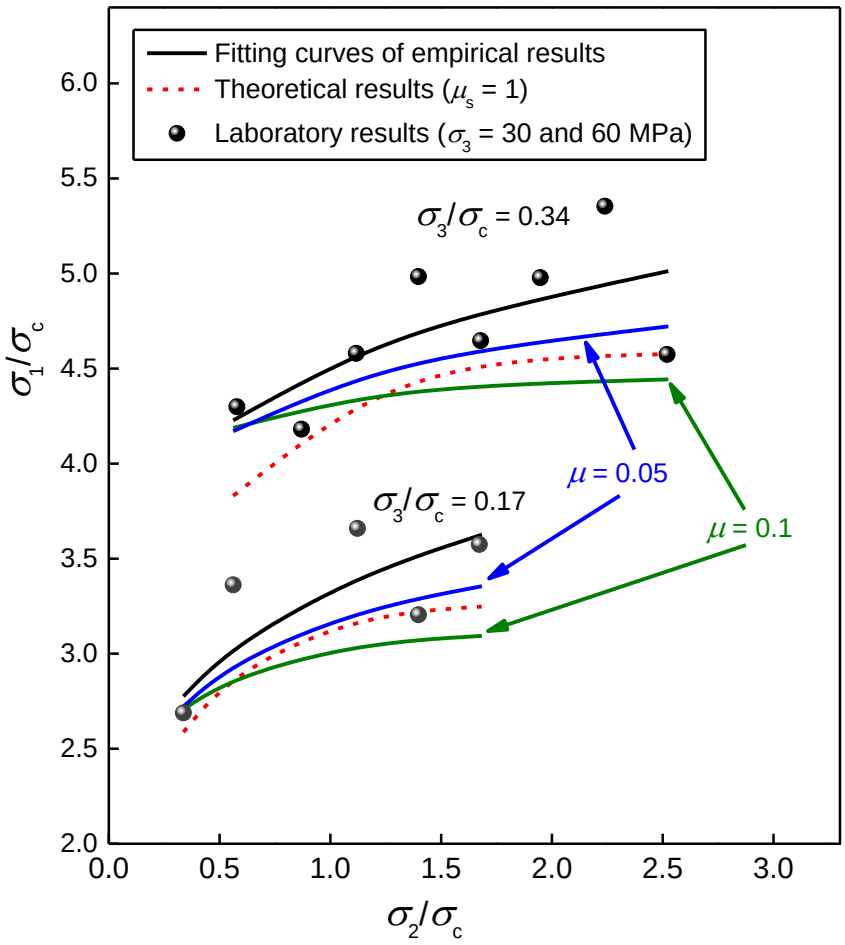

Figure 4-22 Comparison of corrected empirical failure envelopes and theoretical failure envelopes for KTB amphibolite.

4.4.6 End effect on post-peak deformation behavior of rock in true triaxial compression test

It is understood that the end effect can affect the peak strength of rock in true triaxial compression test. Hence, it is reckoned that the end effect can affect the post-peak deformation behavior of rock as well. There are no solid laboratory test results that show the post-peak stress–strain curves of rocks in true triaxial compression tests, especially near the low confining pressure range. On the other hand, the above studies (Chapter 3, Sections 4.1 to 4.4.5) indicate that the numerical model is well-suited to study the influence of the end effect on the strength and deformation behavior of rock in laboratory compression tests. Therefore, using the same

numerical model shown in Figure 4-4b, a heuristic study on the end effect in true triaxial compression test is conducted by the numerical experiment, with a focus on the post-peak stress–strain curve of rocks at low confining pressures.

The strength and deformation behavior of Westerly granite is illustrated in this numerical experiment. The physical and deformation parameters of the rock are the same as those listed in Table 4-2. The M-C strength parameters at peak load are the same as those listed in Table 4-4 at the confining pressure level of 20 MPa. The assumed strain-softening parameters of the rock are presented in Table 4-9.

Table 4-9 Strain-softening parameters of the rock specimens in simulation

Cohesion yield stress (MPa)	Shear plastic strain	Tension cut-off stress (MPa)	Tensile plastic strain
33	0	15	0
0.1	0.071	0.01	0.012

Figure 4-23 presents the relation between the axial stress (σ_1) and the axial strain (ε_1) for the square prismatic specimens under same σ_3 (σ_3 = 10 MPa) but different σ_2 loading conditions. Curves (a) to (c) represent σ_2 loading condition that is applied by platen loading at different σ_2 levels. In addition, Curve (a*) represent a stress state the same as that of Curve (a). The only difference between these two cases is that the σ_2 loading condition of Curve (a*) is applied by pressure loading (refer to definitions of platen loading and pressure loading in Section 4.2.4).

The complete stress–strain curves of the specimens under different loading conditions are different from each other. Although their confining pressures are the same and their σ_2 is applied by steel platens, the peak and post-peak strengths of the specimens are higher if σ_2 is higher (Curves (a), (b), and (c)). Furthermore, under the same applied σ_3 and σ_2, the peak and post-peak

strengths of the specimen are higher if σ_2 is applied by steel platens (Curves (a) and (a*)). Therefore, the end effect can enhance the post-peak ductility of rocks in true triaxial compression test.

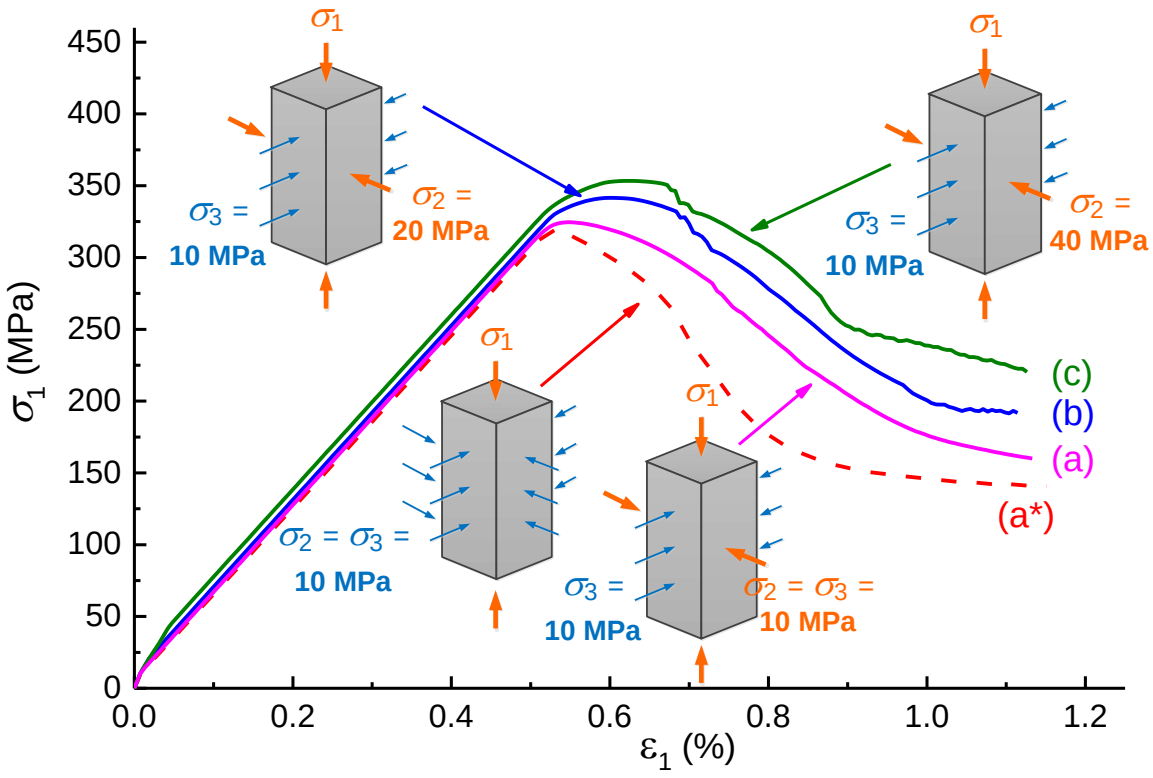

Figure 4-23 σ_1–ε_1 relations of the specimens under different loading conditions in true triaxial compression tests (μ = 0.1).

4.5 Summary

End effect plays a role in affecting laboratory test results of rock strength. This study emphasizes that the end effect cannot be eliminated completely in laboratory tests; as a result, the actual σ_2 effect on rock strength may be overestimated in some previous laboratory test results. The influence of the end effect on rock strength in true triaxial compression test was studied using a numerical experiment approach where steel platens were modeled explicitly. More importantly, the influence of σ_2 on rock strength was isolated by using the 2D M-C failure criterion, which

depends only on σ_1 and σ_3. Thus, any enhancement to the rock strength with the increase of σ_2 can be attributed to the end effect.

The modeling results revealed that the end effect can result in an apparent σ_2 effect, as long as the lateral rock specimen-steel platen contacts are frictional and the specimen in the σ_2 loading direction is squat. Some rocks show strong σ_2 effect while others do not, due to different end constraints initiated by different rock deformation behaviors. When the strengthening caused by the increase of σ_2 predicted by a theoretical failure criterion was added to the strengthening caused by the end effect, the results were in good agreement with the observed σ_2 effect from some previous laboratory tests, indicating that the observed σ_2 effect in true triaxial compression test can be partially influenced by the end effect, particularly when σ_3 was low.

It is understood that previous laboratory test results are still useful for developing 3D empirical failure criteria, provided that the contribution of the end effect to the observed σ_2 effect is well quantified. An alternative for developing 3D empirical failure criteria is to decrease the end effect to a level where the apparent σ_2 effect is very small, so that the obtained test results are more meaningful for characterizing the actual σ_2 effect.

Two test conditions—the specimen geometry and the contact condition—were investigated numerically in the above studies. Next, the *LSS* of stiff test machines, a test condition that is rarely studied before and related to the geometry and contact condition of the rock specimen-test machine system, will be discussed in next chapter.

Chapter 5

5 Influence of loading system stiffness on the post-peak stress–strain curves of rocks in uniaxial compression test

In this chapter, the influence *LSS* on stable post-peak deformation behavior of rock in uniaxial compression test was studied. Three test machine models with idealized rigid loading, platen loading, and frame-platen loading of varied *LSS* values were considered and their modeling results were compared. Inspired by the laboratory test results of Bieniawski et al. (1969), who used a stiff test machine that could vary its *LSS*, the goal of this study is to numerically confirm that *LSS* can influence the post-peak stress–strain curve of stable rock failure.

This study is primarily a numerical investigation because very limited testing data were available for calibration (refer to literature review in Section 2.3.4). However, the validity of the numerical model for simulating the influence of *LSS* can still be confirmed by other means. Firstly, the capacity of the numerical tool was examined in Chapters 3 and 4 by comparing the modeling results with laboratory test results; the numerical tool was found to be well-suited for simulating the test conditions in laboratory tests (refer to the research approaches in Section 1.2.3).

In addition, laboratory test results of unstable post-peak failure of rocks and previous theories on two special loading conditions of *LSS* (*LSS* = λ or ∞, where λ is the post-peak stiffness of a rock specimen; refer to Section 5.1.2 for the definition of ideal loading condition in which *LSS* = ∞) can be used as benchmarks to examine the results obtained from the numerical modeling. Therefore, a comprehensive numerical experiment was carried out to study the influence of *LSS* on the post-peak stress–strain curves of rock in laboratory tests.

5.1 Numerical models and modeling parameters

5.1.1 Simulation statement

ABAQUS^{2D} is employed in the numerical experiment, with a focus on obtaining the post-peak stress–strain curves of stable rock failure. Uniaxial compression test is widely used in laboratory property testing and the numerical simulation is restricted to this type of compression test. In addition, because the research focus is the *LSS* in the direction normal to the specimen-platen contact surfaces, shear constraint (i.e., friction; refer to discussion in Section 2.2) along the surfaces is excluded using frictionless contact condition.

Note that the strain-softening behavior is assumed for the post-peak deformation behavior of the rock specimen under the axial-strain-controlled loading in uniaxial compression (refer to justifications in Section 3.2), and the *LSS* of test machines is assumed greater than the absolute value of the post-peak stiffness of the rock specimen (λ). Thus, rock failures in the numerical experiment are stable and will follow the characteristics of Class I failure type (Wawersik and Fairhurst, 1970; Salamon, 1970). In such a case, the servo-controlled test machine will act like a traditional stiff test machine. Therefore, the elastic response of a traditional stiff test machine (Figure 2-9) and its influence on the post-peak stress–strain curve of a rock specimen are investigated in the numerical modeling.

It is hypothesized that *LSS* plays a role in defining the post-peak stress–strain curve of rock even if the rock fails in a stable fashion. The research approach is: firstly, a base case under a direct axial-strain-controlled loading is obtained. This loading condition is different from that applied by a test machine with a finite *LSS*; hence, the rock behaviors obtained under these two loading conditions can be different. The base case is the benchmark to examine the potential impact of finite *LSS*. Next, the rock behaviors in different test machines are modeled, and the influence of

LSS on the post-peak stress–strain curve of the same rock specimen is investigated by comparing the result of the base case with the ones obtained with different *LSS* values. Aside from the loading platen, the loading frame and the ram are simulated eventually in the model to characterize the *LSS* of traditional stiff test machines realistically (Figure 2-9).

5.1.2 Ideal loading condition

The rock property for the base case under uniaxial compression is defined first before carrying out a parametric study. According to the ISRM SMs for determining UCS (Fairhurst and Hudson, 1999), a rectangular specimen with a height of 100 mm and a width of 50 mm is used for the simulation. Referring to the justifications in the previous studies (Chapters 3 and 4), the pre-peak behavior of a hard rock specimen in compression is simplified as linear elastic. A standard M-C failure criterion with a tension cut-off is employed to determine the peak strength of the rock. The strength and deformation parameters of the rock are presented in Table 5-1.

Table 5-1 Strength and deformation parameters of the rock in simulation

Parameters	Value
Poisson's ratio, ν	0.18
Young's modulus, E (GPa)	30
Cohesion, c (MPa)	30
Tension cut-off, σ_t (MPa)	7
Friction angle, φ (◦)	24
Dilation angle, ψ (◦)	24

As discussed in Section 5.1.1, a strain-softening model of the rock is used to define the post-peak deformation behavior. The strain-softening behavior is defined by degrading the cohesion yield stress and tension cut-off stress of the rock as a functions of plastic strain (Table 5-2).

Table 5-2 Strain-softening parameters of the rock in simulation

Cohesion yield stress (MPa)	Shear plastic strain	Tension cut-off stress (MPa)	Tensile plastic strain
30.0	0	7.0	0
26.7	0.020	0.1	0.009
17.3	0.065		
9.0	0.123		
1.0	0.171		

The stress–strain curve is obtained by applying a constant loading velocity at a rate of 0.016 m/s symmetrically onto the top and bottom ends of the specimen shown in Figure 5-1. This loading method implies that the *LSS* in the loading direction of the specimen is infinite (∞) and it is called the ideal loading condition. The size of the elements is 2.5 mm in its longest dimension; the maximum deviation factor for the curvature control of element size is 0.1. The shape of the elements is quad; the elements are generated by using the structured technique. The element type is 4-node bilinear plane strain quadrilateral; the integration algorithm for the chosen element type is reduced integration using hourglass control.

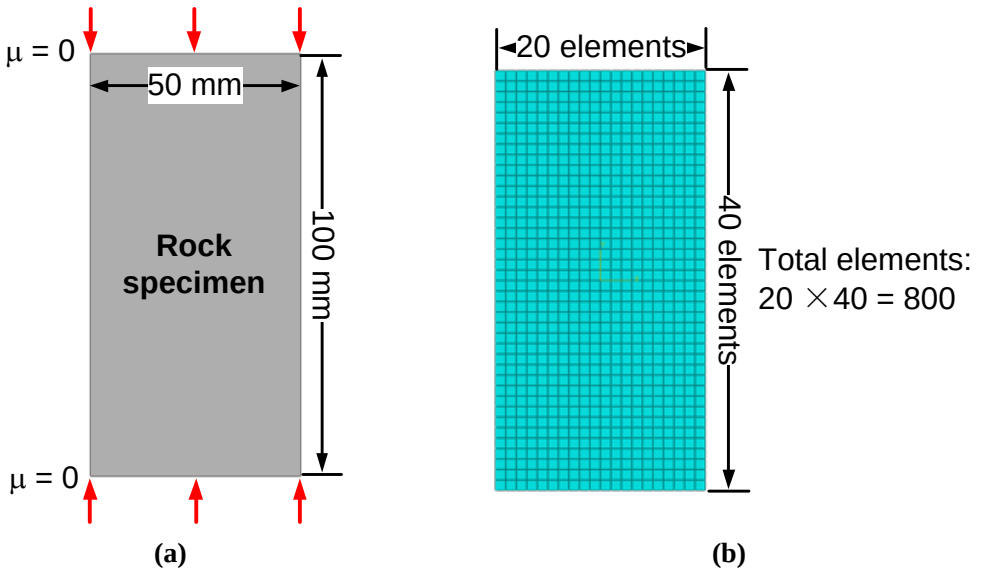

Figure 5-1 Rock specimen under uniaxial compression applied by the ideal loading condition: (a) schematic of the loading condition, and (b) FEM model.

Figure 5-2 presents the complete stress–strain curve of the rock under the ideal loading condition in uniaxial compression. Rock behavior obtained under the ideal loading condition is considered as the base case because the rock is free from the influence of *LSS* on its behavior. Hence, once the geometry and the applied loading velocity of the rock specimen are determined, the result of the base case for comparing with other results under different *LSS* values is indicated by the stress–strain curve shown in Figure 5-2. The steepest descending slope of the curve is indicated by a red line, which tells that the post-peak stiffness of the rock in stress–strain curve (E_p) is about 47 GPa, or λ = 24 GN/m if the load–deformation relation is used (Equation 2-4).

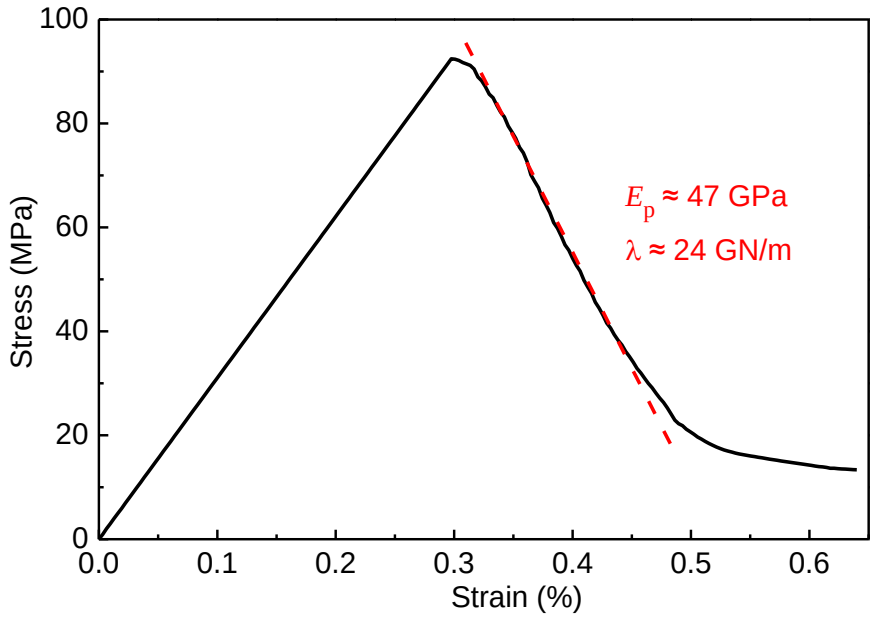

Figure 5-2 Stress–strain curve of a rock specimen under the ideal loading condition in uniaxial compression.

5.1.3 Numerical models of test machines

In this section, different models of test machines, from the simplified one to more complex ones consisting of some essential loading components, are introduced in the numerical models. *LSS* is the control variable that is varied in the study. The range of *LSS* spans from relatively soft

condition to extremely stiff condition. In addition to the ideal loading condition, rigid loading, finite *LSS* of platen loading, and finite *LSS* of frame-platen loading are considered. In the more complex test machine models, the actual geometrical relation between the test machine and the rock specimen is considered in a qualitative manner because precise modeling of all the components in a test machine is beyond the intended scope of this study.

The simplest loading condition uses rigid bodies representing the test machine. A rigid body is an idealization of a solid body with infinite stiffness and the deformation in the rigid body is zero. Hence, if a constant loading velocity is applied to a rigid body, it will move at the same velocity vector as the applied load. The numerical model of a rock specimen in uniaxial compression, applied by two rigid platens, is shown in Figure 5-3. This loading condition is termed as the rigid loading condition. Because the influence of *LSS* is eliminated, rock behaviors under the rigid loading condition are expected to be close to that of the base case. Hence, it is reasonable to state that if *LSS* approaches infinity, the rock behavior should approach that of the base case.

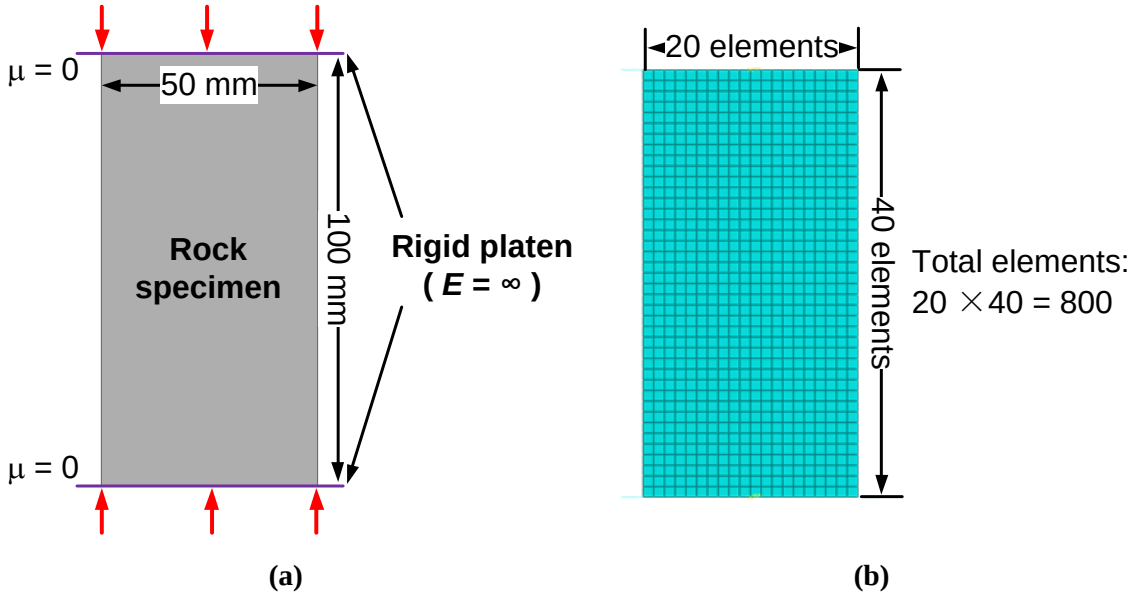

Figure 5-3 Rock specimen under uniaxial compression applied by the rigid loading condition: (a) schematic of the loading condition, and (b) FEM model.

The numerical model of a rock specimen under uniaxial compression applied by two identical loading platens is shown in Figure 5-4. This loading condition is termed as the platen loading condition. A constant loading velocity, which is the same as that under the ideal loading condition, is applied to the specimen through the loading platens. In this case, the composite stiffness of the test machine is manifested by these two loading platens, and the stiffness of which can be calculated using Equation 2-4. The Young's moduli of the loading platens are varied to study the influence of *LSS* on the post-peak deformation behavior.

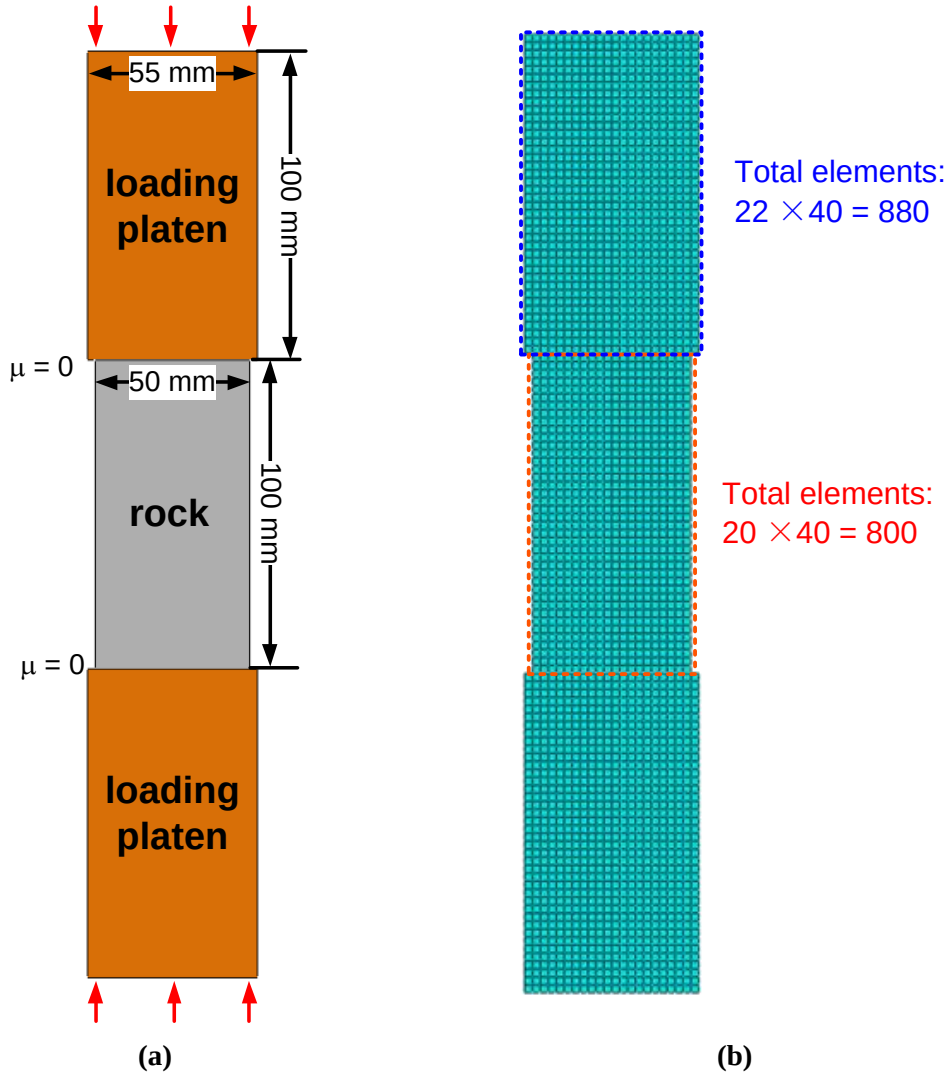

Figure 5-4 Rock specimen under uniaxial compression applied by the platen loading condition: (a) schematic of the loading condition, and (b) FEM model.

Next, a simplified frame-platen loading test machine is simulated. Two loading platens of the same geometry are in contact with the specimen and a loading frame encapsulating the specimen-platen complex is incorporated (Figure 5-5). The Young's moduli of the loading frame and the platens are the same. Inspired by the thermal loading mechanism developed by Cook and Hojem (1966) and Wawersik (1968) independently, the loading platen underneath the specimen is assigned an orthotropic thermal property, i.e., thermal expansion of the platen occurs only in the vertical direction (parallel to the specimen height) and the thermal expansion in the horizontal direction is zero. This is an attempt to simulate the loading ram in a traditional stiff test machine and in this fashion the loading frame that encapsulates the specimen-platen-ram complex similar to that shown in Figure 2-9 can be imbedded in the numerical model.

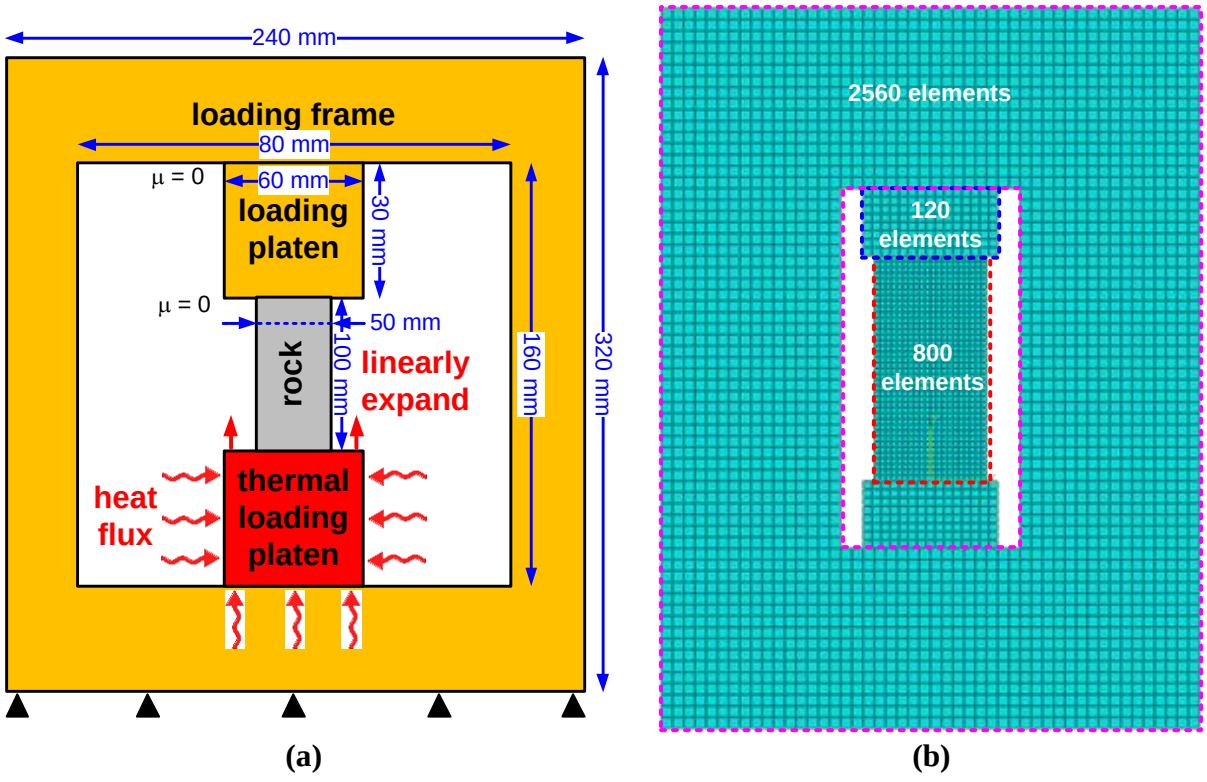

Figure 5-5 Rock specimen under uniaxial compression applied by the frame-platen loading condition: (a) schematic of the loading condition, and (b) FEM model.

The loading platen at the bottom consisting of an idealized material is called the thermal loading platen and the test machine is called the frame-platen loading test machine. When a constant heat flux is provided to the thermal loading platen, the platen will expand linearly in the vertical direction to contract the rock specimen in a way quite similar to that a fluid ram does[3]. In reality, the fluid in a fluid ram can reduce *LSS* significantly. If such a frame-platen loading test machine is not considered, high *LSS* values cannot be achieved in the numerical model. Consequently, three essential loading components of a test machine (Section 2.3.1)—loading platen, loading frame, and loading ram—are conceptually imbedded in the numerical model (Figure 5-5) and this is termed as the frame-platen loading condition.

The heat flux applied to the thermal loading platen is calibrated so that the specimen under the frame-platen loading condition is contracted at a displacement rate the same as that in other loading conditions. Table 5-3 presents the calibrated thermal parameters for the thermal loading platen.

Table 5-3 Calibrated thermal parameters for the thermal loading platen used in simulation

Thermal parameters	Value
Conductivity at Room Temperature (RT) ($W \cdot m^{-1}K^{-1}$)	0.15
Expansion coefficient in the vertical direction at RT (K^{-1})	0.0007
Specific heat at RT ($J \cdot kg^{-1}K^{-1}$)	1900
Heat flux (W)	2.005×10^{10}

Figure 5-6 compares the calibrated displacement–time relation of the specimen under the frame-platen loading condition with that under the ideal loading condition. The displacement under the

[3] Note that no loading components other than the thermal loading platen are defined with thermal property and heat conduction; thus, there is no heat conduction at the contacts of the thermal loading platen.

frame-platen loading condition is recorded at the top end of the thermal loading platen, and the whole body of which is continuously exposed to a constant heat flux.

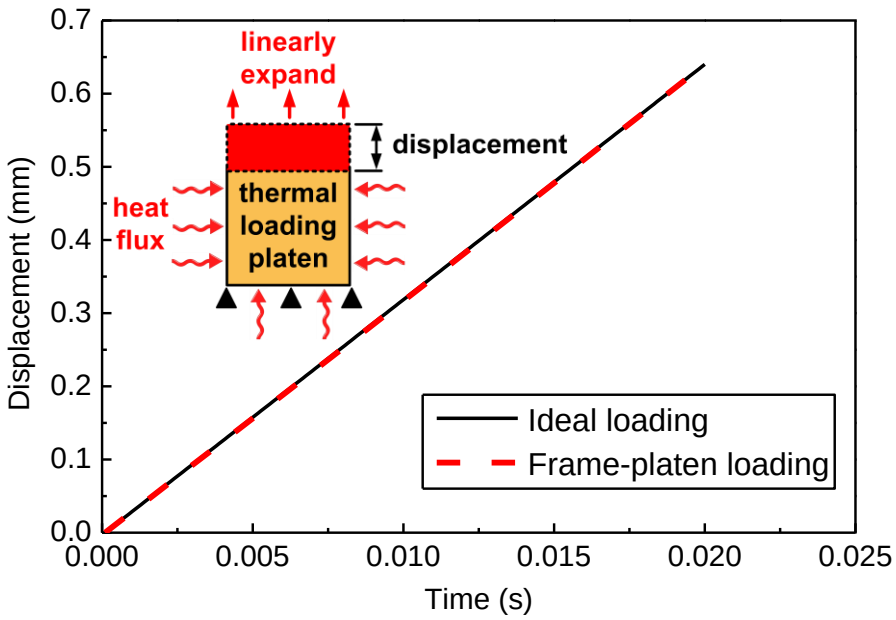

Figure 5-6 Displacement–time relations of rock specimens under two loading conditions.

The Young's moduli of the loading frame and the platens are varied to change *LSS*. To compare the rock behaviors between the frame-platen loading test machine model and the platen loading test machine model, the Young's modulus of the frame-platen loading test machine needs to be adjusted in order to equalize the *LSS* of frame-platen loading test machine model and that of the platen loading test machine model. According to the definition of stiffness (Section 2.3.3), Figure 5-7 illustrates how the *LSS* of a frame-platen loading test machine (LSS_F) is calibrated in the numerical modeling. If a pair of concentrated reaction load (F) is applied to the top and bottom loading platens through two rigid platens, the relative displacement ($\delta_1 + \delta_2$) of these two rigid platens will cause an elastic response of the test machine. Similarly, the *LSS* of the platen loading test machine (LSS_P) can be calibrated in this fashion.

Figure 5-8 presents the calibrated load–displacement relations of the two test machines, along with the theoretical LSS_P value (LSS_{theory}) of 2577 GN/m calculated using Equation 2-4. Based on the slopes of the fitting lines for the load–displacement relations (Fakhimi et al., 2016), LSS_F and LSS_P are obtained as 2579 GN/m and 2575 GN/m, respectively. In this way, the Young's modulus of the frame-platen loading test machine can be adjusted to yield *LSS* the same as that of the platen loading test machine.

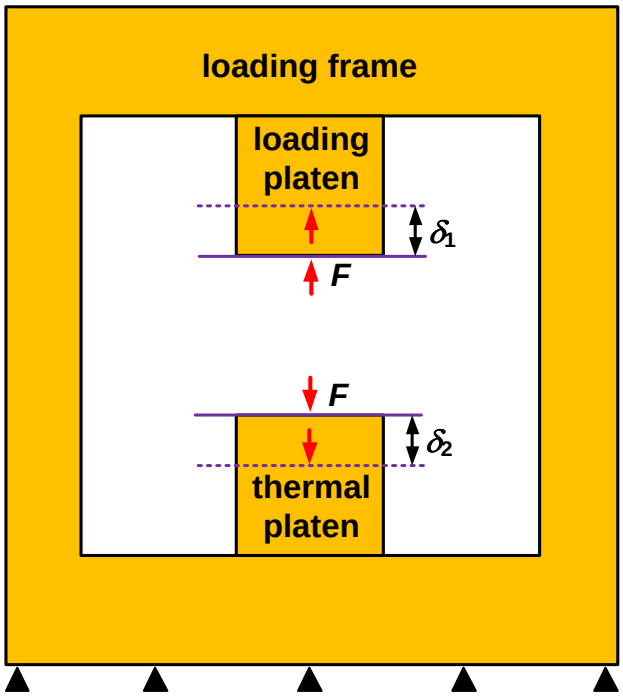

Figure 5-7 Calibration of frame-platen loading test machine's *LSS* in numerical modeling.

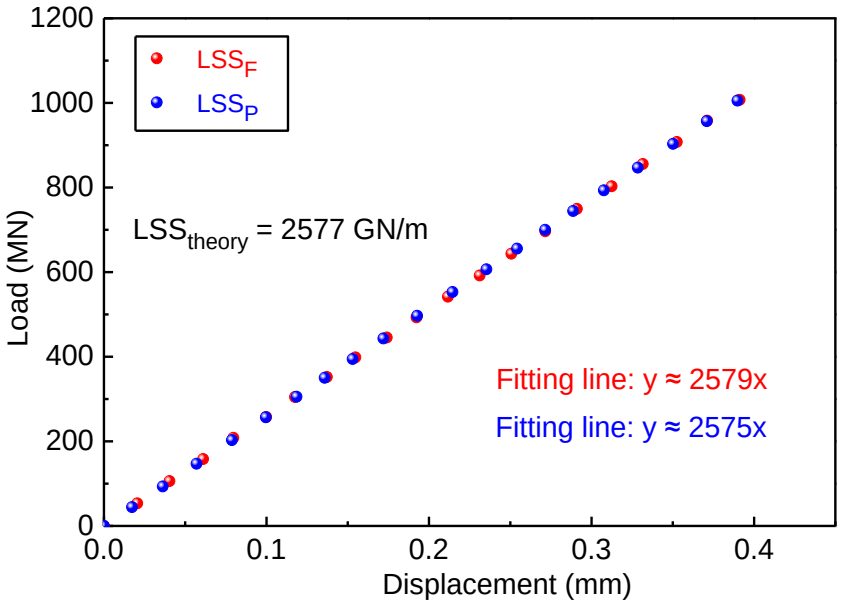

Figure 5-8 Calibrated load–displacement relations of two test machines.

5.2 Modeling results and discussions

5.2.1 Rigid loading results

Figure 5-9 shows the stress–strain curve of the rock specimen under the rigid loading condition (refer to Figure 5-3), along with that under the ideal loading condition (refer to Figure 5-1). It is seen that the two curves are very close to each other. The modeling results show that the influence of *LSS* on the post-peak stress–strain curve of rock can be eliminated by assigning a rigid property to the test machine. Thus, the obtained post-peak stress–strain curve of rock should approach that of the base case if *LSS* becomes very stiff.

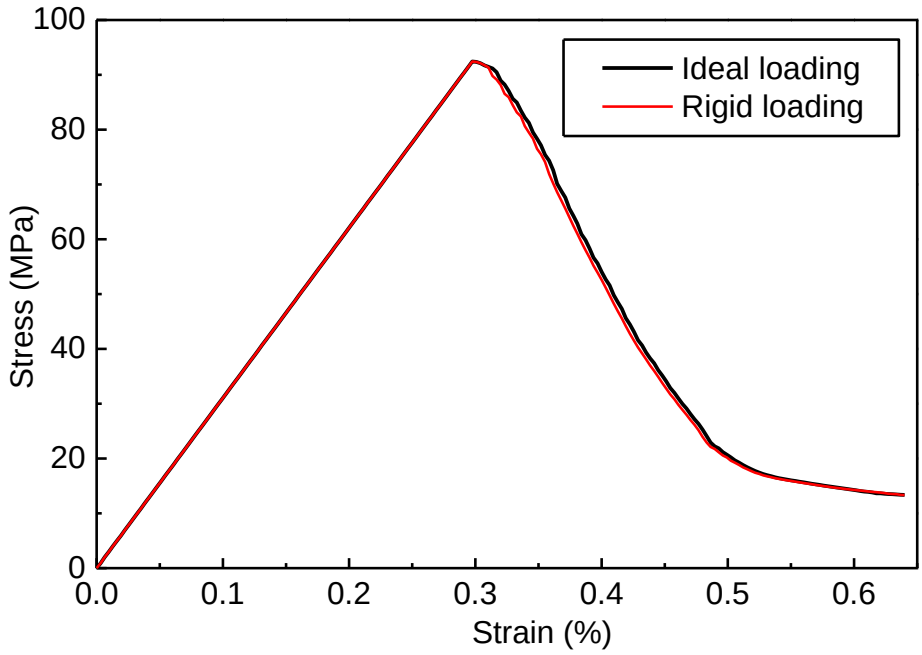

Figure 5-9 Stress–strain curves of the rock under ideal and rigid loading conditions.

5.2.2 Platen loading results

Figure 5-10 presents the stress–strain curves of the rock under the platen loading condition (refer to Figure 5-4) with different *LSS* values ranging from 19 GN/m to 2577 GN/m and that under the ideal loading condition. It is seen that different *LSS* values result in different post-peak stress–strain curves of the rock, even though the peak strengths are the same. With the increase of *LSS*, the post-peak stress–strain curve of the rock first becomes steeper (colored solid curves) than that of the base case (black dash curve), and becomes the steepest at *LSS* = 825 GN/m. As *LSS* further increases, the post-peak stress–strain curve becomes less steep and gradually approaches (colored dash curves) that of the base case.

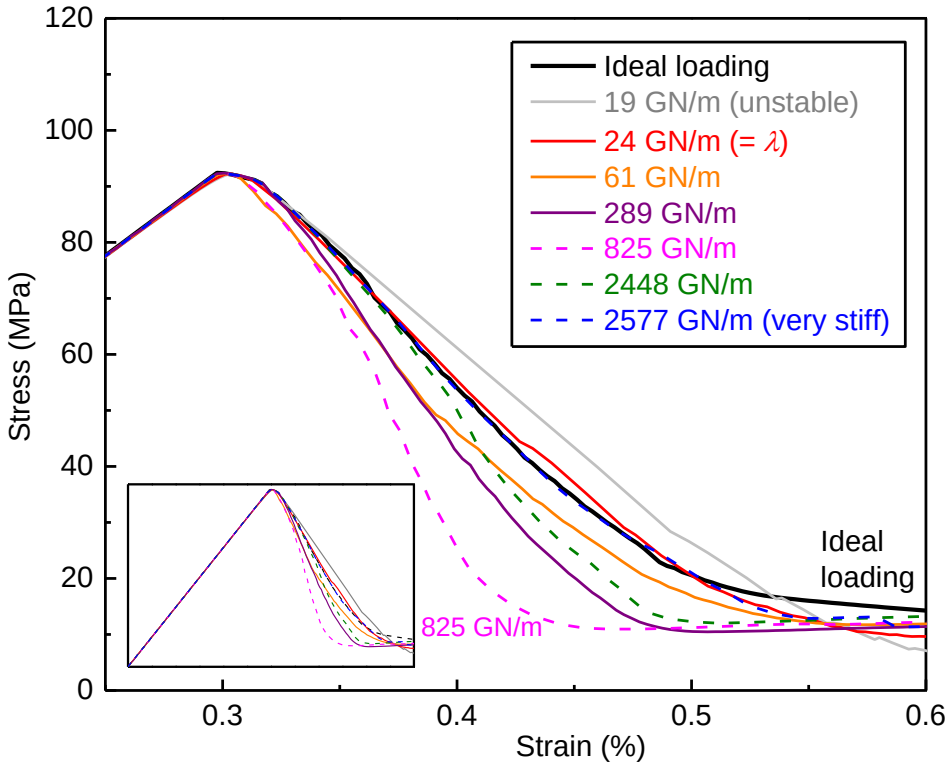

Figure 5-10 Post-peak stress–strain curves of the rock under the ideal loading condition and the platen loading condition with different *LSS* values; the complete stress–strain curves are shown in the insert.

When *LSS* = 19 GN/m < λ (= 24 GN/m), unstable rock failure is observed. The slope of the post-peak stress–strain curve of the unstable rock failure (grey solid curve) is flatter than that under the ideal loading condition, indicating that excessive energy is released from the test machine to the rock specimen. The modeling result of the unstable rock failure agrees well with laboratory and field observations (Shepherd et al., 1981; Milev et al., 2001; Blake and Hedley, 2003; Zhang et al., 2012).

When *LSS* = 24 GN/m = λ, which is the minimum or the critical *LSS* to ensure that stable rock failure occurs (refer to Equation 2-6), the obtained post-peak stress–strain curve (red solid curve is close to the curve under the ideal loading condition. There are no solid laboratory observations

on the rock deformation behavior under the loading condition of $LSS = \lambda$, but the modeling result with $LSS = \lambda$ agrees with the results by other researchers using DEM numerical models (Kias and Ozbay, 2013; Hemami and Fakhimi, 2014) and more recently using a 3D FEM numerical model (Manouchehrian and Cai, 2015).

The above modeling results show that *LSS* influences the post-peak stress–strain curve of rock even though the rock failure process is stable. According to the Loading System Reaction Intensity (*LSRI*, defined as the ratio of the maximum velocity of the loading platen at the rock specimen-loading platen contact to the applied loading velocity) proposed by Manouchehrian and Cai (2015) to identify stable and unstable rock failures, there is a sudden reaction movement of the loading platen towards the failing rock if the rock failure is unstable; in contrast, the reaction of the loading platen during a stable rock failure is not easily noticeable. Manouchehrian and Cai (2015) pointed out that *LSRI* is normally smaller than 2 when stable rock failures occur.

Table 5-4 presents the relation between *LSRI* and *LSS* under the platen loading condition. The calculated *LSRI* values confirm that the rock failures are stable when *LSS* is greater than λ. Referring to the stress–strain curves of stable rock failures in Figure 5-10, it is seen that as *LSS* increases, the post-peak stress–strain curves gradually departure from that of the base case and reach the steepest descending slope when *LSS* = 825 GN/m. Then, the post-peak stress–strain curves become less steep as *LSS* increases and is close to that of the base case when *LSS* is very stiff.

Table 5-4 Relation between *LSRI* and *LSS* under the platen loading condition

LSS (GN/m)	2577	2448	825	289	61	24	19
LSRI	2.0	1.6	1.9	2.0	2.4	10.6	**21**

It is observed that for the stable rock failures captured in the simulation, the stress distributions in the rock specimen are not the same for different *LSS* values. Figure 5-11 and Figure 5-12 present σ_1 and σ_3 distributions respectively in the rock specimen in the post-peak deformation stage at axial strain $\varepsilon = 0.4\%$ under the platen loading condition for $LSS \geq \lambda$, along with σ_1 and σ_3 distributions under the ideal loading condition. When *LSS* is critical or very stiff, the platen loading condition will result in stress distributions in the rock specimen similar to that under the ideal loading condition. Hence, the post-peak stress–strain curve obtained under either the critical *LSS* or very stiff *LSS* loading condition is very close to the curve under the ideal loading condition.

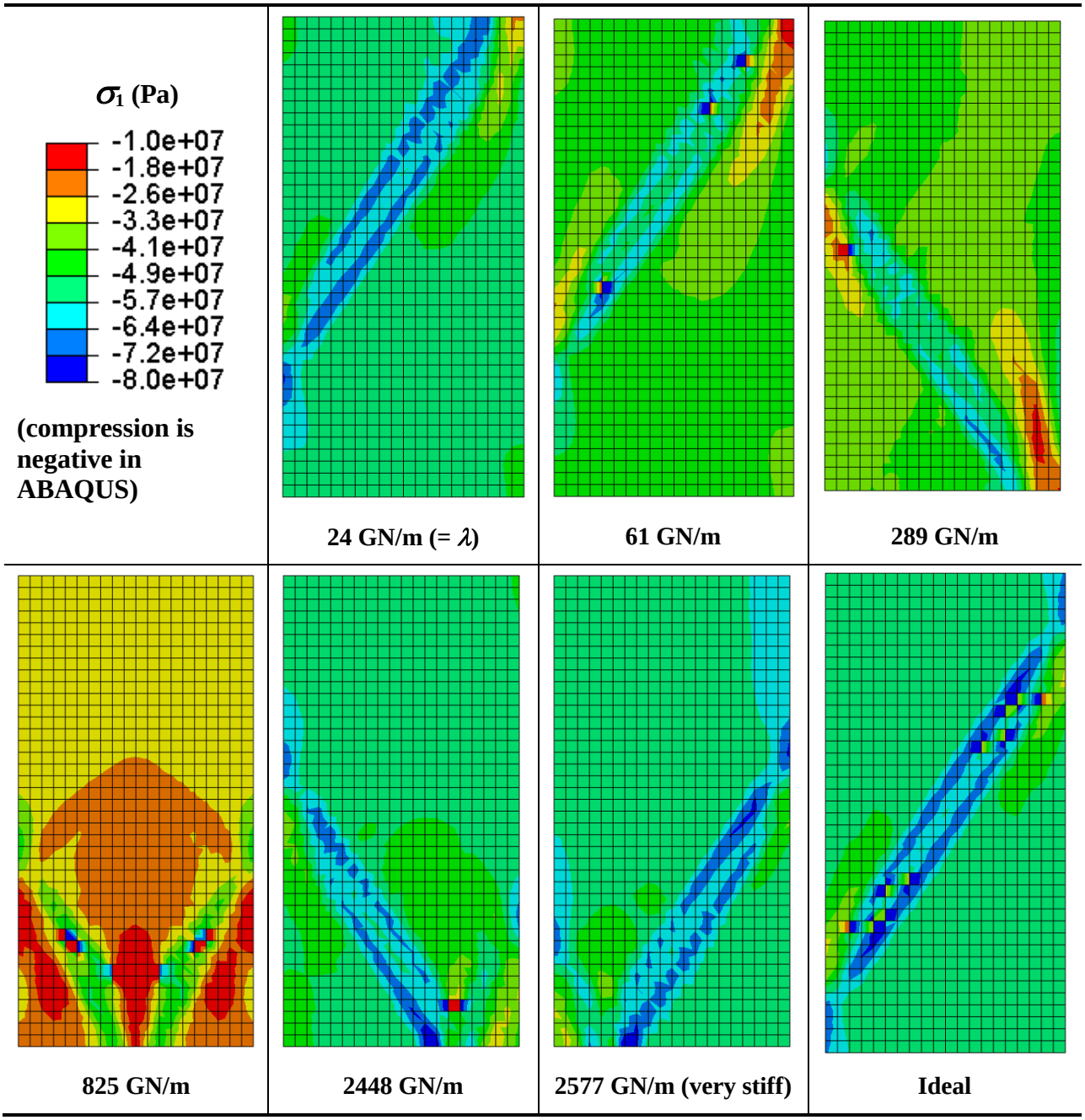

Figure 5-11 σ_1 distributions in the rock specimen at $\varepsilon = 0.4\%$ in the post-peak deformation stage under the platen loading condition for $LSS \geq \lambda$ and the ideal loading condition.

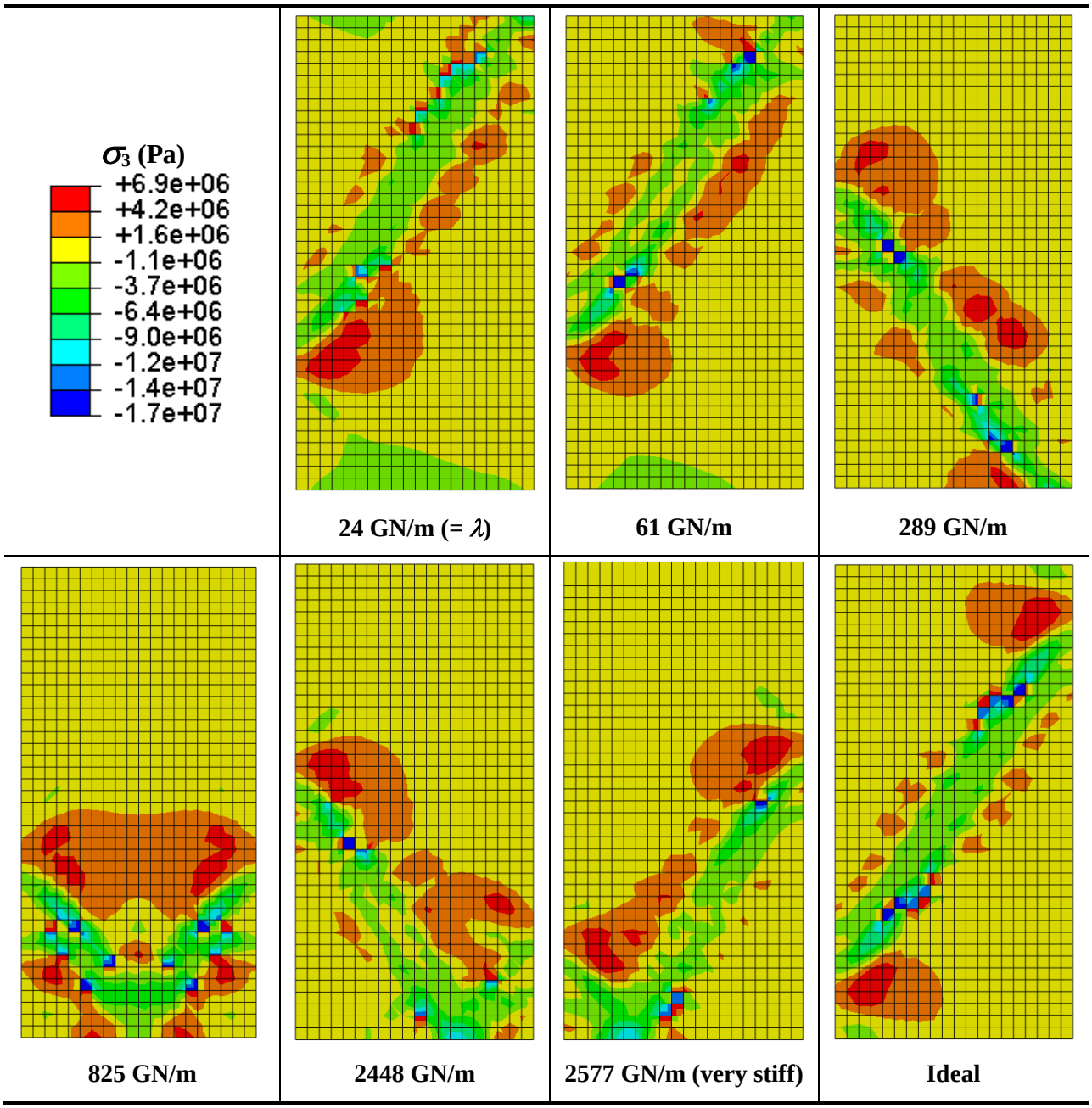

Figure 5-12 σ_3 distributions in the rock specimen at $\varepsilon = 0.4\%$ in the post-peak deformation stage under the platen loading condition for $LSS \geq \lambda$ and the ideal loading condition.

It is important to investigate the consumed energy in the rock specimen because both the stress–strain curves and the stress distributions in the rock specimen are macroscopic behaviors of the rock specimen in response to the input energy (E_{in}) provided by an external energy source

(independent of the rock specimen-test machine system) to the rock specimen-test machine system. Figure 5-13 illustrates the energy in a rock specimen and a test machine, where the test machine is idealized and represented by a spring and E_{in} is provided to the rock specimen-test machine system. As the load is increased to the peak load of the rock specimen, both the energy stored in the test machine (E_t) and the energy consumed by the rock deformation (E_r) increases, and the energy conservation equation at the peak load is:

$$E_{in} = E_t + E_r \tag{4-1}$$

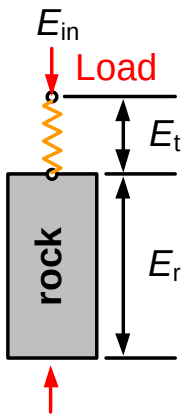

Figure 5-13 Illustration of consumed energy in a rock specimen and a test machine during rock failure with the supply of external input energy.

In the post-peak deformation stage, Equation 4-1 still holds true and asterisk (*) is used to differentiate the energy items at the post-peak deformation stage from those at the peak load. The energy conservation equation at the post-peak deformation stage is:

$$E_{in}{}^* = E_t{}^* + E_r{}^* \tag{4-2}$$

The energy stored in the test machine is released ($\Delta E_t = E_t - E_t^*$) to the rock specimen due to the unloading of the test machine. Meanwhile, as discussed in Section 2.3.3, additional input energy ($\Delta E_{in} = E_{in}^* - E_{in}$) is required to cause further deformation of the rock when the rock failure is

stable. Hence, the energy conservation Equation 4-2 during the unloading of the test machine while ΔE_{in} is introduced into the system can be expressed in an incremental form as:

$$E_{in} + \Delta E_{in} = (E_t - \Delta E_t) + (E_r + \Delta E_t + \Delta E_{in}) \quad 4\text{-}3$$

Energy consumed in the rock specimen in the post-peak deformation stage ($\Delta E_r = E_r^* - E_r$) is composed of two energy items:

$$\Delta E_r = \Delta E_t + \Delta E_{in} \quad 4\text{-}4$$

Based on traditional viewpoints regarding ΔE_r during unloading of a test machine (Bieniawski et al., 1969; Salamon, 1970; Hudson et al., 1972b; Hudson and Harrison, 2000), Figure 5-14 illustrates conceptually the relation between ΔE_r and *LSS* for stable rock failure, where the rock behavior of the base case is simplified by red straight lines.

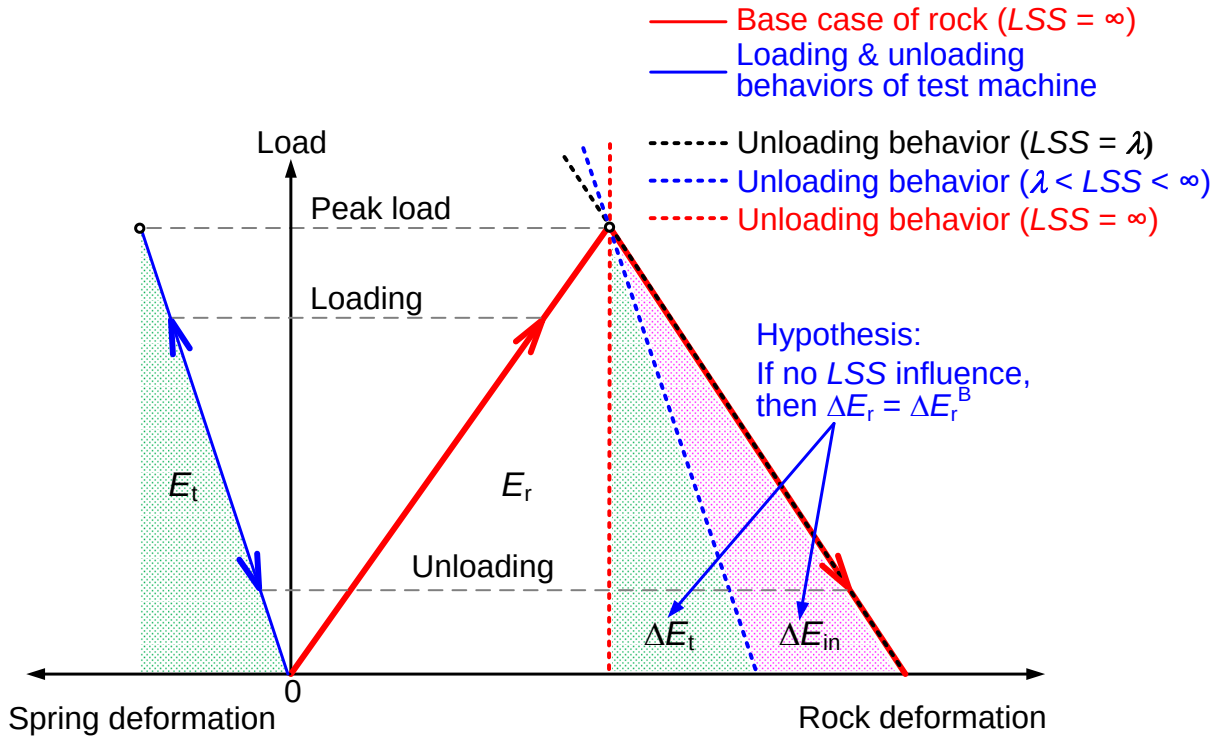

Figure 5-14 Conceptual illustration of the relation between consumed energy in a rock specimen and *LSS* during stable rock failure.

$LSS = \infty$ and $LSS = \lambda$ are two special cases of stable rock failure. In the subsequent discussions, ΔE_r^B is used to refer to the energy consumed in the rock to obtain the post-peak stress–strain curve of the base case under the ideal loading condition ($LSS = \infty$), compared with ΔE_r consumed in the rock under a test machine of a finite *LSS*. Because a test machine with $LSS = \infty$ cannot store and release any energy, ΔE_r^B has to be provided wholly by ΔE_{in} from the external energy source. On the other hand, no additional input energy ΔE_{in} is required for $LSS = \lambda$ to obtain the rock behavior shown in Figure 5-14, because the energy released from the test machine ΔE_t is just the right amount ($\Delta E_t = \Delta E_r$) needed to drive rock failure. When *LSS* is finite and greater than λ, in addition to ΔE_t released from the test machine, additional input energy ΔE_{in} from the external energy source is required to drive rock failure.

The relation between ΔE_r and ΔE_r^B is important for verifying the hypothesis of this study—the post-peak stress–strain curve of stable rock failures varies with *LSS*. Obviously, ΔE_r cannot be greater than ΔE_r^B; otherwise, unstable rock failure will occur. If the obtained rock behavior under a finite $LSS > \lambda$ and that under the ideal loading condition are the same, then ΔE_r under various $LSS > \lambda$ should be constant and equal to ΔE_r^B. I.e., *LSS* has no influence on the post-peak stress–strain (or load–displacement) curve. In such a case, a specific amount of ΔE_{in}, aside from ΔE_t, is required so that their summation is always equal to ΔE_r^B.

The modeling results demonstrate that different ΔE_r consumed in the post-peak deformation stage results in different post-peak stress–strain curves under various *LSS*, hence the post-peak stress–strain curve is affected by *LSS*. Figure 5-15 compares the variation of ΔE_r and ΔE_r^B values with strains starting at the peak load in the rock under the platen loading condition for $LSS \geq \lambda$.

ΔE_r is obtained by subtracting the accumulative energy consumed in the rock in the post-peak deformation stage (E_r^*) by that at the peak load (E_r). ΔE_r approaches ΔE_r^B only if the rock is loaded under a very stiff loading condition (2577 GN/m). The ΔE_r values under the critical *LSS* loading condition (24 GN/m) are close to the ΔE_r^B values, but not as close to that under the very stiff *LSS* loading condition. Referring to Equation 4-4, ΔE_r is comprised of ΔE_t and ΔE_{in}, thus the relation between these two energy items and *LSS* needs to be examined.

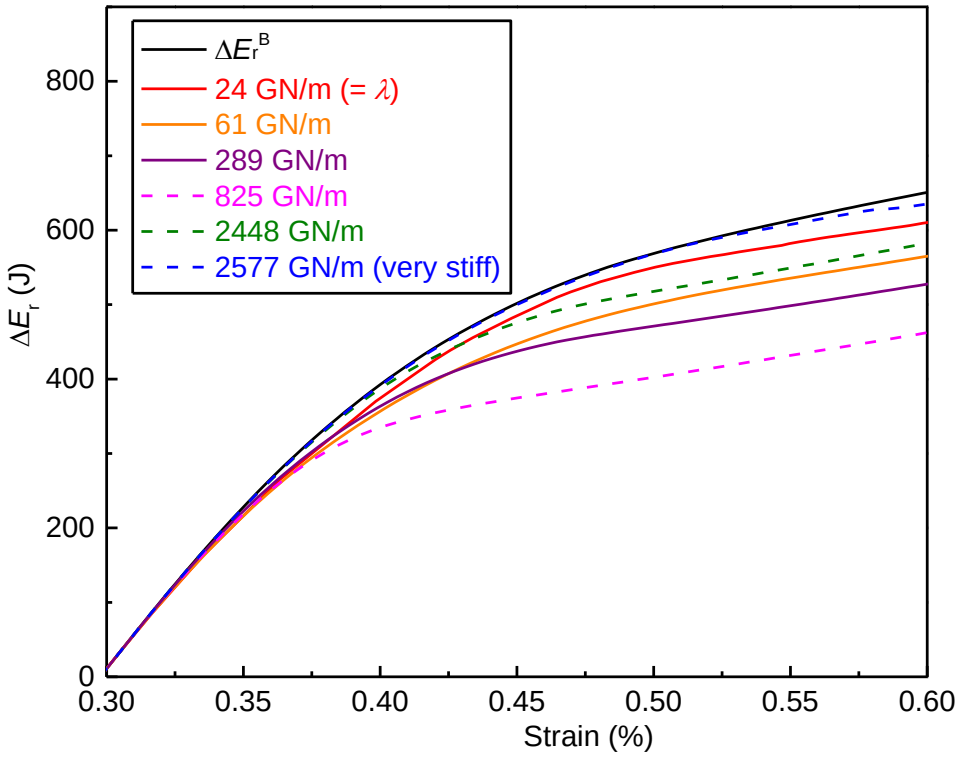

Figure 5-15 Variation of ΔE_r and ΔE_r^B ($LSS = \infty$) with strain under the platen loading condition for $LSS \geq \lambda$.

Figure 5-16 compares the variation of ΔE_t and ΔE_r^B values with strains starting at the peak load in the rock under the platen loading condition for $LSS \geq \lambda$. ΔE_t is obtained by subtracting the strain energy stored in the test machine at the peak load (E_t) by that in the post-peak deformation stage (E_t^*).

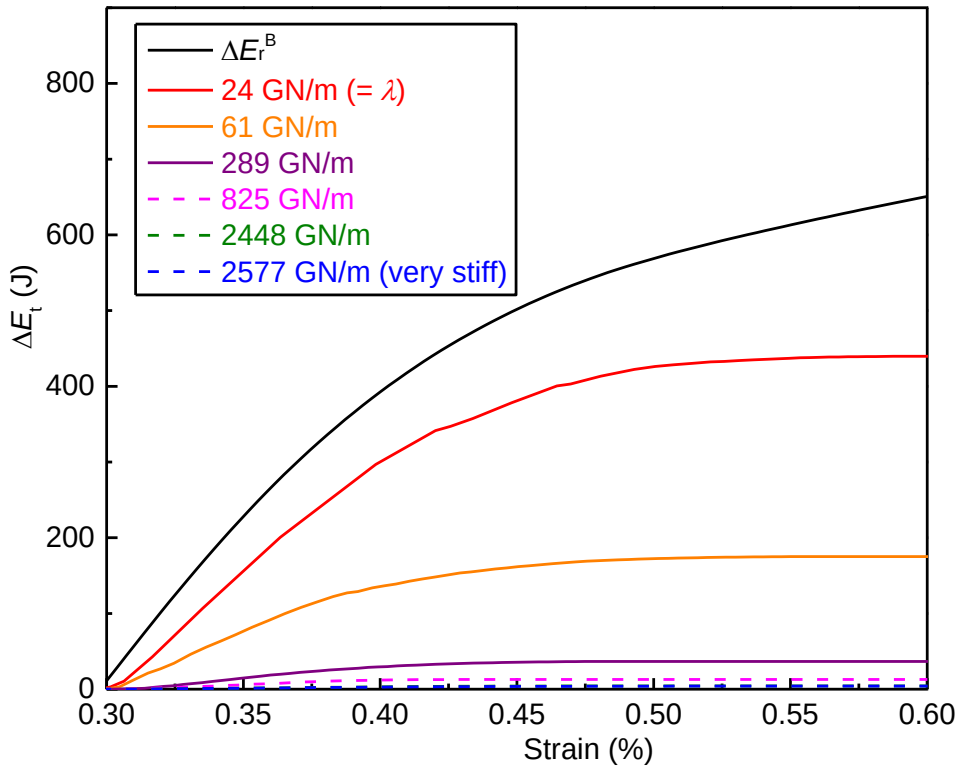

Figure 5-16 Variation of ΔE_t and ΔE_r^B ($LSS = \infty$) with strain under the platen loading condition for $LSS \geq \lambda$.

ΔE_t decreases with the increase of *LSS*, because the stiffer a test machine is, the lower the test machine's capacity of storing and releasing energy is. In particular, ΔE_t is the highest when *LSS* = λ = 24 GN/m (within the range of $LSS \geq \lambda$). In this case, the test machine can provide the energy needed to ensure that the obtained post-peak stress–strain is close to that of the base case. Note that for the case of critical *LSS* loading condition, $\Delta E_t < \Delta E_r^B$, which is different from the illustration shown in Figure 5-14, where $\Delta E_t = \Delta E_r^B$. This is because that the post-peak load–deformation curve of the rock shown in Figure 5-14 has been idealized as a straight line, which is rarely the case for rock. In the numerical modeling, the post-peak load–deformation (or stress–strain) curve is nonlinear. λ is the stiffness at the point where the descending load–deformation curve is the steepest (refer to Section 2.3.3). Therefore, the ΔE_t value under the critical *LSS*

loading condition is lower than ΔE_r^B, and additional input energy ΔE_{in} is needed to drive rock failure (to increase ΔE_r).

Figure 5-17 compares the variation of ΔE_{in} and ΔE_r^B values with strain starting at the peak load in the rock under the platen loading condition for $LSS \geq \lambda$. ΔE_{in} is obtained by subtracting the accumulative external energy input to the rock specimen-test machine system at the post-peak deformation stage (E_{in}^*) by that at the peak load (E_{in}).

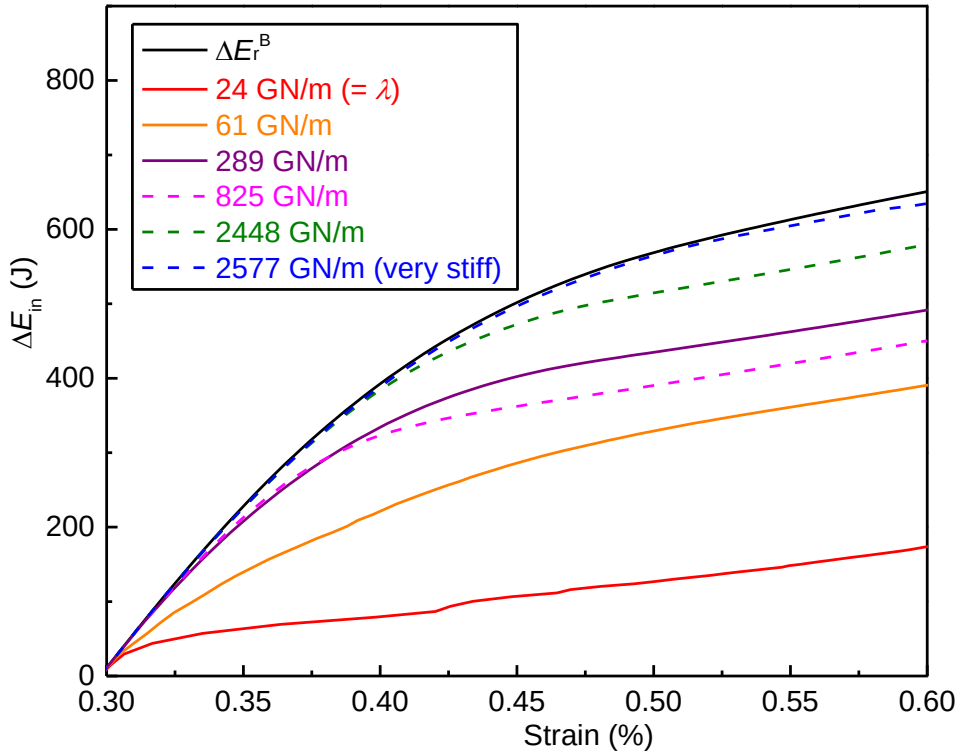

Figure 5-17 Variation of ΔE_{in} and ΔE_r^B ($LSS = \infty$) with strain under the platen loading condition for $LSS \geq \lambda$.

ΔE_{in} increases with the increase of *LSS*, except for the cases for *LSS* = 289 and 825 GN/m. If *LSS* is very stiff, ΔE_{in} matches ΔE_r^B well because ΔE_t is very small. It is inferred that the ΔE_{in} input to the rock for driving rock failure from an external energy source is somewhat influenced by the test machine so that ΔE_r is always lower than ΔE_r^B. Only if the test machine is perfectly stiff, i.e.,

the test machine is a rigid body, the influence of the test machine on the rock to absorb the right amount of energy $\Delta E_{in} = \Delta E_r^B$ can be eliminated and the post-peak stress–strain curve in this case is the same as that in the base case. This has been demonstrated by using the rigid loading model (refer to Figure 5-3) to obtain the post-peak stress–strain curve (Figure 5-9).

Modeling results presented from Figure 5-15 to Figure 5-17 are summarized in Figure 5-18.

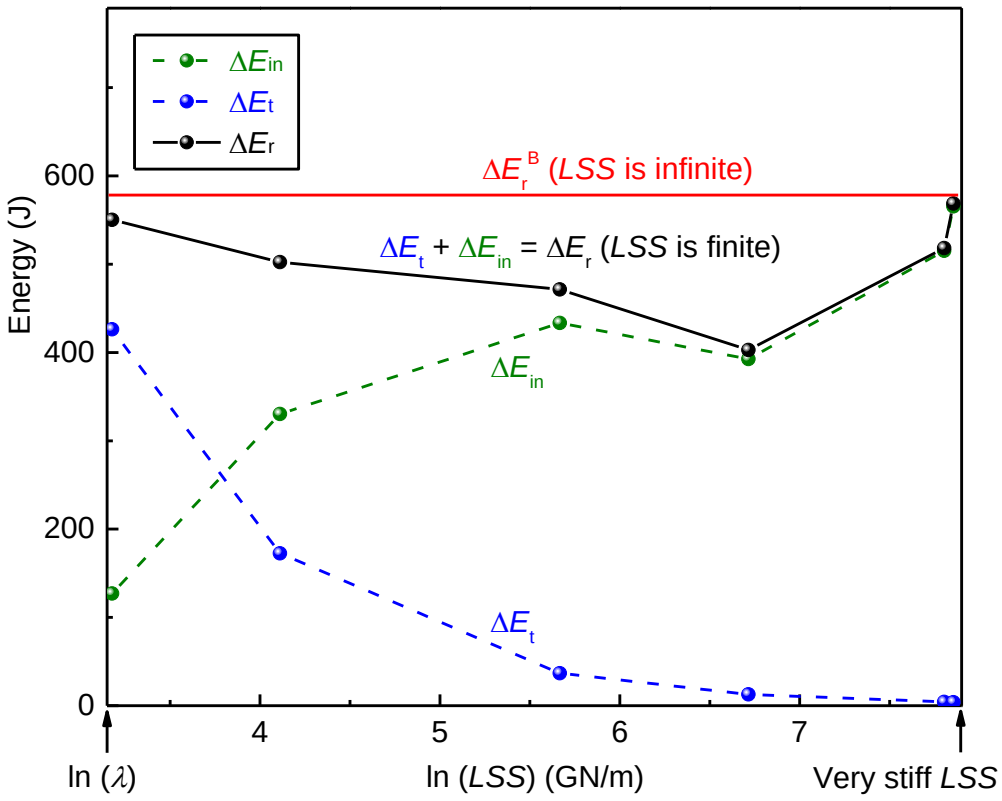

Figure 5-18 Evolution of energy in the rock with the increase of *LSS* in the post-peak deformation stage (ε = 0.5% as an illustration; trend is the same for other strain levels).

It is understood that when *LSS* is increased, ΔE_t decreases and ΔE_{in} increases simultaneously at different rates and their summation is not a constant. Hence, as *LSS* increases the slopes of the post-peak stress–strain curves first become steeper than that of base case obtained under the ideal loading condition, then become less steep, and finally approach that of base case.

5.2.3 Frame-platen loading results

The influence of *LSS* on stable failure of rock under the frame-platen loading condition (refer to Figure 5-5) is investigated and the results are presented in this section. The *LSRI* values shown in Table 5-5 confirm that for a *LSS* value the same as that under the platen loading condition, rock failure is stable under the frame-platen loading condition.

Table 5-5 Relation between *LSRI* and *LSS* under the frame-platen loading condition

LSS (GN/m)	2577	2448	825	289	61	24	19
LSRI	1.0	1.0	1.0	1.1	1.5	3.4	**5.8**

Figure 5-19 compares the stress–strain curves under the frame-platen loading condition with different *LSS* values ranging from 19 GN/m to 2577 GN/m with that under the ideal loading condition. As *LSS* increases, the slope of the post-peak stress–strain curves of the rock increases gradually and then reaches the steepest at *LSS* = 289 GN/m. With further increase of *LSS*, the slopes of the post-peak stress–strain curves decrease and eventually approach that of the base case's post-peak stress–strain curve as *LSS* becomes very stiff (2577 GN/m).

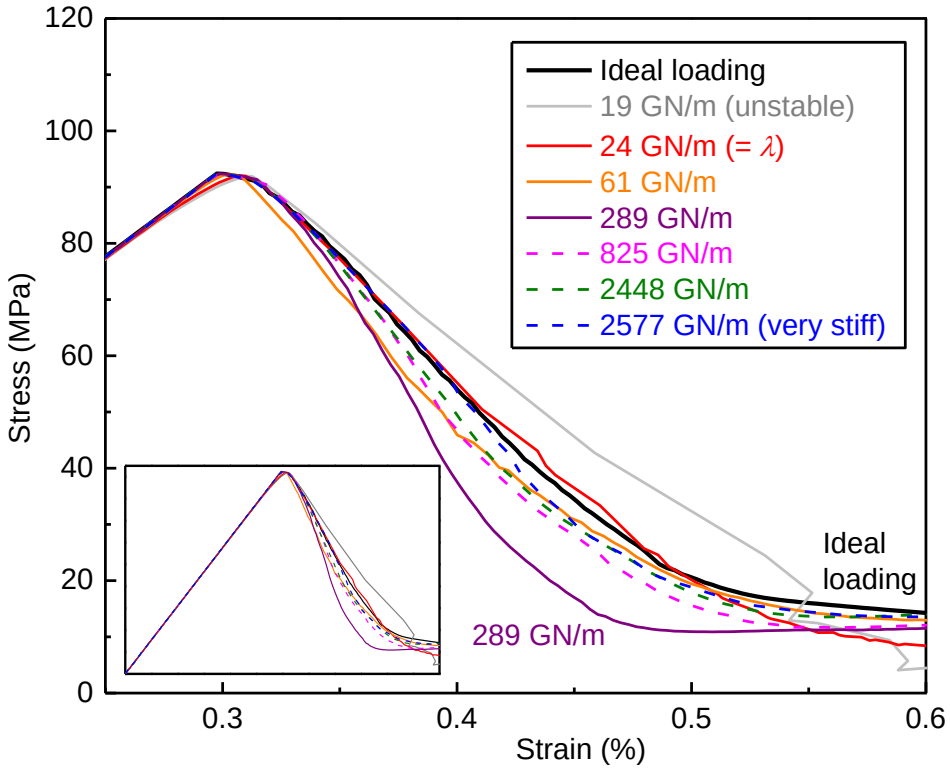

Figure 5-19 Stress–strain curves of the rock under the ideal loading condition and the frame-platen loading condition with different *LSS* values; the complete stress–strain curves are shown in the insert.

Figure 5-20 compares the stress–strain curves of the rock under the frame-platen and platen loading conditions with different *LSS* values. It is seen that unless *LSS* is very stiff or equal to λ, which are the special *LSS* loading conditions that lead the obtained post-peak deformation behaviors of the rock close to that of the base case, the post-peak stress–strain curves of the rock under the two loading conditions are different even though their *LSS* values are the same. It seems that the platen loading condition leads to a steeper descending slope of the stress–strain curves than that under the frame-platen loading condition (e.g., *LSS* = 825 GN/m).

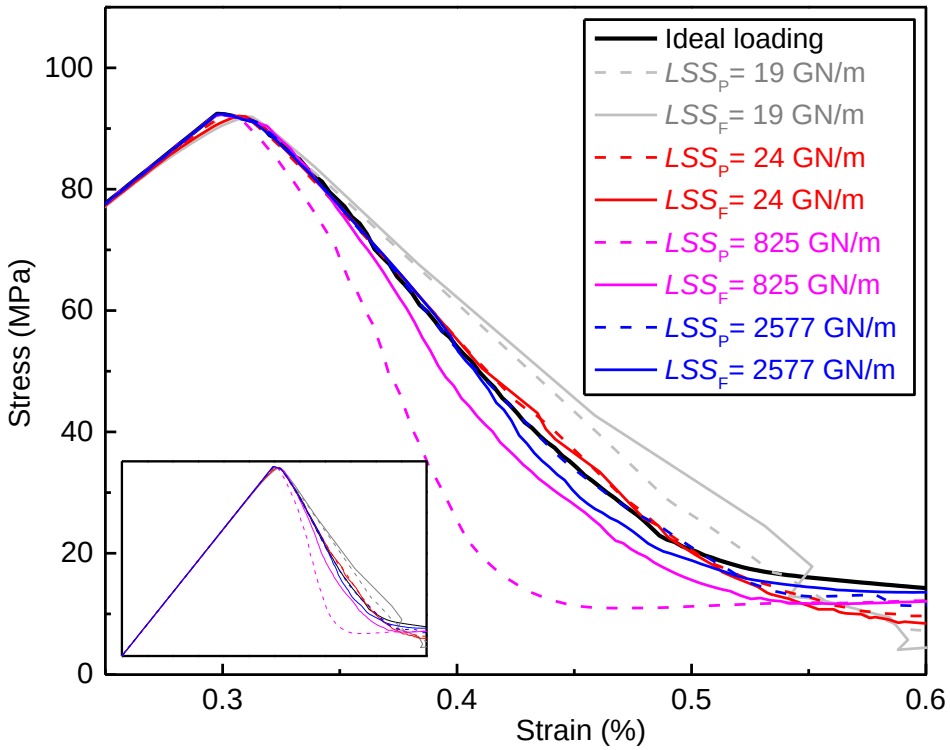

Figure 5-20 Comparison of stress–strain curves of the rock under the platen (subscripts "P") and frame-platen (subscripts "F") loading conditions with different *LSS*; the complete stress–strain curves are shown in the insert.

Figure 5-21 presents σ_1 distributions of the two test machines (loading conditions) in the post-peak deformation stage, at an axial strain of ε = 0.4%. It is seen that tensile stresses (white contoured areas) dominate in the frame-platen loading test machine because the loading frame is in tension to balance the load applied to the specimen; however, compressive stresses dominate in the platen loading test machine.

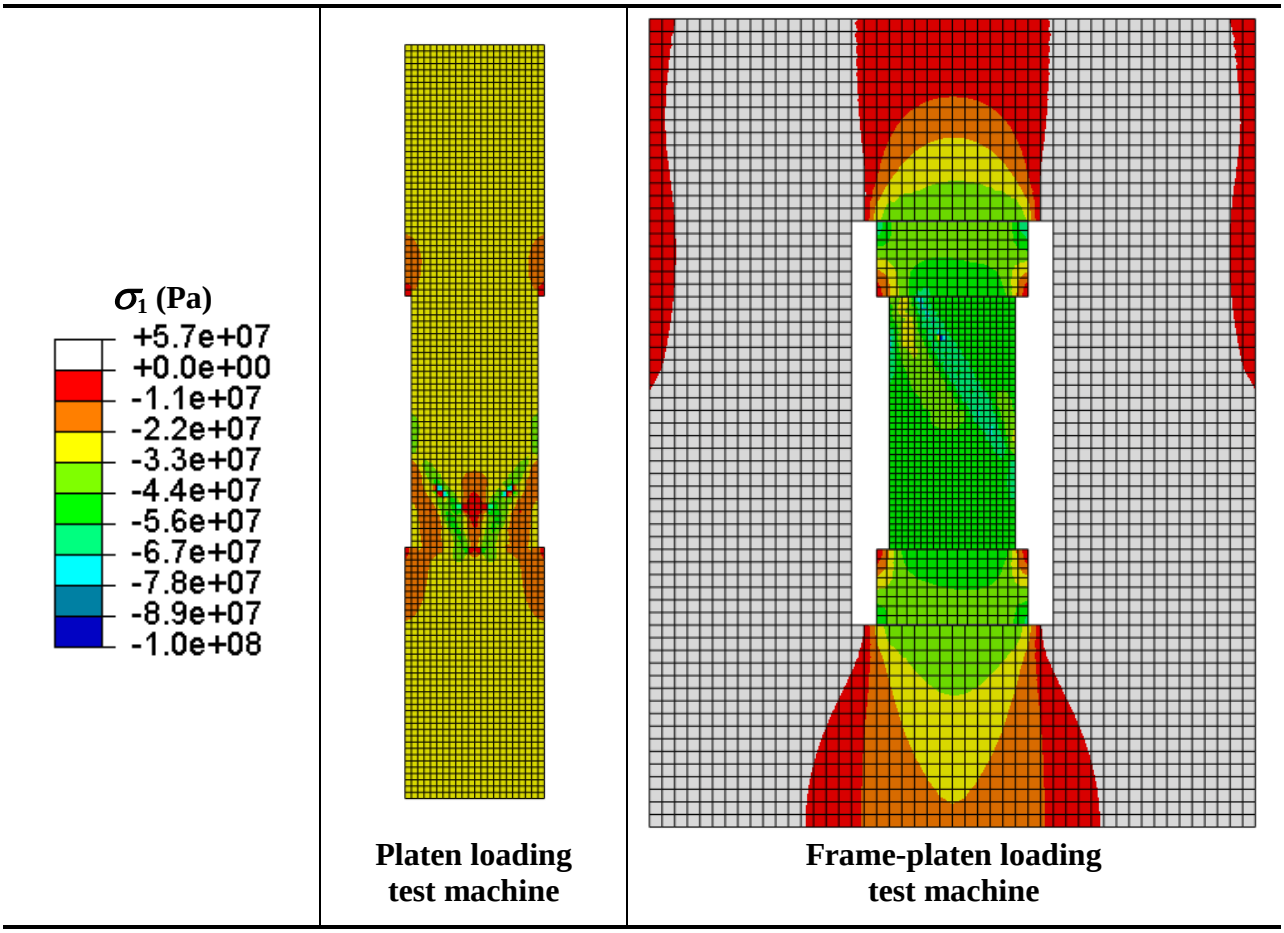

Figure 5-21 σ_1 distributions of the two test machines (for *LSS* = 825 GN/m) in the post-peak deformation stage (ε = 0.4%).

It is reckoned that these two test machines with different loading conditions can affect additional input energy ΔE_{in} provided to drive the rock failure process and hence the post-peak stress–strain curves of the rock. ΔE_{in} in the two test machines are plotted in Figure 5-22 as a function of strain. The ΔE_{in} in the frame-platen loading test machine is indeed different from that in the platen loading test machine. As a result, the ΔE_r values between the frame-platen loading and platen loading test machines are different and this is reflected in the difference in the post-peak stress–strain curves of the rock (Figure 5-20). This indicates that the post-peak stress–strain curves of a

rock obtained from a laboratory test is affected not only by *LSS* but also by the method of loading.

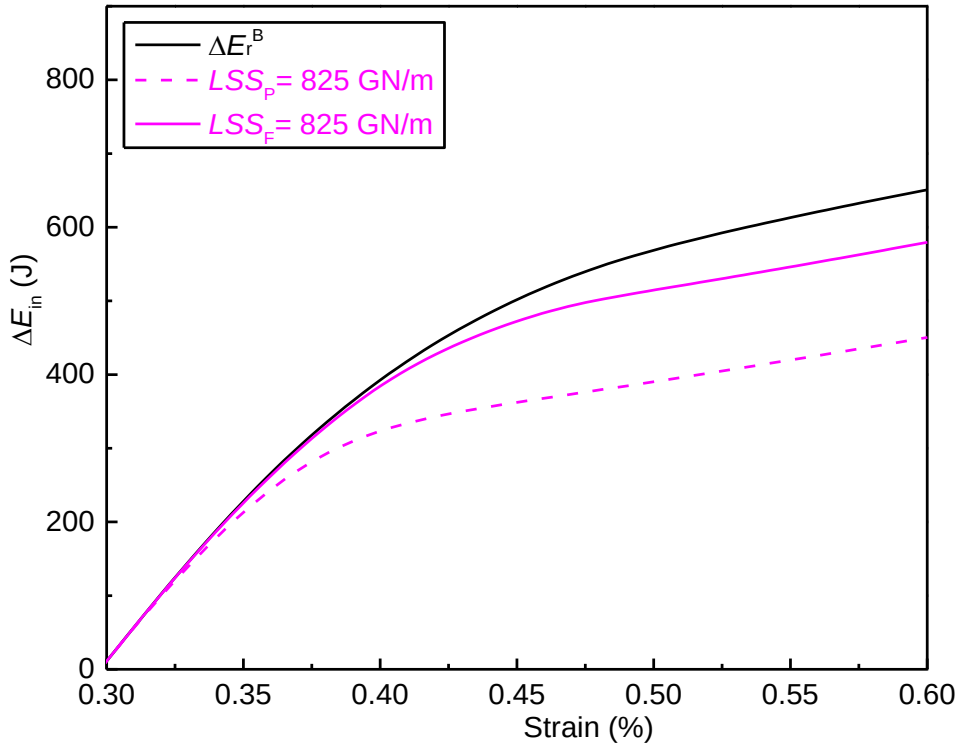

Figure 5-22 Variation of ΔE_{in} and ΔE_r^B ($LSS = \infty$) with strain in the rock by the two test machines in the post-peak deformation stage for LSS = 825 GN/m.

5.2.4 Heuristic study on the influence of LSS on the failure types of different cross-sectional-shaped specimens

In this section, an attempt of applying the study results of cross-sectional shape effect (Chapter 3), combined with the insights gained from the study of *LSS* (Sections 5.1 to 5.2.3) to improve pillar design, is illustrated by a simplified numerical experiment. It is known that in underground mines, if the Local Mine Stiffness (LMS) of a pillar is softer than the post-peak stiffness of the pillar, pillar-burst will be encountered (Salamon, 1970). The influence of LMS on the failure types of pillars can be simplified and modeled by applying uniaxial compression loading to a rock specimen. In such a case, LMS is conceptually manifested by *LSS*.

This study aims at evaluating the instability of different cross-sectional-shaped specimens with the same slenderness ratio under a relatively soft *LSS* loading condition. Hence, three different cross-sectional-shaped specimens with a slenderness ratio of 2.0, the same as those used in Chapter 3 (Figure 3-6), are adopted in the simulation models (Figure 5-23). In addition, steel properties (E = 200 GPa, ν = 0.3) are assigned to the loading platens and μ = 0.1 is assumed for the rock specimen-steel platen contacts (Figure 5-23); thus, the contact frictional behavior in this numerical experiment is the same as that in the study of cross-sectional shape in Chapter 3.

The rock failure types in Chapter 3 are stable because the *LSS* of the steel platen loading condition in those cases is much stiffer than the critical *LSS* loading condition of the rock specimens (λ). In this study, *LSS* is prescribed to a relatively soft *LSS*; thus, unstable rock failures might occur. In this fashion, the instability of different shaped rock specimens under the critical *LSS* loading condition can be examined by comparing their post-peak stress–strain curves with those under the stiff *LSS* loading condition (Figure 3-8).

The post-peak deformation behavior of the cylindrical specimen shown in Figure 3-8 is referred to choose the prescribed value for *LSS*. The post-peak stiffness of the cylindrical specimen determined from the stress–strain curve (E_p) is roughly 62 GPa (λ = 1.217 GN/m). The calculation of E_p based on the stress–strain curve might be subjective because the post-peak stress–strain curve of rocks can never be a perfectly straight line (refer to the discussion on E_p in Section 5.2.2). Therefore, to observe at least one unstable rock failure case under the critical *LSS* loading condition for the cylindrical specimen (Equation 2-6), a relatively smaller value of 60 GPa is assumed for the actual E_p of the cylindrical specimen. In such a case, the prescribed *LSS* is equal to 1.178 GN/m (Table 5-6). Because the loading platens in different simulation models

have different cross-sectional shapes, the height of different loading platens is varied to ensure that their *LSS* is equal to 1.178 GN/m (Table 5-6).

Figure 5-23 Simulation model of a rock specimen under a relatively soft *LSS* loading condition (cylindrical specimen as an illustration).

Table 5-6 Calculation of the post-peak stiffness of the rock specimen (λ) and the *LSS* of loading platens

	E_p or E (GPa)	Diameter or side length (m)	Cross-sectional area (m^2)	Total height (m)	λ or *LSS* (GN/m)
Rock specimen	62	0.050	0.0020	0.10	1.217
Cylindrical platen	200	0.052	0.0021	0.18×2	1.178
Square platen	200	0.052×0.052	0.0027	0.23×2	1.178
Rectangular platen	200	0.036×0.072	0.0026	0.22×2	1.178

Figure 5-24 presents the complete stress–strain curves of different cross-sectional-shaped specimens under the stiff and prescribed *LSS* loading conditions in uniaxial compression.

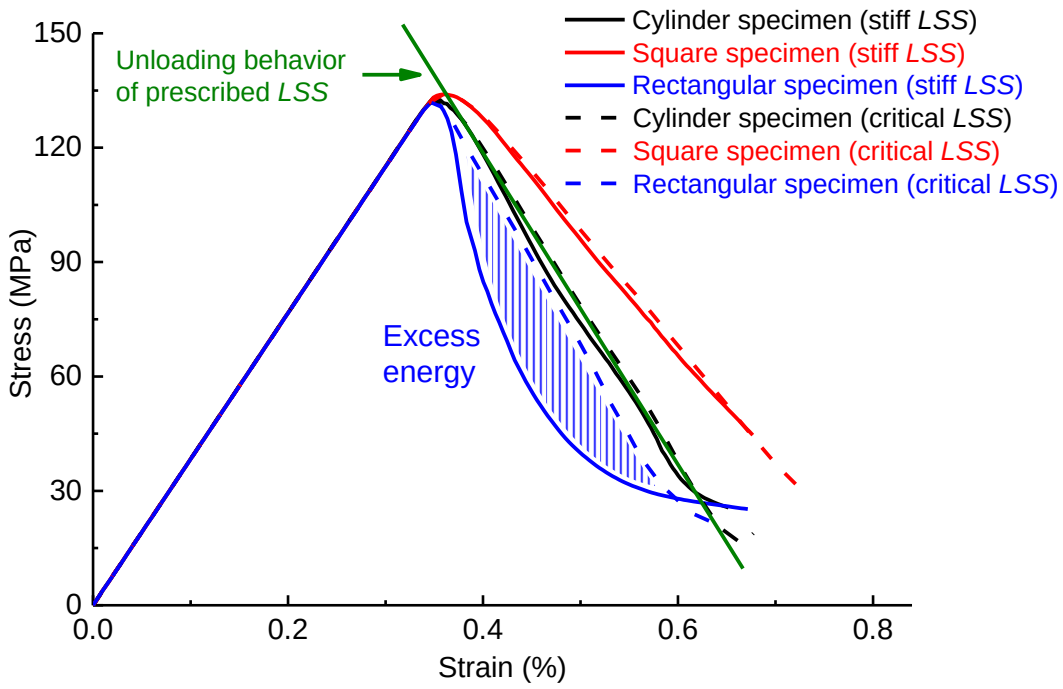

Figure 5-24 Complete stress–strain curves of different cross-sectional-shaped specimens under stiff (solid curves) and prescribed (dash curves) *LSS* loading conditions.

Similar to the modeling results shown in Figure 3-8, the post-peak stress–strain curves of the specimens under the prescribed *LSS* loading condition are influenced by their cross-sectional shapes. Moreover, the post-peak stress–strain curves under the prescribed *LSS* loading condition

are all flatter than those under the stiff *LSS* loading condition with the same cross-sectional shape. In particular, compared with other shaped specimens, the rectangular prismatic specimen shows a much flatter post-peak stress–strain curve under the prescribed *LSS* loading condition than that under the stiff *LSS* loading condition. The large difference of post-peak stress–strain curves indicate excess energy stored in the loading platens under the prescribed *LSS* loading condition might be released to the rectangular prismatic specimen, thus the rock failure type in this case can be unstable (Section 5.2.2).

Table 5-7 compares the *LSRI* of different cross-sectional-shaped specimens under the prescribed *LSS* loading condition together with their peak strengths. The peak strengths of different shaped specimens are very close. The calculated *LSRI* values confirm that the failure types of the square and cylindrical shaped specimens under the prescribed *LSS* loading condition are semi-stable (Manouchehrian and Cai, 2015). Under the same prescribed *LSS*, compared with the square and cylinder specimens, the failure type is more violent for a rectangular prismatic specimen with the same slenderness ratio. Hence, it is inferred that for the same cross-section area and slenderness ratio, rectangular-shaped rock specimens are vulnerable to rock instability.

Table 5-7 *LSRI* values and peak strengths of different cross-sectional-shaped specimens under the prescribed *LSS* loading condition

	Cylindrical specimen	Square prismatic specimen	Rectangular prismatic specimen
LSRI	4.1	3.0	**17.6**
Peak strength (MPa)	133	134	132

5.3 Summary

Great efforts had been made by other researchers to develop stiff laboratory test machines to capture post-peak stress–strain curves of rock for rock engineering design; however, the influence of the *LSS* of a stiff test machine on the post-peak deformation behavior of rock is poorly understood. This is in part due to the difficulty in varying *LSS* to conduct laboratory tests using rock specimens with nearly identical mechanical properties. Numerical experiments provide a solution to address this problem.

This numerical experiment focuses on studying the post-peak stress–strain curves of stable rock failure under the test condition of different *LSS* values. Based on the modeling results, Figure 5-25 illustrates conceptually that for stable rock failure to occur under a finite *LSS* (e.g., rock laboratory testing using a stiff test machine), both ΔE_t and ΔE_{in} contribute to ΔE_r, and ΔE_r is always smaller than ΔE_r^B. Furthermore, the modeling results suggest that ΔE_{in} is affected by the test machine with a finite *LSS* ($> \lambda$). Consequently, the descending slope of the post-peak stress–strain curve of a rock under a finite *LSS* loading condition is always steeper than that under the ideal loading condition ($LSS = \infty$). Furthermore, ΔE_{in} and ΔE_r are varied with *LSS*, and it is therefore concluded that the post-peak stress–strain curves of stable rock failure is influenced by *LSS*.

This conclusion drawn by the numerical modeling is partially supported by the incomplete laboratory test results on nearly identical material specimens, which showed that different stress–strain curves of concrete (Hudson et al., 1972b based on Whitney, 1943) and ice (Sinha and Frederking, 1979) were obtained by different test machines. Most importantly, the modeling

results confirmed the laboratory test results of Bieniawski et al. (1969), revealing that the descending slopes for the post-peak stress–strain curves of rocks were dependent on *LSS*.

In this study, the influence of *LSS* on the stable post-peak failure of rock was investigated. Future study will consider the influence of *LSS* on different rock failure types, especially the unstable post-peak failure, which is strongly related to the strain energy stored in the test machine in laboratory testing. A heuristic study is presented in Appendix A.

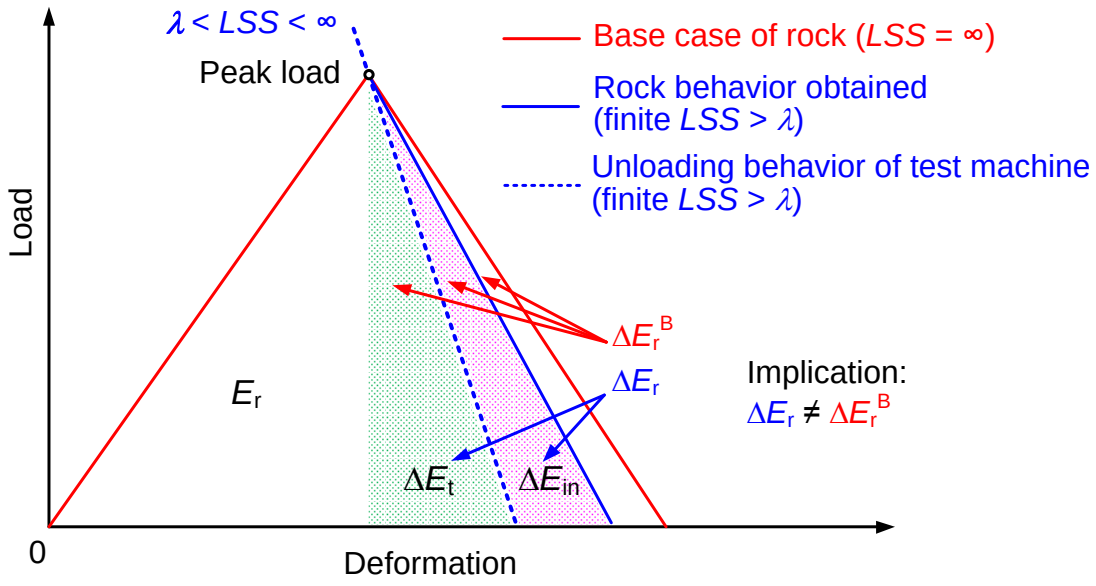

Figure 5-25 Comparison of the load–deformation curve of the base case (*LSS* = ∞) with that under a finite *LSS* > *λ*.

Chapter 6

6 Conclusions, implications, and future work

The numerical experiments on the studies of the influence of specimen geometry, contact condition, and *LSS* on rock strength and deformation behaviors confirmed that the interpretation of the post-peak deformation behavior of rock is "a rupture locus that is characteristic of the specimen shape, material, and loading system" (cited in Hudson, 1993). Most importantly, this dissertation made a contribution to identify how the post-peak deformation behavior of a rock specimen is affected by its cross-sectional shape, the end effect, and the *LSS* in laboratory tests. Implications and future work inspired by this dissertation can pave the way to make the best use of laboratory testing for obtaining more meaningful test results and to interpret test results properly.

6.1 Conclusions and Discussions

6.1.1 Conclusions

This dissertation first examined the influence of the cross-sectional shape of a rock specimen on its strength and post-peak deformation behavior in uniaxial compression tests. Cylindrical, square, and rectangular shaped specimens with various slenderness ratios were studied. The research found that the cross-sectional shape has a very small influence on the UCS of rock, but it has a large impact on the post-peak deformation behavior. The modeling results, which are supported by laboratory test results, revealed that the UCS of a square prismatic specimen is actually higher than that of a cylindrical specimen for the same slenderness ratio. The UCS of a cylindrical specimen is not significantly higher than that of a rectangular prismatic specimen, implying that hoop tension contributes little to affecting rock strength. The measurable strength

difference between the cylindrical and square shaped specimens, observed both in the laboratory test and the modeling results, is attributed to the relatively large cross-sectional areas of the square prismatic specimens used. If the slenderness ratio of a square prismatic specimen is calculated by dividing its height by an equivalent diameter showing the same cross-sectional area as a cylindrical specimen, then the square prismatic specimen will have the same UCS as that of the cylindrical specimen.

With regard to the post-peak deformation behavior, the numerical modeling results reveal that it is the relation between the distribution of confined and tensile zones during the post-peak deformation process that actually contributes to the cross-sectional shape effect. For specimens with the same slenderness ratio, the square prismatic specimen shows the flattest post-peak descending slope of the stress–strain curve. The rectangular prismatic specimen has the steepest descending slope of the stress–strain curve and that of the cylindrical specimen is between the two.

Laboratory test results show that the use of anti-friction measures cannot eliminate the end effect completely, especially when the rock specimen is squat in the loading direction. The influence of end effect on rock strength in true triaxial compression test was studied using the numerical approach. The influence of σ_2 on rock strength was purposely excluded from the material model, so that any increase of rock strength with the increase of σ_2 while the applied σ_3 was kept constant, can be attributed to the end effect. The modeling results demonstrated that end constraint at the rock specimen-steel platen contacts has a large influence on rock strength, because the actual σ_3 in the specimen is increased due to the end constraint at the σ_2 loading

contacts. Thus, the end effect can result in an apparent σ_2 effect that contributes to the observed strength increase due to σ_2 in true triaxial compression test.

The conclusions drawn from this study can explain why some rocks show a significant σ_2 effect while others do not. Different end constraints can be initiated by different rock deformation behaviors. For non-dilatant rocks that exhibit little lateral expansion under compression (e.g., those two Long Valley Caldera rocks), there are very small relative deformations at the rock specimen-steel platen contacts. Thus, the end effect is small and so is the σ_2 effect. This study also made a contribution to better understanding true triaxial compression test results by decomposing the observed σ_2 effect on rock strength in laboratory tests into two parts: one from the end effect and the other from the actual σ_2 effect. The actual σ_2 effect was explained using the theory of Wiebols and Cook (1968). When the theoretical results of σ_2 effect was added to the apparent σ_2 effect caused by the end effect, the results were in good agreement with the observed σ_2 effect from some previous laboratory tests, indicating that the observed σ_2 effect in some true triaxial compression tests can be partially influenced by the end effect.

In the numerical experiment, the post-peak stress–strain curves of rock specimens with the same material property under uniaxial compression were examined using test machines with different *LSS* values. The modeling results indicate that the post-peak stress–strain curve of stable rock failures depends on *LSS*. The slopes of the post-peak stress–strain curves with finite *LSS* are all steeper than that with $LSS = \infty$. In other words, the post-peak deformation behaviors of rocks obtained from test machines with finite *LSS* are more brittle than the one obtained by an extremely stiff test machine. This difference is attributed to the energy provided by the external energy source in both the platen loading and frame-platen loading conditions to drive the rock

failure process in the post-peak deformation stage. For a test machine with *LSS* = ∞, the energy release from the test machine is zero and the obtained post-peak stress–strain curve is very close to that obtained under the ideal loading condition. When *LSS* is finite, the amount of energy released from the test machine, combined with that supplied from the external energy source, determines the post-peak stress–strain curve of the rock. In this case, both these two energy items are influenced by *LSS*.

6.1.2 Discussions

Insight gained from the study of the cross-sectional shape effect can assist in interpreting laboratory test results more objectively. One suggestion is to use the equivalent diameter of a non-circular cross-section to define the slenderness ratio of a specimen. In this fashion, consistent presentation of the test results can be achieved. For the same cross-sectional area and slenderness ratio, a rectangular cross-sectional-shaped specimen under a prescribed *LSS* loading condition in uniaxial compression might be more vulnerable to rock instability than the other cross-sectional-shaped specimens.

Considering that the end effect can result in an apparent σ_2 effect that may mislead the interpretation of true triaxial compression test results, some suggestions are made for future study of the σ_2 effect. Firstly, previous laboratory test results are still useful in developing 3D empirical failure criteria for rock. A correction can be made by employing a reverse strategy to subtract the apparent σ_2 effect from the observed σ_2 effect, provided that the actual end effect in the true triaxial compression test results can be quantified. This approach can be referred to the heuristic study illustrated in Section 4.4.5. Otherwise, one can refer to the test results obtained at high σ_3, where the apparent σ_2 effect caused by the end effect is relatively small. Moreover,

when true triaxial compression tests are conducted to study the σ_2 effect, attention should be paid to minimizing the end effect. The follow-up laboratory work shows that using a novel test machine and effective anti-friction measures, the end effect can be decreased and the apparent σ_2 effect could be minimized. As a result, the characteristics of the obtained σ_2 effect are very close to the σ_2 effect predicted by the theoretical failure criterion.

One important insight gained from the numerical experiment on the influence of *LSS* on rock behavior is that perhaps there is no need to develop extremely stiff test machines for rock property testing. The modeling results suggest that even if a test machine is stiff enough to ensure stable rock failure, as long as its *LSS* is neither extremely rigid nor equal to the post-peak stiffness of the rock, the obtained post-peak stress–strain curve is always *LSS*-dependent and different from that of the base case. However, obtaining an unbiased post-peak stress–strain curve of rock that can characterize the intrinsic mechanical behavior of rock was the motivation for developing stiff test machines in the 1960s in the first place (Section 2.3.1).

On the other hand, test machines that can vary *LSS* are useful. The study on the influence of *LSS* on the post-peak deformation behavior of rock makes a contribution to suggest an alternative approach to develop test machines with potentially lower manufacturing cost and can obtain more meaningful test results. The post-peak stress–strain curve of rock is important in underground rock engineering design, but it is neither necessary nor practical to obtain such a curve for the rock under the ideal loading condition because the ideal loading condition does not exist in an underground rock engineering setting. Alternatively, it might be useful to investigate the stiffness at local strata in a mine (Local Mine Stiffness – LMS) and to study its influence on the post-peak deformation behavior of rock or pillars. LMS is an important subject in

underground rock engineering. Once the LMS surrounding a rock of interests (e.g. a pillar) is quantified, test machines with variable *LSS* values that can accommodate the accepted range of measured LMS can be used for rock property testing. The test machine developed by Bieniawski et al. (1969) can vary its *LSS*. Manufacturing and control techniques have advanced since then and it is now possible to develop a test machine that can vary its *LSS* in a more controllable manner. In this way, the post-peak deformation behavior of rock obtained by such a test machine with *LSS* matching the LMS would be more meaningful for the rock engineering design.

6.2 Future work

The numerical modeling suggests that under the same loading condition in underground mines, a rectangular cross-sectional-shaped pillar might be exposed to a higher risk of violent pillar failures than other cross-sectional-shaped pillars of the same cross-sectional area and slenderness ratio, because the rectangular prismatic specimen shows the most brittle post-peak failure curve. In an underground mining setting, LMS is a key loading condition that determines the likelihood of violent pillar failures (Salamon, 1970). Future study should simulate the failure types of different cross-sectional-shaped pillars of the same cross-sectional area under the same LMS. Although preliminary, Section 5.2.4 illustrates how this type of study could benefit designing stable pillars.

Using heterogeneous models, researchers have found that σ_2 has a small influence on rock strength when $\sigma_3 = 0$ and σ_2 is not high (Cai, 2008b). The conclusions drawn from the numerical experiment regarding the σ_2 effect in this dissertation are based on the modeling results using a homogeneous model. Thus, in future work, it needs to consider the heterogeneity of rock properties to quantify the end effect on rock strength in true triaxial compression test. According

to the follow-up laboratory test results and supported by the numerical and theoretical results, previous test results that showed a significant σ_2 effect at low σ_3 might include a large end effect. Hence, future work should focus on quantifying the actual σ_2 effect under low σ_3 because it is important for rock engineering practices.

The modeling results show that the trend of the post-peak stress–strain curves of the rock obtained by the frame-platen loading test machine is consistent with those obtained by the platen loading test machine. However, the post-peak stress–strain curves obtained by the frame-platen loading test machine are different from those by the platen loading test machine, even though the *LSS* values are the same under both loading test machines. This discrepancy indicates that the method of loading can supply different amounts of energy to the rock in the post-peak deformation stage. Hence, the post-peak stress–strain curves of a rock obtained from a laboratory test can be affected not only by *LSS* but also by the loading method. Future study will consider the influence of a frame-platen loading test machine on unstable rock failure, a process that is strongly related to the energy stored in the test machine. A heuristic study presented in Appendix A investigates how the energy stored in the frame-platen loading test machine can affect the rock failure types. In addition, LMS is important for determining whether pillar-burst will occur or not. Hence, future study should investigate pillar stability under different LMS.

Most importantly, this thesis emphasizes that the intrinsic material property of a rock is so obscured by the complexity of the test conditions that can be practically applied. Thus, it is considered that adopting the numerical experiment approach in tandem with back analysis of test results is the best or, probably the only way to establish intrinsic rock property. Hence, it is

worthwhile to make an effort to develop a standard approach to establish the intrinsic rock property for application in rock engineering design.

References

Al-Ajmi AM, Zimmerman RW. Relation between the Mogi and the Coulomb failure criteria. *International Journal of Rock Mechanics and Mining Sciences*. 2005; 42: 431-9.

Al-Chalabi M, Huang C. Stress distribution within circular cylinders in compression. *International Journal of Rock Mechanics and Mining Sciences & Geomechanics Abstracts*. 1974; 11: 45-56.

Alejano L, Alonso E. Considerations of the dilatancy angle in rocks and rock masses. *International Journal of Rock Mechanics and Mining Sciences*. 2005; 42: 481-507.

Alonso E, Alejano L, Varas F, Fdez-Manin G, Carranza-Torres C. Ground response curves for rock masses exhibiting strain-softening behaviour. *International Journal for Numerical and Analytical Methods in Geomechanics*. 2003; 27: 1153-85.

Amadei B, Stephansson O. Rock stress and its measurement: Springer Science & Business Media. 1997.

Babcock CO. Changes in breaking strength of model rock pillars resulting from end constraint: US Dept. of the Interior, Bureau of Mines. 1968.

Babcock CO. Effect of increasing end constraint on the compressive strength of model rock pillars. US Dept. of the Interior, Bureau of Mines; 1969.

Barla G, Barla M, Camusso M, Martinotti M. Setting up a new direct shear testing apparatus. In: Sousa LR, Olalla C, NF G, editors. Proceedings of the 11th Congress of the International Society for Rock Mechanics. Lisbon, Portugal: Taylor & Francis. 2007. p. 415-8.

Baumgart F. Stiffness – an unknown world of mechanical science? *Injury-International Journal for the Care of the Injured*. 2000; 31: 14-23.

Bazant ZP. Size effect in blunt fracture: concrete, rock, metal. *Journal of Engineering Mechanics*. 1984; 110: 518-35.

Bazant ZP, Belytschko TB, Chang T. Continuum theory for strain-softening. *Journal of Engineering Mechanics*. 1984; 110: 1666-92.

Bazant ZP, Planas J. Fracture and size effect in concrete and other quasibrittle materials: CRC press. 1997.

Beck D. Applications of Hydro-Mechanically Coupled 3D Mine and Reservoire Scale, Discontinuous, Strain-Softening Dilatant Models with Damage. 49th US Rock Mechanics/Geomechanics Symposium: American Rock Mechanics Association. 2015.

Beskos DE. Boundary element methods in dynamic analysis. *Applied Mechanics Reviews*. 1987; 40: 1-23.

Bewick RP, Amann F, Kaiser P, Martin C. Interpretation of UCS test results for engineering design. 13th ISRM International Congress of Rock Mechanics: International Society for Rock Mechanics. 2015.

Bhat H, Sammis C, Rosakis A. The micromechanics of westerley granite at large compressive loads. *Pure and Applied Geophysics*. 2011; 168: 2181-98.

Bieniawski ZT. Mechanism of rock fracture in compression. South African Council for Scientific and Industrial Research: Mechanics Engineering Institution; 1966. p. 77.

Bieniawski ZT. Mechanism of brittle fracture of rock: part II—experimental studies. *International Journal of Rock Mechanics and Mining Sciences & Geomechanics Abstracts*. 1967a; 4: 407-23.

Bieniawski ZT. Mechanism of brittle fracture of rock: part I—theory of the fracture process. *International Journal of Rock Mechanics and Mining Sciences & Geomechanics Abstracts*. 1967b; 4: 395-406.

Bieniawski ZT. In situ strength and deformation characteristics of coal. *Engineering Geology*. 1968; 2: 325-40.

Bieniawski ZT, Denkhaus HG, Vogler UW. Failure of fractured rock. *International Journal of Rock Mechanics and Mining Sciences & Geomechanics Abstracts*. 1969; 6: 323-41.

Bieniawski ZT. Time-dependent behaviour of fractured rock. *Rock Mechanics*. 1970; 2: 123-37.

Bieniawski ZT. Rock mass classification in rock engineering. In: Bieniawski ZT, editor. proceedings of the Symposium on Exploration for Rock Engineering. Johannesburg: Balkema. 1976. p. 97-106.

Bieniawski ZT, Bernede MJ. Suggested methods for determining the uniaxial compressive strength and deformability of rock materials: Part 1. Suggested method for determining deformability of rock materials in uniaxial compression. *International Journal of Rock Mechanics and Mining Sciences & Geomechanics Abstracts*. 1979; 16: 138-40.

Bieniawski ZT. Rock mechanics design in mining and tunnelling: A.A. Balkema. 1984.

Bieniawski ZT. Engineering rock mass classifications: a complete manual for engineers and geologists in mining, civil, and petroleum engineering. New York: Wiley. 1989.

Blake W, Hedley DG. Rockbursts: case studies from North American hard-rock mines. Littleton, Colorado: Society for Mining, Metallurgy, and Exploration. 2003.

Bobet A, Einstein H. Fracture coalescence in rock-type materials under uniaxial and biaxial compression. *International Journal of Rock Mechanics and Mining Sciences*. 1998; 35: 863-88.

Bobet A. Influence of the loading apparatus on the stresses within biaxial specimens. *ASTM Geotechnical Testing Journal*. 2001; 24: 256-72.

Brace W. Volume changes during fracture and frictional sliding: a review. Rock Friction and Earthquake Prediction: Springer. 1978. p. 603-14.

Brady B. Effects of inserts on the elastic behavior of cylindrical materials loaded between rough end-plates. *International Journal of Rock Mechanics and Mining Sciences & Geomechanics Abstracts*. 1971; 8: 357-69.

Brady BHG, Brown ET. Rock mechanics: for underground mining: Springer Science & Business Media. 2013.

Brown ET, Hudson JA, Hardy MP, Fairhurst C. Controlled failure of hollow rock cylinders in uniaxial compression. *Rock Mechanics*. 1972; 4: 1-24.

Brown ET. Estimating the mechanical properties of rock masses. Proceedings of the 1st southern hemisphere international rock mechanics symposium: SHIRMS. 2008. p. 3-21.

Cai M, Kaiser PK, Tasaka Y, Maejima T, Morioka H, Minami M. Generalized crack initiation and crack damage stress thresholds of brittle rock masses near underground excavations. *International Journal of Rock Mechanics and Mining Sciences*. 2004a; 41: 833-47.

Cai M, Kaiser PK, Uno H, Tasaka Y, Minami M. Estimation of rock mass deformation modulus and strength of jointed hard rock masses using the GSI system. *International Journal of Rock Mechanics and Mining Sciences*. 2004b; 41: 3-19.

Cai M, Kaiser PK, Tasaka Y, Minami M. Determination of residual strength parameters of jointed rock masses using the GSI system. *International Journal of Rock Mechanics and Mining Sciences*. 2007; 44: 247-65.

Cai M. Influence of stress path on tunnel excavation response–numerical tool selection and modeling strategy. *Tunnelling and Underground Space Technology*. 2008a; 23: 618-28.

Cai M. Influence of intermediate principal stress on rock fracturing and strength near excavation boundaries—insight from numerical modeling. *International Journal of Rock Mechanics and Mining Sciences*. 2008b; 45: 763-72.

Cai M. Practical estimates of tensile strength and Hoek-Brown strength parameter mi of brittle rocks. *Rock Mechanics and Rock Engineering*. 2010; 43: 167-84.

Cai M, Kaiser PK. In-situ rock spalling strength near excavation boundaries. *Rock Mechanics and Rock Engineering*. 2014; 47: 659-75.

Cai M, Zhao X, Kaiser PK. On field strength of massive rocks. *Chinese Journal of Rock Mechanics and Engineering*. 2014; 33: 1-13.

Carneiro F. A new method to determine the tensile strength of concrete. Proceedings of the 5th meeting of the Brazilian Association for Technical Rules, Section 3. Portuguese. 1943. p. 126-9.

Cerrolaza M, Garcia R. Boundary elements and damage mechanics to analyze excavations in rock mass. *Engineering Analysis with Boundary Elements*. 1997; 20: 1-16.

Chang C, Haimson B. True triaxial strength and deformability of the German Continental Deep Drilling Program (KTB) deep hole amphibolite. *Journal of Geophysical Research: Solid Earth (1978–2012)*. 2000; 105: 18999-9013.

Chang C, Haimson B. Non-dilatant deformation and failure mechanism in two Long Valley Caldera rocks under true triaxial compression. *International Journal of Rock Mechanics and Mining Sciences*. 2005; 42: 402-14.

Chen WF, Han DJ. Plasticity for structural engineers: J. Ross Publishing. 2007.

Choi S, Thienel K-C, Shah S. Strain softening of concrete in compression under different end constraints. *Magazine of Concrete Research*. 1996; 48: 103-15.

Claborn FJ. Development of a strain softening constitutive model for rock [Master Thesis]: Rice University; 1988.

Colmenares L, Zoback M. A statistical evaluation of intact rock failure criteria constrained by polyaxial test data for five different rocks. *International Journal of Rock Mechanics and Mining Sciences*. 2002; 39: 695-729.

Cook NGW. The failure of rock. *International Journal of Rock Mechanics and Mining Sciences*. 1965; 2: 389-403.

Cook NGW, Hojem JPM. A rigid 50-ton compression and tension testing machine. *Journal of the Southern African Institute of Mining and Metallurgy*. 1966; 1: 89-92.

Cook NGW, Hodgson K, Hojem JPM. A 100 MN jacking system for testing coal pillars underground. *Journal of the Southern African Institute of Mining and Metallurgy*. 1971; 71: 215-24.

Cook NGW, Hojem JPM. A 200-ton stiff testing machine. *Journal of the Southern African Institute of Mining and Metallurgy*. 1971.

Cook RD. Concepts and applications of finite element analysis: John Wiley & Sons. 2007.

Cundall PA. A computer model for simulating progressive, largescale movements in blocky rock systems. Proceedings of Symposium of International Society of Rock Mechanics. Nancy: International Society for Rock Mechanics (ISRM). 1971. p. 129-36.

Cundall PA. Formulation of a three-dimensional distinct element model—Part I. A scheme to detect and represent contacts in a system composed of many polyhedral blocks. *International Journal of Rock Mechanics and Mining Sciences & Geomechanics Abstracts*. 1988; 25: 107-16.

Dai F, Wei M, Xu N, Ma Y, Yang D. Numerical assessment of the progressive rock fracture mechanism of cracked chevron notched Brazilian disc specimens. *Rock Mechanics and Rock Engineering*. 2015; 48: 463-79.

Das MN. Influence of width/height ratio on post-failure behaviour of coal. *International Journal of Mining and Geological Engineering*. 1986; 4: 79-87.

Dehler W, Labuz JF. Stress path testing of an anisotropic sandstone. *Journal of Geotechnical and Geoenvironmental Engineering*. 2007; 133: 116-9.

Diederichs MS. The 2003 Canadian Geotechnical Colloquium: Mechanistic interpretation and practical application of damage and spalling prediction criteria for deep tunnelling. *Canadian Geotechnical Journal*. 2007; 44: 1082-116.

Eberhardt E, Stead D, Stimpson B, Read R. Identifying crack initiation and propagation thresholds in brittle rock. *Canadian Geotechnical Journal*. 1998; 35: 222-33.

Eberhardt E. The Hoek-Brown Failure Criterion. *Rock Mechanics and Rock Engineering*. 2012; 45: 981-8.

Egger P. Design and construction aspects of deep tunnels (with particular emphasis on strain softening rocks). *Tunnelling and Underground Space Technology*. 2000; 15: 403-8.

Fairhurst C, Hudson JA. Draft ISRM suggested method for the complete stress-strain curve for intact rock in uniaxial compression. *International Journal of Rock Mechanics and Mining Sciences*. 1999; 36: 279-89.

Fakhimi A, Hosseini O, Theodore R. Physical and numerical study of strain burst of mine pillars. *Computers and Geotechnics*. 2016; 74: 36-44.

Fang Z, Harrison JP. A mechanical degradation index for rock. *International Journal of Rock Mechanics and Mining Sciences*. 2001; 38: 1193-9.

Fang Z, Harrison JP. Development of a local degradation approach to the modelling of brittle fracture in heterogeneous rocks. *International Journal of Rock Mechanics and Mining Sciences*. 2002; 39: 443-57.

Feng X-T, Hudson JA. Rock Engineering Design. London: CRC Press. 2011.

Feng X-T, Zhang X, Kong R, Wang G. A Novel Mogi Type True Triaxial Testing Apparatus and Its Use to Obtain Complete Stress–Strain Curves of Hard Rocks. *Rock Mechanics and Rock Engineering*. 2016: 1-14.

Fjær E, Ruistuen H. Impact of the intermediate principal stress on the strength of heterogeneous rock. *Journal of Geophysical Research: Solid Earth*. 2002; 107.

Frantziskonis G, Desai C. Constitutive model with strain softening. *International Journal of Solids and Structures*. 1987; 23: 733-50.

Gaffney E. Measurements of dynamic friction between rock and steel. Defense Nuclear Agency; 1976.

Galileo G. Discorsi e Dimostrazioni Matematiche Intorno a Due Nuove Scienze (English: Two New Sciences). Elsevier, Leiden 1638.

Gercek H. Poisson's ratio values for rocks. *International Journal of Rock Mechanics and Mining Sciences*. 2007; 44: 1-13.

Gerstle KB, Zimmerman RM, Winkler H, Traina LA, Taylor MA, Schickert G, et al. Behavior of concrete under multiaxial stress states. *Journal of the Engineering Mechanics Division*. 1980; 106: 1383-403.

Gerstle KH, Linse DL, Bertacchi P. Strength of concrete under multiaxial stress states. *ACI Special Publication*. 1978; 55.

Gettu R, Mobasher B, Carmona S, Jansen D. Testing of concrete under closed-loop control. *Advanced Cement Based Materials*. 1996; 3: 54-71.

Ghazvinian A, Sarfarazi V, Schubert W, Blumel M. A study of the failure mechanism of planar non-persistent open joints using PFC2D. *Rock Mechanics and Rock Engineering*. 2012; 45: 677-93.

Golder H, Akroyd T. An apparatus for triaxial-compression tests at high pressures. *Géotechnique*. 1954; 4: 131-6.

Goodman RE. Introduction to rock mechanics: Wiley New York. 1989.

Griggs DT. Deformation of rocks under high confining pressures: I. Experiments at room temperature. *The Journal of Geology*. 1936: 541-77.

Grote K-H, Antonsson EK. Springer handbook of mechanical engineering: Springer Science & Business Media. 2009.

Haimson B, Chang C. A new true triaxial cell for testing mechanical properties of rock, and its use to determine rock strength and deformability of Westerly granite. *International Journal of Rock Mechanics and Mining Sciences*. 2000; 37: 285-96.

Haimson B, Chang C. True triaxial strength of the KTB amphibolite under borehole wall conditions and its use to estimate the maximum horizontal in situ stress. *Journal of Geophysical Research: Solid Earth (1978–2012)*. 2002; 107: ETG 15-1-ETG -4.

Hallbauer D, Wagner H, Cook NGW. Some observations concerning the microscopic and mechanical behaviour of quartzite specimens in stiff, triaxial compression tests. *International Journal of Rock Mechanics and Mining Sciences & Geomechanics Abstracts*. 1973; 10: 713-26.

Han J, Li S, Li S, Wang L. Post-peak stress-strain relationship of rock mass based on Hoek-Brown strength criterion. *Procedia Earth and Planetary Science*. 2012; 5: 289-93.

Handin J. An application of high pressure in geophysics: experimental rock deformation. *Transactions American Society of Mechanical Engineers*. 1953; 75: 315-24.

Hawkes I, Mellor M. Uniaxial testing in rock mechanics laboratories. *Engineering Geology*. 1970; 4: 179-285.

Hawkins A. Aspects of rock strength. *Bulletin of Engineering Geology and the Environment*. 1998; 57: 17-30.

He C, Okubo S, Nishimatsu Y. A study of the class II behaviour of rock. *Rock Mechanics and Rock Engineering*. 1990; 23: 261-73.

He H, Shi L, Bai B. The effect of the true triaxial test subjected to different loading types on end friction. *Journal of Transport Science and Engineering (in Chinese)*. 2014; 30: 1-5.

He M, Miao J, Feng J. Rock burst process of limestone and its acoustic emission characteristics under true-triaxial unloading conditions. *International Journal of Rock Mechanics and Mining Sciences*. 2010; 47: 286-98.

He M, Nie W, Zhao Z, Guo W. Experimental investigation of bedding plane orientation on the rockburst behavior of sandstone. *Rock Mechanics and Rock Engineering*. 2012; 45: 311-26.

Heal D. Observations and analysis of incidences of rockburst damage in underground mines [PhD Thesis]. Australia: University of Western Australia; 2010.

Hemami B, Fakhimi A. Numerical simulation of rock-loading machine interaction. 48th US Rock Mechanics/Geomechanics Symposium: American Rock Mechanics Association. 2014.

Hibbitt H, Karlsson B, Sorensen P. Abaqus analysis user's manual version 6.10. Providence, RI, USA: Dassault Systèmes Simulia Corp. 2011.

Hoek E, Franklin JA. A simple triaxial cell for field and laboratory testing of rock. *Trans Instn Min Metal Sect*. 1968; A 77: A22-66.

Hoek E, Brown ET. Practical estimates of rock mass strength. *International Journal of Rock Mechanics and Mining Sciences*. 1997; 34: 1165-86.

Hoek E, Kaiser PK, Bawden WF. Support of underground excavations in hard rock: CRC Press. 2000.

Hoek E, Carranza-Torres C, Corkum B. Hoek-Brown failure criterion-2002 edition. Proceedings of NARMS-Tac. 2002. p. 267-73.

Hoek E. Practical Rock Engineering. 2007: Online. ed. Rocscience. 2007.

Hoskins JR, Horino FG. Effect of end conditions on determining compressive strength of rock samples: US Dept. of the Interior, Bureau of Mines. 1968.

Hudson JA. Effect of time on the mechanical behaviour of failed rock. *Nature*. 1971; 232: 185-6.

Hudson JA, Brown ET, Fairhurst C. Optimizing the control of rock failure in servo-controlled laboratory tests. *Rock Mechanics*. 1971; 3: 217-24.

Hudson JA, Brown ET, Fairhurst C. Shape of the complete stress-strain curve for rock. Stability of Rock Slopes: ASCE. 1972a. p. 773-95.

Hudson JA, Crouch SL, Fairhurst C. Soft, stiff and servo-controlled testing machines: a review with reference to rock failure. *Engineering Geology*. 1972b; 6: 155-89.

Hudson JA. Comprehensive rock engineering, principles, practice and projects. Vol 3: Rock testing and site characterization. London, United Kingdom: Pergamon Press. 1993.

Hudson JA, Harrison JP. Engineering rock mechanics - an introduction to the principles: Elsevier. 2000.

Hudson JA, Harrison JP. Engineering rock mechanics - illustrative worked examples: Elsevier. 2001.

Hudson JA. The future for rock mechanics and the ISRMS. ISRM International Symposium-5th Asian Rock Mechanics Symposium: International Society for Rock Mechanics. 2008.

Ingles O, Lee I, Neil R. The influence of stress history on lateral strain. *Rock Mechanics and Rock Engineering*. 1973; 5: 203-13.

Jaeger JC. Shear failure of anistropic rocks. *Geological Magazine*. 1960; 97: 65-72.

Jaeger JC, Cook NGW. Fundamentals of rock mechanics. Mathuen, London: Chapman and Hall. 1979.

Jaeger JC, Cook NGW, Zimmerman RW. Fundamentals of rock mechanics: John Wiley & Sons. 2007.

Jansen DC, Shah SP. Effect of length on compressive strain softening of concrete. *Journal of Engineering Mechanics*. 1997; 123: 25-35.

Jing L, Hudson JA. Numerical methods in rock mechanics. *International Journal of Rock Mechanics and Mining Sciences*. 2002; 39: 409-27.

Jing L. A review of techniques, advances and outstanding issues in numerical modelling for rock mechanics and rock engineering. *International Journal of Rock Mechanics and Mining Sciences*. 2003; 40: 283-353.

Joseph T, Barron K. The post-failure characteristics of rock. *CIM bulletin*. 2003; 96: 66-74.

Kaiser PK, McCreath D. Rock support in mining and underground construction: CRC Press. 1992.

Kaiser PK. Canadian Rockburst Support Handbook: Prep. for Sponsors of the Canadian Rockburst Research: Geomechanics Research Centre. 1996.

Kaiser PK, Diederichs MS, Martin CD, Sharp J, Steiner W. Underground works in hard rock tunnelling and mining. ISRM International Symposium: International Society for Rock Mechanics. 2000.

Kaiser PK, Yazici S, Maloney S. Mining-induced stress change and consequences of stress path on excavation stability—a case study. *International Journal of Rock Mechanics and Mining Sciences*. 2001; 38: 167-80.

Katona MG. A simple contact–friction interface element with applications to buried culverts. *International Journal for Numerical and Analytical Methods in Geomechanics*. 1983; 7: 371-84.

Kawamoto T, Ichikawa Y, Kyoya T. Deformation and fracturing behaviour of discontinuous rock mass and damage mechanics theory. *International Journal for Numerical and Analytical Methods in Geomechanics*. 1988; 12: 1-30.

Khair AW. Effects of specimen size and geometry on post-failure behaviour of coal. Assessment and prevention of failure phenomena in rock engineering. 1993. p. 343-9.

Kias E, Ozbay U. Modeling unstable failure of coal pillars in underground mining using the discrete element method. 47th US Rock Mechanics/Geomechanics Symposium: American Rock Mechanics Association. 2013.

Kiendl OG, Maldari T. A comparison of physical properties of concrete made of three varieties of coarse aggregate [BSc Thesis]: University of Wisconsin; 1938.

Kimura T, Esaki T, Kameda N, Nishida T. Experimental and theoretical studies on strain softening behavior of rocks. The 28th US Symposium on Rock Mechanics: American Rock Mechanics Association. 1987.

Kotsovos M. Effect of testing techniques on the post-ultimate behaviour of concrete in compression. *Materiaux Et Construction*. 1983; 16: 3-12.

Labuz JF, Biolzi L. Class I vs Class II stability: a demonstration of size effect. *International Journal of Rock Mechanics and Mining Sciences & Geomechanics Abstracts*. 1991; 28: 199-205.

Labuz JF, Bridell JM. Reducing frictional constraint in compression testing through lubrication. *International Journal of Rock Mechanics and Mining Sciences & Geomechanics Abstracts*. 1993; 30: 451-5.

Labuz JF, Biolzi L. Experiments with rock: remarks on strength and stability issues. *International Journal of Rock Mechanics and Mining Sciences*. 2007; 44: 525-37.

Labuz JF, Zang A. Mohr–Coulomb failure criterion. *Rock Mechanics and Rock Engineering*. 2012: 1-5.

Laursen TA. Computational contact and impact mechanics: fundamentals of modeling interfacial phenomena in nonlinear finite element analysis: Springer Science & Business Media. 2013.

Lee D, Juang C, Chen J, Lin H, Shieh W. Stress paths and mechanical behavior of a sandstone in hollow cylinder tests. *International Journal of Rock Mechanics and Mining Sciences*. 1999; 36: 857-70.

Lee Y-K, Pietruszczak S. A new numerical procedure for elasto-plastic analysis of a circular opening excavated in a strain-softening rock mass. *Tunnelling and Underground Space Technology*. 2008; 23: 588-99.

Li D, Li CC, Li X. Influence of sample height-to-width ratios on failure mode for rectangular prism samples of hard rock loaded in uniaxial compression. *Rock Mechanics and Rock Engineering*. 2011; 44: 253-67.

Li X, Du K, Li D. True triaxial strength and failure modes of cubic rock specimens with unloading the minor principal stress. *Rock Mechanics and Rock Engineering*. 2015: 1-12.

Liang C, Zhang Q, Li X, Xin P. The effect of specimen shape and strain rate on uniaxial compressive behavior of rock material. *Bulletin of Engineering Geology and the Environment*. 2015: 1-13.

Lisjak A, Grasselli G. A review of discrete modeling techniques for fracturing processes in discontinuous rock masses. *Journal of Rock Mechanics and Geotechnical Engineering*. 2014; 6: 301-14.

Liu B, Zhang J, Du q. A study of size effect for compression strength of rock. *Chinese Journal of Rock Mechanics and Engineering (in Chinese)*. 1998; 17: 611-4.

Lo KY, Lee CF. Stress analysis and slope stability in strain-softening materials. *Géotechnique*. 1973; 23.

Lockner DA, Byerlee JD, Kuksenko V, Ponomarev A, Sidorin A. Quasi-static fault growth and shear fracture energy in granite. *Nature*. 1991; 350: 39-42.

Lockner DA. Rock failure. Rock Physics & Phase Relations: A Handbook of Physical Constants. Washington: American Geophysical Union Reference Shelf. 1995. p. 127-47.

Lockner DA. A generalized law for brittle deformation of Westerly granite. *Journal of Geophysical Research*. 1998a; 103: 5107-23.

Lockner DA. A generalized law for brittle deformation of Westerly granite. *Journal of Geophysical Research: Solid Earth (1978–2012)*. 1998b; 103: 5107-23.

Manouchehrian A, Cai M. Simulation of unstable rock failure under unloading conditions. *Canadian Geotechnical Journal*. 2015; 53: 22-34.

Martin CD, Chandler NA. The progressive fracture of Lac du Bonnet granite. *International Journal of Rock Mechanics and Mining Sciences & Geomechanics Abstracts*. 1994; 31: 643-59.

Martin CD. Seventeenth Canadian geotechnical colloquium: the effect of cohesion loss and stress path on brittle rock strength. *Canadian Geotechnical Journal*. 1997; 34: 698-725.

Martin CD, Maybee WG. The strength of hard-rock pillars. *International Journal of Rock Mechanics and Mining Sciences*. 2000; 37: 1239-46.

Martin CD, Kaiser PK, Christiansson R. Stress, instability and design of underground excavations. *International Journal of Rock Mechanics and Mining Sciences*. 2003; 40: 1027-47.

Meikle P, Holland C. The effect of friction on the strength of model coal pillars. *Trans Soc Mining Eng*. 1965; 232: 322-7.

Meng F, Zhou H, Zhang C, Xu R, Lu J. Evaluation methodology of brittleness of rock based on post-peak stress–strain curves. *Rock Mechanics and Rock Engineering*. 2015; 48: 1787-805.

Michelis P. True triaxial cyclic behavior of concrete and rock in compression. *International Journal of Plasticity*. 1987; 3: 249-70.

Milev A, Spottiswoode S, Rorke A, Finnie G. Seismic monitoring of a simulated rockburst on a wall of an underground tunnel. *Journal of the South African Institute of Mining and Metallurgy*. 2001; 101: 253-60.

Mishra B, Nie D. Experimental investigation of the effect of change in control modes on the post-failure behavior of coal and coal measures rock. *International Journal of Rock Mechanics and Mining Sciences*. 2013; 60: 363-9.

Mogi K. Effect of the intermediate principal stress on rock failure. *Journal of Geophysical Research*. 1967; 72: 5117-31.

Mogi K. Fracture and flow of rocks under high triaxial compression. *Journal of Geophysical Research*. 1971; 76: 1255-69.

Mogi K. On the pressure dependence of strength of rocks and the Coulomb fracture criterion. *Tectonophysics*. 1974; 21: 273-85.

Mogi K. Experimental rock mechanics: CRC Press. 2007.

Morsy K, Peng S. Evaluation of a mine panel failure using the local mine stiffness criterion-a case study. Transactions. 2002. p. 8-19.

MTS. MTS Model 815 and 816 Rock Mechanics Test Systems. User's manual. 2013.

Munjiza A, John N. Mesh size sensitivity of the combined FEM/DEM fracture and fragmentation algorithms. *Engineering Fracture Mechanics*. 2002; 69: 281-95.

Nayak GC, Zienkiewicz OC. Elasto-plastic stress analysis. A generalization for various contitutive relations including strain softening. *International Journal for Numerical Methods in Engineering*. 1972; 5: 113-35.

Naylor DJ, Pande GN, Simpson B, Tabb R. Finite elements in geotechnical engineering. Swansea, U. K.: Pineridge Press Ltd. 1981.

Needleman A. Material rate dependence and mesh sensitivity in localization problems. *Computer methods in applied mechanics and engineering*. 1988; 67: 69-85.

Obert L, Duvall W. Rock mechanics and the design of structures in rock: Wiley, New York. 1967.

Ofoegbu G, Curran J. Yielding and damage of intact rock. *Canadian Geotechnical Journal*. 1991; 28: 503-16.

Ofoegbu G, Curran J. Deformability of intact rock. *International Journal of Rock Mechanics and Mining Sciences & Geomechanics Abstracts*. 1992; 29: 35-48.

Ojo O. Use of end caps in the determination of compressive strength of rocks. *Geotechnical & Geological Engineering*. 1993; 11: 147-53.

Okubo S, Nishimatsu Y. Uniaxial compression testing using a linear combination of stress and strain as the control variable. *International Journal of Rock Mechanics and Mining Sciences & Geomechanics Abstracts*. 1985; 22: 323-30.

Ortlepp W. Rock fracture and rockbursts: an illustrative study. Johannesburg: South African Institute of Mining and Metallurgy. 1997.

Pan P, Feng X, Hudson J. The influence of the intermediate principal stress on rock failure behaviour: a numerical study. *Engineering Geology*. 2012; 124: 109-18.

Pariseau W. Fitting failure criteria to laboratory strength tests. *International Journal of Rock Mechanics and Mining Sciences*. 2007; 44: 637-46.

Park K, Kim Y. Analytical solution for a circular opening in an elastic–brittle–plastic rock. *International Journal of Rock Mechanics and Mining Sciences*. 2006; 43: 616-22.

Paterson MS, Wong T-F. Experimental rock deformation: the brittle field: Springer. 2005.

Pellegrino A, Sulem J, Barla G. The effects of slenderness and lubrication on the uniaxial behavior of a soft limestone. *International Journal of Rock Mechanics and Mining Sciences*. 1997; 34: 333-40.

Peng S. Stresses within elastic circular cylinders loaded uniaxially and triaxially. *International Journal of Rock Mechanics and Mining Sciences & Geomechanics Abstracts*. 1971; 8: 399-432.

Peng S. Time-dependent aspects of rock behavior as measured by a servocontrolled hydraulic testing machine. *International Journal of Rock Mechanics and Mining Sciences & Geomechanics Abstracts*. 1973; 10: 235-46.

Pietruszczak S, Mroz Z. Finite element analysis of deformation of strain - softening materials. *International Journal for Numerical Methods in Engineering*. 1981; 17: 327-34.

Potts DM, Zdravkovic L, Zdravković L. Finite element analysis in geotechnical engineering: application: Thomas Telford. 2001.

Potyondy D, Cundall P. A bonded-particle model for rock. *International Journal of Rock Mechanics and Mining Sciences*. 2004; 41: 1329-64.

Rae P, Dattelbaum D. The properties of polytetrafluoroethylene (PTFE) in compression. *Polymer*. 2004; 45: 7615-25.

Rashed G, Peng S. Change of the mode of failure by interface friction and width-to-height ratio of coal specimens. *Journal of Rock Mechanics and Geotechnical Engineering*. 2015; 7: 256-65.

Read H, Hegemier G. Strain softening of rock, soil and concrete - a review article. *Mechanics of Materials*. 1984; 3: 271-94.

Renner J, Rummel F. The effect of experimental and microstructural parameters on the transition from brittle failure to cataclastic flow of carbonate rocks. *Tectonophysics*. 1996; 258: 151-69.

Rist MA, Sammonds PR, Murrell SAF. Strain rate control during deformation of ice: An assessment of the performance of a new servo-controlled triaxial testing system. *Cold Regions Science and Technology*. 1991; 19: 189-200.

Rudnicki JW, Rice J. Conditions for the localization of deformation in pressure-sensitive dilatant materials. *Journal of the Mechanics and Physics of Solids*. 1975; 23: 371-94.

Rummel F, Fairhurst C. Determination of the post-failure behavior of brittle rock using a servo-controlled testing machine. *Rock Mechanics*. 1970; 2: 189-204.

Sainsbury D, Hart R, Detournay C, Nelson M. Continuum and distinct element numerical modeling in geomechanics–2011. Proc 2nd Int FLAC/DEM Symp. 2011. p. 852.

Sakurai S, Farazmand A, Adachi K. Assessment of the stability of slopes from surface displacements measured by GPS in an open pit mine. In: Deák G, ZG Agioutantis Z, editors. Sustainable Exploitation of Natural Resources, Proc 3rd Int Seminar ECOMINING—Europe in 21st Century. Milos Island, Greece. 2009. p. 239-48.

Salamon MDG. Stability, instability and design of pillar workings. *International Journal of Rock Mechanics and Mining Sciences & Geomechanics Abstracts*. 1970; 7: 613-31.

Schöpfer MP, Childs C, Manzocchi T. Three - dimensional failure envelopes and the brittle - ductile transition. *Journal of Geophysical Research: Solid Earth*. 2013; 118: 1378-92.

Schulson E. The structure and mechanical behavior of ice. *JOM*. 1999; 51: 21-7.

Senent S, Jimenez R, Reyes A. Numerical simulation of the influence of small-scale defects on the true-triaxial strength of rock samples. *Computers and Geotechnics*. 2013; 53: 142-56.

Shao J, Rudnicki JW. A microcrack-based continuous damage model for brittle geomaterials. *Mechanics of Materials*. 2000; 32: 607-19.

Sheng D, Westerberg B, Mattsson H, Axelsson K. Effects of end restraint and strain rate in triaxial tests. *Computers and Geotechnics*. 1997; 21: 163-82.

Shepherd J, Rixon L, Griffiths L. Outbursts and geological structures in coal mines: a review. International Journal of Rock Mechanics and Mining Sciences & Geomechanics Abstracts: Elsevier. 1981. p. 267-83.

Shi L, Li X, Bai B, Li Q, Feng X-T. Numerical analysis of loading boundary effects in Mogi-type true triaxial tests. In: Kwaśniewski M, Li X, Takahashi M, editors.True triaxial testing of rocks. Leiden, the Netherlands: CRC Press. 2012. p. 19-34.

Sinha NK, Frederking RMW. Effect of test system stiffness on strength of ice. Fifth International Conference on Port and Ocean Engineering under Arctic Condition: NRC; 1979.

Smith D. David Kirkaldy (1820-1897) and Engineering Materials Testing. *Transactions of the Newcomen Society*. 1980; 52: 49-65.

Snowdon R, Ryley M, Temporal J, Crabb G. The effect of hydraulic stiffness on tunnel boring machine performance. *International Journal of Rock Mechanics and Mining Sciences & Geomechanics Abstracts*. 1983; 20: 203-14.

Späth W. Einfluß der Federung der Zerreißmaschine auf das Spannungs-Drehungs-Schaubild: Verlag Stahleisen. 1935.

Stavrogin AN, Tarasov BG. Experimental physics and rock mechanics: CRC Press. 2001.

Stephansson O. What can fractıre mechanics do for us? Proceedings of the ISRM Regional Sympoisum EUROCK2011: Rock Mechanics a Challenge for Society. Helsinki, Balkema. 2001. p. 21-5.

Sture S, Ko HY. Strain - softening of brittle geologic materials. *International Journal for Numerical and Analytical Methods in Geomechanics*. 1978; 2: 237-53.

Takahashi M, Koide H. Effect of the intermediate principal stress on strength and deformation behavior of sedimentary rocks at the depth shallower than 2000 m. ISRM international symposium: International Society for Rock Mechanics. 1989.

Tang C, Tham L, Lee P, Tsui Y, Liu H. Numerical studies of the influence of microstructure on rock failure in uniaxial compression—part II: constraint, slenderness and size effect. *International Journal of Rock Mechanics and Mining Sciences*. 2000; 37: 571-83.

Tang L, Ke M, Yan J-h. A key problem overlooked during experiments to determine rock properties in the post-peak region. *International Journal of Rock Mechanics and Mining Sciences*. 2004; 41: 55-60.

Tarasov B, Potvin Y. Universal criteria for rock brittleness estimation under triaxial compression. *International Journal of Rock Mechanics and Mining Sciences*. 2013; 59: 57-69.

Terzaghi K. Rock defects and loads on tunnel supports. In: Proctor R, White T, editors. Rock Tunneling with Steel Support. Youngstown, OH: Commercial Shearing and Stamping Company. 1946. p. 17–99.

Thuro K, Plinninger R, Zäh S, Schütz S. Scale effects in rock strength properties. Part 1: Unconfined compressive test and Brazilian test. IRSM Regional Symposium EOROOC 2001. Espoo, Finland. 2001. p. 169-74.

Ulusay R. The present and future of rock testing: highlighting the ISRM suggested methods. The ISRM suggested methods for rock characterization, testing and monitoring: 2007-2014: Springer. 2015a. p. 1-22.

Ulusay R. The ISRM Suggested Methods for Rock Characterization, Testing and Monitoring: 2007-2014: Springer. 2015b.

Van Heerden W. In situ complete stress-strain characteristics of large coal specimens. *Journal of the South African Institute of Mining and Metallurgy*. 1975; 75: 207-17.

Van Mier J, Shah S, Arnaud M, Balayssac J, Bascoul A, Choi S, et al. Strain-softening of concrete in uniaxial compression. *Materials and Structures*. 1997; 30: 195-209.

Van Vliet M, Van Mier J. Experimental investigation of concrete fracture under uniaxial compression. *Mechanics of Cohesive - Frictional Materials*. 1996; 1: 115-27.

Varas F, Alonso E, Alejano L, Man ń GF. Study of bifurcation in the problem of unloading a circular excavation in a strain-softening material. *Tunnelling and Underground Space Technology*. 2005; 20: 311-22.

Vardoulakis I, Labuz JF, Papamichos E, Tronvoll J. Continuum fracture mechanics of uniaxial compression on brittle materials. *International Journal of Solids and Structures*. 1998; 35: 4313-35.

Vermeer PA, De Borst R. Non-associated plasticity for soils, concrete and rock. *Heron*. 1984; 29.

von Kármán T. Festigkeitsversuche unter allseitigem Druck [Strength measurements under uniform pressure]. *Zeit Ver dt Ing*. 1911; 55: 1749-57.

Vutukuri VS, Lama RD, Saluja SS. Handbook on mechanical properties of rocks: testing techniques & results: Trans Tech Publications. 1974.

Wang S, Zheng H, Li C, Ge X. A finite element implementation of strain-softening rock mass. *International Journal of Rock Mechanics and Mining Sciences*. 2011; 48: 67-76.

Wang Y, Tonon F. Modeling Lac du Bonnet granite using a discrete element model. *International Journal of Rock Mechanics and Mining Sciences*. 2009; 46: 1124-35.

Wawersik WR. Detailed analysis of rock failure in laboratory compression tests [PhD Thesis]: University of Minnesota; 1968.

Wawersik WR, Fairhurst C. A study of brittle rock fracture in laboratory compression experiments. *International Journal of Rock Mechanics and Mining Sciences & Geomechanics Abstracts*. 1970; 7: 561-75.

Wawersik WR, Brace WF. Post-failure behavior of a granite and diabase. *Rock Mechanics*. 1971; 3: 61-85.

Whitney C. Discussion on VP Jensen's paper. *ACI Materials Journal*. 1943; 39: 584.

Wiebols G, Cook NGW. An energy criterion for the strength of rock in polyaxial compression. *International Journal of Rock Mechanics and Mining Sciences & Geomechanics Abstracts*. 1968; 5: 529-49.

Wriggers P. Computational contact mechanics: Springer Science & Business Media. 2006.

Wu Y, Zhang W. Prevention of rockbursts in coal mines in China. Proceedings of the 4th International Symposium on Rockbursts and Seismicity in Mines, Rotterdam. 1997. p. 361-6.

Xu Y, Cai M. Numerical Simulation of End Constraint Effect on Post-peak Behaviors of Rocks in Uniaxial Compression. 49th US Rock Mechanics/Geomechanics Symposium. San Francisco, USA,: American Rock Mechanics Association. 2015.

Xu Y, Cai M. Influence of End Effect on Rock Strength in True Triaxial Compression Test. *Canadian Geotechnical Journal*. 2016a: available online.

Xu Y, Cai M. Influence of Loading System Stiffness on the Post-peak Behavior of Stable Rock Failures. *Rock Mechanics and Rock Engineering*. 2016b: submitted.

Xu Y, Cai M. Numerical study on the influence of cross-sectional shape on strength and deformation behaviors of rocks under uniaxial compression. *Computers and Geotechnics*. 2017; 84: 129-37.

You M, Su C. Influence of length of fine and coarse crystal marble specimens on uniaxial compression tests. *Chinese Journal of Rock Mechanics and Engineering (in Chinese)*. 2004; 23: 3754-60.

You M. True-triaxial strength criteria for rock. *International Journal of Rock Mechanics and Mining Sciences*. 2009; 46: 115-27.

Young RP. Seismic methods applied to rock mechanics. *ISRM News Journal*. 1993; 1: 4-18.

Young T, Kelland P. A Course of Lectures on Natural Philosophy and the Mechanical Arts: pt. I. Mechanics. pt. II. Hydrodynamics. pt. III. Physics: Taylor and Walton. 1845.

Yuan S, Harrison JP. An empirical dilatancy index for the dilatant deformation of rock. *International Journal of Rock Mechanics and Mining Sciences*. 2004; 41: 679-86.

Yuan S, Harrison JP. A review of the state of the art in modelling progressive mechanical breakdown and associated fluid flow in intact heterogeneous rocks. *International Journal of Rock Mechanics and Mining Sciences*. 2006; 43: 1001-22.

Zhang C, Feng X-T, Zhou H, Qiu S, Wu W. Case histories of four extremely intense rockbursts in deep tunnels. *Rock Mechanics and Rock Engineering*. 2012; 45: 275-88.

Zhao J. Applicability of Mohr–Coulomb and Hoek–Brown strength criteria to the dynamic strength of brittle rock. *International Journal of Rock Mechanics and Mining Sciences*. 2000; 37: 1115-21.

Zhao X, Cai M. A mobilized dilation angle model for rocks. *International Journal of Rock Mechanics and Mining Sciences*. 2010; 47: 368-84.

Zhao X, Cai M, Wang J, Ma L. Damage stress and acoustic emission characteristics of the Beishan granite. *International Journal of Rock Mechanics and Mining Sciences*. 2013; 64: 258-69.

Zhao X, Cai M. Influence of specimen height-to-width ratio on the strainburst characteristics of Tianhu granite under true-triaxial unloading conditions. *Canadian Geotechnical Journal*. 2014; 52: 890-902.

Zhao X, Wang J, Cai M, Cheng C, Ma L, Su R, et al. Influence of unloading rate on the strainburst characteristics of Beishan granite under true-triaxial unloading conditions. *Rock Mechanics and Rock Engineering*. 2014; 47: 467-83.

Zhao X, Cai M, Wang J, Li P. Strength comparison between cylindrical and prism specimens of Beishan granite under uniaxial compression. *International Journal of Rock Mechanics and Mining Sciences*. 2015: 10-7.

Zienkiewicz OC, Valliappan S, King IP. Elasto-plastic solutions of engineering problems 'initial stress', finite element approach. *International Journal for Numerical Methods in Engineering*. 1969; 1: 75-100.

Zienkiewicz OC, Taylor RL. The finite element method for solid and structural mechanics: Butterworth-heinemann. 2005.

Zipf RK. MULSIM/NL application and practitioner's manual: US Department of the Interior, Bureau of Mines. 1992a.

Zipf RK, Jr. Analysis of stable and unstable pillar failure using a local mine stiffness method. Proceedings of the Workshop on Coal Pillar Mechanics and Design. Washington, DC: U. S. Bureau of Mines. 1992b. p. 128-43.

Zoback ML. First-and second-order patterns of stress in the lithosphere: the world stress map project. *Journal of Geophysical Research: Solid Earth*. 1992; 97: 11703-28.

Appendix A

A. Influence *LSS* on rock failure types – *a heuristic study on the energy stored in the frame-platen loading test machine for driving rock failure process*

In Chapter 5, a simulation model of a frame-platen loading test machine was built to investigate the influence of *LSS* on the post-peak deformation behavior of rock. Three key loading components of stiff test machines—the loading platens, the loading frame, and the loading ram––were considered in the model. Consequently, this model can characterize the *LSS* of a stiff test machine. The modeling results revealed that in the post-peak deformation stage both the additional energy ΔE_{in} input from an external energy source and the energy ΔE_t released from the test machine contribute to the observed post-peak stress–strain curves of rocks and hence the behavior of rock failure. In this appendix, the influence of *LSS* on the post-peak deformation behavior of rock is further investigated, with a focus on examining how the energy stored in the frame-platen loading test machine can affect the rock failure types.

A.1 Simulation statement

The research focus is ΔE_t (the stored energy released from a test machine in the post-peak deformation stage) and its impact on post-peak failure of rocks; hence, the contribution of ΔE_{in} to driving rock failure in the post-peak deformation stage will be excluded. Studying the influence of ΔE_t on the rock failure process is important for both rock laboratory testing and underground engineering. In laboratory testing, it is always suspected that the violent failure process observed when testing hard rocks could be primarily attributed to the sudden release of stored energy from the test machines (Cook, 1965; Salamon, 1970; He et al., 2010; He et al., 2012; Zhao and Cai, 2014), rather than the axial-strain-controlled loading of the loading ram when the servo-

controlled loading method is employed (Rummel and Fairhurst, 1970). In deep mining, even after the axial loading of a local strata to pillars is stopped (e.g., the mining activities are ceased), pillar-bursts can occur (Wu and Zhang, 1997; Blake and Hedley, 2003; Heal, 2010). Therefore, the potential influence of ΔE_t on rock failure types is focused in this heuristic study.

ΔE_t is the result of energy input from an external energy source to the frame-platen loading test machine in the pre-peak deformation stage, and then ΔE_t becomes the released energy from the test machine to a rock specimen in the post-peak deformation stage. In the numerical experiment, ΔE_{in} from the external energy source is nixed at peak load or at a certain point in the post-peak deformation stage. In laboratory testing, this is in accordance with cutting off the power supply of the loading ram. This can be achieved in the numerical modeling by cutting off the constant heat flux supply of the thermal loading platen underneath the rock specimen (Figure 5-5). As a result, the external energy supplied to the rock specimen-test machine system is stopped (ΔE_{in} starting from this point is zero) and ΔE_t is the only energy item that can possibly further deform the rock specimen in the post-peak deformation stage (Equation 4-4).

The simulation model is the same as that shown in Figure 5-5b, and the mechanical parameters of the rock specimen and the test machine are the same as those listed in Table 5-1 to Table 5-3. Two *LSS* values calibrated in Chapter 5 for the frame-platen loading test machine–61 GN/m (greater than critical *LSS* loading condition λ) and 24 GN/m (= λ)–plus a soft *LSS* of 16 GN/m calibrated in the same fashion illustrated in Figure 5-7, are selected for the numerical modeling. As a result, three rock failure types are expected: stable for 61 GN/m, critical for 24 GN/m, and unstable for 16 GN/m. The time to stop supplying external energy E_{in} is varied under different

LSS values to ensure that the rock failure processes can be observed and the influence of ΔE_t on rock failure process can be studied.

A.2 Results and discussions

Figure A-1 presents the stress–strain curve of the rock under *LSS* = 61 GN/m, compared with that under the ideal loading condition, where ΔE_{in} is supplied in the whole deformation process.

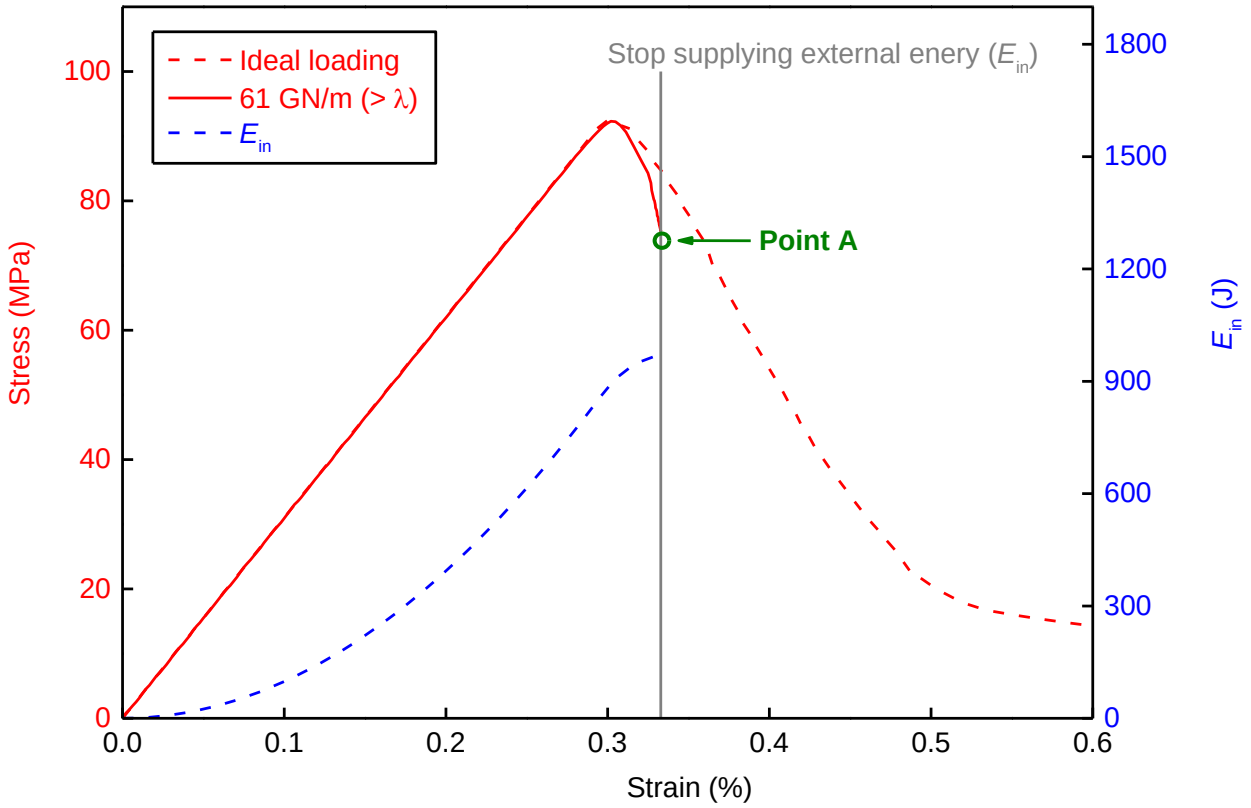

Figure A-1 Stress–strain curve of the rock under *LSS* = 61 GN/m, compared with that under the ideal loading condition.

E_{in} is stopped at an axial strain level of ε = 0.33% (Point A) when an obvious strain-softening behavior can be identified. It is seen that as soon as E_{in} is stopped (i.e., external loading is stopped), rock deformation terminates at ε = 0.33%. Rock failure under this loading condition is

stable. In other words, ΔE_t alone cannot drive the rock failure process; the rock failure process cannot proceed without addition energy ΔE_{in} input from the external energy source.

Figure A-2 presents the stress–strain curve of the rock under the critical *LSS* loading condition (*LSS* = λ). E_{in} is stopped at an axial strain level of ε = 0.32% (Point A), when the strain-softening curve's descending slope becomes steep and approaches E_p (Section 5.1.2).

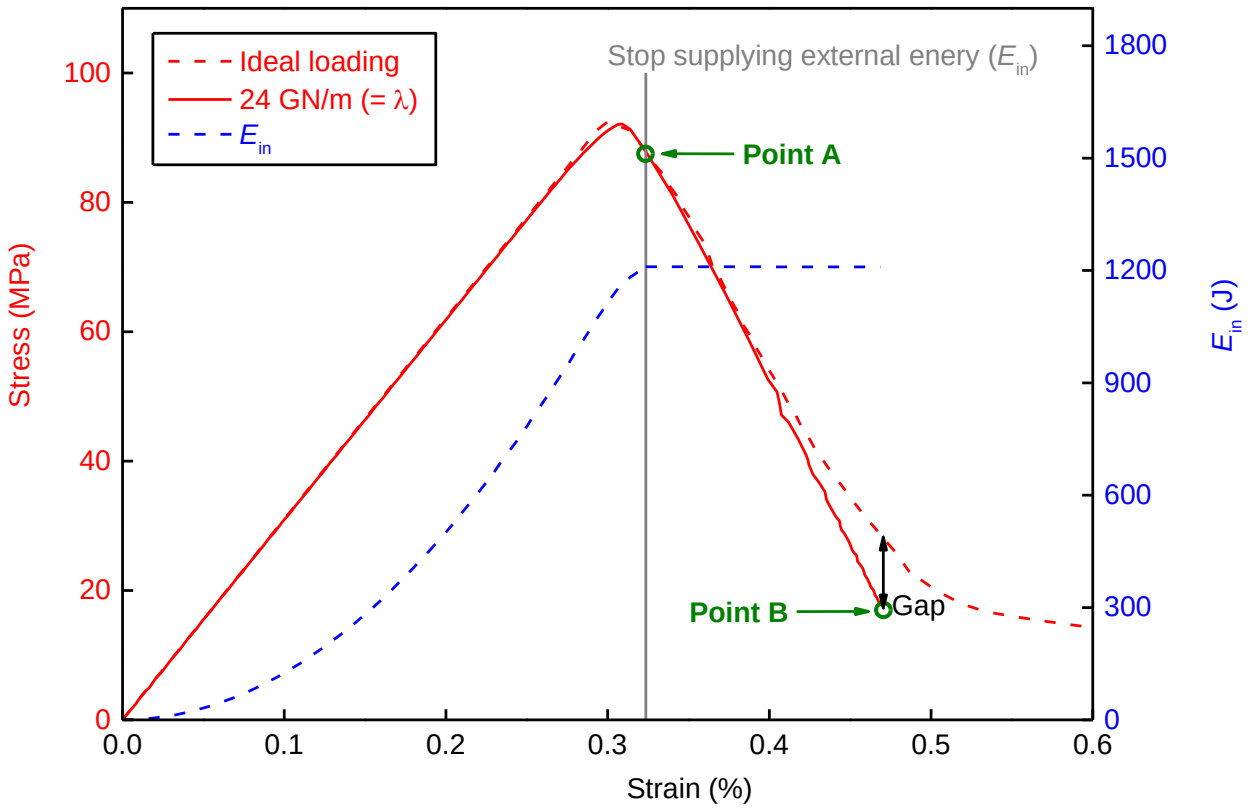

Figure A-2 Stress–strain curve of the rock under critical *LSS* loading condition, compared with that under the ideal loading condition.

The rock continues to deform after E_{in} is stopped. It is seen that the stress drop of the strain-softening curve follows a path the same as the unloading path of the test machine in the stress–strain space for 24 GN/m (refer to Figure 5-14 and Figure 5-25). Rock deformation terminates at

an axial strain level of $\varepsilon = 0.47\%$ (Point B) when there is a large gap between the strain-softening curve under the critical *LSS* loading condition and that under the ideal loading condition. This gap indicates that unless there is addition energy ΔE_{in} input from the external energy source to deform the rock, the rock failure process cannot proceed further beyond Point B by the released energy ΔE_t provided by the test machine.

Figure A-3 presents the stress–strain curve of the rock under *LSS* = 16 GN/m. In this case, E_{in} is stopped as soon as the rock strength has been reached (Point A).

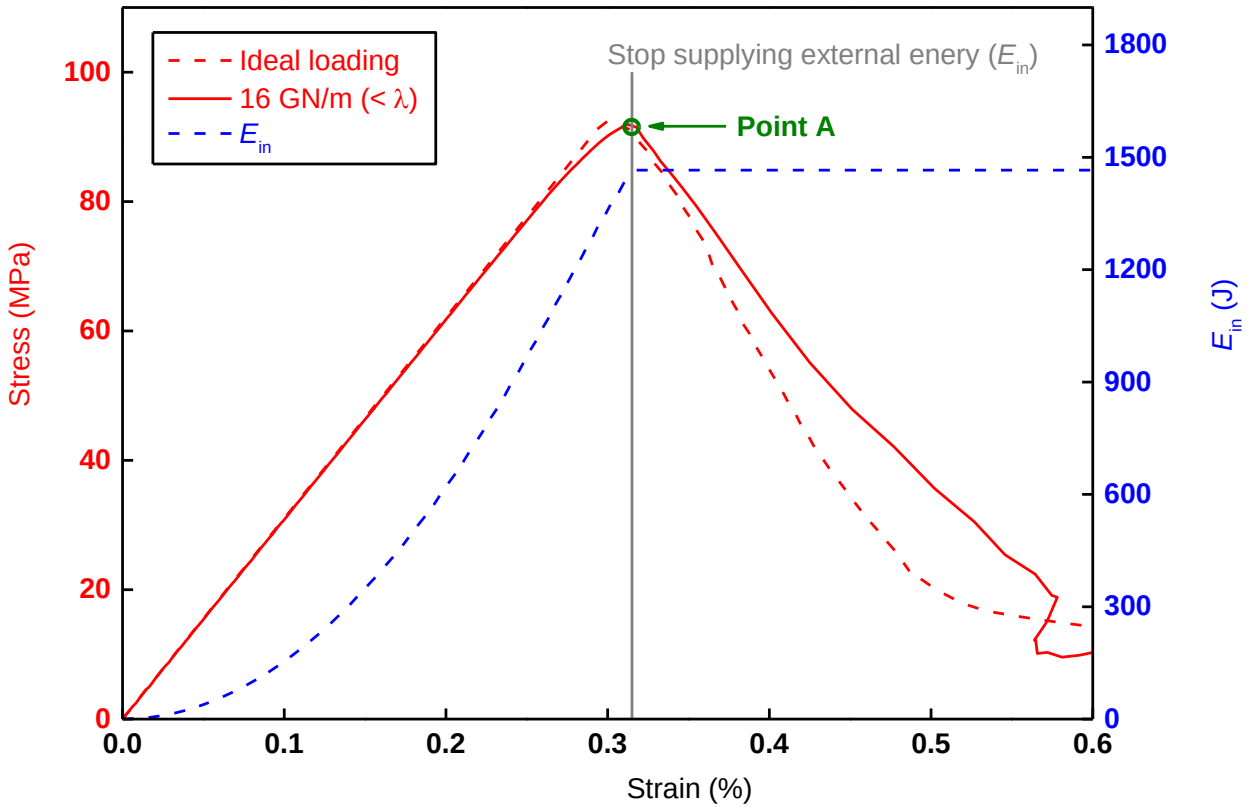

Figure A-3 Stress–strain curve of the rock under *LSS* = 16 GN/m, compared with that under the ideal loading condition.

Driven by the released energy ΔE_t from the test machine, the rock specimen continues to deform in the post-peak deformation stage and that in turn promotes stress decrease. The stress drop of the strain-softening curve follows a path the same as the unloading path of the test machine in the stress–strain space for *LSS* = 16 GN/m, which is less than the critical *LSS*. The strain-softening curve under *LSS* = 16 GN/m is more ductile than that under the ideal loading condition, indicating that there is extra energy released from the test machine to deform the rock. In laboratory testing, this amount of extra energy, which cannot be absorbed by the rock itself, can result in violent rock failure (rockburst). Therefore, the rock failure type under this loading condition is unstable.

Table A-1 shows the relation between *LSRI* (Manouchehrian and Cai, 2015) and *LSS*. Compared with the *LSRI* values under the frame-platen loading condition with the same *LSS* value shown in Table 5-5, in which ΔE_{in} is provided in the whole deformation process, the *LSRI* values are somewhat lower in this numerical experiment but rock failure types can be distinctively identified. This preliminary study indicates that even if external loading is stopped, a rock can fail if $LSS \leq \lambda$. In such a case, the strain energy stored in the loading system is sufficient to drive the rock failure process in the post-peak deformation stage. To avoid such failures, simply stopping or retracting the advancement of loading ram might not be enough; the *LSS* of a test machine has to be stiffer than the critical *LSS* loading condition of the rock.

Table A-1 Relation between *LSRI* and *LSS* together with interpreted rock failure types

LSS (GN/m)	61	24 = λ	16
LSRI	1.19	2.23	6.89
Rock failure types	Stable	Critical	Unstable

This study makes a contribution to demonstrating the theory (Salamon, 1970) that depending on the *LSS* of a test machine, the stored energy of the test machine alone without additional energy supply for deforming rock specimens can drastically change rock failure types.